An Experimental Investigation of the Effects of Surface Defects on the Laminar-Turbulent Transition of a Boundary Layer with Wall Suction

Jeanne Methel

THÈSE

En vue de l'obtention du

Doctorat de l'Université de Toulouse

Délivré par : *l'Institut Supérieur de l'Aéronautique et de l'Espace (ISAE-SUPAERO)*

Spécialité : *Dynamique des Fluides*

Présentée et soutenue le 04/11/2019 **par :**

Cam-Tu Jeanne METHEL

An Experimental Investigation of the Effects of Surface Defects on the Laminar-Turbulent Transition of a Boundary Layer with Wall Suction

---

JURY

Jens H. M. FRANSSON	Rapporteur
Jacques BORÉE	Rapporteur
Christophe AIRIAU	Président, Examinateur
Laurent MALARD	Examinateur
Grégoire CASALIS	Directeur de thèse
Maxime FORTE	Codirecteur de thèse

École doctorale :
ED MEGEP (ED468)
Unité de Recherche :
ONERA/DMPE
Date :
20 novembre 2019 (contenant un résumé français)

Dissertation submitted for the degree of

Doctor at the University of Toulouse

Awarded by: *l'Institut Supérieur de l'Aéronautique et de l'Espace (ISAE-SUPAERO)*

Specialty: *Fluid Dynamics*

Defended on November 4th, 2019 by:

Cam-Tu Jeanne METHEL

An Experimental Investigation of the Effects of Surface Defects on the Laminar-Turbulent Transition of a Boundary Layer with Wall Suction

---

Date: November 4th, 2019

To cite this dissertation:

> Jeanne Methel. An Experimental Investigation of the Effects of Surface Defects on the Laminar-Turbulent Transition of a Boundary Layer with Wall Suction. ISAE-SUPAERO, Université de Toulouse, 2019.

BibTeX entry:

```
@phdthesis{methel2019dissertation,
author={Methel, Jeanne},
title={An Experimental Investigation of the Effects of Surface
    Defects on the Laminar-Turbulent Transition of a Boundary
   Layer with Wall Suction},
school={ISAE-SUPAERO, Universit\'{e} de Toulouse},
year={2019},
address={Toulouse, France}
}
```

An Experimental Investigation of the Effects of Surface Defects on the Laminar-Turbulent Transition of a Boundary Layer with Wall Suction

by

Cam-Tu Jeanne Methel

PhD dissertation defended on
November 4th, 2019.
ISAE-SUPAERO, Université de Toulouse, France.

Abstract

The projected increase in air traffic volume has led to a renewed interest in drag reduction research to reduce aviation's environmental impact. One solution is wall suction, which can effectively postpone the laminar-turbulent transition of a boundary layer developing over an aircraft's wetted area. Since a boundary layer in the laminar regime has lower skin-friction coefficient than in the turbulent regime, a delayed transition results in lower drag and reduced fuel consumption. However, implementing a suction system is likely to introduce surface defects, especially at the junction between the suction and solid panels. Additionally, surface defects generally tend to promote transition, and could therefore cancel any drag reduction achieved by wall suction.

The aim for the present research is to study the combined effects of surface defects and wall suction on the transition of a Blasius boundary layer in two-dimensional incompressible flow. First, an experimental protocol was developed and implemented to verify the quality of the aerodynamic conditions in the test facility, and establish a reference for the smooth case with different suction distributions. As expected, wall suction always delayed transition, compared to the configuration without suction, and had varying effectiveness depending on the suction configuration. Concurrently, porous panels without suction were found to destabilize the boundary layer. Subsequently, three types of surface defects (wires, forward-facing steps and gaps) were tested with wall suction. No significant differences between configurations with and without suction were observed. In particular, the critical defect dimensions (height and/or width), for which transition occurs at the defect location, were identical regardless of the suction configuration. For subcritical defects (where transition is not triggered immediately) however, wall suction could still delay transition, albeit less effectively than in the smooth case.

Keywords: Boundary layer, Laminar-turbulent transition, Laminar Flow Control, Tollmien-Schlichting instabilities, Wall Suction, Surface defects.

Acknowledgments

If there is one phrase that comes to mind for these acknowledgments, it is "*It takes a village to raise a child*". In the present case, I can honestly say that it took a whole department (and even more, to be honest!) to "raise" me into a researcher. I would therefore like to single out the people who truly made a contribution during my three years at ONERA.

At the tip of the iceberg, I would first like to extend my thanks to the two reviewers, Dr. Jens Fransson and Dr. Jacques Borée who took the time to read this dissertation, and thanks to whom the present work greatly benefited. Thank you also to Dr. Christophe Airiau and Dr. Laurent Malard for being committee members, and for their interest in this work.

J'aimerais aussi saluer Pierre Millan et Estelle Piot pour m'avoir accueilli au sein de leur département DMPE et unité ITAC, respectivement, et de m'avoir laissé mener mes expériences quelque peu sonores, au détriment de toute la productivité du côté sud-ouest du bâtiment. Je leur suis aussi reconnaissante de m'avoir permis de participer à des congrès ainsi que de ne m'avoir jamais fait payer la facture d'électricité de ma soufflerie.

Ensuite, j'aimerais remercier mon directeur de thèse Grégoire Casalis qui, en dépit de la "distance" (nouveau portail oblige), a su être présent aux moments clefs de cette thèse pour me faire part de son expérience et de ses bons conseils. Sa pédagogie n'a jamais fait faute et a toujours amené beaucoup de nuance à ces travaux.

À Maxime Forte, my boss et co-directeur de thèse, qui malgré le nombre incalculable de fois où il m'aura "viré", je lui suis inexprimablement reconnaissante du temps, lui aussi incalculable, qu'il aura passé à m'écouter, à m'encourager, à me guider et à se salir les mains sur ma manip. Sa grande rigueur et sa passion scientifique ("Pendant que j'étais en train de faire la route cet après midi, je me suis demandé...") m'auront orienté tout le long de cette thèse et je serai éternellement reconnaissante d'avoir eu la chance de travailler en sa compagnie. Grâce à lui, j'aurai vu la plus grande soufflerie du monde, un magicien fou, un lampadaire de (trop) près et son adorable petite fille qui voulait jouer avec moi au Jardin des Plantes lors des moments les plus tendus de la rédaction. Avec tout le respect et l'affection imaginables: MERCI MAX!

À Olivier Vermeersch, mon encadrant "théorie" mais pas "théorique", qui lui aussi m'aura toujours gardé sa porte ouverte, quel que soit le niveau de..."confusion" de mes questions, je le remercie de son soutien constant et de ses encouragements précieux. Sa contribution scientifique et ses relectures éclairs auront été d'une valeur inestimable. Je lui exprime aussi ma sincère gratitude pour toutes les opportunités extra-thèse qu'il m'aura permis ainsi que ses bons conseils pour l'après-thèse.

À Fabien Méry, mon encadrant "honorifique" qui malgré sa participation entièrement bénévole à cette thèse m'aura lui aussi accordé un nombre d'heures inimaginables (et "non-pointables", je suis sûre), je le remercie sincèrement. Sans l'ombre d'un doute, son enthousiasme, ses encouragements et même son humour sans merci, auront grandement contribué à cette thèse.

Je tiens ensuite à exprimer ma gratitude à toutes les personnes qui ont formé le support "technique" et sans qui cette thèse n'aurait pas abouti. Un grand merci à Valérie Duplessis pour son soutien et son amitié ainsi qu'à Corinne Plantade pour son aide au quotidien. Je remercie

aussi Nicolas Fasano pour ses bons conseils, sa pédagogie et son potager devant l'atelier (qui, à un moment, était bien la seule chose qui "marchait" dans ma thèse) ainsi que Thomas Batmalle pour son assistance éclectique, allant de coder du LabVIEW à préparer du foie gras pour le repas de Noël.

Je suis aussi reconnaissante envers Floris Bigot pour sa réactivité et son aide dans les moments tendus ainsi qu'à Michel Schiavi et Francis Bisme pour leur contribution lors du montage initial de la manip. Marie-Louise Moretto ne m'aura pas seulement aidé aux achats mais elle m'a aussi longuement écouté lors de mes (inombrables) soucis techniques, je l'en remercie. Un grand merci à Patrick Nicouleau et à Philippe Brunet d'avoir redémarré ma soufflerie quand tous les plombs sautaient, ainsi qu'à Jean-Paul Nigoul qui m'a non seulement aidé au service impression mais qui m'a aussi ramené des urgences lorsque je m'étais déboîtée la cheville. Et j'aimerais aussi remercier très chaleureusement Marie Sanchez, qui ne s'est pas seulement occupée des locaux dans lesquels je travaillais, mais qui a aussi su égayer mes matins avec son affection et son espièglerie.

Je remercie aussi chaleureusement tous les "permanents" (quel étrange concept!) du DMPE Toulouse, du Fauga-Mauzac et même certains de Paris pour leur contribution technique ou morale à cette thèse et qui, en tant qu'ensemble, auront fait office d'énorme canard en plastique. Dans l'unité ITAC en particulier, je tiens à reconnaître Hugues Deniau pour sa gentillesse et toutes nos supers conversations (Trumpiiiie), Delphine Sebbane pour son aide toujours disponible, Jean-Philippe Brazier d'avoir été à l'écoute et Gréguy Delattre pour l'intérêt qu'il aura porté à cette thèse. Un merci spécial à Lucas Pascal avec qui on a bien rigolé (snowballs) et qui m'aura chaleureusement invité à partager de supers moments avec ses chouettes colocs (Alix, Élise, Célie, Alexia, Adèle, Max) que je remercie aussi.

Hors ITAC, je remercie Christophe Corato, Jouke Hijlkema, François Chedevergne, Julien Troyes, Jean-Michel Lamet, Lionel Tesse, Pierre Berthoumieu, Pierre Gajan, Hervé Bézard, Hélène Gaible, Geoffroy Illac, Francis Micheli, Olivier Rouzaud, Guillaume Puigt, Frédéric Bigot, Cécile Ghouila Houri et Pierre Moré de Lille, Michaël Ridel et François Monsieur 50 Hz du DEMR, l'équipe de l'atelier du DMPE/SRE, l'équipe de S2 de Modane et de F2 du Fauga: chacun a participé de près ou de loin à faire de cette thèse un moment agréable et mémorable.

En toute subjectivité, je tiens aussi à identifier et exprimer ma sincère reconnaissance aux permanents DMPE ayant le meilleur passe-temps du monde: Olivier Léon, le bloc-eur à la pince d'acier, Claire Laurent, la grimpeuse aux petites filles qui chatouillent sans pitié et Olivier Dessornes, le Bleausard qui m'aura fait découvrir LE bloc et le concept de "la collante". Rock on!!

Vient ensuite la tâche délicate de "catégoriser" les doctorants: je m'excuse d'avance de toute "erreur". Je remercie tout d'abord mes co-doctorants de promotion: Émilie Jahanpour mon unique co-doctorantE toujours souriante, Thibault Xavier mon camarade de spectacles, Jean-François Poustis mon co-martyr des JDD, Baptiste Thoraval mon compère de cinéma, Anthony Desclaux mon comparse de manips récalcitrantes, Quentin Levard un des clandestins du Fauga avec qui on aura toujours bien rigolé aux repas de Noël, Loic Van Ghèle le cuisinier aux mille talents et Jean-Etienne Durand l'autre clandestin que j'aurais plus souvent vu en ville qu'à l'ONERA. Malgré les campus et les étages différents, on aura quand même souvent trouvé l'occasion de passer de bons moments ensemble, tant au labo qu'à l'extérieur, et je vous en remercie!

Je remercie aussi les anciens, François N., François L., Jéré Derré, Maxime B., Stéphanie B. et Natacha S. pour leurs conseils (que je ne comprends que maintenant hélas!) ainsi que les générations suivantes (Julien S.-J., Loïc A., Damien T., Gaétan C., Eric N.-V., Adèle V., Victor L., Ludovic T., Yann M., Pierre S., Loris C., Rémi H., Tanguy T., Romain P., Adrian C.-G., Beatrice F., Arthur C., Nadine B., Pierre V.-M. et Valentin M.) et les post-doctorants (Christian

C., Romain F., Alexis M., Hala G.) pour la bonne ambiance et les vendredi matins gourmands et salutaires! Un petit clin d'œil fraternel à mon "little brother" Félix Ducaffy et mes "baby brothers" de thèse Adrien Rouviere et Thomas Jaroslawski: on ne choisit pas sa famille, même de thèse, alors FAÎTES DU BRUIT!! (I mean it, literally.)

Et puis, il y en a forcément quelques uns avec qui on a des atomes plus crochus. À mon co-bureau Sylvain Morilhat, le marin féru de littérature et de cuisine (la galette qui roule, qui roule...), avec qui on aura passé de nombreuses soirées à discuter et qui n'aura jamais hésité à prendre le temps de m'expliquer moultes sujets, un grand merci. J'exprime aussi toute ma gratitude à Rémi Roncen, le Wizard (or is it Warlock?) de l'humour tordant qui m'aura apporté son soutien perpétuel par ses encouragements, sa bonne humeur et d'inombrables pauses déjeuner/goûter/thé/café. Merci à Loïc Jecker, l'éleveur de levures variées, pour toutes nos conversations stimulantes qui auront été des coupures appréciées, surtout en troisième année. Je remercie aussi Lola Rousseau de m'avoir fait découvrir les pâtes à LA carbonara et pour les bons moments en randonnée, malgré des bovins belligérants. E Lorenzo Lanzillotta, ti ringrazio profondamente per avere aperto la porta della tua casa e delle tue montagne con tanta generosità e per essere un così grandissimo amico. (Che vergogna... Scusa per gli errori e per fortuna, non senti gli accenti tonici!)

Durant la thèse, j'ai aussi eu la chance de profiter de mes chères Pyrénées (ne le dîtes pas à Max, il risquerait de me virer) et je remercie donc Christophe Martin, celui qui m'aura initié à l'alpinisme, ainsi que Thibault Pouiller et Cindy Sauvaigo, qui auront partagé la même corde que moi, pour ces supers moments en montagne. Je remercie aussi affectueusement ma grande amie Chantal Sibrac de m'avoir accueilli si gentiment au sein de sa famille et pour tous nos moments de grimpe (dedans, dehors, sur spits et sur friends...) qui ont été essentiels à ma santé mentale.

Et finalement, je tiens aussi à exprimer ma reconnaissante à toutes les personnes "d'avant la thèse" qui m'ont apporté leur soutien et leur amitié durant la thèse. Merci à Charlotte Cobb, ma plus ancienne amie qui aura toujours été là pour moi, à Julia Experton qui aura été une amie fidèle et à François Sanson pour sa confiance et son amitié.

I would also like to thank my friends peppered across different countries: Nicoletta Fala, whose close contact and constant friendship evaporated the kilometers (miles?) and whose support was indispensable, Adam Ouammou and Kimranpal Mann with whom I had some of the best culinary adventures and who shared their hospitality and affection with me so generously, as well as Jas'Minique Potter, Amanda Brock, Nyansafo Aye-Addo, Theresa d'Aquila and Bryce Heckaman who have maintained their friendship despite the distance. Thank you also to Dr. Gregory Blaisdell for his help in getting admission to this PhD program and in some of my other endeavors. I also want to express my sincere gratitude to Philip and Christy Owen, who have allowed me a little spot in their wonderful family and who have supported me through all of my graduate degrees.

Je tiens aussi à remercier Florian Monteghetti pour son "apparition" durant la thèse et qui m'aura apporté son soutien, son affection et sa rigueur pendant les moments les plus difficiles de la thèse. Merci et vivement la suite!

Et bien sûr, last but most definitely not least, je remercie de tout mon coeur ma famille: mon papa, ma maman, my second dad et Michelle dont la confiance et l'affection inconditionnelles m'ont toujours guidé et encouragé.

La technique résout les problèmes et apporte des satisfactions mais elle n'est qu'un moyen et reste pauvre si on la sépare de l'esprit qui la guide.

Gaston Rébuffat

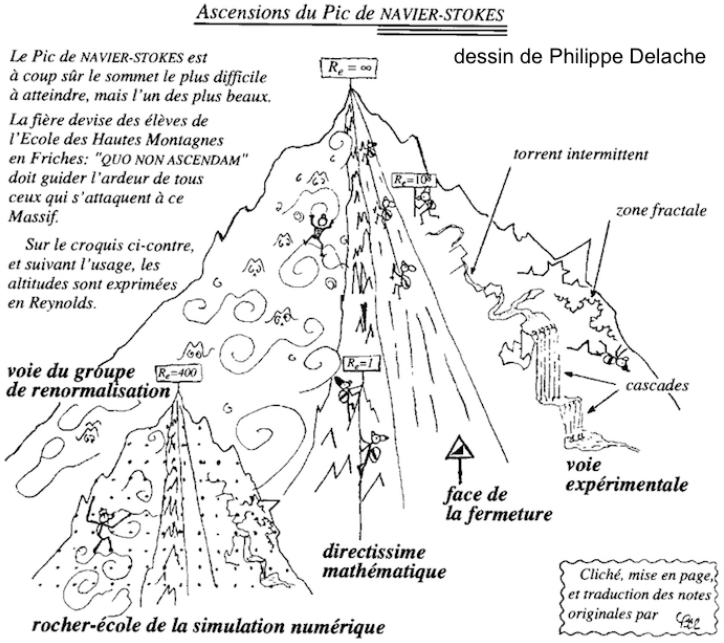

Contents

Table of Contents ix

List of Figures xiii

List of Tables xv

Acronyms xvii

Notation xix

Introduction xxi

I Literature Review 1

1 Laminar-Turbulent Transition of a Boundary Layer 3
1.1 Boundary layer theory . . . 3
1.1.1 Prandtl boundary layer equations . . . 4
1.1.2 Boundary layer parameters . . . 6
1.1.3 The Blasius solution for a laminar boundary layer . . . 8
1.2 Modeling and prediction of the laminar-turbulent transition . . . 9
1.2.1 Path to transition . . . 11
1.2.2 Small perturbation theory and the Orr-Sommerfeld equation . . . 12
1.2.3 Predicting transition location: the e^N method . . . 14
1.2.4 Numerical tools . . . 16

2 Laminar Flow Control Using Wall Suction 17
2.1 Laminar flow technologies . . . 17
2.2 Boundary layer stabilization using wall suction . . . 18
2.3 Design parameters for wall suction applications . . . 20
2.4 Current challenges to the widespread implementation of HLFC . . . 21
2.5 Effect of a porous wall without suction on transition . . . 22
2.5.1 Definitions . . . 22
2.5.2 Porous wall effect on boundary layer properties . . . 23
2.5.3 Attempts at using a porous wall for Laminar Flow Control purposes . . . 24

3 Effects of Two-Dimensional Surface Defects on Transition 27
3.1 Transition mechanisms in the presence of 2D surface defects . . . 27
3.1.1 General effects of surface defects on transition mechanisms . . . 28
3.1.2 Identification of the parameters of interest . . . 29

3.2 Flow geometry and resulting effects of 2D surface defects on transition 31
3.2.1 Steps: Forward-Facing Steps (FFS) and Backward-Facing Steps (BFS) . . 31
3.2.2 Positive surface defects: wires and humps 31
3.2.3 Negative surface defects: gaps 32
3.3 Transition prediction for flows with 2D surface defects 35
3.3.1 Empirical criteria 35
3.3.2 ΔN method 36
3.3.3 Numerical simulation approach 39
3.4 Combined effect of steps and wall suction 39

II Fundamentals for a Laminar-Turbulent Transition Investigation 41

4 Experimental Protocol for a Laminar-Turbulent Transition Study 43
4.1 Presentation of the experimental facility 43
4.1.1 TRIN 2 subsonic wind tunnel 43
4.1.2 Flat plate model 45
4.1.3 Instrumentation and data acquisition systems 45
4.2 Validation of the experimental protocol 49
4.2.1 Test section flow characterization 49
4.2.2 Baseline flat plate measurements 51
4.3 Measurement uncertainty analysis 55
4.3.1 Boundary layer profiles 56
4.3.2 Transition position 60
4.3.3 Pressure coefficient 60

III Experimental Investigations with a Wall Suction System 65

5 Wall Impedance and Suction Effects on Laminar-Turbulent Transition 67
5.1 Wall suction parameters and suction configurations 67
5.1.1 Suction panel geometric parameters 67
5.1.2 Summary of the reference 1995 study 68
5.2 Effects of a porous wall without suction 70
5.2.1 Experimental characterization 70
5.2.2 Numerical analysis 75
5.3 Effect of wall suction and suction distribution 79

6 Combined Effects of Wires and Wall Suction 89
6.1 Geometric characteristics of the wires 89
6.2 Transition location and mean flow 90
6.3 Spectral and numerical stability analyses 95

7 Combined Effects of Forward-Facing Steps and Wall Suction 99
7.1 Geometric characteristics of the FFS 99
7.2 Transition location and mean flow 100
7.3 Unsteady data analysis 106
7.4 Numerical analysis and comparison with existing ΔN models 112

8 Combined Effects of Gaps and Wall Suction **117**
8.1 Geometric characteristics of the gaps 117
8.2 Transition location and mean flow 118
8.3 Unsteady data analysis 123
8.4 Numerical analysis and comparison with an existing model 131

9 Comparison of the effects of all surface defects combined with suction **135**
9.1 Transition criteria 135
9.2 Transition mechanisms 136

Conclusion **139**

IV Appendices **143**

A Flat plate leading edge geometry **145**

B Wall suction uniformity across chambers **147**
B.1 Suction uniformity tests for each suction chamber 147
B.2 Suction uniformity tests for the suction configurations used in present study . . . 151

V French summary / Résumé **153**

Bibliography **177**

List of Figures

1.1 Schematic representation of boundary layer evolution 4
1.2 Displacement thickness δ_1 7
1.3 Momentum thickness θ 7
1.4 Schematic of boundary layer profiles with varying shape factors 8
1.5 Flow visualization of TS waves 12
1.6 Boundary layer parameter evolution during transition 13
1.7 Stability diagram and N factor evolution for a wave at frequency f_1 15

2.1 The different approaches to maintain laminar flow over an airfoi 18
2.2 Mean velocity and TS profiles with and without suction 19
2.3 Flow visualization of horseshoe vortices around perforation with suction 21
2.4 Inside the leading edge of the DLR Do 228 for HLFC flight test 22
2.5 Schematic TS instability interacting with porous wall 23
2.6 Neutral stability curves for various wall permeability 25

3.1 Effect of freestream turbulence and wires on transition Reynolds number 30
3.2 Types of two-dimensional surface defects presented in this document 31
3.3 Flow geometry around BFS and FFS from Perraud and Séraudie 2000 32
3.4 Summary of the experimental data of gaps on transition at ONERA 34
3.5 Graphical summary of the ΔN method and sample results 37
3.6 Experimental ΔN correlations for BFS and FFS 38
3.7 Numerical ΔN correlations with respect to relative height for FFS and BFS . . . 38

4.1 CAD overview of the TRIN 2 subsonic wind tunnel (Susie) 44
4.2 Photograph of the test section with flat plate 44
4.3 Numerically optimized leading edge shape 46
4.4 General layout of the flat plate detailing the suction region 46
4.5 PSD(u') showing test facility ground interference 47
4.6 Schematic representation of the Δy correction 48
4.7 Streamwise fluctuations for transition position on solid wall panel 48
4.8 Test section flow characterization 50
4.9 Microphone set-up at the test section entrance for acoustic characterization . . . 50
4.10 Acoustic data acquisition system with side view of the profiled microphone . . . 51
4.11 Overall SPL evolution over range of operating unit Reynolds numbers 51
4.12 Acoustic characterization at varying unit Reynolds numbers 52
4.13 Nominal pressure coefficient distribution along the flat plate 53
4.14 Integral values of the boundary for the solid wall (no porosity) flat plate 53
4.15 Two-dimensional transition position for the solid wall panel 54
4.16 Identification of ∼600 Hz TS profile 54

4.17 N-factor evolution for Blasius flow at operating Reynolds number 55
4.18 Output from statistical calibration for sample test 57
4.19 Calibration curve uncertainties for sample test 58
4.20 Normalized mean velocity profile for sample test with uncertainties 61
4.21 ormalized mean velocity profile for all tests with uncertainties 62
4.22 Streamwise evolution of numerical TS profiles 62
4.23 Streamwise velocity fluctuations for various constant height hotwire traverses . . 63
4.24 Nominal pressure coefficient distribution with uncertainties 63

5.1 Amplitude evolution of instabilities for suction cases from Casalis et al. 1996 . . 69
5.2 Streamwise evolution of mean velocity profiles for all panels without suction . . . 71
5.3 Two-dimensional transition position for all panels 71
5.4 Streamwise velocity fluctuations for all panel configurations without suction . . . 72
5.5 PSD(u') at a position upstream of the transition location 73
5.6 PSD(u') at x ∼508 mm for all panels 73
5.7 Velocity fluctuation profiles for all panels without suction 74
5.8 Streamwise evolution of the u' profile maximum amplitude for all panels 75
5.9 Neutral stability curve for real-only impedance 76
5.10 Neutral stability curve of imaginary-only impedance 77
5.11 Neutral stability curves based on experimental impedance values 78
5.12 N factor envelope curves from numerical analysis with impedance 78
5.13 Isocontours of α_i from linear stability theory with and without suction 79
5.14 Boundary layer profiles for all suction configurations (panel P2) 80
5.15 Experimental and numerical boundary layer profiles with suction 81
5.16 Streamwise velocity fluctuations for all suction configurations 81
5.17 Streamwise evolution of experimentally-evaluated shape factor H 82
5.18 Streamwise velocity fluctuations for *full suction* for panels P2 and P3 83
5.19 Effect of suction on u' profile evolution for panel P2 84
5.20 Effect of suction on u' profile evolution for panel P3 85
5.21 TS-profile maximum amplitude evolution for panels P2 and P3 86
5.22 Maximum N factor envelope curve for all suction configurations 87
5.23 Wall suction distribution effect on the instability at a particular frequency 88

6.1 Overview of the flat plate with the different wire locations and dimensions 90
6.2 Streamwise velocity fluctuations for different wires and suction configurations . . 92
6.3 Boundary layer profiles 1 mm downstream of the wire 93
6.4 Transition parameters variation with respect to relative wire height 94
6.5 PSD(u') upstream of WIR-300µm-640 for all suction configurations 96
6.6 PSD(u') just upstream of respective $\mathrm{Re_{xT}}$ for different wires 97
6.7 Neutral stability curves for profiles with and without inflection point 98

7.1 Overview of the flat plate with an FFS 100
7.2 Streamwise velocity fluctuations for different FFS relative heights 102
7.3 Mean velocity profiles in the FFS region for h/δ_1 ∼0.6 103
7.4 Mean velocity profiles in the FFS region for h/δ_1 ∼1.4 (crit.) 103
7.5 Mean velocity profile in the FFS region for different FFS height 104
7.6 Transition position summary for all tested FFS 105
7.7 PSD(u') upstream and downstream of the subcritical FFS 106
7.8 PSD(u') at the transition Reynolds number for the subcritical FFS 107
7.9 PSD(u') (y = 300 µm) around the FFS for C1/0.400 107

7.10 PSD(u') at the transition Reynolds number for C1/0.400 108
7.11 Velocity fluctuation profiles around the FFS for *no suction*. 109
7.12 Velocity fluctuation profiles upstream and downstream of the FFS for C1/0.400 . 110
7.13 Velocity fluctuation profiles around the FFS for *full suction* 111
7.14 Evolution of TS profiles for different FFS heights and suction configurations . . . 111
7.15 Evolution of the TS profiles maxima for different suction configurations 114
7.16 ΔN evaluation for the solid panel with FFS 115
7.17 ΔN as a function of h/δ_1 115
7.18 All suction configurations with FFS compared with other ΔN data sets 115

8.1 Overview of the flat plate with the two gap inserts 118
8.2 Streamwise velocity fluctuations for different gaps ($x_{\mathrm{GAP}} = 640$ mm) 120
8.3 Streamwise velocity fluctuations for different gaps ($x_{\mathrm{GAP}} = 360$ mm) 121
8.4 Evolution of the mean velocity profiles over critical gap 122
8.5 Re_{xT} as a function of b/h 123
8.6 Δ_{xT} vs different gap parameters 124
8.7 Comparison with experimental data from previous ONERA studies 125
8.8 PSD(u') upstream (a) and downstream (b) of a subcritical gap 125
8.9 PSD(u') at the transition position for subcritical gap ($x_{\mathrm{GAP}} = 640$ mm) 126
8.10 PSD(u') upstream (a) and downstream (b) of gaps for C1/0.400 126
8.11 PSD(u') at the transition position of different gaps for C1/0.400 127
8.12 PSD(u') downstream of critical GAP-1200µm-18mm 128
8.13 Evolution of u' profiles for GAP-1200µm-8mm ($x_{\mathrm{GAP}} = 640$ mm) 129
8.14 Evolution of u' profiles for GAP-1200µm-2.4mm ($x_{\mathrm{GAP}} = 360$ mm) 130
8.15 Evolution of u' profiles for critical GAP-1200µm-20mm ($x_{\mathrm{GAP}} = 640$ mm) 130
8.16 Evolution of u' profiles for critical GAP-1200µm-18mm ($x_{\mathrm{GAP}} = 360$ mm) 131
8.17 TS profiles maximum for a subcritical and critical gap ($x_{\mathrm{GAP}} = 640$ mm) 131
8.18 TS profiles maximum for a subcritical and critical gap ($x_{\mathrm{GAP}} = 360$ mm) 132
8.19 Comparison of the u' profile maxima for gaps at both locations for C1/0.400 . . 132
8.20 ΔN values evaluated for all suction configurations and gap dimensions 133
8.21 All suction configurations with gaps compared with a ΔN model 133

9.1 Comparison of the Δ_{xT} parameter for all wires and FFS (without detail) 136
9.2 Comparison of the Δ_{xT} parameter for all wires and FFS (with details) 136
9.3 PSD(u') at Re_{xT} for selected subcritical defects for *full suction* 137
9.4 PSD(u') at Re_{xT} for selected critical defects for *full suction* 138

B.1 Suction uniformity inside chamber C1 148
B.2 Suction uniformity inside chamber C3 149
B.3 Suction uniformity for all suction configurations 151

List of Tables

1.1 Blasius solution for laminar flow on a flat plate with zero pressure gradient . . . 10

3.1 Summary the flow geometries around cavities from Sinha et al. 1982 34

4.1 Instrument uncertainties as provided by manufacturer 59
4.2 Hotwire calibration data sets and related uncertainty parameters 60

5.1 Panel parameters 68
5.2 Experimental x_T for all configurations in Juillen et al. 1995 69
5.3 Numerical and experimental transition position for all panels without suction . . 79
5.4 Transition positions for all suction cases and all suction panels 82
5.5 Transition positions and N factors for all suction configurations (panel P2) . . . 85

6.1 Summary of the wire (WIR) geometry and position. 90
6.2 Local boundary layer thickness (numerical value) at surface defect location . . . 91
6.3 $\mathrm{Re_{xT}}$ for panel P1 ($p = 0\%$) 95
6.4 $\mathrm{Re_{xT}}$ for suction panel P2 ($p = 0.26\%$) 95
6.5 $\mathrm{Re_{xT}}$for suction panel P3 ($p = 1.34\%$) 95

7.1 Relative heights for FFS at streamwise position $x_{\mathrm{FFS}} = 430$ mm 100
7.2 Relative heights for FFS at streamwise position $x_{\mathrm{FFS}} = 640$ mm 100
7.3 Relative heights for FFS and panel P1. 101

8.1 All tested gap dimensions for $x_{\mathrm{GAP}} = 640$ mm 118
8.2 All tested gap dimensions for $x_{\mathrm{GAP}} = 360$ mm 119

A.1 Leading edge coordinates on the lower side 145
A.2 Leading edge coordinates on the upper side 146

B.1 Suction chamber pressure drop measurements over chamber C1 147
B.2 Suction chamber pressure drop measurements over chamber C2 148
B.3 Suction chamber pressure drop measurements over chamber C3 148
B.4 Suction chamber pressure drop measurements over chamber C4 149
B.5 Suction chamber pressure drop measurements over chamber C6 149
B.6 Suction chamber pressure drop measurements over chamber C7 150
B.7 Suction chamber pressure drop measurements over chamber C8 150
B.8 Suction chamber pressure drop measurements over chamber C9 150

Acronyms

BFS	Backward-Facing Step
CAD	Computer Aided Design
FFS	Forward-Facing Step
HLFC	Hybrid Laminar Flow Control
LFC	Laminar Flow Control
LST	Linear Stability Theory
NLF	Natural Laminar Flow
PSD	Power Spectral Density
rms	room mean square
rpm	revolutions per minute
TS	Tollmien Schlichting

Notation

Greek letters

α	Wave number (complex variable)
δ_1	Displacement thickness
δ_{99}	Boundary layer thickness at $0.99u_e$
θ	Momentum thickness
μ	Dynamic viscosity
ν	Kinematic viscosity
ρ	Density
σ	Standard deviation
ω	Angular frequency

Roman letters

Cp	Pressure coefficient
d	Suction hole diameter
H	Shape factor
h	Wire diameter
N	Amplification factor
p	Porosity
Re	Reynolds number
U	Streamwise (x) component of velocity
u'	Streamwise (x) component of velocity fluctuation
x	Streamwise coordinate
y	Normal coordinate to the flate plate wall
z	Spanwise coordinate

Subscripts

∞	Freestream
atm	atmospheric
dyn	Dynamic
e	Boundary layer edge
ref	Reference
SD	Surface defect
xT, T	Transition location

Introduction

In the present dissertation, the effects of surface defects on the laminar-turbulent transition of a boundary layer undergoing wall suction are experimentally investigated and analyzed. The purpose of this study is to: provide insight on the physics of the competing effects of the stabilizing wall suction and generally destabilizing surface defects on boundary layer stability; as well as offer validation data for numerical models. The current lack of transition prediction models that can account for this combined effect is one of the remaining obstacles preventing the more widespread implementation of wall suction as a drag reduction technology on conventional aircraft.

This introduction is divided in three parts. First, a general overview of the individual effects of wall suction and surface defects on boundary layer transition is briefly discussed, followed next by a presentation of the scope and objectives of the present investigation. Finally, a detailed outline of the present document is provided.

Background

The projected increase in air traffic volume, coupled with the need to reduce air pollution for environmental sustainability, has led to a renewed interest in laminar flow research to reduce aviation's fuel consumption. In particular, the objective of any laminar flow technology is to reduce skin friction drag, which can represent up to 40% of the total drag for a typical civil transport aircraft (Marec 2001).

Boundary Layer Transition

The concept of a boundary layer for flows at high Reynolds numbers was first introduced and modeled by Prandtl 1904. In the presence of relative motion between a body and a surrounding flow, the boundary layer region, located close to the body's wall, acts as an interface between the freestream region, where flow can be assumed to be inviscid, and the zero velocity (no-slip) boundary condition at the wall. High shear stresses are consequently present because of the large velocity gradients that occur across this thin region. Additionally, the boundary layer is characterized by the presence of viscous forces that are of the same order as inertial forces.

In the remainder of the present document, two-dimensional flow will be assumed unless otherwise stated. Past the stagnation point, the boundary layer first develops in the laminar regime, then goes through a more or less extended transition region, and finally settles into the fully turbulent regime. In a low freestream turbulence flow, freestream perturbations enter the boundary layer through the receptivity phase. The main process that then drives the boundary layer to transition is the linear amplification of primary modes (also known as Tollmien-Schlichting instabilities) up to a certain threshold amplitude, past which secondary and other non-linear instabilities quickly amplify and lead to the breakdown to turbulence.

The linear amplification stage can effectively be reproduced numerically using Linear Stability Theory (LST). Although mode amplification is exponential, the term "linear" refers to the assumptions that each mode is considered to develop itself independently from the others. Based on LST, amplification factors (N factors) are calculated at each frequency of interest. One transition prediction method consists in defining the transition position as the location where a threshold N_T factor is reached. This threshold N_T can be determined, for example, using Mack's relation (Mack 1977), which relates freestream turbulence and N_T, or from experimental data. In general, the efforts to predict transition and increase the extent of laminar flow over an aircraft's wetted area is driven by the fact that laminar flow has lower skin friction coefficient than turbulent flow (approximately five times lower).

Wall Suction

Two main approaches can be used to maximize the streamwise extent of laminar flow regions and delay laminar-turbulent transition: a passive approach, by using Natural Laminar Flow (NLF) airfoils, and an active approach, by implementing a Laminar Flow Control (LFC) technology. A combination of both techniques, Hybrid Laminar Flow Control (HLFC) can also be implemented. NLF airfoils were successfully developed to achieve larger laminar flow regions, compared to conventional airfoils, over the wings and empennage of commercial aircraft. However, this passive approach consists in optimizing the profile geometry around a single design point and cannot account for different operating conditions. LFC and HLFC technologies, on the other hand, can be adapted during operation so that laminar flow can be achieved over a wider operating range.

One LFC technology is to stabilize the boundary layer using wall suction. Applying wall suction on a boundary layer increases its mean velocity profile curvature (and therefore its stability), and redistributes the disturbance energy closer to the wall where there is higher viscous dissipation. As a result, the growth of boundary layer instabilities is reduced and transition is delayed.

This technique was found to be effective as early as in the 1950s, and numerous test flights and experimental data are available in the literature to attest to this fact (Braslow 1999). Based on various studies, the main design parameters for an independent wall suction system (i.e., excluding any integration issues) that were identified were: suction distribution, panel porosity, panel geometry, and suction velocity.

Numerical studies were also performed to model the effect of wall suction on boundary layer stability. Various numerical approaches demonstrated that suction is most effective when applied upstream of location where the secondary instabilities start to amplify. In attempt to use a "simple" approach, implementation of the e^N method on results from HLFC flight tests was also attempted but found to be unsatisfactory because the transition criterion used for this method seemed to vary between test flights and wind tunnel experiment. Based on these studies, wall suction modeling still requires sophisticated numerical tools that cannot easily be incorporated in the aircraft design cycle.

Surface Defects

Current manufacturing techniques do not allow to conceive the implementation of wall suction technology without introducing surface defects (e.g., gaps, forward- and backward-facing steps) at the junction between the porous and solid wall regions. Surface defects generally tend to destabilize the boundary layer either by modifying local receptivity, further amplifying existing instabilities or changing the mean flow stability by introducing inflection points in the mean

velocity profiles because of the small separation bubbles that can form around a defect. If transition occurs inside the bubble, non-linear effects can also occur inside the separation bubble.

A surface defect is termed "critical" by Tani (Tani 1961) when transition occurs immediately downstream of the defect position. In other cases, the transition position can gradually move upstream from the smooth case position, advancing closer to the surface defect location: the defects are subcritical. In these intermediate situations, the main defect parameters that can affect transition are relative geometric parameters (with respect to boundary layer thickness) and pressure gradient. In general, three-dimensional surface defects are found to generate complex three-dimensional flows and significantly amplify instabilities, resulting in much lower critical dimensions with respect to two-dimensional defects.

To model the effect of critical surface defects, the simplest approach first consisted in determining empirical criteria based on experimental data. The first criteria mainly depended on freestream properties, and were later refined to include local flow properties. As computational capabilities improved, numerical simulations were performed to study the flow around a surface defect and the resulting effect on boundary layer stability, using for example Direct Numerical Simulations or Linearized Navier-Stokes equations. Although more precise than empirical criteria, these types of numerical simulations can be relatively expensive, warranting the use of intermediate approaches.

For the less destabilizing two-dimensional surface defects, an intermediate solution consists in the ΔN approach, based on both numerical and experimental data, and LST calculations. Using this approach, the effect of surface defects on instabilities is modeled as an abrupt shift in N factors, a ΔN, that is determined based on the relative geometric parameters of the defect with respect to local boundary layer thickness. Finally, another way to predict transition with a defect can be by directly modeling a surface imperfection and calculating the resulting flow using Direct Numerical Simulations.

Framework and Objectives

Test flights or wind tunnel experiments have shown that wall suction could effectively stabilize the boundary layer, and thereby delay its laminar-turbulent transition. Numerical transition prediction models were also developed to take into account the stabilizing effect of wall suction on the boundary layer. In parallel, transition criteria were also determined for surface defects such as gaps, forward- and backward-facing steps on "natural" boundary layers, *i.e.,* without suction. However, experimental data are currently not available in the open literature to determine whether or not a boundary layer with suction behaves similarly to one without suction in the presence of a surface defect. As mentioned previously, the relative height of a surface defect with respect to the boundary layer thickness significantly influences transition. Furthermore, wall suction tends to reduce boundary layer thickness. Additional investigations are therefore required to further understand the combined effects of wall suction and surface defects on boundary layer stability. With this additional information, transition prediction models can then be modified to account for this interaction more accurately.

The objective of the present study is therefore to perform an experimental characterization of the combined effects of surface defects and wall suction on the laminar-turbulent transition of a boundary layer in two-dimensional incompressible flow. The first objective consisted in designing and building an experimental set-up and protocol to perform a transition study. Next, the practical implementation of wall suction along with characterizing the effects of suction cases without surface defects was necessary to establish baseline references. During this process, the non-negligible effect of a porous wall (through which suction is applied) on transition was established, and further investigated both experimentally and numerically. Finally three types

of surface defects (wires, forward-facing steps and gaps) were introduced on the wind tunnel model to investigate their influence on the transition of a boundary layer undergoing wall suction. Experimental characterization and analysis were performed based on measurements of the transition position, mean velocity boundary layer profiles, as well as power spectral densities and profiles of the streamwise velocity fluctuations.

Dissertation Outline

Chapters 1, 2, 3

In the first chapter, a general description of the boundary layer and the laminar-turbulent transition process in an incompressible and low freestream turbulence flow is given. A more in-depth review of the available literature on suction and porous walls effects is then discussed in Chapter 2. Chapter 3 then focuses on the effects of surface defect on transition. The few existing studies (to the author's knowledge) on the combined effects of surface defects and wall suction are also presented.

Chapter 4

Next, the objective was **to develop and validate an experimental protocol to investigate the laminar-turbulent transition of a Blasius boundary layer in a two-dimensional incompressible flow**. In this type of low freestream turbulence flow, "natural" transition occurs, resulting from the linear amplification of Tollmien-Schlichting instabilities. The test facility and flat plate model used to obtain a two-dimensional zero-pressure gradient (ZPG) flow are therefore presented in Section 2.1, along with all the necessary instrumentation and data acquisition systems. In Section 2.2, the test section flow is characterized to validate the implementation of the experimental protocol. In particular, baseline flat plate measurements are acquired to verify the presence of a two-dimensional ZPG flow in which transition is the result of the amplification of Tollmien-Schlichting instabilities. Finally, uncertainty analysis is performed in Section 2.3 to complete measurement characterization.

Chapter 5

In the following chapter, the **effects of a porous wall and suction on boundary layer transition** are investigated using the experimental protocol developed in the previous chapter. Section 5.1 justifies the choice of suction configurations with different spatial distributions that result in various transition locations. The suction panel geometries are therefore presented and the results from a reference study from 1995 are discussed. Based on these findings, suction configurations for the present investigation are selected. In Section 5.2, the effect of a porous panel without suction (i.e., wall admittance) on boundary layer stability is investigated both experimentally and numerically. Finally, Section 5.3 focuses on the effect of wall suction and its spatial distribution on transition. An experimental characterization using mean flow and unsteady data is first performed and then compared to numerical results from Linear Stability Theory (LST).

Chapters 6, 7, 8

Next, the **experimental characterization of the combined effect of wall suction and surface defects on boundary layer transition** was performed. The suction configurations defined in the previous chapter were used as a baseline reference over which surface defects could then be introduced. Each chapter corresponds to a type of tested defect: Chapters 6, 7 and 8 focus on the effect of wires, forward-facing steps and gaps, respectively, combined with wall suction. Each chapter begins with a presentation of the defect geometry and position, followed by a discussion on mean flow measurements and transition positions. Unsteady data analysis and LST calculations are then performed to enable comparison with existing numerical models whenever available.

Chapter 9

In the final chapter, the effects on boundary layer stability of all three types of surface defects combined with suction are summarized. Section 9.1 compares the transition criteria of each type of defect while Section 9.2 provides an explanation for these differences based on the varying transition mechanisms involved.

Part I

Literature Review

Chapter 1

Laminar-Turbulent Transition of a Boundary Layer

Contents

1.1 Boundary layer theory 3
1.1.1 Prandtl boundary layer equations 4
1.1.2 Boundary layer parameters 6
1.1.3 The Blasius solution for a laminar boundary layer 8
1.2 Modeling and prediction of the laminar-turbulent transition 9
1.2.1 Path to transition 11
1.2.2 Small perturbation theory and the Orr-Sommerfeld equation 12
1.2.3 Predicting transition location: the e^N method 14
1.2.4 Numerical tools 16

This chapter first introduces the concept of the boundary layer through Prandtl's boundary layer equations, and focuses specifically on the Blasius solution for a laminar boundary layer (Section 1.1). Next, the path to laminar-turbulent transition is presented along with the theoretical and numerical tools that can be used to model and predict transition position (Section 1.2).

1.1 Boundary layer theory

Using potential flow (incompressible and irrotational) theory, in which the effect of viscosity is neglected, the drag generated by the flow around an aerodynamic body cannot be evaluated. In this theory, the fluid offers no resistance to a shape change since there is a perfect slip condition at the body surface. This situation, known as d'Alembert's paradox, was resolved by the introduction of the concept of a boundary layer by Prandtl 1904. He was able to reconcile the excellent results of potential flow theory, in terms of lift prediction, to the notion of friction drag by recognizing that a flow with large Reynolds numbers around an aerodynamic body could be divided in two regions. One region is the "outer" freestream flow where pressure forces dominate, and potential flow theory is applicable. The second region, close to the body surface, is the "inner" boundary layer flow where friction forces are of the same order as inertial forces.

The boundary layer can be seen as a region of high shear stresses. These stresses are due to the presence of large velocity gradients close to the wall: over a restricted wall-normal distance, flow velocity goes from zero (with respect to the body reference frame) at the wall because of

the no-slip condition, up to the freestream velocity. Boundary layer thickness δ, in the wall-normal direction, is then defined as the distance between the wall, and the height at which the streamwise velocity is equal to the local freestream velocity, u_e. A thickness δ_{99} is more commonly used, which represents the distance where u/u_e is equal to 0.99.

A boundary layer developing spatially can be divided into three main streamwise regions corresponding to three states: laminar, transitional, and turbulent. A schematic representation of this evolution over a flat plate is shown in Figure 1.1 along with some representative streamwise velocity distributions. In the freestream region upstream of the flat plate, the velocity distribution is assumed to be uniform. Inside the boundary layer, non-uniform velocity distributions can be observed. In particular, as the boundary layer transitions from the laminar to the turbulent regime, the velocity gradient close to the wall also increases. Shear stresses are therefore greater in a turbulent boundary layer than in a laminar boundary layer. The main regions of interest in this study are primarily the laminar and transitional regimes, which will be further discussed in the following sections.

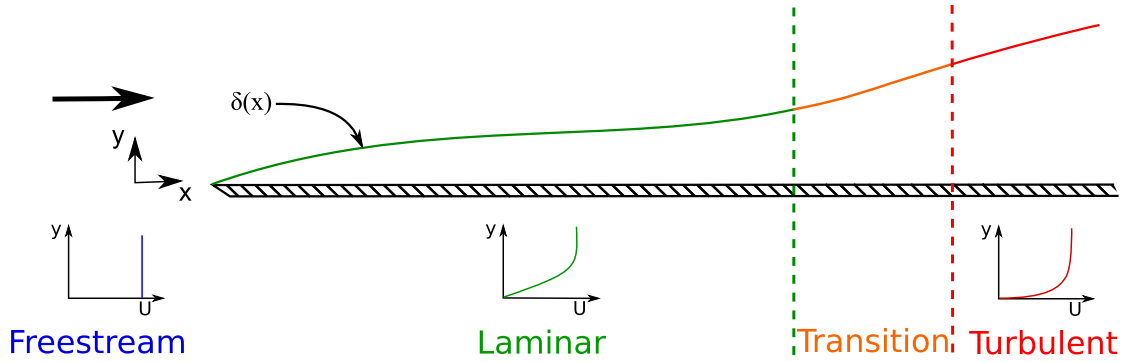

Figure 1.1. Schematic representation of boundary layer evolution over a flat plate with zero pressure gradient.

1.1.1 Prandtl boundary layer equations

In the present development of Prandtl's boundary layer equations, the flow is assumed to be two-dimensional and incompressible with negligible body forces. Additionally, flow over a flat plate is considered so that the Navier-Stokes equations can be expressed in Cartesian coordinates. The streamwise direction is defined in x, and the wall-normal direction in y. Defining the velocity vector $\vec{U}$ as

$$\vec{U} = (u, v), \tag{1.1}$$

the continuity and Navier-Stokes equations are written as:

$$\frac{\partial u}{\partial x} + \frac{\partial v}{\partial y} = 0 \tag{1.2a}$$

$$\frac{\partial u}{\partial t} + u\frac{\partial u}{\partial x} + v\frac{\partial u}{\partial y} = -\frac{1}{\rho}\frac{\partial P}{\partial x} + \nu\left(\frac{\partial^2 u}{\partial x^2} + \frac{\partial^2 u}{\partial y^2}\right) \tag{1.2b}$$

$$\frac{\partial v}{\partial t} + u\frac{\partial v}{\partial x} + v\frac{\partial v}{\partial y} = -\frac{1}{\rho}\frac{\partial P}{\partial y} + \nu\left(\frac{\partial^2 v}{\partial x^2} + \frac{\partial^2 v}{\partial y^2}\right). \tag{1.2c}$$

Equation 1.2a is the continuity equation and Equations 1.2b and 1.2c are the momentum equations in the x- and y-direction respectively. Variable P is the static pressure, and ρ and ν are the density and kinematic viscosity, respectively. The kinematic viscosity is also defined as $\nu =$

μ/ρ, with μ the dynamic viscosity. Performing scale analysis, variables are non-dimensionalized using the notion introduced by the concept of a boundary layer that there are two length scales of interest, L and δ, such that:

$$x^* = \frac{x}{L}, \tag{1.3a}$$
$$y^* = \frac{y}{\delta}, \tag{1.3b}$$
$$u^* = \frac{u}{U_\infty}, \tag{1.3c}$$
$$v^* = v\frac{L}{U_\infty \delta}, \tag{1.3d}$$
$$P^* = \frac{P}{\rho_\infty U_\infty^2} \text{ and} \tag{1.3e}$$
$$t^* = t\frac{U_\infty}{L}. \tag{1.3f}$$

In this case, L is the characteristic length at the scale of the aerodynamic body under study, δ is the boundary layer thickness, U_∞ is the freestream velocity, and ρ_∞ the freestream density. The non-dimensional Navier-Stokes equations are then:

$$\frac{\partial u^*}{\partial x^*} + \frac{\partial v^*}{\partial y^*} = 0 \tag{1.4a}$$
$$\frac{\partial u^*}{\partial t^*} + u^*\frac{\partial u^*}{\partial x^*} + v^*\frac{\partial u^*}{\partial y^*} = -\frac{\partial P^*}{\partial x^*} + \frac{\nu}{U_\infty L}\frac{\partial^2 u^*}{\partial (x^*)^2} + \frac{\nu}{U_\infty L}\left(\frac{L}{\delta}\right)^2\frac{\partial^2 u^*}{\partial (y^*)^2} \tag{1.4b}$$
$$\frac{\partial v^*}{\partial t^*} + u^*\frac{\partial v^*}{\partial x^*} + v^*\frac{\partial v^*}{\partial y^*} = -\left(\frac{L}{\delta}\right)^2\frac{\partial P^*}{\partial y^*} + \frac{\nu}{U_\infty L}\frac{\partial^2 v^*}{\partial (x^*)^2} + \frac{\nu}{U_\infty L}\left(\frac{L}{\delta}\right)^2\frac{\partial^2 v^*}{\partial (y^*)^2}. \tag{1.4c}$$

As mentioned before, the boundary layer is the region where viscous forces are of the same order as inertial forces. This relationship can be described as:

$$\frac{\text{viscous forces}}{\text{inertial forces}} \simeq \frac{\mu\frac{U_\infty}{\delta^2}}{\rho\frac{U_\infty^2}{L}} = \frac{\mu}{\rho U_\infty L}\frac{L^2}{\delta^2} = \frac{\nu}{U_\infty L}\left(\frac{L}{\delta}\right)^2 = 1. \tag{1.5}$$

Moreover, by defining the Reynolds number Re as the ratio:

$$\mathrm{Re} = \frac{U_\infty L}{\nu}. \tag{1.6}$$

and substituting this definition into Equation 1.5, the following expression can be written:

$$\frac{\delta}{L} = \frac{1}{\sqrt{\mathrm{Re}}}. \tag{1.7}$$

Equation 1.7 therefore means that the boundary layer thickness δ is very small compared to the characteristic length L in the case of very large Reynolds number. Substituting both relations 1.6 and 1.7 into the non-dimensional momentum equations gives:

$$\frac{\partial u^*}{\partial t^*} + u^*\frac{\partial u^*}{\partial x^*} + v^*\frac{\partial u^*}{\partial y^*} = -\frac{\partial P^*}{\partial x^*} + \frac{1}{\mathrm{Re}}\frac{\partial^2 u^*}{\partial (x^*)^2} + \frac{\partial^2 u^*}{\partial (y^*)^2} \tag{1.8a}$$
$$\frac{1}{\mathrm{Re}}\left(\frac{\partial v^*}{\partial t^*} + u^*\frac{\partial v^*}{\partial x^*} + v^*\frac{\partial v^*}{\partial y^*}\right) = -\frac{\partial P^*}{\partial y^*} + \frac{1}{\mathrm{Re}^2}\frac{\partial^2 v^*}{\partial (x^*)^2} + \frac{1}{\mathrm{Re}}\frac{\partial^2 v^*}{\partial (y^*)^2}. \tag{1.8b}$$

Knowing that the Reynolds number is "very large", Equations 1.8 can be simplified as:

$$\frac{\partial u^*}{\partial t^*} + u^* \frac{\partial u^*}{\partial x^*} + v^* \frac{\partial u^*}{\partial y^*} = - \frac{\partial P^*}{\partial x^*} + \frac{\partial^2 u^*}{\partial (y^*)^2} \tag{1.9a}$$

$$0 = - \frac{\partial P^*}{\partial y^*}. \tag{1.9b}$$

As a note, Equation 1.9b indicates that there is no wall-normal gradient in static pressure inside the boundary layer. At any given streamwise position, the static pressure inside the boundary layer is therefore equal to that of the freestream flow.
Finally, reverting to dimensional parameters, Prandtl's boundary layer equations for incompressible two-dimensional flow are expressed as:

$$\frac{\partial u}{\partial x} + \frac{\partial v}{\partial y} = 0 \tag{1.10a}$$

$$\rho \frac{\partial u}{\partial t} + \rho u \frac{\partial u}{\partial x} + \rho v \frac{\partial u}{\partial y} = - \frac{\mathrm{d}P}{\mathrm{d}x} + \mu \frac{\partial^2 u}{\partial y^2} \tag{1.10b}$$

$$\frac{\partial P}{\partial y} = 0 \tag{1.10c}$$

with the following boundary conditions:

$$\text{for } y = 0: \qquad u = 0 \quad \text{and} \tag{1.11}$$

$$y \to \infty: \qquad u = U_\infty. \tag{1.12}$$

These equations govern the boundary layer flow. They are used to calculate the corresponding mean velocity profiles, depending on the boundary conditions and the pressure gradient.

1.1.2 Boundary layer parameters

Earlier in the chapter, the boundary layer was described in terms of its thickness δ_{99}. Although this parameter gives a measure of the physical thickness of the boundary layer with respect to its velocity distribution, other definitions were developed to provide additional information regarding properties more closely related to fluid mechanics.

Friction coefficient

As mentioned earlier, one of the initial reasons for the introduction of the boundary layer concept was to have tools to correctly predict skin friction drag. The friction coefficient due to viscous effects is therefore a parameter of interest, and is defined as:

$$C_f = \frac{\tau_w}{\frac{1}{2}\rho U_e^2} \quad \text{where} \quad \tau_w = \mu \frac{\partial u}{\partial y}|_{y=0}, \tag{1.13}$$

where τ is the local shear stress at the wall, and U_e and ρ are the local freestream velocity and density, respectively. The skin friction drag is evaluated by integrating each contribution of the local skin friction coefficient over the entire length of the body of interest.

Displacement thickness

The presence of a boundary layer results in a mass flow rate deficit compared to the corresponding potential flow solution. The displacement thickness δ_1 is the distance normal to the reference plane by which the wall should be shifted in the inviscid flow case to obtain the same mass flow rate as in viscous flow case. In an incompressible flow of density ρ, this displacement thickness can be expressed as:

$$\delta_1 = \int_0^{\delta} \left(1 - \frac{\rho u}{\rho U_e}\right) \mathrm{d}y = \int_0^{\delta} \left(1 - \frac{u}{U_e}\right) \mathrm{d}y. \tag{1.14}$$

A graphical representation of the displacement thickness is given in Figure 1.2.

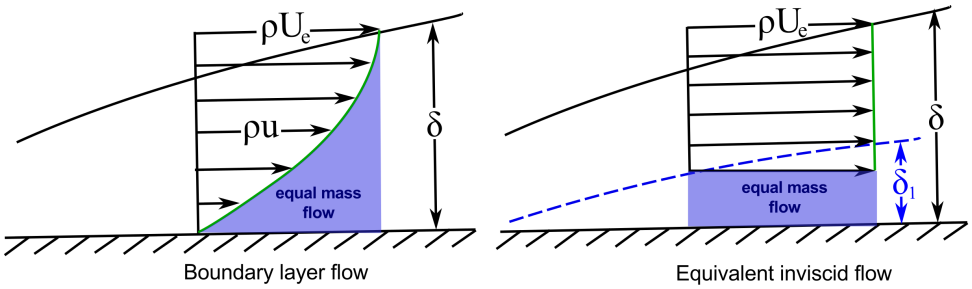

Figure 1.2. Displacement thickness δ_1 (adapted from Cousteix 1988).

Momentum thickness

In a similar fashion, the momentum thickness for an incompressible flow can be defined as follows:

$$\theta = \int_0^{\delta} \frac{\rho u}{\rho U_e}\left(1 - \frac{u}{U_e}\right) \mathrm{d}y = \int_0^{\delta} \frac{u}{U_e}\left(1 - \frac{u}{U_e}\right) \mathrm{d}y. \tag{1.15}$$

This integral length of the boundary layer corresponds to the additional thickness θ that should be added to the displacement thickness δ_1 to achieve the same momentum in the inviscid flow as in the equivalent boundary layer flow. This equivalence is expressed as:

$$\int_0^{\delta} \rho u^2 dy = \int_{\delta_1+\theta}^{\delta} \rho U_e^2 \, \mathrm{d}y. \tag{1.16}$$

Figure 1.3 graphically represents the momentum thickness.

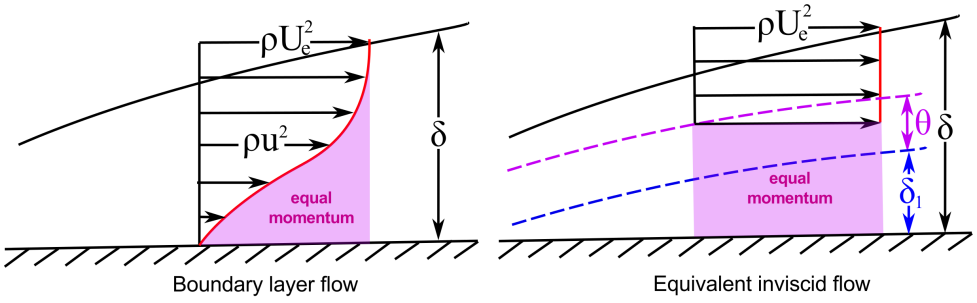

Figure 1.3. Momentum thickness θ (adapted from Cousteix 1988).

Shape Factor

As suggested by its name, the shape factor H conveys information about the shape of a boundary layer's mean velocity profile. By definition, H is expressed as:

$$H = \frac{\delta_1}{\theta}. \tag{1.17}$$

The shape factor can be a concise way to characterize a boundary layer. Figure 1.4 illustrates the relationship between shape factor and overall boundary layer profile: lower values of shape factor tend to indicate a *fuller* profile (i.e., where the curvature d^2U/dy^2 is larger). For example, in the particular case of a flat plate with no pressure gradient, a laminar (Blasius) boundary layer has a shape factor equal to 2.59, whereas for a turbulent boundary layer it is approximately 1.4.

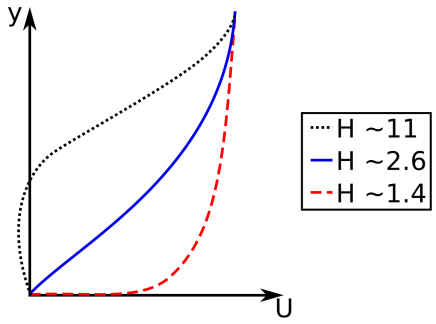

Figure 1.4. Schematic of boundary layer profiles with varying shape factors.

1.1.3 The Blasius solution for a laminar boundary layer

In the special case of a boundary layer developing over a flat plate with zero pressure gradient ZPG (*i.e.,* $dP/dx = 0$) in a stationary flow, the Prandtl equations from Equation 1.10 can be rewritten as:

$$\frac{\partial u}{\partial x} + \frac{\partial v}{\partial y} = 0 \tag{1.18a}$$

$$u\frac{\partial u}{\partial x} + v\frac{\partial u}{\partial y} = \nu\frac{\partial^2 u}{\partial y^2}. \tag{1.18b}$$

By introducing the streamfunction ψ such that:

$$u = \frac{\partial \psi}{\partial y} \text{ and } v = -\frac{\partial \psi}{\partial x}, \tag{1.19}$$

Equations 1.18a and 1.18b can be reduced to an expression involving a single unknown ψ:

$$\frac{\partial \psi}{\partial y}\frac{\partial^2 \psi}{\partial y \partial x} - \frac{\partial \psi}{\partial x}\frac{\partial^2 \psi}{\partial y^2} = \nu\frac{\partial^3 \psi}{\partial y^3}. \tag{1.20}$$

Using dimensional analysis and great intuition, Blasius further simplified Equation 1.20 by defining the following set of non-dimensional parameters:

$$\eta = y\sqrt{\frac{u_e}{2\nu x}} \tag{1.21a}$$

$$\frac{u}{u_e} = f'(\eta) \tag{1.21b}$$

$$\psi = \sqrt{2\nu u_e x} f(\eta) \tag{1.21c}$$

which will subsequently be used to solve the dimensional velocity components:

$$u = u_e f' \tag{1.22a}$$

$$v = \sqrt{\frac{\nu u_e}{2x}}(\eta f' - f). \tag{1.22b}$$

Equation 1.20 then reduces to the form of:

$$f''' + f f'' = 0 \tag{1.23}$$

with boundary conditions:

$$\text{for } \eta = 0: \quad f(0) = f'(0) = 0 \quad \text{(no slip, impermeable/solid wall)} \tag{1.24a}$$

$$\text{for } \eta \to \infty: \quad f'(\eta) \to 1 \quad \text{(freestream)}. \tag{1.24b}$$

As a note, by expressing ψ as a function of separated variables (in Equation 1.21c, ν, u_e and x are simply scaling factors, to the same degree as the constant 2), Blasius exposed a similarity property between velocity profiles on a ZPG flat plate. Self-similar solutions imply that once a single boundary layer profile is solved, all other boundary layer profiles can be found through scaling using the appropriate x and u_e. As a reference, and because these values are used throughout this document, the coordinates of the Blasius profile for laminar flow over a flat plate are given in Table 1.1.

Finally, once the velocity profiles are determined, boundary layer integral values for a ZPG flow over a flat plate, also referred to as *Blasius flow* can be defined. With $\mathrm{Re}_x = u_e x/\nu$, boundary layer thickness evolution is expressed as:

$$\delta_{99}(x) = \frac{4.92x}{\sqrt{\mathrm{Re}_x}}, \tag{1.25}$$

displacement thickness as:

$$\delta_1(x) = \frac{1.721x}{\sqrt{\mathrm{Re}_x}}, \tag{1.26}$$

and momentum thickness:

$$\theta(x) = \frac{0.664x}{\sqrt{\mathrm{Re}_x}}. \tag{1.27}$$

As a result, the shape factor is a constant value:

$$H = 2.591. \tag{1.28}$$

Another parameter of interest used throughout this document is given explicitly as:

$$\mathrm{Re}_{\delta 1} = 1.721\sqrt{\mathrm{Re}_x}. \tag{1.29}$$

Finally, the skin-friction coefficient C_f on a flat, evaluated along length L is:

$$C_f = \frac{0.664}{\sqrt{\mathrm{Re}_x}}. \tag{1.30}$$

1.2 Modeling and prediction of the laminar-turbulent transition

As briefly mentioned at the beginning of this chapter, a boundary layer growing over a flat plate passes through a transition state as it goes from the laminar to turbulent regime. Now that the laminar boundary layer has been introduced, the following section focuses on the laminar-turbulent transition, and more specifically its physical mechanisms and the theoretical tools used to determine its onset and position.

$\eta = y\sqrt{\frac{u_e}{2\nu x}}$	f(η)	f'(η)=$\frac{u}{u_e}$
0.0	0.0000	0.0000
0.1	0.0024	0.0470
0.2	0.0094	0.0939
0.3	0.0211	0.1408
0.4	0.0376	0.1876
0.5	0.0586	0.2342
0.6	0.0844	0.2806
0.7	0.1147	0.3265
0.8	0.1497	0.3720
0.9	0.1891	0.4167
1.0	0.2330	0.4606
1.2	0.3337	0.5453
1.4	0.4507	0.6244
1.6	0.5830	0.6967
1.8	0.7289	0.7611
2.0	0.8868	0.8167
2.2	1.0550	0.8633
2.4	1.2315	0.9011
2.6	1.4148	0.9306
2.8	1.6033	0.9529
3.0	1.7956	0.9691
3.2	1.9906	0.9804
3.4	2.1875	0.9880
3.5	2.2863	0.9907
4.0	2.7839	0.9978
4.5	3.2832	0.9994

Table 1.1. Blasius solution for laminar flow on a flat plate with zero pressure gradient.

1.2.1 Path to transition

Depending on the intensity of environmental disturbances, different paths to transition were identified by Morkovin et al. 1994. In the case of the present study, a two-dimensional boundary layer over a smooth flat plate develops in a freestream flow with low turbulence and low noise (i.e., low disturbance). Under these conditions, the "natural" path to transition can be expected and is described in detail in this section.

The **environmental disturbances** mentioned above can result from vorticity or acoustic perturbations in the freestream flow, or surface defects at the wall, for example. During the initial **receptivity** phase, these small freestream perturbations enter the boundary layer, and excite its primary modes. Receptivity is therefore the conversion process between the external disturbances and the boundary layer instabilities. Freestream disturbances tend to have wavelengths at given frequencies that need to go through a scattering process in order to be rescaled to boundary layer instabilities. Once some of these frequencies match the amplified natural modes (or **primary instabilities**) of the boundary layer, also known as Tollmien-Schlichting (TS) instabilities, the linear amplification process begins.

These TS waves are streamwise viscous instabilities that are convected downstream, and that can either be amplified or attenuated. The reason this phase is considered linear is due to the fact that instabilities evolve independently from one another. This assumption is further verified by the fact that the wave amplitude can correctly be modeled by linear stability theory, which will be further discussed in the following section.

Wave amplification can be altered by such parameters as pressure gradient, wall temperature or wall suction, for example. Interestingly, the existence of such waves was first discovered theoretically in parallel by Tollmien 1929 and Schlichting 1930, while the experimental validation by Schubauer and Skramstad 1948 occurred subsequently.

Past a certain wave amplification threshold, **nonlinear interactions** between TS instabilities occur as **secondary instabilities** (Herbert 1988) start to grow significantly, quickly leading to the formation of turbulent spots. Secondary instabilities are the "necessary condition" for two-dimensional TS waves to break up into three-dimensional structures. Similar to the development of TS waves in a reference mean flow, three-dimensional secondary instabilities grow and decay on the TS waves. Once their amplitude is large enough, secondary instabilities start to interact with primary instabilities. Non-linear interactions occur between the TS instabilities, which rapidly leads to **breakdown** and the appearance of the first turbulent spots. Laminar-turbulent transition is initiated. Once the boundary layer is completely dominated by increasingly large turbulent spots, transition is complete and the boundary layer is considered **turbulent**. A flow visualization of the TS waves and the breakdown to the first turbulent spots in shown on Figure 1.5.

During the laminar-turbulent transition process, the boundary layer parameters such as shape factor (H), displacement and momentum thicknesses (δ_1 and θ), and skin friction coefficient (C_f) also evolve, as shown qualitatively in Figure 1.6. In particular, although both displacement and momentum thicknesses always increase, their ratio, as described by the shape factor, decreases during transition before settling to a lower value than in the laminar regime. On the other hand, the skin friction coefficient increases significantly during transition.

Finally, note that transition occurs over a more or less extended streamwise region. The intermittency parameter, which gives a measure of the proportion of turbulent spots with respect to laminar flow, can be used to describe this region. While the flow is laminar, intermittency is equal to zero. The onset of transition, which corresponds to the appearance of the first turbulent spot, has an intermittency that first departs from zero. (Experimentally, since a zero intermittency is impossible to achieve, the threshold to determine the onset of transition is slightly greater than 0, for example 0.005.) Throughout the transition region, intermittency

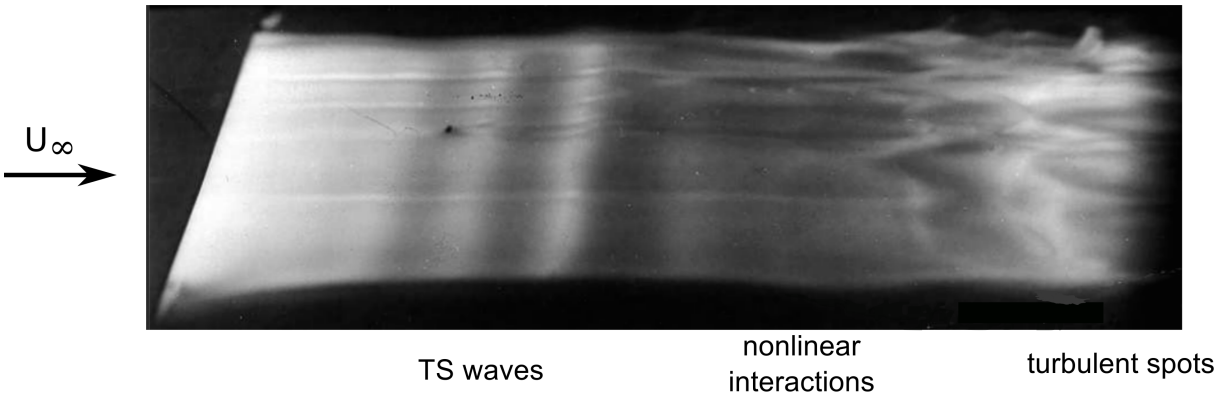

Figure 1.5. Flow visualization of TS waves on a flat plate in a water tunnel (Werlé, ONERA).

increases until reaching unity, which corresponds to fully-developed turbulence.

1.2.2 Small perturbation theory and the Orr-Sommerfeld equation

During the linear amplification phase, the growth of primary modes can be computed using linear stability theory. Depending on whether the primary modes are considered to evolve in space or in time, their definitions are modified so that either the spatial or temporal linear stability theory is used. The working principle is to understand, for a given base flow, which initially small perturbations tend to amplify to the point of triggering transition. Moreover, for this study with a two-dimensional base flow, only two-dimensional perturbations will be considered.

This assumption can be validated by first using Squire's theorem (Squire 1933). This theorem proves in temporal linear stability theory that, for each three-dimensional unstable perturbation at a given Reynolds number, there exists a corresponding two-dimensional unstable perturbation at a lower Reynolds number (i.e., in a two-dimensional subsonic flow, two-dimensional perturbations are more "dangerous" than three-dimensional perturbations). Next, recalling Gaster's relation (Gaster 1962), the properties of a disturbance growing in time can be related to those of a disturbance of equal wave number growing in space. This bridge between temporal and spatial stability theories justifies modeling perturbations in only two dimensions for the present case.

To perform the small perturbation method on the two-dimensional Navier-Stokes equation, the first step consists in using a Reynolds decomposition of the instantaneous flow properties (pressure P and velocity components u and v) into a mean and fluctuating value. An instantaneous property $\mathbf{Q}$ can be divided as such:

$$\mathbf{Q} = \bar{Q} + q', \tag{1.31}$$

where $\bar{Q}$ is the mean component and q' is the fluctuating component. With this decomposition, the instantaneous and the mean properties should each be a solution to the Navier-Stokes equations. Next, the flow is assumed to be two-dimensional, incompressible, and parallel, where $\bar{v} = 0$ and u is only a function of y such that $\bar{u} = \bar{u}(y)$. Substituting the Reynolds decomposition of each property in the 2D incompressible Navier-Stokes equations, and subtracting the Navier-

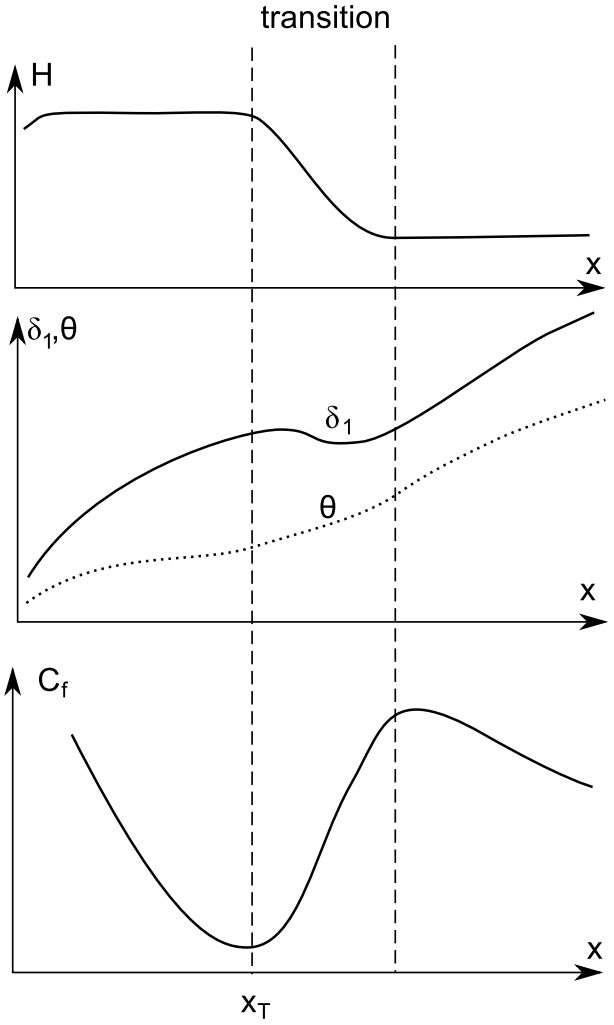

Figure 1.6. Boundary layer parameter evolution during transition.

Stokes equations for the mean flow gives the governing equations for small perturbations:

$$\frac{\partial u'}{\partial x} + \frac{\partial v'}{\partial y} = 0 \tag{1.32a}$$

$$\frac{\partial u'}{\partial t} + \overline{u}\frac{\partial u'}{\partial x} + v'\frac{d\overline{u}}{dy} + \frac{\partial p'}{\partial x} - \frac{1}{\mathrm{Re}}\left(\frac{\partial^2 u'}{\partial x^2} + \frac{\partial^2 u'}{\partial y^2}\right) = 0 \tag{1.32b}$$

$$\frac{\partial v'}{\partial t} + \overline{u}\frac{\partial v'}{\partial x} + \frac{\partial p'}{\partial y} - \frac{1}{\mathrm{Re}}\left(\frac{\partial^2 v'}{\partial x^2} + \frac{\partial^2 v'}{\partial y^2}\right) = 0. \tag{1.32c}$$

Next, the small perturbation is assumed to be a normal mode of the form:

$$q'(x,y,t) = \hat{q}(y) \cdot e^{i(\alpha x - \omega t)}. \tag{1.33}$$

Since a boundary layer grows in space, the spatial linear stability theory is used. Therefore, $\alpha = \alpha_r + i\alpha_i$, the wave number, is a complex quantity, and $\omega = 2\pi f$, the angular frequency, is real. The perturbation equation can therefore be reformulated as:

$$q'(x,y,t) = \hat{q}(y) \cdot e^{-\alpha_i x} \cdot e^{i(\alpha_r x - \omega t)}. \tag{1.34}$$

The variable $\hat{q}(y)$ corresponds to the eigenfunction that gives the mode structure through the boundary layer. Substituting the normal-mode form of the perturbation from Equation 1.34 into Equation 1.32, the following equations are obtained:

$$\mathrm{i}\alpha\hat{u} + \frac{\mathrm{d}\hat{v}}{\mathrm{d}y} = 0 \tag{1.35a}$$

$$-\mathrm{i}\omega\hat{u} + \mathrm{i}\alpha\bar{u}\hat{u} + \hat{v}\frac{\mathrm{d}\bar{u}}{\mathrm{d}y} + \mathrm{i}\alpha\hat{p} - \frac{1}{\mathrm{Re}}\left(-\alpha^2\hat{u} + \frac{\mathrm{d}^2\hat{u}}{\mathrm{d}y^2}\right) = 0 \tag{1.35b}$$

$$-\mathrm{i}\omega\hat{v} + \mathrm{i}\alpha\bar{u}\hat{v} + \frac{\mathrm{d}\hat{p}}{\mathrm{d}y} - \frac{1}{\mathrm{Re}}\left(-\alpha^2\hat{v} + \frac{\mathrm{d}^2\hat{v}}{\mathrm{d}y^2}\right) = 0. \tag{1.35c}$$

This system of equation can be reduced to a single equation, function of $\hat{v}$, the well-known Orr-Sommerfeld equation:

$$\frac{\mathrm{d}^4\hat{v}}{\mathrm{d}y^4} - 2\alpha^2\frac{\mathrm{d}^2\hat{v}}{\mathrm{d}y^2} + \alpha^4\hat{v} - \mathrm{iRe}\left[(\alpha\bar{u} - \omega)\left(\frac{\mathrm{d}^2\hat{v}}{\mathrm{d}y^2} - \alpha^2\hat{v}\right) - \alpha\hat{v}\frac{\mathrm{d}^2\bar{u}}{\mathrm{d}y^2}\right] = 0 \tag{1.36}$$

with boundary conditions where, commonly, the no-slip condition is enforced at the wall:

$$\text{at } y = 0 : \hat{v} = 0 \; ; \; \frac{\mathrm{d}\hat{v}}{\mathrm{d}y} = 0$$

and disturbances go to zero far from the wall, in the freestream flow:

$$\text{for } y \to \infty : \hat{v} \to 0 \; ; \; \frac{\mathrm{d}\hat{v}}{\mathrm{d}y} \to 0.$$

The solutions (eigenvalues) to the Orr-Sommerfeld equation 1.36 are found using a dispersion relation, i.e., only specific combinations of Reynolds number Re, wave number α and angular frequency ω can constitute eigenvalues. This local analysis therefore allows to identify whether a particular wave with a given frequency at a given Reynolds number will be amplified or attenuated. These solutions are most commonly presented in the form of a stability diagram. In particular, given the rightmost term of Equation 1.34, the stability of the perturbation can be directly related to the sign of the amplification rate α_i such that:

$\alpha_i < 0$: the wave is amplified
$\alpha_i > 0$: the wave is attenuated
$\alpha_i = 0$: the wave is neither amplified nor attenuated

1.2.3 Predicting transition location: the e^N method

The Orr-Sommerfeld equation can be used to determine the local stability of a wave with a given frequency at any point in the region of linear amplification. However, since receptivity mechanisms cannot currently be precisely modeled, the absolute value of the wave amplitude is difficult to evaluate. The amplification, defined as the ratio of amplitudes A/A_0, is used instead, and is expressed as:

$$\ln\left(\frac{A(x)}{A_0}\right) = \int_{x_0}^{x} -\alpha_i \mathrm{d}x = N_f(x), \tag{1.37}$$

where A_0 is the initial wave amplitude at point x_0 (the critical point at which the instability starts to amplify) for a given frequency. The relationship between a stability diagram introduced in the previous section and the amplification N_f of three chosen frequencies is given in Figure 1.7.

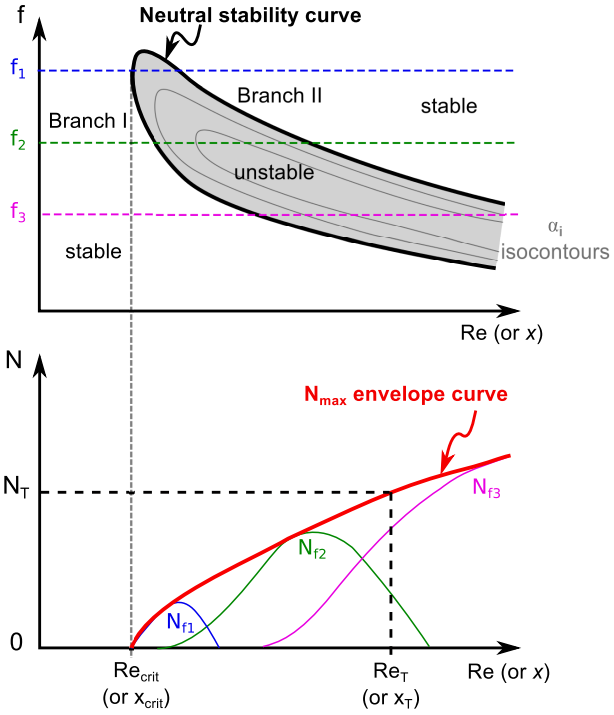

Figure 1.7. Stability diagram and N factor evolution for a wave at frequency f_1.

However, since there is no *a priori* knowledge of which frequency will be responsible for triggering transition, an envelope curve of the maximum N_f factors is defined as:

$$N(x) = \max_f [N_f(x)]. \tag{1.38}$$

This N factor is the basis for the e^N method, developed by both Van Ingen 1956 and Smith and Gamberoni 1956 independently, and used to determine laminar-turbulent transition location. With this method, transition starts once the N factor reaches a certain threshold value N_T. Abscissa Re_T (or x_T) corresponds to the position of the onset of transition, as illustrated in Figure 1.7.

In the case of TS-wave induced transition, an empirical law given by Mack 1977 relates the turbulence level Tu to the threshold value N_T. This relationship was established using a compilation of numerous wind tunnels' data across the world and is given as follows:

$$N_T = -8.43 - 2.4 \cdot \ln(Tu) \quad \text{for } 10^{-3} \leq Tu \leq 10^{-2}. \tag{1.39}$$

Crouch 1997 compared different transition prediction tools from an industrial application point of view. Although being a simple method with relatively good transition prediction, it is important to keep in mind that the e^N method only takes into account the linear growth of disturbances, and combines effects from freestream turbulence, excitation, and nonlinear breakdown into a single parameter: the threshold N_T. Crouch suggests that non-linear amplitude-based methods (such as non-linear parabolized stability equations) represent the most accurate tools for transition prediction but that complexity in implementation or prohibitively high computational costs prevent their application in an industrial setting. Instead, the author suggests that, for flows with relatively low freestream turbulence level, a promising compromise between the two methods mentioned above is a linear amplitude-based method coupled to a variable N-factor approach once the linear approximation breaks down, so that receptivity effects can be included and prediction improved.

1.2.4 Numerical tools

For this investigation, two in-house ONERA numerical tools were used and are very briefly introduced in this section.

Boundary layer code: 3C3D

The ONERA code 3C3D solves Prandtl's boundary layer equations for three-dimensional boundary layers using a method of characteristics along local streamlines (Houdeville 1992). In the context of this study, the code was used to calculate numerical laminar boundary layer profiles for input in linear stability analyses, and integral boundary layer parameters. A normal velocity can be imposed at the wall to replicate the effect of wall suction on the boundary layer.

Linear stability code: CASTET

The ONERA code CASTET is a linear stability code that solves the Orr-Sommerfeld equation for three-dimensional compressible flows. For this study, numerical boundary layer profiles, calculated using 3C3D, were input into CASTET to obtain local stability information, such as what is summarized in Figure 1.7.

Chapter 2

Laminar Flow Control Using Wall Suction

Contents

2.1 Laminar flow technologies 17
2.2 Boundary layer stabilization using wall suction 18
2.3 Design parameters for wall suction applications 20
2.4 Current challenges to the widespread implementation of HLFC 21
2.5 Effect of a porous wall without suction on transition 22
2.5.1 Definitions 22
2.5.2 Porous wall effect on boundary layer properties 23
2.5.3 Attempts at using a porous wall for Laminar Flow Control purposes 24

The concept of the boundary layer and its laminar-turbulent transition now being established, the purpose of this chapter is to broadly present wall suction as method to stabilize the boundary layer and delay its transition. First, a brief overview of the different technologies to promote laminar flow (Section 2.1). The stabilizing effect of wall suction, in particular, is presented (Section 2.2), followed by the different design parameters that need to be taken into account when developing a suction system (Section 2.3). A discussion on the current challenges that still hinder the more widespread implementation of wall suction is also provided (Section 2.4). Finally, a short literature survey on the effects observed, mainly numerically, of a porous wall on boundary layer stability is provided (Section 2.5).

2.1 Laminar flow technologies

Current environmental and economic constraints on the aviation industry have led to a renewed interest in technologies to reduce aircraft fuel consumption. One solution is to reduce the skin friction drag, which can represent up to 40% of the total drag of a typical commercial airliner (Marec 2001). As mentioned in the previous chapter, a laminar boundary layer has a lower skin friction coefficient than a turbulent boundary layer. Therefore, an aircraft's skin friction and overall drag can be significantly reduced when maximizing the extent of laminar flow over its wetted area by delaying laminar-turbulent transition. In fact a study on business jets by Holmes et al. 1985 found that a 15% skin friction drag reduction with respect to a baseline configuration could be achieved if flow over the wings and empennage was kept laminar.

Two main approaches exist to control transition: a passive approach (Natural Laminar Flow, NLF) and an active approach (Laminar Flow Control, LFC). Implementation of NLF consists

in designing airfoil profiles that "naturally" maintain laminar flow with geometries that generate favorable pressure gradients over the largest possible regions. On the other hand, boundary layer stabilization using LFC requires the use of an additional technology, such as wall suction, blowing or wall cooling.

A third approach emerged, Hybrid Laminar Flow Control (HLFC), which combines both NLF and LFC at strategic positions. The most common HLFC technique considered by aircraft manufacturers includes LFC (i.e., wall suction) in the leading edge region followed by a NLF geometry. A schematic representation of all three approaches is given in Figure 2.1.

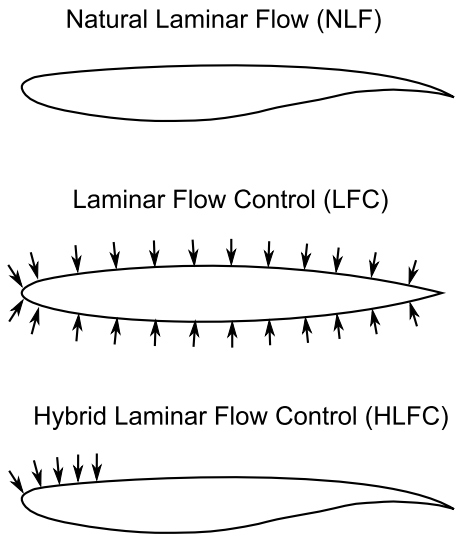

Figure 2.1. The different approaches to maintain laminar flow over an airfoil.

The present chapter (and document) mainly focuses on LFC through wall suction. However the topic of this dissertation, i.e., the combined effects of wall suction and surface defects, is also relevant to HLFC technologies, where surface defects can arise at the junction between a suction panel and an impermeable wall.

2.2 Boundary layer stabilization using wall suction

The purpose of any type of Laminar Flow Control (LFC) technique is to increase the stability of the laminar boundary layer. For low speed two dimensional flows, the linear amplification of Tollmien-Schlichting waves is attenuated through an active form of control so that secondary instabilities, and therefore the onset of laminar-turbulent transition, are delayed.

As summarized by Saric et al. 2011, the curvature of a boundary layer mean velocity profile $\partial^2 U/\partial y^2$(i.e., the second derivative of the streamwise velocity with respect to the wall-normal direction) has a significant influence on boundary layer stability. Evaluating the boundary layer momentum equation near the wall, and assuming that μ is only a function of temperature T results in the following expression:

$$\mu \frac{\partial^2 U}{\partial y^2} = \frac{\partial P}{\partial x} - \left(\frac{d\mu}{dT}\right)\left(\frac{\partial T}{\partial y}\right)\frac{\partial U}{\partial y} + (\rho \mathbf{V_0})\frac{\partial \mathbf{U}}{\partial \mathbf{y}} \quad \text{as } y \to 0. \tag{2.1}$$

Given that a profile is more stable when its curvature is more negative, the equation thus illustrates the different effects that can be called upon to stabilize the boundary layer. On the right-hand side of the equation, the first term describes boundary layer stabilization using the pressure gradient, the working principle behind NLF airfoils. If flow is accelerated as a result of

a negative pressure gradient (i.e. a *favorable* pressure gradient), the boundary layer is less likely to transition. The second term is the modification of the near-wall viscosity through thermal exchange. In the case of air, the boundary layer is stabilized by cooling the wall such that $dT/dy > 0$.

Finally, the last term is the relevant parameter in the case of wall suction where a negative V_0 corresponds to the suction velocity at the wall. The equation illustrates that, theoretically, as suction velocity increases (V_0 becoming more negative), the boundary layer curvature term becomes more negative, which indicates that the boundary layer is stabilized. As shown on Figure 2.2, excerpted from Reynolds and Saric 1986, the mean velocity profile on which suction is applied is slightly fuller. In addition to the modifications to mean velocity distribution, Figure 2.2 also illustrates how suction also slightly affects the fluctuating velocity profiles.

In the previous paragraph, the term "theoretically" was used to acknowledge the possibility of "oversuction", where wall suction actually results in boundary layer destabilization. Further details on this phenomenon will be discussed in a subsequent section. The effect of wall suction therefore results in the attenuation of the linear amplification process: TS waves reach their critical amplification further downstream from the "natural" transition case, thereby delaying transition.

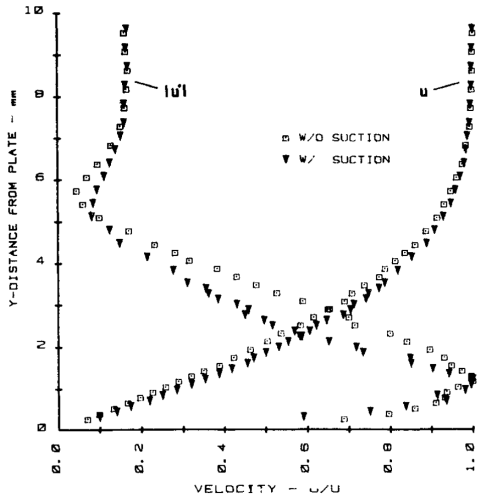

Figure 2.2. Comparison of experimental mean velocity and TS profiles with and without suction (from Reynolds and Saric 1986).

Although maintaining laminar flow over an aircraft's entire wetted area is an unrealistic expectation, the effectiveness of wall suction was repeatedly proven, and its application over key regions can lead to significant skin friction drag reduction. Test flights performed as early as in the 1940s by Wetmore et al. 1941 and the 1950s by Head 1955, with wall suction through slots or porous walls, showed its effectiveness in maintaining laminar flow over the regions of interest. Despite these encouraging results, structural constraints and the potential presence of fuel reservoirs depending on the surface limited the use of wall suction to the leading edge regions of the wings and empennage. Wind tunnel and test flight experiments were also performed to better understand the effects of the different parameters (suction distribution, suction panel porosity, etc.) in suction systems. A brief overview of the results from these studies will be given in the following section but more details can be found in Joslin 1998 and Braslow 1999.

2.3 Design parameters for wall suction applications

With increasing manufacturing capabilities, especially in terms of laser-drilling, wall suction through perforated metal sheet or porous panels has recently been favored over the use of slot suction. Between 1985 and 1991, both Dassault on a Falcon 50 and Boeing on a B757 performed some of the first test flights with wall suction through perforated titanium sheets. For both aircraft, suction was applied in the leading edge region of the wings (while keeping compatibility with the anti-icing systems and the flaps) and proved effective in maintaining large regions of laminar flow. According to Maddalon 1991, in the case of the B757, laminar flow was found as far as 65% of chord, which corresponds to a local skin friction drag reduction of 29% with respect to the turbulent wing. Concurrent to the test flights, wind tunnel experiments were also conducted to identify the key parameters that influenced the performance of independent suction systems (i.e. without taking into account any issues related to the integration of such a system on an actual airframe.)

Juillen et al. 1995 experimentally investigated the effects of discontinuous suction and **suction distribution** over a flat plate with Blasius flow. The suction region, located downstream of the critical abscissa, was divided into nine independent suction chambers in the streamwise direction. This set-up was intended to be similar to a real application of a suction system where stringers are necessary to maintain the structural integrity of the wing surface and prevent recirculation in the case of swept wings. For a constant suction mass flow rate, the authors found that the suction distribution had a significant influence on transition position. Laminar-turbulent transition could be similarly delayed with suction applied over all the chambers as well as over strategic chambers, located upstream of the position where secondary instabilities start to grow. Of all the suction distribution tested, authors reported cases where the onset of transition was delayed by as much as 35% of the transition position without suction. Similar results had also been reported by Maddalon et al. 1990 from a flight experiment with suction through micro-perforated panels near the leading edge region of a swept wing, where suction flow rate and location were modified. Larger regions of laminar flow were also achieved for configurations that had earlier chord-wise suction, i.e. where instabilities were still small.

A follow-up study on the same experimental set-up as Juillen et al. 1995 was subsequently performed to investigate the effect of **suction panel porosity**, defined as the ratio of the open area with respect to the total area (Juillen et al. 1999). Different porosities were achieved through different hole spacing-to-diameter ratios. Results showed that levels of porosity did not have as strong of an influence on transition location as suction distribution.

Another component of interest in the design of a suction system for HLFC is the **suction panel geometry**, which can be divided into four controllable parameters: panel thickness, and perforations' diameter, spacing and pattern. Reneaux and Blanchard 1992 concluded that hole diameters should not be so small that the sucked flow is over-accelerated, and destabilizes the boundary layer by the formation of horseshoe vortices. On the other hand, perforations should not be so large that the holes now constitute a source of surface roughness or that the pressure drop across the panel is not sufficiently strong to prevent outflow from the chambers back into the boundary layer. Perforations should therefore be small with respect to the boundary layer thickness. Additionally, MacManus and Eaton 1996 found that, although the perforate inlet shape did not have a significant effect on the flow, streamwise vorticity could be increased for inclined perforations.

Reneaux and Blanchard 1992 also found that a triangular hole pattern, compared to a square pattern, allowed for higher critical suction velocities, above which suction starts to destabilize the boundary layer (i.e., oversuction). Authors also acknowledged the lack and need for transition criteria for a boundary layer undergoing suction, and strongly recommended that additional

studies be performed to address this issue.

Finally, **suction velocity** is another parameter of interest. As mentioned earlier, as suction velocity increases, the boundary layer generally tends to be more stabilized. In an experimental study, Gregory 1962 was able to visualize, using smoke, horseshoe vortices form around holes with diameters of the order of several millimeters through which suction was being applied, as shown in Figure 2.3. As suction velocity increased, the horseshoe vortices of adjacent holes started interacting with each other, and actually destabilized the boundary layer enough to trigger transition. A further increase in suction velocity resulted in a stabilizing interaction between the different horseshoe vortices and the boundary layer became laminar again. This experiment, along with another experimental study by Crowley and Atkin 2016, therefore show how sensitive transition can be with respect to suction velocity. Arnal et al. 2000 likened the effect of holes with suction to that of roughness elements due to the streamtubes entering the perforations.

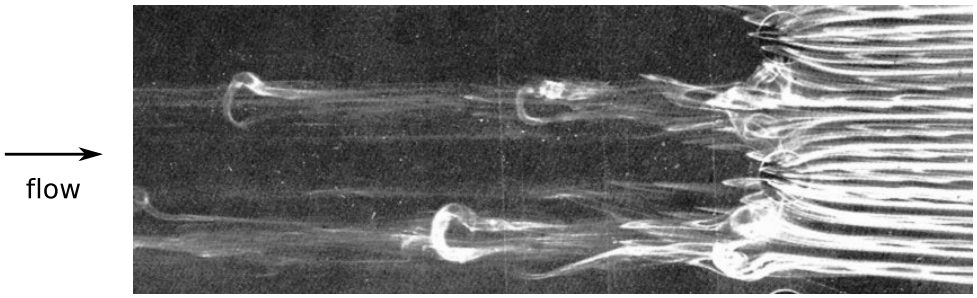

Figure 2.3. Flow visualization using smoke of the horseshoe vortices in a laminar boundary layer undergoing suction through perforations (taken from Gregory 1962).

2.4 Current challenges to the widespread implementation of HLFC

As interest in HLFC technologies regained interest in the early 1990s, the numerous wind tunnel experiments and flight tests that occurred at that time (summarized by Joslin 1998 and Schrauf 2004) testify to the complexity of implementing these technologies for more widespread and commercial applications. More recently, Krishnan et al. 2017 gave a review of the current status of HLFC systems, and divided the main challenges that still need to be addressed into five categories. The first challenge is related to the suction system. The pressure differential across the permeable surface can be achieved: either passively, by using the "natural" pressure gradient generated across an aerodynamic surface, such as on the current Boeing 787-9 empennage or in the configuration suggested by Zahn and Rist 2018; or actively with a pump or compressor. When considering the latter case, the added complexity of fitting such a system in the limited space available in the leading edge region, as shown in Figure 2.4, is another factor to take into account. Additional data would therefore be necessary to quantitatively determine how the increased cost incurred by the added weight and complexity of an active suction system is outweighed by the drag reduction benefits of applying wall suction.

The next challenge consists in maintaining the HLFC surface free of surface contamination, especially from insects, which represent a cyclic and recurrent issue during operation. Although various approaches to tackle this issue have been tested (e.g., applying solvents that loosen insect residue, covering the surface with a sacrificial layer, using a Kruger flap as a shield near the leading edge region or blowing air through permeable surfaces), none has emerged as a definitive solution, and current tests are still ongoing.

Figure 2.4. Inside the leading edge of the DLR Do 228 for HLFC flight test (from Meyer et al. 2003).

In addition to insect contamination, ice formation is another challenge that has to be addressed, for both laminar flow and safety considerations. On one hand, HLFC systems have to be designed to be compatible with existing anti-icing and de-icing systems as well as potential Kruger flaps/slats. On the other hand, introducing wall suction on the vertical or horizontal stabilizers would require installing an additional anti-icing system (Krishnan et al. 2017). The interaction between wall suction and anti-icing systems still have to be investigated.

Another concern with commercial implementation of wall suction is in designing the control and monitoring system. For example, if decisions in route planning are heavily influenced by the projected fuel burn with HLFC, an entire monitoring and backup system needs to be designed to assist pilots who have to modify their course in case of malfunction of the suction system.

Finally, the last challenge is related to the reliability of an HLFC system. In particular, any non-conformity from the nominal surface roughness, either due to external factors (e.g. insect contamination or bird strikes) or aircraft-related issues (e.g. corrosion or deviation from manufacturing tolerances) could result in increased fuel burn, and cancel the predicted benefits of wall suction. Further understanding the flow physics and ultimately the sensitivity of the laminar-turbulent transition of a sucked boundary layer is therefore needed to allow for the development of robust design tools.

2.5 Effect of a porous wall without suction on transition

Some studies recognized the interaction between the boundary layer and a passive porous surface, and either tried to understand its effect on both laminar or turbulent boundary layers, or attempted to harness this effect to stabilize a boundary layer. In the following section, a summary of these findings is given after a brief introduction on the different terms used to describe the porous walls.

2.5.1 Definitions

Suction panels can be referred to using many different definitions. A few terms that can commonly be found in order to avoid any confusion are:

- **permeable, (passive) porous, non-zero admittance, perforated :** refers to surface through which flow can penetrate
- **compliant wall :** commonly refers to a flexible surface, either passive or controlled actively for flow control purposes (Carpenter 1990)
- **acoustic impedance :** the property to characterize the opposition of a medium to the flow resulting from an acoustic pressure. Tollmien-Schlichting waves propagating in the

boundary layer can also generate a fluctuating pressure field, which forces air through the porous medium (Carpenter and Porter 2001). Generally, the impedance is defined as:

$$Z_w = \frac{\text{fluctuating component of pressure at the wall}}{\text{unsteady normal velocity at the wall}} \tag{2.2}$$

- **acoustic admittance :** the reciprocal property of acoustic impedance
- **liner :** a material consisting of a porous panel mounted over a network of cavities (e.g., honeycomb or plenum chambers), generally used for noise reduction by dissipating incident acoustic energy through the working principle of a Hemholtz resonator. Distributed wall suction systems, where a perforated panel is mounted over suction chambers, could also be considered as an atypical liner, as shown in Figure 2.5.

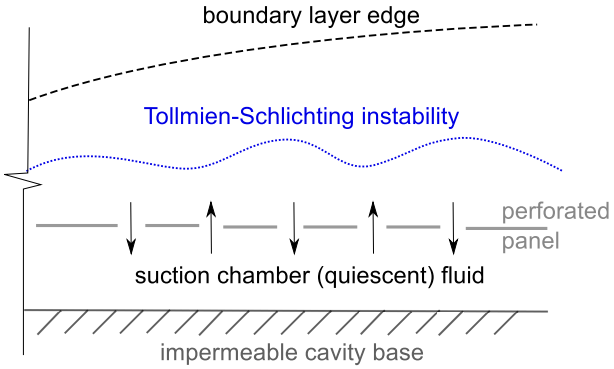

Figure 2.5. Schematic showing the analogy with a liner of a TS instability interacting with porous wall (from Carpenter and Porter 2001).

2.5.2 Porous wall effect on boundary layer properties

Lekoudis 1978 numerically studied the effect of passive porous walls on the stability of a two-dimensional incompressible boundary layer. With a large plenum chamber under the porous sheet, travelling waves formed inside the plenum and interacted with the boundary layer above the sheet. In this study, certain values of chamber depth, sheet thickness and perforation spacing were tested, and resulted in a stabilizing effect on the boundary layer. However, Lekoudis also cited two studies in Russian (that could not be acquired by the present author) by Gaponov in which a destabilizing effect due to the non-zero disturbance velocity at the wall was calculated for a similar configuration of a suction panel over a plenum chamber. One possible explanation was based on numerical results from Burden 1970 where wall porosity destabilized a laminar boundary layer. Burden suggested that local velocity fluctuations through the pores of the wall promoted fluctuations already present in the boundary layer, resulting in increased Reynolds stresses. Regardless of some of the contradictory observations published by the different authors cited above, all of their results tend to indicate that there exists a non-negligible effect from a porous wall on boundary layer stability.

Another approach to understanding the effect of a porous wall on boundary layer stability is in terms of receptivity. Heinrich et al. 1988 identified the two main regions where receptivity occurs and can therefore be modified. The first region is near the leading edge, where boundary layer thickness is small but grows rapidly. The second region is located in regions of lower wall curvature, in which the boundary layer, naturally developing more slowly, has to make a rapid adjustment due to short-scale perturbations such as gaps, steps or changes in wall

boundary conditions. Inside this second region, Crouch 1994 identified two receptivity mechanisms: localized receptivity, due to localized surface variations such as steps, gaps or humps; and non-localized receptivity due to extended regions of short-scale variations such as waviness, distributed roughness or uneven suction.

In the context of hybrid laminar flow control (HLFC), wall suction is only applied over a limited region (often near the leading edge) resulting in porous/impermeable and impermeable/-porous wall junctions. Additionally, in the case of a suction region divided in discrete chambers, the boundary layer will have to repeatedly adjust itself between porous and impermeable surfaces.

At these junctions, the two types of receptivity mechanisms mentioned above can occur according to Heinrich et al. 1988. The first mechanism (localized receptivity) is due to the adjustment in the mean boundary layer flow because of the presence of a surface discontinuity at the wall junctions. The second receptivity mechanism (non-localized receptivity) can be related to the change in wall-admittance between the porous/impermeable (or *vice-versa*) surfaces, as diffracted acoustic waves with short local length scales couple with the TS waves. This case can occur even in the absence of suction through the porous surface. Choudhari 1994 numerically studied the effect of non-zero wall admittance, and found that resistance-dominated surface impedances have a more destabilizing effect than reactance-dominated surface impedances for a two-dimensional boundary layer over a flat plate. Crouch 1994 also points out that non-localized acoustic receptivity is the strongest source of excitation for TS waves (although localized surface disturbances and vortical freestream disturbances can also be a source of non-negligible receptivity).

2.5.3 Attempts at using a porous wall for Laminar Flow Control purposes

With the rising interest in HLFC, investigations were recently performed on the effects of porous wall on boundary layer properties either as an alternative laminar flow control method, or in the context of increasing the accuracy of wall suction models.

Carpenter and Porter 2001 studied passive porous walls for LFC applications. Their idea was to stabilize the boundary layer by reducing or removing the energy production from the Reynolds stresses. Since, in the absence of viscosity, the streamwise and normal velocity perturbations are out of phase by 90 degrees exactly, Reynolds stresses are zero and no energy is transferred to the TS waves. Viscosity is responsible for bringing about the appropriate phase change so that TS waves can grow. Authors then noticed that wall admittance is often complex, meaning that the flow through the pores is usually out of phase with the driving pressure generated by the TS waves as they push flow through the porous wall. Although the main purpose of the article was to determine some of the key parameters for a porous wall to have a stabilizing effect, authors found that for a large number of cases, a porous wall could have a destabilizing effect on the boundary layer and result in TS wave growth.

On the other hand, Tilton and Cortelezzi 2015 set out to understand why linear stability theory using the no-slip condition coupled to a normal velocity at the porous wall boundary usually overpredicted the effectiveness of wall suction on boundary layer stability. Permeability was therefore taken into account in their model of wall suction. In that configuration, an *asymptotic suction boundary layer* (ASBL) forms, where the boundary layer flow is allowed to penetrate the porous wall and plenum chamber underneath. The authors were able to show that wall permeability significantly destabilized TS waves. Figure 2.6 indeed shows that for increasing value of wall permeability, the critical Reynolds number decreases and the range of “dangerous" non-dimensional frequencies F widens. This destabilizing influence of a porous surface thereby explained why previous linear stability models where not able to better capture the effect of wall suction. By reproducing results from an experimental and numerical study on an ASBL

performed by J. Fransson and Alfredsson 2003 in which permeability was not taken into account, Tilton and Cortelezzi concluded that for $\mathrm{Re}_{\delta_1} \leq 2500$, the effect of wall permeability becomes less significant.

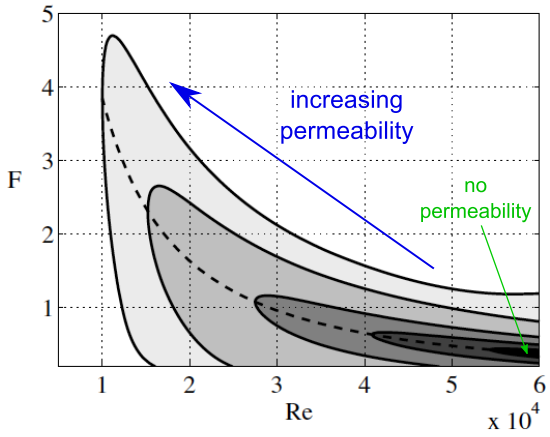

Figure 2.6. Neutral stability curves showing the decrease in critical Reynolds number for increasing wall permeability (from Tilton and Cortelezzi 2015).

A permeable surface without suction was therefore observed to have a non-negligible effect on boundary layer stability. Regardless of whether or not this effect could be used as a passive laminar flow control technique, understanding the interaction between boundary layers and porous walls seems to be one area of investigation which could help improve transition prediction models for HLFC purposes.

Chapter 3

Effects of Two-Dimensional Surface Defects on Transition

Contents

3.1 Transition mechanisms in the presence of 2D surface defects 27
3.1.1 General effects of surface defects on transition mechanisms 28
3.1.2 Identification of the parameters of interest 29
3.2 Flow geometry and resulting effects of 2D surface defects on transition 31
3.2.1 Steps: Forward-Facing Steps (FFS) and Backward-Facing Steps (BFS) . . . 31
3.2.2 Positive surface defects: wires and humps 31
3.2.3 Negative surface defects: gaps 32
3.3 Transition prediction for flows with 2D surface defects 35
3.3.1 Empirical criteria 35
3.3.2 ΔN method 36
3.3.3 Numerical simulation approach 39
3.4 Combined effect of steps and wall suction 39

Despite notable improvements in aircraft manufacturing and assembly techniques, surface defects can still be present on critical parts. On aerodynamics surfaces, such as the wings or empennage, these defects can either be two-dimensional (steps, gaps, waviness, etc.) or three-dimensional (screw heads, perforations, insects, ice, etc.). In the context of the present document, only two-dimensional surface defects will be discussed.
This chapter therefore provides a general overview of the effects of two-dimensional surface defects on boundary layer transition. First, the transition mechanisms that take place in the presence of defects are discussed (Section 3.1). Next, the flow geometries that are generated due to the presence of chosen surface defects (steps, wires, humps or gaps) are presented (Section 3.2) followed by a discussion of the different approaches that can be used to predict transition due to defects (Section 3.3). Finally, some existing studies on the combined effect of surface defects and wall suction are presented (Section 3.4).

3.1 Transition mechanisms in the presence of 2D surface defects

In a two-dimensional boundary layer, laminar-turbulent transition is the result of the linear amplification of TS waves. The initial perturbations that eventually lead to the formation of these TS waves can either come from the freestream flow or from within the boundary layer,

through surface defects, for example. In the latter case, surface defects can influence the flow through two means: by modifying receptivity, and therefore the sensitivity of the boundary layer to additional perturbations; and by further amplifying existing instabilities by modifying the mean flow.

In general, surface defects tend to have a destabilizing effect on the boundary layer that can be divided in two main scenarios: moving the transition location further upstream with respect to the smooth case, and triggering transition at the location of the defect. Since both of these scenarios ultimately result in increased skin friction drag, accurately characterizing the effects of surface imperfections will assist in determining transition criteria for the design, manufacturing and assembly of laminar airfoils.

The general effects of two-dimensional surface defect on laminar-turbulent transition are presented along with the different parameters used to best characterize a surface defect.

3.1.1 General effects of surface defects on transition mechanisms

Surface defects can act on boundary layer stability with the flow around the defect either remaining attached or separating once or multiple times. In the first case, with an attached boundary layer, the surface discontinuity can affect transition by modifying receptivity or further amplifying currently established instabilities (Arnal et al. 2008). In the second case, in addition to the effects mentioned for the attached case, small separation bubbles can form around the defects. The first effect of these separation bubbles is to change the mean flow stability by introducing inflection points in the mean velocity profiles, which make the profile inviscidly unstable, according to the Rayleigh theorem of linear stability theory (Rayleigh 1880). The second effect is to generate non-linear effects inside the separation bubble when transition is triggered inside the bubble (Dovgal et al. 1994).

For this last case, Tani 1961 characterized the surface defect as “critical" (or “supercritical"). He performed experimental investigations on the effects of wires on the transition of a ZPG flat plate, and suggested that the transition mechanisms change depending on whether or not the defect is critical. According to his definition, in the presence of subcritical surface defects, the boundary layer separates at the defect location but laminarly reattaches, and transition is still the result of the linear amplification of TS waves. More explicitly, in the present document, a subcritical surface defect refers to the case where transition occurs far (in the order of multiple defect heights) from the defect location. On the other hand, when a defect is critical or supercritical, transition occurs immediately downstream of the defect location. The different means through which surface defects change boundary layer stability are further discussed in the present section.

Klebanoff and Tidstrom 1972 studied in detail the effects of positive surface defects on the transition mechanism. The authors performed an experimental investigation on a ZPG flat plate with wires of varying diameters and at different locations. The majority of their findings correspond to the subcritical case. Their first major observation is that downstream of a subcritical two-dimensional defect, the transition mechanism is the same as on a smooth flat plate: transition is the result of the linear amplification of viscous-driven instabilities. These findings were significant in invalidating the postulate that vortex shedding from the defect starts to govern transition. In fact, the authors note that they did not observe “highly concentrated discrete vortices" upstream of the final breakdown to turbulence.

Instead, a “recovery region" was defined (which now corresponds to the “separation region") downstream of the surface defect in which the mean flow shows signs of distortion due to the surface defect. The “recovery position" then corresponded to the location after which the flow returns to the type of distribution that would be encountered in a smooth configuration. Within the recovery region, amplification of frequencies corresponding to the TS instabilities was much

greater than outside the recovery region. Additionally, high frequencies, outside the range of TS instabilities, were observed in the recovery region but damped out completely. However, closer to critical flow conditions, the high frequencies that are initially damped, then start to amplify again. Authors attribute this latter behavior as an indication of potential non-linear interactions.

Nayfeh et al. 1990 found similar results when they performed stability calculations for flows across a two-dimensional rounded hump. Both primary and secondary (or subharmonic) instabilities were amplified as the boundary layer traveled over the hump, and in general amplification increased when the hump height was increased. Additionally, if a separation bubble formed downstream of the hump, then amplification of the primary and secondary instabilities was significantly larger than in the case without separation.

Klebanoff and Tidstrom 1972 also analyzed boundary layer profiles upstream and downstream of some of their surface defects. Below a given Reynolds number, differences in amplification inside the recovery zone became negligible, regardless of the surface defect's relative height. However, as unit Reynolds number increased, the downstream boundary layer profiles were increasingly inflectional. The authors postulated that if surface defects of considerably greater relative heights than those in their study were to be tested, transition may result from an inflection-type instability rather than from viscous-driven instabilities.

As numerical and experimental tools improved, investigations started focusing on boundary layer receptivity. Receptivity can be modified by forcing the boundary layer to adjust rapidly over a short streamwise scale. In a numerical investigation, Goldstein 1985 was able to show that the conversion of low frequency freestream disturbances to high frequency boundary layer instabilities (i.e., receptivity) is more likely in regions where the boundary layer mean flow changes quickly. Surface defects therefore force a short scale variation on the mean flow, and enhance the boundary layer's sensitivity to freestream disturbances.

Michalke and Al-Maaitah 1992 performed calculations to investigate the other source of changes in receptivity: small separation bubbles close to surface discontinuities. Using the product of the amplitude of an excited unstable wave with its local growth to characterize receptivity, authors found that velocity profiles inside the separation bubble and close to separation were much more receptive to excitation, compared to Blasius flow profiles.

On the experimental side, Dovgal and Kozlov 1990 also investigated the influence of separation bubbles, due to the presence of steps and humps, on receptivity. They found that only the instabilities, excited upstream of the separation bubble and at frequencies corresponding to the unstable frequencies of the separated layer, penetrated the separated flow and continued to be amplified downstream. The instabilities that were otherwise further amplified downstream had been generated at the separation point.

3.1.2 Identification of the parameters of interest

In one early study, Fage 1943 experimentally studied the effect of different types of surface defects (rounded and rectangular humps and rounded cavities) on the transition of a zero-pressure gradient flat plate, and established empirical relations to predict the minimum defect height to start affecting transition.

These relations were a first attempt at predicting a critical height for a surface discontinuity; however, a later reanalysis of various available data by Dryden 1953 in the 1950s established a more relevant correlation between the transition Reynolds number and the defect's relative height with respect to the local boundary layer thickness. Additionally, surface defects (mainly wires, in Dryden's review) with increasing heights were found to gradually move transition upstream (i.e., closer to the defect), instead of abruptly bringing transition to the discontinuity location, as was previously conjectured. More generally, studies, such as those on gaps summa-

rized by Béguet et al. 2016 or on forward-facing steps by Costantini et al. 2015, showed that transition criteria are more relevant when expressed in terms of **non-dimensional geometric parameters (e.g., height- or depth-to-width ratio)** and **local flow properties (e.g., boundary layer thickness or local Reynolds number)**.

Comparing data by Stuper 1949 and Tani and Hama 1953, Dryden also hypothesizes that the relative effect of a defect on transition (for example, reducing the transition Reynolds number by half with a wire of relative height 0.5) is not significantly affected by **freestream turbulence**. Further investigations summarized by Tani 1961 refine Dryden's hypothesis by showing the negligible effect of freestream turbulence once the surface defect is close to being critical, meaning that transition occurs at the location of the defect. For subcritical defect relative heights, freestream turbulence has a noticeable effect, as shown in Figure 3.1. For a given wire relative height under ∼0.6, the initial transition Reynolds number Re_{xT} increases while freestream turbulence decreases. For these low wire heights, freestream turbulence therefore still has an influence on transition. However, all curves collapse onto a single curve for greater wire heights: transition is dominated by the surface defect.

Finally, the overall **pressure gradient** of the mean flow can have an influence on the stability of a boundary layer going over a surface discontinuity, as shown in Forte et al. 2015. However, since the investigations presented in this document were performed on a ZPG flat plate, this effect will briefly be discussed later.

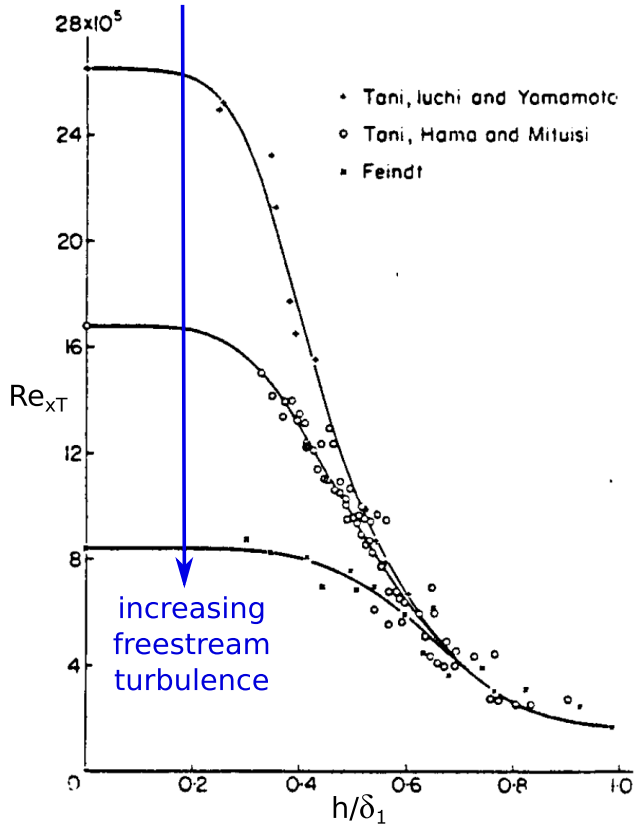

Figure 3.1. Effect of freestream turbulence variation on transition Reynolds number for a range of surface defect (wires) relative heights (from Tani 1961).

3.2 Flow geometry and resulting effects of different types of two-dimensional surface defects on transition

The specific effects on boundary layer transition are presented for different types of two-dimensional surface discontinuities: forward- and backward-facing steps, humps and wires, and gaps as illustrated on Figure 3.2. Since only two-dimensional defects are conditions, the dimension in the y-direction, h, corresponds to the wire or step height or to the gap depth and in the x-direction, b, corresponds to the gap width.

Figure 3.2. Types of two-dimensional surface defects presented in this document.

3.2.1 Steps: Forward-Facing Steps (FFS) and Backward-Facing Steps (BFS)

The most general means through which rectangular steps influence boundary layer stability is through small separation bubbles. Sinha et al. 1981 experimentally studied separating flow downstream of a BFS. The authors found that reattachment length linearly increased with Reynolds number in the case of laminar reattachment but started to decrease once transition occurred within the separation bubble. Turbulence intensity profiles downstream of the critical step displayed two local maxima: the upper one corresponded to the shear layer undergoing transition and continuously increased in the streamwise direction, while the lower one was in the recirculating region and decreased in magnitude as the inflection point in the mean velocity profile moved towards the wall.

To compare the effects of BFS and FFS, Perraud and Séraudie 2000 and Perraud 1997 solved two-dimensional incompressible Navier-Stokes equations asumming steady laminar flow around each type of step to perform linear stability calculations for freestream velocities between 50 $m.s^{-1}$ and 150 $m.s^{-1}$. Based on these results, a general schematic of the flow geometry around a BFS and an FFS is shown in Figure 3.3. In the case of the FFS, an initial separation bubble formed upstream of the step, confined to a region of length between 2 and 6 step heights. For the FFS with greater height, a second separation bubble, which could extend of 6 to 12 step heights, was found. On the other hand, in the case of the BFS, the separation bubble that formed could reach up to 30 step heights in length.

The larger separation bubbles found around a BFS seem to indicate that a BFS has a more adverse effect on boundary layer stability than an FFS. Wang and Gaster 2005 experimentally studied the effect of both FFS and BFS on transition at different freestream velocities, and actually found that the BFS induced earlier transition than the FFS. In the previously mentioned study by Dovgal and Kozlov 1990 (where the effect of separation bubbles due to surface defects were experimentally studied), authors also measured velocity fluctuations downstream of a BFS as having a magnitude almost twice that of the velocity fluctuations downstream of an FFS. A BFS therefore generally tends to destabilize the boundary layer more significantly than an FFS.

3.2.2 Positive surface defects: wires and humps

Another type of surface defect that was investigated is wires and humps. In his study on the effect of wires on a ZPG flat plate, Tani 1961 found that, in general, as a wire's relative height

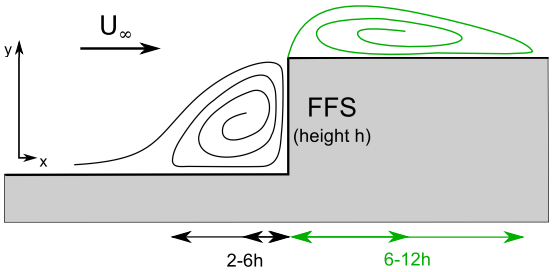

(a) Schematic of the flow geometry around an FFS.

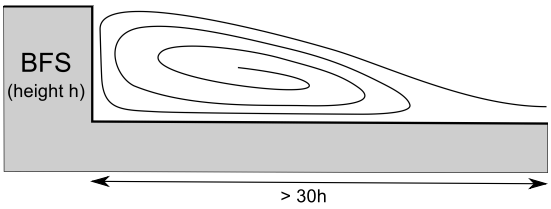

(b) Schematic of the flow geometry around a BFS.

Figure 3.3. Flow geometry around BFS and FFS (schematic using results from Perraud and Séraudie 2000).

with respect to the local boundary layer displacement thickness, h/δ_1, increased, the transition Reynolds number decreased. However, as a note, the transition Reynolds number started to increase and data points departed from the single curve if the ratio of transition location-to-defect location, x_T/x_{SD}, was less than 1.1.

A similar experimental study, with a wire in a two-dimensional flow over a wedge (i.e., with a pressure gradient), was performed by Watanabe and Kobayashi 1991. At locations further downstream from the wire, authors observed that the spectra of the longitudinal velocity fluctuations *u'* exhibited some high frequency components, an indication that the flow was approaching a fully turbulent state. These high frequencies seem similar to those observed by Klebanoff and Tidstrom 1972 for the larger wire diameters that were tested during their study. These observations indicate that the presence of wires results in the amplification of instabilities.

Nayfeh et al. 1987 then performed numerical simulations and stability calculations for flows going over rounded humps of varying height-to-width ratios. The defect's effect on boundary layer stability was determined in terms of growth rate of the instability at the most dangerous frequency. At first, a decrease in growth rate is observed as the boundary layer experiences a favorable pressure gradient over the forward face of the hump. Inversely, on the aft face of the hump, the boundary layer is in an adverse pressure gradient, and instability growth rate increases. If flow separates downstream of the hump, as in the case of large height-to-width h/b ratios, the growth rate is significantly increased compared to the case where flow stays attached. Authors also found that the effect of the hump on boundary layer stability was best characterized by the height of the hump relative to the boundary layer thickness rather than by the location of the hump with respect to Branch I of the neutral curve.

Wörner et al. 2003 also performed a series of DNS to investigate the effect of both rectangular and rounded humps on the stability of a two-dimensional boundary layer. These authors observed the same evolution of the instabilities over the rounded humps as mentioned above, emphasizing that a hump had an overall destabilizing effect. In particular, the height, more than the width of the hump, was found to have the greatest influence on boundary layer destabilization. Finally, although a rounded hump was less destabilizing than a rectangular hump, both types of humps were found to destabilize the boundary layer more than an FFS of comparable size.

In general, positive surface defects such as wires and humps can be likened to an association of an FFS followed by a BFS, and having an overall destabilizing effect on the boundary layer.

3.2.3 Negative surface defects: gaps

Cavities are another type of surface discontinuity that can be found on aerodynamic surfaces. These types of defects can be classified according to their dimensions and the resulting flow

patterns that are generated. Initially, Charwat et al. 1961 divided cavities into two categories. The first one is *open* cavities, where the boundary layer separates at the upstream corner of the cavity, and reattaches near the downstream corner. The second category is *closed* cavities, where the boundary layer reattaches at the bottom of the cavity and separates again, ahead of the downstream cavity wall. Authors suggest that the distinction between open and closed cavities occurred for values of width-to-depth ratios close to 11, given the high speed flows under investigation.

Sarohia 1977 also performed an experimental investigation for lower velocity flows over shallow cavities on axisymmetric bodies. At these low freestream velocities, the width-to-depth ratio division between open and closed cavities was found to be closer to 7 or 8. Open cavities were then further divided into *deep* and *shallow* cavities. *Deep* cavities were observed to act as resonators, in accordance with previous results from Rossiter 1964, with the shear layer over the cavity providing a forcing mechanism. In some cases, the resonant oscillations were established and corresponded to the natural acoustic modes of the cavity. On the other hand, in *shallow* cavities, the cavity oscillations are the result of propagating disturbances that are amplified inside the shear layer. Simultaneously, a periodic shedding of vortices with the same frequency as the cavity oscillation occurs. The author found that the laminar-turbulent transition of the cavity shear layer was delayed by the large amplitude oscillations up to a certain maximum cavity width.

An experimental study by Sinha et al. 1982 then provided detailed information on the flow geometry around two-dimensional cavities in low velocity flow over a flat plate. Cavity depth-to-width ratio was again found to be the appropriate parameter to differentiate *deep*, *closed shallow*, *open shallow* and *open* cavities. In accordance with the two previously mentioned studies, the width-to-depth ratio dividing a closed and open cavity was approximately equal to 10. The importance of the ratio between the boundary layer thickness at the cavity location and the cavity depth was suggested but the authors recommended that further investigations were necessary to properly understand its influence.

Based on static pressure distributions, Sinha *et al.* also related the flow over a closed cavity to the association of a BFS followed by a FFS. In an open cavity however, the flow was mainly governed by a single laminar eddy with some occasional secondary vortices near the corners. Finally, the flow geometry inside deep gaps was more complicated, with multiple laminar vortices rotating over one another. A summary of the different types of cavities and their flow geometry and parameters are given in Table 3.1.

Perraud et al. 2014 performed numerical studies on different types of two-dimensional surface defects to further determine the parameters to characterize a gap. In addition to width-to-depth ratio, authors suggested that both gap location and width had a significant influence on the instability amplification. In a numerical and experimental investigation of the effects of gaps in a two-dimensional flow with pressure gradient performed by Forte et al. 2015, cavities with varying width-to-height ratios were tested on an ONERA-D airfoil. In a strongly favorable pressure gradient, where the boundary layer was stable and remained laminar up to 90% of chord, transition moves directly downstream of the gap once critical conditions were reached. On the other hand, in a less favorable pressure gradient (and therefore less stable boundary layer), transition was found to gradually move upstream, as the gap started to destabilize the boundary layer. In particular, width seemed to be the driving parameter when determining transition criteria. In fact, depth did not seem to have a significant effect on transition for width-to-depth ratio greater than 5. Comparisons with an earlier study by Olive and Blanchard 1982, on the influence of gaps on a flat plate in low velocity flow, confirmed the existence of width-to-displacement thickness and depth-to-displacement thickness values below which a gap does not affect transition. A summary of the studies performed at ONERA on the effects of

Re_h	Re_b	h/b	δ_h/h	Classification	Flow configuration
662	6333	0.104	2.22	shallow, open	
662	19000	0.035	2.22	shallow, closed	
1324	9500	0.139	1.1	shallow, open	
1324	19000	0.069	1.1	shallow, closed	
2648	1058	2.5	0.56	deep	
2648	2648	1	0.56	open	
2648	5296	0.5	0.56	open	
2648	19000	0.139	0.56	open	

Table 3.1. Summary the different flow geometries around cavities with various parameters (from Sinha et al. 1982).

gaps on transition is given by Béguet *et al.* and the results are summarized in Figure 3.4.

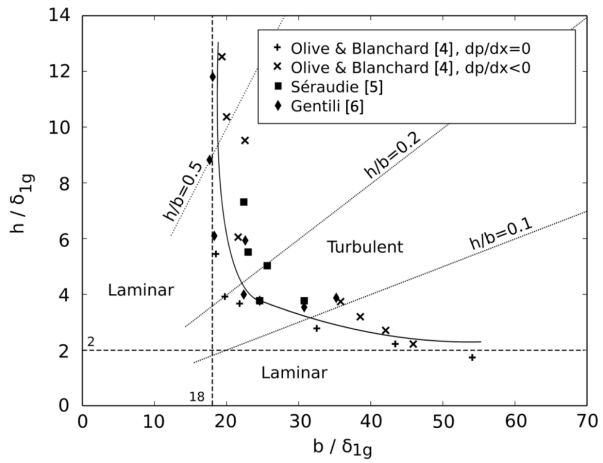

Figure 3.4. Summary of the experimental data of gaps on transition at ONERA (from Béguet et al. 2016). Note: In this figure, δ_{1g} corresponds to δ_1 in the rest of the present document.

Finally, Zahn and Rist 2015 performed some two-dimensional DNS that included acoustic phenomena to investigate the effect of deep gaps on transition. Although previous studies, such as the one by Perraud et al. 2014, suggest that extremely deep gaps should not affect linear stability, the present authors observed an influence on TS amplification of gaps with Reynolds numbers based on depth Re_d ranging $48{\cdot}10^3$ to $168{\cdot}10^3$ because of resonance effects inside the gaps. In addition to the amplification of existing TS waves, new TS waves were also generated by the wall-normal velocity fluctuations generated by a standing wave at the entrance of the deep gaps.

Overall, depending on a gap's width-to-depth ratio and category, the flow geometry within the gap can be different and can affect the boundary layer through different mechanisms. However, although location and width-to-depth ratio are parameters that can affect transition, width was found to be the most significant parameter to determine the effect of a gap on boundary layer stability.

3.3 Transition prediction for flows with 2D surface defects

3.3.1 Empirical criteria

Empirical criteria were developed for different types of two-dimensional surface defects commonly found on aerodynamic surface: forward- and backward-facing steps, humps and gaps. This type of criteria offers the advantage of being relatively simple and easy to use at the cost of reduced accuracy and limited information on the actual transition position. These limitations can be attributed to the fact that criteria are often determined based on selected defect parameters (*e.g*, width only for gaps) and databases combining data from disparate sources such as test flights, wind tunnel experiments on flat plate and profiles, etc. Empirical criteria are therefore useful in an initial design approach but need to be carefully considered.

Effect of Forward- and Backward-Facing Steps

Forward- and backward-facing steps (FFS and BFS, respectively) are first introduced since they are one of the simplest and most common type of surface defect found on aerodynamic surfaces. During test flights performed on the X-21, Nenni and Gluyas 1966 determined the following transition criteria:

$$\mathrm{Re}_h = \frac{U_\infty h}{\nu} = 900 \quad \text{for BFS}$$
$$\mathrm{Re}_h = \frac{U_\infty h}{\nu} = 1800 \quad \text{for FFS}$$

with U_∞ is the freestream velocity, ν the kinematic viscosity and h the height of the step. These criteria are still used as a reference but recent studies (Costantini et al. 2015, Béguet et al. 2016) state that using local flow properties could be more appropriate than using freestream flow properties. Further test flights on a T-34C with rounded FFS by Holmes et al. 1985 determined the additional criterion:

$$\mathrm{Re}_h = \frac{U_\infty h}{\nu} = 2700 \quad \text{for rounded FFS.}$$

This criterion, although less commonly used compared to the ones for the rectangular FFS and BFS, highlights that geometry can be modified to minimize the destabilizing effect of a FFS on laminar-turbulent transition.

In general, test flights therefore confirm that a BFS has a greater destabilizing effect on a boundary layer than a FFS.

Effect of humps and gaps

Humps and gaps are another common type of surface defect that can be found on aerodynamic surfaces, especially at the junction between moving panels. In particular, a rectangular hump can be modeled as an FFS followed by a BFS. Based on this assumption, and on the results from the DNS by Wörner et al. 2003 for example, the transition criteria of rectangular humps could be associated to those of BFS in similar flow conditions.

Gaps can also be seen as combination as a BFS and an FFS, except in a slightly more favorable layout. Nenni and Gluyas 1966, who also tested gaps during their test flights on the X-21, defined the following transition criterion:

$$\mathrm{Re}_b = \frac{U_\infty b}{\nu} = 15000 \quad \text{for gaps perpendicular to the flow direction.}$$

According to this criterion, gap depth has no influence on transition, while Forte et al. 2015 and Olive and Blanchard 1982 showed that the influence of depth had to be take into account past a given width-to-depth ratio, as shown on Figure 3.4. Additionally, one of the main disadvantage of this criterion is that freestream, instead of local, flow conditions are used.

Based on the later studies by Sinha et al. 1982, Olive and Blanchard 1982 and those summarized in Béguet et al. 2016, criteria based on the width and depth of the gaps with respect to the local boundary layer thickness were defined:

$$\frac{b}{\delta_{1,r}} \geq 18 \quad \text{and}$$
$$\frac{h}{\delta_{1,r}} \geq 2.$$

These criteria are conjunct for a gap to trigger transition.

3.3.2 ΔN method

In section 1.2.3, the e^N method was introduced as a tool to determine the transition position based on the location at which TS waves are amplified beyond a threshold N_T value. The ΔN method enables the extension of the e^N method to cases including a surface defect: the N factor for a configuration without any surface defect is artificially shifted by a value of ΔN (determined according to the defect characteristics and flow parameters). The transition position is therefore moved as the threshold value N_T is reached more rapidly.

The change in N factor distribution can be divided in two parts N_{peak} and ΔN, as illustrated on Figure 3.5a. At the location of the surface defect, x_{SD}, the N factor increases abruptly to an N_{peak} value. This increase is due to the local amplification of high frequency instabilities. If N_{peak} is greater or equal to N_T, transition is triggered at the defect location. Next, if N_{peak} is less than N_T, the N factor distribution resumes its growth, now shifted by a ΔN value with respect to the N factor distribution without the defect. In this case, the shift is the result of the amplification of lower frequency instabilities, and extends over a much greater region. Different methods exist to determine the ΔN by characterizing the effect of various defect sizes on transition location either through entirely numerical means (Laminar Reynolds-Average Navier Stokes combined with LST, Linearized Navier Stokes, etc.) or through a combination of experimental results and LST calculations.

Figure 3.5b shows examples of how various types of surface defects at the same location and with the same height h can affect N factor distributions. According to this figure, the BFS (red dotted curve) has a much more destabilizing effect, shifting the transition location from $x_{T,Flat\ plate}$ to $x_{T,BFS}$ while the FFS (green dashed curve) has no significant effect on the transition location. In the present case, the effect of the gap cannot simply be characterized by the gap depth since, depending on its width, the transition location can significantly be affected by this parameter.

Using the experimental data on a ZPG flat plate discussed earlier, Wang and Gaster 2005 established relationships for the ΔN as a function of the relative height of a BFS or FFS. Their empirical correlations are provided as a useful tool to predict the effect of steps of different relative heights on transition, shown in Figure 3.6.

Crouch et al. 2006 further extended these correlations by investigating the additional effect of pressure gradient to the ΔN correlations for BFS and FFS. For each type of surface discontinuity, a linear relationship was established for the ΔN as a function of the steps' relative height. The

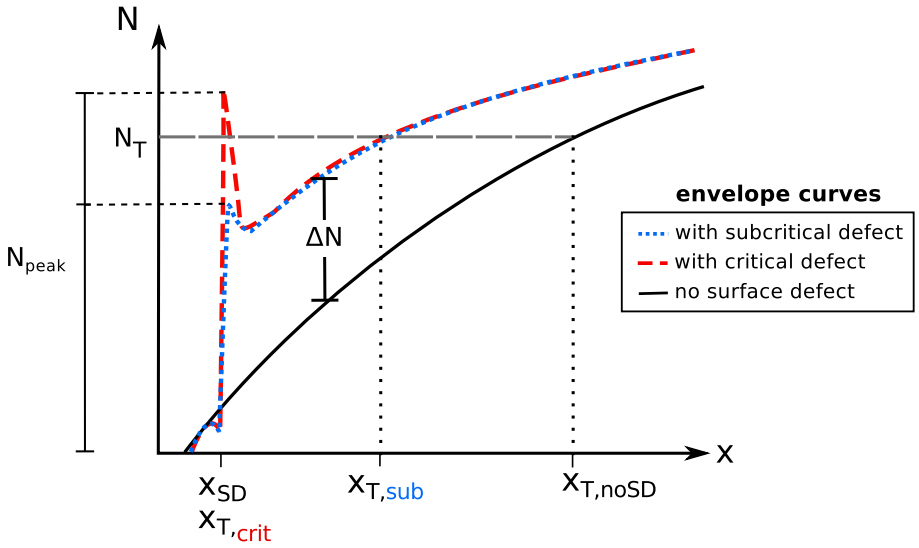

(a) Graphical representation of the different parameters used by the ΔN method.

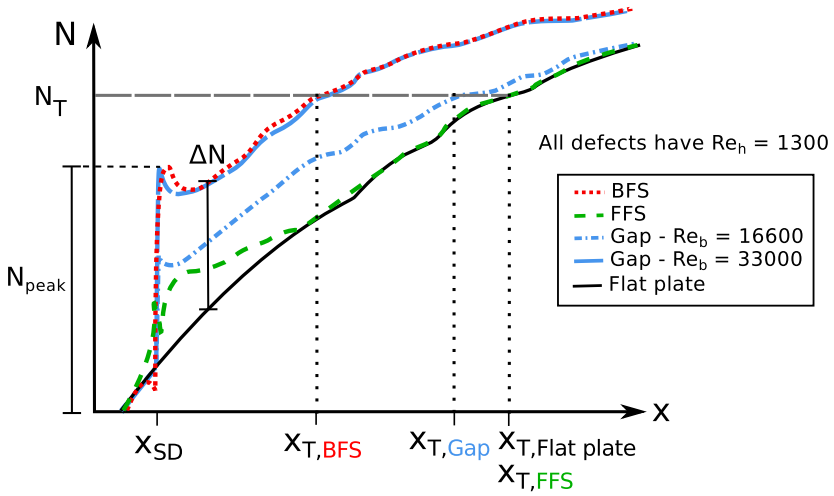

(b) Example of the effects of various types of surface defects, as modeled by the ΔN method from Perraud 1997).

Figure 3.5. Graphical summary of the ΔN method and sample results.

following correlations were defined for step relative heights h/δ_1 below 1.5:

$$\Delta N = 1.6h/\delta_1 \quad \text{for FFS} \tag{3.1}$$

$$\Delta N = 4.4h/\delta_1 \quad \text{for BFS.} \tag{3.2}$$

These correlations were defined based on the adverse pressure gradient data set but can serve as a conservative ΔN approximation for steps in favorable pressure gradients, as shown on Figure 3.7 taken from Crouch et al. 2006.

On the other hand, Perraud *et al.* determined the following, different, ΔN correlations for steps in a zero pressure gradient flow for FFS:

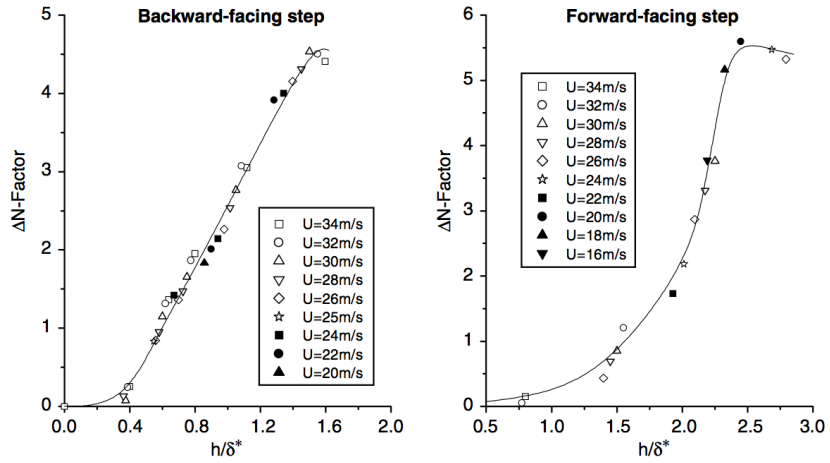

Figure 3.6. ΔN correlations with respect to relative height for BFS and FFS (from Wang and Gaster 2005). Note: In this figure, δ^* corresponds to δ_1 in the rest of the present document.

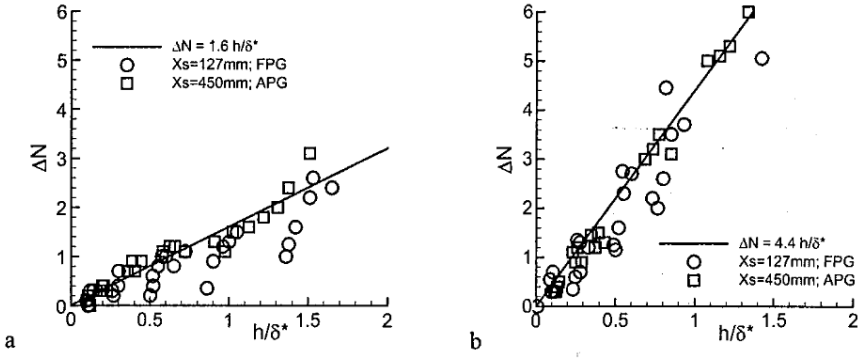

Figure 3.7. ΔN correlations for FFS (left) and BFS (right) in adverse and favorable pressure gradients, resp. APG and FPG (from Crouch et al. 2006). Note: In this figure, δ^* corresponds to δ_1 in the rest of the present text.

$$\Delta N = 0 \quad \text{for} \quad \mathrm{Re}_h < 200 \tag{3.3}$$

$$\Delta N = 0.0005\mathrm{Re}_h - 0.1 \quad \text{for} \quad 200 < \mathrm{Re}_h < 700 \tag{3.4}$$

$$\Delta N = A \cdot \arctan(B(\mathrm{Re}_\theta^2 - \mathrm{Re}_{\theta 0}^2)) \cdot \exp(C(\mathrm{Re}_\theta^2 - \mathrm{Re}_{\theta 0}^2)) \quad \text{for} \quad \mathrm{Re}_h > 700 \quad \text{and} \quad \mathrm{Re}_\theta < \mathrm{Re}_{\theta 0} \tag{3.5}$$

with A, B, and C coefficients defined in Perraud et al. 2014 and for BFS:

$$\Delta N = 0.0025\mathrm{Re}_h. \tag{3.6}$$

Based on numerical simulations of gaps with width-to-depth ratios ranging from 1.4 to 5 in a Mach 0.3 flow, Perraud *et al.* suggested the following relations for N_{peak} and ΔN_{far}:

$$N_{peak} = 1 \cdot 10^{-4} \frac{\mathrm{Re}_b}{\mathrm{Re}_{\theta 0}} + 2.09 \cdot 10^{-4}\mathrm{Re}_b - 7.93 \cdot 10^{-3}\mathrm{Re}_{\theta 0} + 4.97 \tag{3.7}$$

$$\Delta N_{far} = 8.6 \cdot 10^{-3} \frac{\mathrm{Re}_b}{\mathrm{Re}_{\theta 0}} + 3.5 \cdot 10^{-5}\mathrm{Re}_b - 2.4 \cdot 10^{-3}\mathrm{Re}_{\theta 0} + 2.244. \tag{3.8}$$

3.3.3 Numerical simulation approach

Another approach for predicting the effect of certain types of surface defects on laminar-turbulent transition is to perform numerical simulations on the flow of interest, in particular using Linearized Navier-Stokes (LNS) or Direct Numerical Simulations (DNS). In the case of an LNS, the linearized Navier-Stokes equations with small-amplitude perturbations are solved, while, in a DNS, the full Navier-Stokes equations are solved without simplifying assumptions about the baseline flow. Because neither of these methods make constraining assumptions about the baseline flow (e.g., parallel flow assumption), complex flow geometries, such as ones including surface defects, can therefore be investigated. Once the flow solution is computed, these results are then either used to calculate the amplification factor, N factor, evolution (for LNS) or to directly access the amplitude of the instability under investigation (for DNS). Note that the computational costs for DNS are much greater than those associated to LNS calculations.

Currently, these two methods are used in the context of boundary layer stability analysis to perform parametric studies on different types of surface defects. As mentioned earlier in Section 3.2.2, Wörner et al. 2003 performed DNS on humps and steps to characterize their effect on the stability of a two-dimensional boundary layer. The authors tested different FFS and hump dimensions and were able to compare the effects on TS wave amplitude. Similarly, Franco-Sumariva and Hein 2018 developed an LNS method to study the growth of instabilities across significant surface perturbations (such as rectangular and rounded humps or porous walls) but with a reduced computational cost compared to equivalent DNS calculations. Although the results presented by the authors consisted only in replicating already-known results, the LNS method presented showed a promising capability to study the effect of surface defects on boundary layer stability. Such data can then be used to further understand the physical phenomena through which surface defects affect boundary layer transition, or can be collected into a database, or even help develop more accurate models of the ΔN type.

3.4 Combined effect of steps and wall suction

Although transition criteria for surface defect on solid walls exists, none currently exist for cases with wall suction, such as in HLFC applications. However, a few studies have been performed on the combined effect of steps and wall suction, and are summarized in this section.

Flight experiments in the late 1950s reported by Carmichael et al. 1957 and Carmichael and Pfenninger 1959 were performed on a wing glove of an F-94 aircraft. The intent was to investigate the effect of waviness on boundary layer transition, and suction slots were used over 41% and 95% of the wing chord (i.e., the adverse pressure gradient region) to maintain laminar flow. The authors found that slot suction minimized the effect of greater wave sizes on transition. Based on these data, Carmichael 1959 defined an empirical relation for the critical wave height-to-width ratio, as a function of the width of the wave and the freestream Reynolds number, above which laminar flow did not reach the trailing edge. This relationship is a first attempt to establish a transition criterion based on the combined effect of suction and a surface defect; however, according to Al-Maaitah et al. 1990, this criterion is only valid for the particular configuration and flow conditions under investigation. Additionally, suction was applied discontinuously through slots because of the limited manufacturing capabilities of the time: current wall suction is now more distributed through micro-perforated sheets. Finally, this criterion was intended as a reference for manufacturing tolerances and therefore no explanation of the physical phenomena in action is provided.

Hahn and Pfenninger 1973 performed a wind tunnel experiment on a flat plate to study more specifically a backward-facing step immediately followed by a suction region comprised of 32

suction slots. The effect of suction flow rate and location on the reattachment length downstream of the step and boundary layer transition was investigated. Authors found that modifying suction mass flow rate could reduce reattachment length and was effective in preventing transition, thereby doubling the transition Reynolds number with respect to step height to a value of 2200. This study, however, does not explain how the transition mechanisms are affected by the combined effect of wall suction and the step. Additionally, the critical Reynolds numbers for the step height are based on freestream, instead of local, flow properties.

A later numerical study by Al-Maaitah et al. 1990 investigated the stability of a boundary layer in a similar configuration, where suction is applied either continuously or at discrete locations around a backward-facing step. The objective of this study was to characterize the viscous-inviscid interaction due to the combined effect of suction and the separation bubble downstream the step respectively. Wall suction was found to reduce the size of the separation bubble and, outside the separation region, stabilize the boundary layer by increasing its curvature. However, in the separation region, wall suction destabilized the boundary layer by moving its inflection point closer to the wall, and increasing the vorticity near the wall. Wall suction therefore reduced viscous instability but increased the shear layer instability.

Finally, a two-dimensional DNS was more recently performed by Zahn and Rist 2018 to investigate the effect of suction being applied through a slot located immediately upstream of a forward-facing step in a compressible flow ($M = 0.6$) over a flat plate. Wall suction was found to be effective in cancelling the increased amplification generated by some of the steps under investigation. However, past a critical threshold, suction was unable to prevent transition, and changes in the step geometry (such as rounding) were necessary to prevent transition.

In all these studies, wall suction was used to minimize the destabilizing effect of a surface imperfection on boundary layer transition. Although some studies explain the competing effects of wall suction combined with steps, a lack of experimental data systematically characterizing the influence of a variety of surface defects on the transition of a sucked boundary layer still needs to be addressed.

Summary

The present literature survey demonstrates that numerous investigations were performed to establish a firm understanding of the individual effects of either wall suction or surface defect on boundary layer transition. In particular, the effectiveness of wall suction, through both slots and porous panels, was established decades ago; however, its implementation is still not as widespread as could be expected from such an effect LFC technology. Only a few experimental and numerical studies (to the author's knowledge) were performed to understanding the competing effects of the stabilizing suction and the destabilizing defects on laminar-turbulent transition. The objective of the present study is therefore to: provide additional insight on the transition mechanisms involved when both defect and suction are present, as well as specify critical defect dimensions that can be used subsequently to define surface tolerancing in a more industrial setting.

Part II

Fundamentals for a Laminar-Turbulent Transition Investigation

Chapter 4

Experimental Protocol for a Laminar-Turbulent Transition Study

Contents

4.1 Presentation of the experimental facility 43
4.1.1 TRIN 2 subsonic wind tunnel 43
4.1.2 Flat plate model 45
4.1.3 Instrumentation and data acquisition systems 45
4.2 Validation of the experimental protocol 49
4.2.1 Test section flow characterization 49
4.2.2 Baseline flat plate measurements 51
4.3 Measurement uncertainty analysis 55
4.3.1 Boundary layer profiles 56
4.3.2 Transition position 60
4.3.3 Pressure coefficient 60

The experimental protocol developed to provide the foundations for a proper laminar-turbulent transition study is presented. First, the experimental facility is described (Section 4.1), followed by an experimental characterization to validate the experimental protocol (Section 4.2). Finally, measurement uncertainty analysis is performed for the main parameters of interest that will be used throughout the remainder of the present dissertation (Section 4.3).

4.1 Presentation of the experimental facility

A general overview of the experimental facility, the flat plate model and the instrumentation used to perform the present experimental study on laminar-turbulent transition is given in the following sections.

4.1.1 TRIN 2 subsonic wind tunnel

This study was conducted in the TRIN 2 open-return subsonic wind tunnel, shown in Figure 4.1, operating at local atmospheric conditions. Test section speeds range from 20 $m.s^{-1}$ to 50 $m.s^{-1}$, corresponding to equivalent unit Reynolds numbers between $1{\cdot}10^6$ m^{-1} and $3{\cdot}10^6$ m^{-1}.

Atmospheric air is drawn in through an initial honeycomb screen and three layers of finer mesh screens in the settling chamber, to remove any particles, and to successively breakdown the turbulent eddies into smaller structures. The flow is therefore stabilized before being accelerated

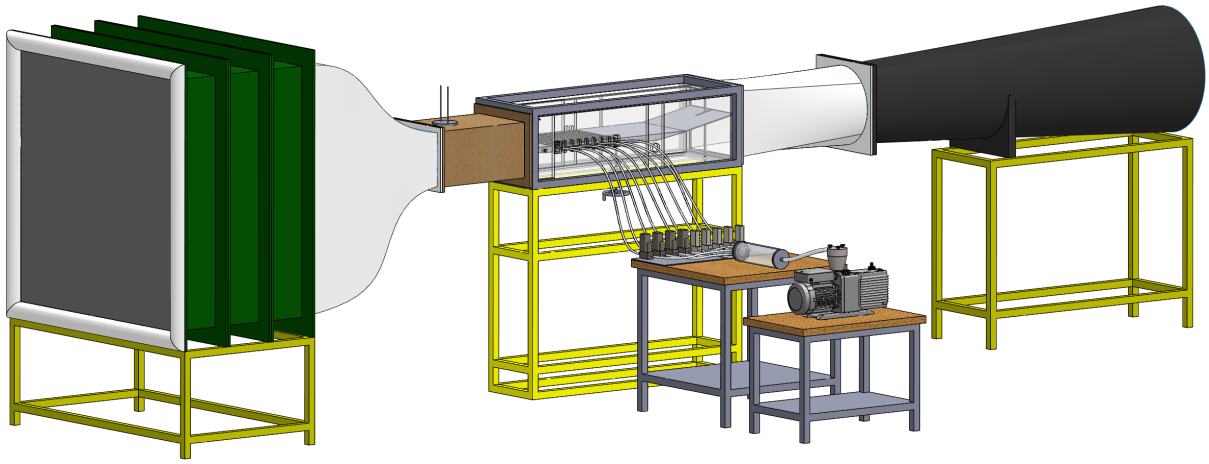

Figure 4.1. CAD overview of the TRIN 2 subsonic wind tunnel (flow is from left to right).

through a converging nozzle with an area ratio of 16. The test section, shown in Figure 4.2, has an entrance of dimensions 0.3 m by 0.4 m (height by width) and a total length of 1.5 m. Test section speed and Reynolds number are determined with a Pitot-static (Prandtl) tube and a total temperature probe (Type T thermocouple) located approximately 0.03 m from the test section ceiling and 0.15 m downstream of the test section entrance, i.e., 0.40 m upstream of the flat plate's leading edge.

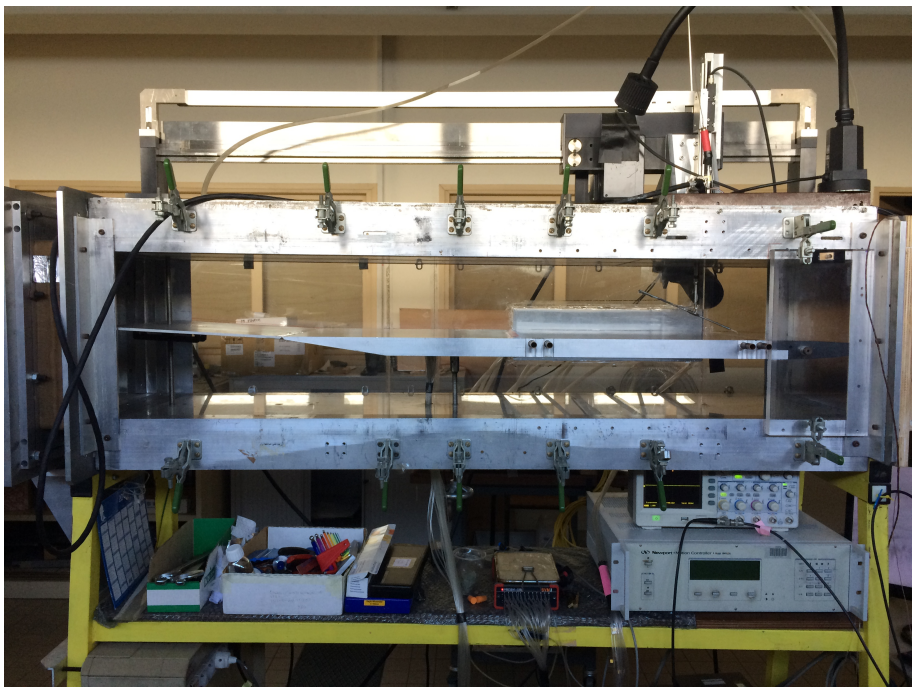

Figure 4.2. Photograph of the test section with flat plate during data acquisition (flow is from right to left).

Flow exits the test section through a 2 m-long diverging nozzle with an area ratio of 3 and is discharged in a noise-reduction chamber (not shown in Figure 4.1). The purpose of this chamber is to prevent pressure waves from the driving fan (located downstream of the test section, at the wind tunnel exhaust) from propagating upstream into the test section. These waves could interfere with the sensitive flow phenomena related to laminar-turbulent transition.

All the walls, floor and ceiling of the noise-reduction chamber are lined with foam and a partition obstructs the flow path between the diverging nozzle exit and the wind tunnel exhaust to create an additional obstacle to the upstream-travelling pressure waves from the fan. The resulting freestream turbulence levels are consequently always below 0.18% (evaluated over frequencies ranging from 3 Hz to 10 kHz). This measure was provided as a reference, but additional details about the freestream turbulence will be discussed later. Flow speed is regulated by modifying the fan blades' incidence using a pneumatic controller while fan rotation speed is kept at a constant value of 1400 revolutions per minute (rpm).

4.1.2 Flat plate model

The flat plate covers the entire width of the test section (wall-to-wall) and is mounted slightly below the test section's mid-height (approximately 44%) so as to be off a symmetry axis where vortical modes can occur (Saric 2008). Figure 4.2 shows the flat plate mounted inside the test section. The leading edge shape, shown in Figure 4.3, that was numerically optimized to minimize any suction peak on the working (upper) side, where measurements are acquired. Potential flow calculations over the flat plate were performed and the leading edge geometry was modified so that the cost function, defined as the velocity at the suction peak on the upper side, was minimum. The lower side is semi-elliptical while the upper side is defined by a third-order Bézier polynomial. This type of polynomial has been used in other leading edge optimization studies, such as the one by J. H. Fransson 2004 for example. Coordinates of the actual geometry are specified in the Appendix. For ease of manufacturing, the leading edge is a separate component with an aluminum core and an epoxy shell. Shims were used to minimize the discontinuity at the junction between the leading edge and the main body, resulting in a forward-facing step of the order of 30 μm, measured with a distance amplifying indicator. This step height, corresponding to a Reynolds number ($Re_{hFFS} = U_e h_{FFS}/\nu_e$) of approximately 80, is significantly lower to the approximate criterion from Nenni and Gluyas 1966 equal to 1800: the discontinuity at the junction is therefore deemed to have a negligible impact on the downstream transition.

The main body of the flat plate is in aluminum, with a thickness of 0.035 m, and a hollow section to accommodate for suction. The total length of the plate from leading to trailing edges is 1.10 m. The suction region, shown in Figure F2.2, starts 0.18 m from the leading edge, and is divided in nine suction chambers with dimensions of 0.019 m (depth, y) by 0.350 m (spanwise width, z). The first and last chamber have a length of 0.049 m (streamwise length, x) while chambers C2 through C8 are 0.048 m long and each are separated by 0.002 m-thick stringers resulting in a total streamwise length of 0.450 m. A 0.340 m flap is also mounted at the flat plate's trailing edge and its incidence can be adjusted independently from the flat plate's angle of attack. The purpose of the flap is to control the location of the stagnation point and the pressure distribution in the leading edge region.

Inside each chamber, suction, initially coming from the 10-mm diameter copper tube, is then distributed by means of four 2 mm-diameter tubes of varying lengths along the spanwise z-direction. Additionally, a micro-perforated U-shaped metallic sheet, also shown in Figure F2.2, is mounted over the four suction tubes to further ensure uniform suction in the spanwise direction. Nine 10 mm-diameter tubes coming out of the side of the flat plate are connected to a manifold and ultimately the suction pump (shown in Figure 4.1).

4.1.3 Instrumentation and data acquisition systems

Static pressure ports are distributed along the entire chord of the flat plate at a spanwise location offset by 0.08 m from the centerline. Eleven ports are located in the leading edge region

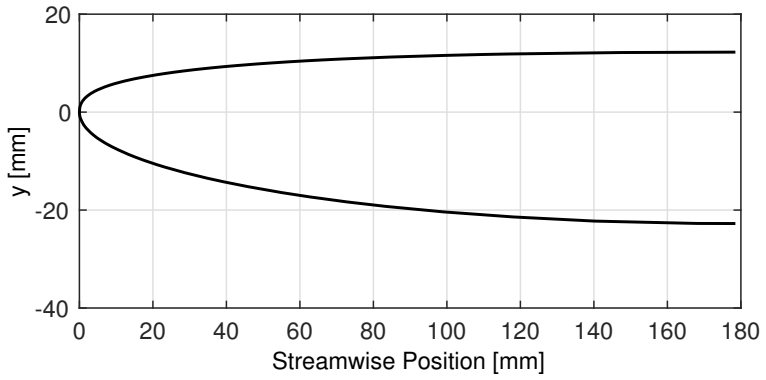

Figure 4.3. Numerically optimized leading edge shape (coordinates given in Appendix).

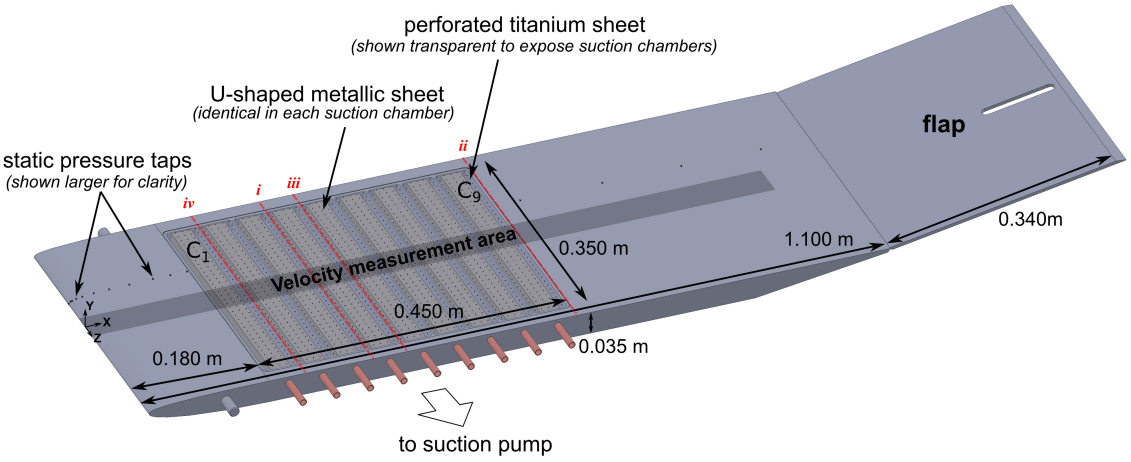

Figure 4.4. General layout of the flat plate detailing the suction region.

(i.e., upstream of the suction region), and four additional ports are located downstream of the suction region. Each suction chamber is also instrumented with three static pressure ports across the span to check for uniform suction. Pressure measurements are acquired using an SVMtec PSC24-USB differential pressure scanner with 8 channels ranging +/-2.5 kPa and the remaining 16 channels ranging +/-5 kPa. The dynamic pressure from the Pitot-static tube is measured with an MKS Baratron Type 220D differential pressure transducer with a range of 20 Torr. The baseline flow condition at which all data were acquired (unless indicated, such as in the case of freestream turbulence measurements) corresponds to a Reynolds number equal to $2.6{\cdot}10^6$ m^{-1} (U_∞ approximately equal 40 $m.s^{-1}$ depending on local atmospheric conditions).

Velocity measurements are acquired using a hot-wire probe mounted on a two-dimensional traverse, with total travel of 0.710 m and 0.15 m in the x- and y-directions respectively. Displacement is done with stepping motors controlled using a Newport Motion Controller MM4006. The initial coordinate at the wall, y_o, is determined by touching the hot-wire probe to the flat plate, and accurate probe position in both directions of displacement is measured using Heidenhain LS388 linear encoders. For boundary layer investigations, flow velocity is measured by constant temperature single-wire hot-wire anemometry using a Dantec Streamline, a 90C10 CTA module and a 55P15 probe. At each of these data points, 200,000 samples were acquired at a frequency of 25 kHz. For turbulence intensity measurements, the 55P15 probe was replaced by a 55P11 model and 2 million samples were acquired at 25 kHz. Probes are calibrated *in situ* at the beginning and completion of each test. Once the hotwire calibration is performed, the voltage

E measured by the hotwire can be converted into velocity U using King's law:

$$U = \left(\frac{E^2 - E_{o,c}^2}{b} \right)^m \tag{4.1}$$

where m and b are parameters determined during calibration, and $E_{o,c}$ is the zero-velocity voltage, corrected for natural convection ($E_{o,c} = 0.92E_o$).

During the initial phase where turbulence intensity was measured, attention was taken to ensure that the recorded hotwire signals had the least amount of parasite perturbations. In particular, interference from the test facility ground was initially observed by the consistent presence of the harmonics of 50 Hz, which corresponds to the power line frequency in Europe, and shown by the grey curve on Figure 4.5. On this graph, the power spectral density (PSD) of the hotwire signal from the 55P11 inside the empty test section at a given unit Reynolds number is shown. When any component of the data acquisition system is connected to the test facility's ground, the 50 Hz harmonics appears. On the other hand, once the grounding is removed, the hotwire signal is unperturbed by any harmonic. To improve signal quality, all instruments were therefore dissociated from the building ground.

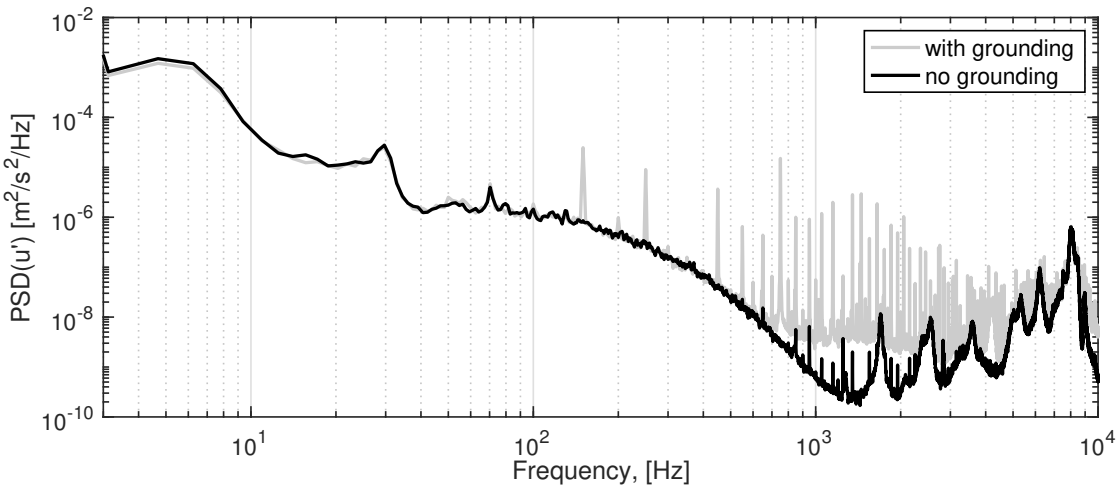

Figure 4.5. PSD(u') at Re = 2.9·10^6 m^{-1} showing test facility ground interference.

To reduce the error in evaluating the hotwire distance from the wall, a camera with a SIGMA 180 mm 1:3:5 MACRO DG lens and a 2x SIGMA EX teleconverter is used to set the zero for each boundary layer profile acquisition. During post-processing, a correction is applied by shifting the entire mean velocity profiles by a shift in the wall-normal y-direction so that there is no slope discontinuity between the first three experimental points closest to the wall and the theoretical (0,0) point where the no-slip condition is assumed. This procedure is schematically shown on Figure 4.6. On average this correction is close to 40 μm, corresponding approximately to the radius of the prongs on which the hotwire is soldered.

All test data are collected using a National Instruments CompactDAQ-9178 with two NI-9215 modules for voltage measurements and an NI-9211 module for temperature readings. Anemometer data are recorded as raw output from the Dantec Streamline (with low-pass filtering for anti-aliasing), and also as a processed signal after A/C coupling, low-pass filtering and amplification by a gain of 10 with a Krohn-Hite 3905C filter/amplifier. Cut-off frequency and sampling rate are set so as to satisfy the Nyquist-Shannon theorem. LabVIEW codes developed in-house were used to perform data acquisition.

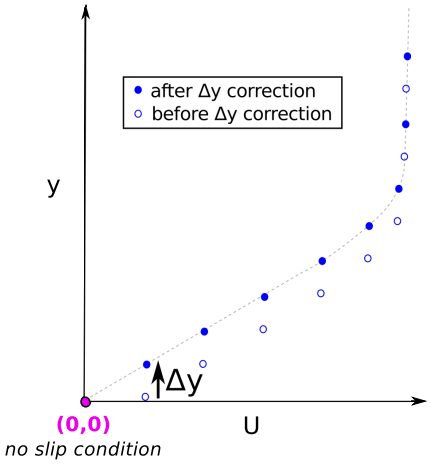

Figure 4.6. Schematic representation of the Δy correction.

The transition location is determined using the Root Mean Square (RMS) values of the anemometer's AC-component after filtering, amplification and conversion to velocity units. As the first turbulent spots appear at the onset of transition, velocity fluctuations inside the boundary layer start to increase, reaching a maximum value before settling back down to a new constant value for fully turbulent flow. As a note, fluctuation levels in the turbulent regime are higher than in the laminar regime. In this study, the location of the onset of transition is identified by the abscissa where non-dimensionalized velocity fluctuations, u'/U_∞, first begin to increase with a slope equal or superior to $2{\cdot}10^{-4}$ mm^{-1}, and after which fluctuations continue to increase. A systematic approach to determining the transition location was necessary and this threshold value was determined empirically based on the fact that repeatable transition locations could be obtained for a given configuration. Further details on the adequacy of this approach will be provided in a subsequent section, where measurement uncertainty is established. As an example, velocity fluctuations in Figure 4.7 indicate that the onset of transition for the solid wall panel case is located 740 mm from the leading edge.

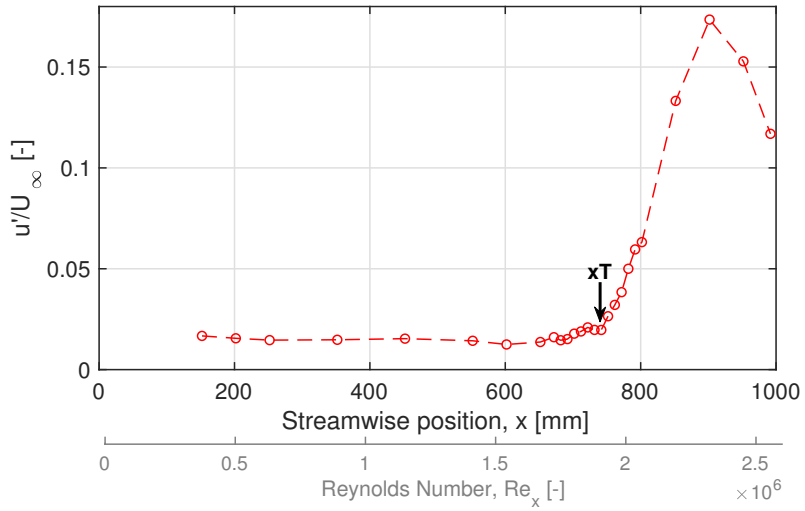

Figure 4.7. Streamwise velocity fluctuations evolution ($y = 300$ µm) to determine transition position on solid wall panel.

Finally, mass flow rate in each suction chamber is monitored and controlled using Brooks

SLA5850 and Bronkhorst F201 thermal mass flow meters with control valves.

4.2 Validation of the experimental protocol

Because the flow physics involved in laminar-turbulent transition is sensitive to small external disturbances, experiments have to be carefully monitored to prevent foreign disturbances from interfering with measurements. The following sections describes the precautions taken to ensure the conditions to perform a proper laminar-turbulent transition experiment.

4.2.1 Test section flow characterization

First, the quality of the flow in the test section with and without the flat plate was assessed to verify that proper laminar-turbulent transition experiments could be performed. In the case of this study, freestream disturbance levels in the test section have to be as low as possible to attempt to reproduce conditions as close as possible to those encountered in flight. Since this expectation is technically difficult to meet in a wind tunnel, the more realistic objective is therefore to achieve low enough freestream disturbance levels so that transition takes the *natural* path, according to Morkovin et al. 1994, as seen in Section 1.2.1.

Hotwire anemometry data were acquired with a Dantec hotwire 55P11 probe placed in the center (in terms of span, height and length) of the empty test section to determine turbulence levels u'/U_∞ by measuring streamwise velocity fluctuations. Turbulence levels were characterized over the entire operating range of the wind tunnel and are summarized in Figure 4.8a. The passband during freestream turbulence data acquisition was set between 3 Hz and 10 kHz. Freestream disturbances were calculated by integrating the power spectral densities of the velocity fluctuations over frequencies also ranging from 3 Hz to 10 kHz according to the following relation:

$$Tu = \frac{1}{U_\infty}\sqrt{\int_3^{10k} \mathrm{PSD}_{u'}(f)\,\mathrm{d}f} \tag{4.2}$$

and as illustrated in Figure 4.8b by the dashed lines.

The flat plate was then mounted inside the test section and the turbulence level was reassessed close to the baseline operating condition, at unit Reynolds number of $2.6{\cdot}10^6$ m^{-1} and in the first half of the test section. This data point is shown as the black cross on Figure 4.8a. Overall, freestream turbulence levels inside the test section with and without the model is below 0.18%, which is considered an acceptable level to perform transition investigations. For this level of freestream turbulence, the transition criteria N_T based on Mack's relation is approximately equal to 6.74.

Once the model was inside the test section, some additional acoustic characterization of the flow was performed. Two PCB microphones were used and data were acquired using a 24-bit NI 9234 module. One microphone with a grid was flush-mounted (PCB-426A03) with respect to the test section wall, and another (PCB-426M03) located at the center of the test section entrance. This last microphone had an ogive nosecone and is referred to as the profiled microphone. The probes mounted inside the test section are shown in Figure 4.9 and a side view of the profiled microphone is shown with the mounting hold and data acquisition system in Figure 4.10.

The overall sound pressure level ($OASPL$) measured by each microphone is shown on Figure 4.11. In general, the sound pressure level (SPL) gives a measure in dB of any pressure fluctuation P' with respect to a reference pressure P_{ref}, and is defined as:

$$SPL = 10\log_{10}\left(\frac{P'^2}{P_{\mathrm{ref}}^2}\right) \quad \text{with} \quad P_{\mathrm{ref}} = 2\cdot 10^{-5}\mathrm{Pa} \tag{4.3}$$

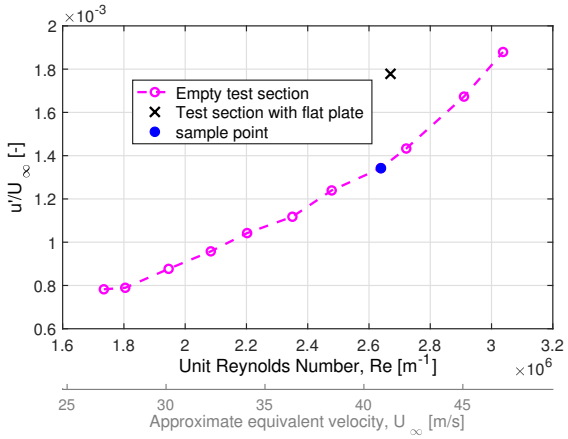

(a) u'/U_∞ levels in the test section with and without the flat plate.

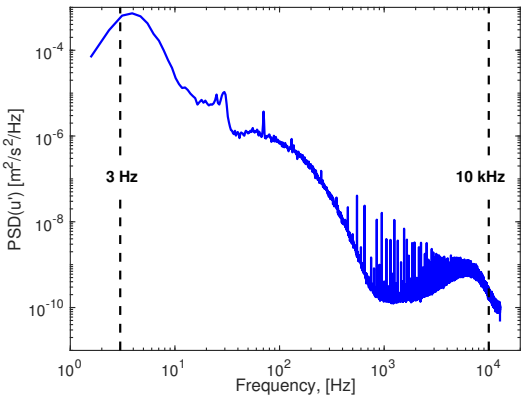

(b) PSD(u') at the sample point in (a) with integration bands.

Figure 4.8. Test section flow characterization: streamwise velocity.

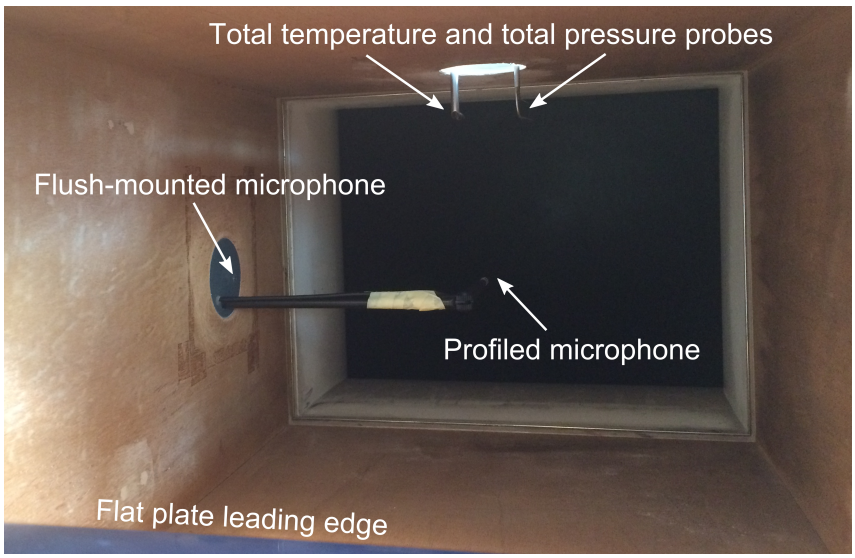

Figure 4.9. Microphone set-up at the test section entrance for acoustic characterization.

and the OASPL is a similar measure but over the entire signal sampled, such that:

$$OASPL = 10\log_{10}\left(\frac{\sum_i P_i'^2}{P_{\text{ref}}^2}\right). \tag{4.4}$$

Regardless of the microphone, the *OASPL* is always below 120 dB, which corresponds to an acceptable level of noise inside the test section. Next, a more detailed representation of these data is through the magnitude spectra such as in Figure 4.12 for operating Reynolds number 0 m^{-1}, $1.6{\cdot}10^6$ m^{-1} and $2.6{\cdot}10^6$ m^{-1}. A bulge around 400 Hz seem to occur regardless of the operating unit Reynolds number but stand out slightly more significantly at Re equal to $1.6{\cdot}10^6$ m^{-1} and spreads over a wider range of frequencies at the higher velocity. Additionally, a peak near 1.2 kHz is also visible at $1.6{\cdot}10^6$ m^{-1} but disappears at $2.6{\cdot}10^6$ m^{-1}. To the author's best knowledge, these phenomena could be attributed to some noise inside the wind tunnel. However, since their magnitudes never exceed 90 dB, these observed peaks are considered low enough that the flow is not significantly disturbed. This final verification confirms the suitability of this wind

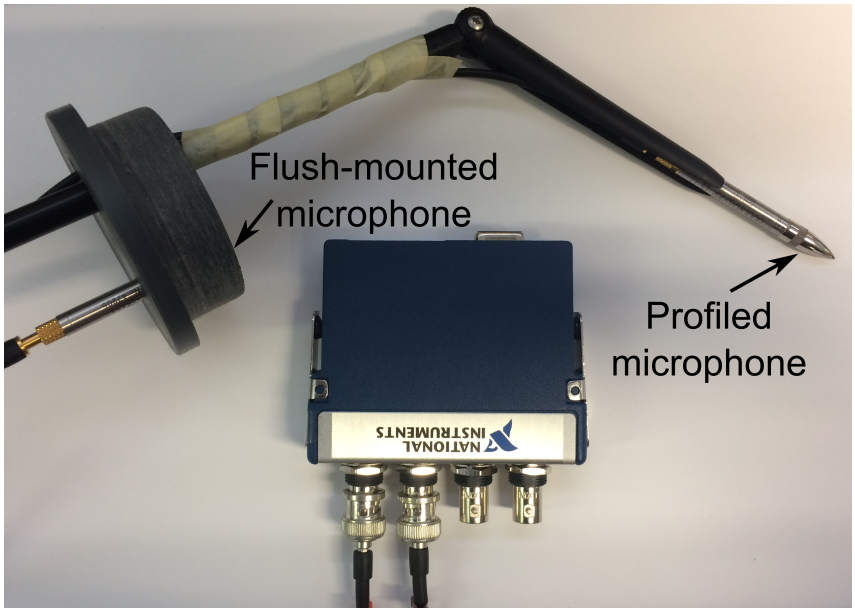

Figure 4.10. Acoustic data acquisition system with side view of the profiled microphone.

tunnel facility for laminar-turbulent transition experiments.

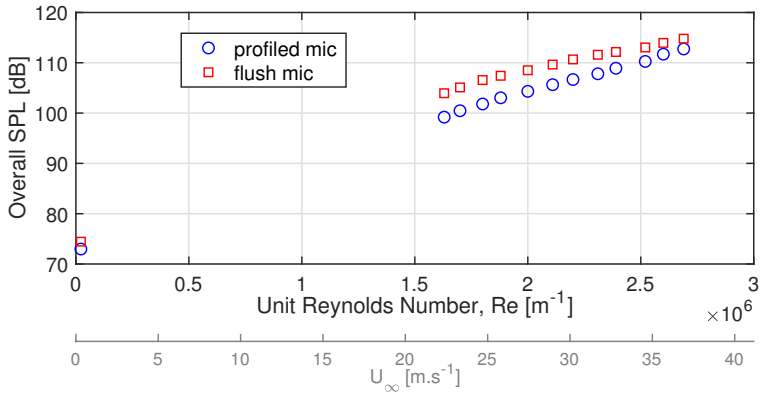

Figure 4.11. Overall SPL evolution over range of operating unit Reynolds numbers.

4.2.2 Baseline flat plate measurements

Guidelines suggested by Saric 2008 and Hunt et al. 2010 for conducting rigorous transition experiments were integrated in the present study and are presented in this section.

One application of the experimental results from this investigation is to use them as validation data for numerical models under development. To facilitate such comparison, the simplest flow condition to simulate was chosen. Flat plate and flap angles of attack were set for a zero pressure gradient over the entire plate's length (excluding the leading edge region) to tend towards a Blasius flow on the upper side. The pressure coefficient distribution for the chosen flat plate and flap angles of attack (0.08 and 3.5 degrees respectively) is shown in Figure 4.13 and the evolution of the boundary layer integral values is given in Figure 4.14. Given the relatively low freestream turbulence of the wind tunnel, the "traditional" path to transition, as defined by Morkovin et al. 1994, is expected to occur as a result of the linear amplification of Tollmien-Schlichting (TS) waves.

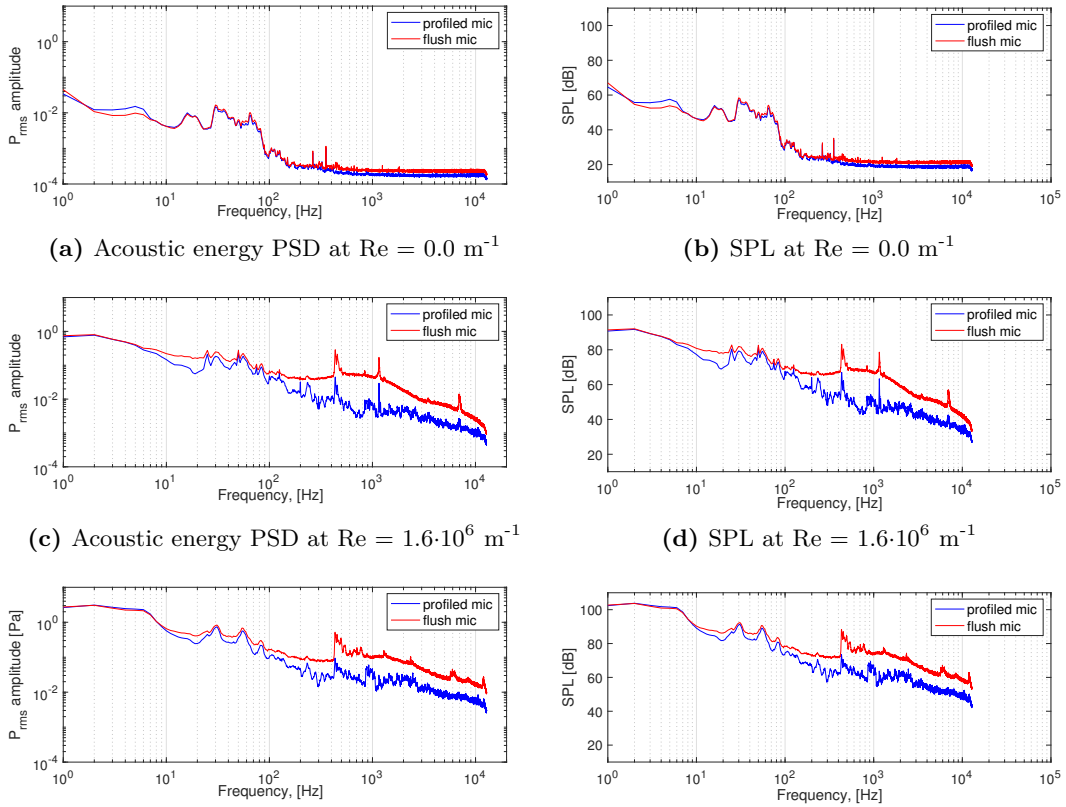

(a) Acoustic energy PSD at Re = 0.0 m^{-1}

(b) SPL at Re = 0.0 m^{-1}

(c) Acoustic energy PSD at Re = $1.6{\cdot}10^6$ m^{-1}

(d) SPL at Re = $1.6{\cdot}10^6$ m^{-1}

(e) Acoustic energy PSD at Re = $2.6{\cdot}10^6$ m^{-1}

(f) SPL at Re = $2.6{\cdot}10^6$ m^{-1}

Figure 4.12. Acoustic characterization of the test section flow at varying unit Reynolds numbers.

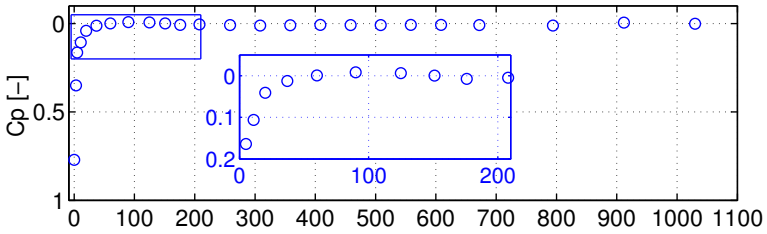

Figure 4.13. Nominal pressure coefficient distribution along the flat plate at Re = $2.6{\cdot}10^6$ m^{-1} ($\sim$40 $m.s^{-1}$).

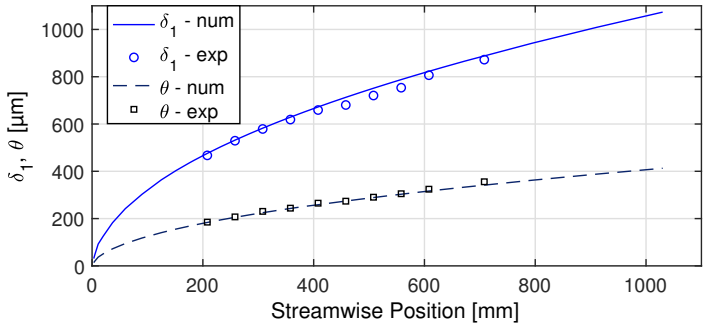

(a) Displacement thickness and momentum thickness evolution.

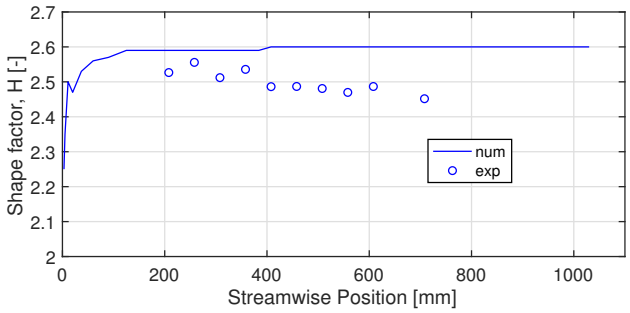

(b) Shape factor evolution.

Figure 4.14. Integral values of the boundary for the solid wall (no porosity) flat plate.

The baseline assumption for a flat plate model spanning the entire test section of this wind tunnel is that the flow, outside of the wall boundary layers, is two-dimensional. The validity of this assumption is verified by checking that the position of the onset of transition is the same ($\pm$25 mm) over a region spanning a minimum of 60 mm, as shown on Figure 4.15. This verification is performed after each change in configuration.

Figure 4.16c is an example of a PSD of the velocity fluctuations at an altitude inside the boundary layer of approximately 400 μm from the wall and for a streamwise position 508 mm from the leading edge at operating Reynolds number $2.6{\cdot}10^6$ m^{-1} ($\sim$40 $m.s^{-1}$). Since this position is upstream but relatively close to the transition location $x_T \sim 740$ mm, TS waves are sufficiently amplified so as to be identified by the bulge in the PSD over the frequencies ranging from 400 Hz to 1 kHz, with a maximum close to 610 Hz. Linear stability analysis, using the ONERA in-house code based on the Orr-Sommerfeld equation CASTET, was also performed on the Blasius velocity profile and revealed that the most amplified frequency was also close to 600 Hz at the transition position, as shown on Figure 4.17. From this numerical analysis, the transition N_T is determined to be 6.2, which is slightly less than the predicted N_T from Mack's relation for a

turbulence level of 0.18%, which is equal to 6.74.

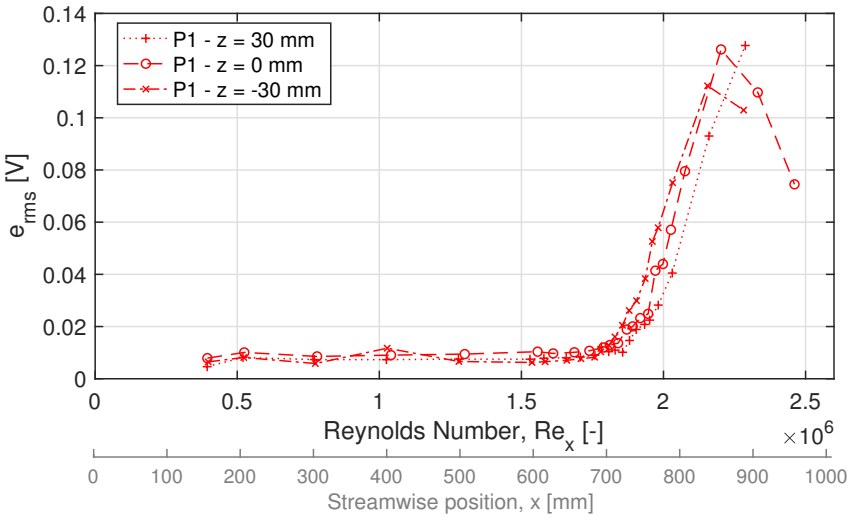

Figure 4.15. Two-dimensional transition position during test section characterization for the solid wall panel.

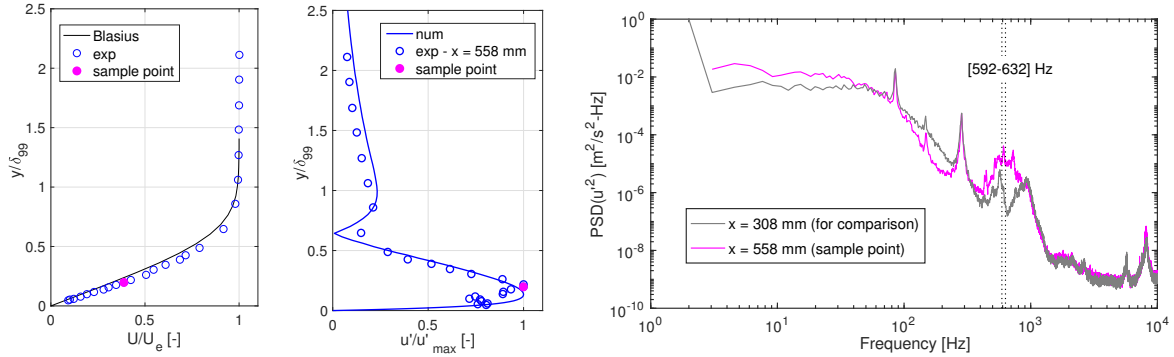

(a) Normalized mean velocity profile (x = 558 mm).

(b) TS-amplitude profile comparison.

(c) PSD inside boundary layer at sample point (558 mm, 400μm) where u' is maximum, with integration range.

Figure 4.16. Identification of ~600 Hz TS profile at x = 558 mm (δ_{99} = 2.43 mm) and Re = 2.6·10^6 m^{-1} (~40 m.s^{-1}).

The unsteady data to evaluate PSD are available for all altitudes inside the boundary layer. Integrating the PSD of each altitude over the narrow range of frequencies between 592 Hz and 632 Hz results in a profile of TS amplitudes at x equal to 558 mm and around an approximate frequency of 610 Hz. Using the Blasius profile scaled to the corresponding δ_1 and U_e of the closest available streamwise position (508 mm), the corresponding TS-amplitude profile for frequency 600 Hz was evaluated using linear stability theory (LST) and compared to experimental data in Figure 4.16b. Good agreement is found between theory and experiment, confirming that laminar-turbulent transition is driven by TS instabilities. This result also suggests that streamwise traverses inside the boundary layer at a constant altitude of 300 µm from the wall are relevant for detecting the start of transition (such as in Figure 4.15), since the TS u' amplitude is maximum close to that region.

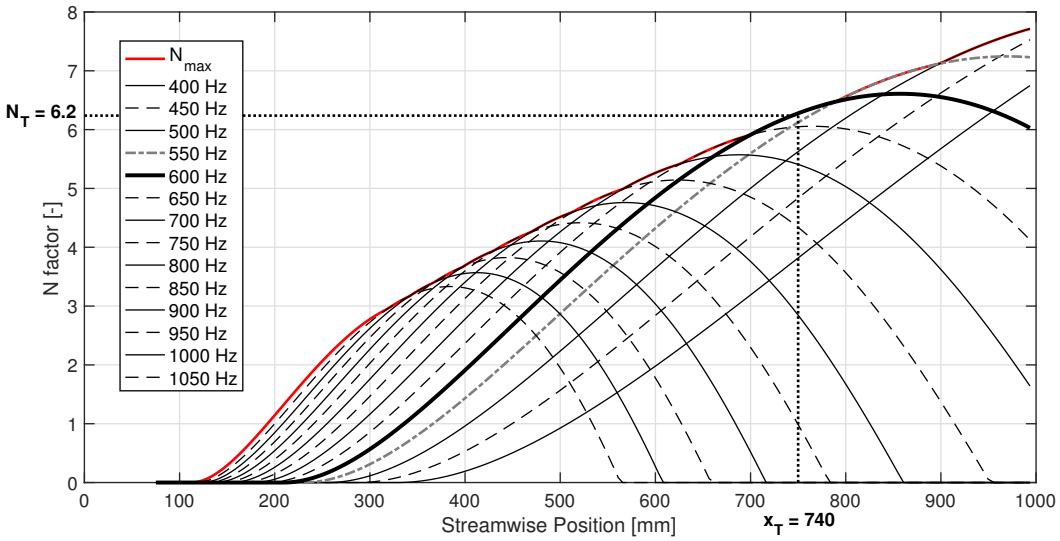

Figure 4.17. N-factor evolution for Blasius flow at operating Re = $2.6{\cdot}10^6$ m^{-1}.

4.3 Measurement uncertainty analysis

In this section, uncertainty analysis for the most representative and recurring types of measurements presented throughout this document is performed. These measurements include: pressure coefficient Kp, streamwise velocity U, transition position x_T, and unit Reynolds number Re.

Although it does not provide information about the quality of the experimental facility, uncertainty analysis allows to get a quantitative notion of the measurement system's limitations. According to **wheeler2010introduction** uncertainty estimates can be divided into two main categories:

- **random uncertainty** $P_{\bar{x}}$, corresponding to fluctuations in the measurements themselves an which can be evaluated using statistical analysis. For small sample sizes (below 30), P_x in the mean of quantity x is defined as:

$$P_x = \pm t \frac{\sigma}{\sqrt{n}} \tag{4.5}$$

  with n the number of samples, t the value determined from Student's t-distribution table for a given confidence interval and degree of freedom (n - 1), and σ the standard deviation of the data set of samples being evaluated.

- **systematic uncertainty** B_x, which gives an indication of the maximum fixed error that occurs for each measurement.

Total uncertainty μ_x can then be calculated using the root sum of squares (RSS):

$$\mu_x = \sqrt{B_x^2 + P_x^2}. \tag{4.6}$$

In general, the uncertainty ΔQ of a calculated parameter Q that is a function of independent variables x_1, x_2,..., x_n can be determine using the RSS such that:

$$\Delta Q = \sqrt{\left(\frac{\partial Q}{\partial x_1}\Delta x_1\right)^2 + \left(\frac{\partial Q}{\partial x_2}\Delta x_2\right)^2 + \cdots + \left(\frac{\partial Q}{\partial x_n}\Delta x_n\right)^2} \tag{4.7}$$

In this section, the methods used to evaluate the uncertainty for all the main parameters of interest (flow velocity, wall-normal y- coordinate, transition position and pressure coefficient) are presented, along with some quantitative examples. Whenever possible, the above-mentioned definitions of uncertainty were used. For each type of measurement, uncertainty quantification is performed on a representative data set, and the results are discussed. The purpose of each of these sections is to graph the uncertainties for each parameter "once and for all", such that, for all similar graphs subsequently shown, the uncertainty can be expected to be of a similar order of magnitude.

4.3.1 Boundary layer profiles

Hotwire anemometry

Two different methods were used to evaluate the uncertainty of the velocity measured with a hotwire probe. For both methods, the systematic uncertainty (i.e., B_x) is considered to occur during the calibration of the hotwire. In this section, each method is first presented in general terms and will then be implemented in a case study of representative data.

The first method is based on the procedure by Yavuzkurt 1984, which uses a classical approach to experimental uncertainty analysis. Contributions to the systematic uncertainty ΔU come from: first, the instruments used to calibrate the hotwire probe (i.e., in this case, the calibration instruments are the Pitot-static and total temperature probes); and second, the error between the velocity measured with the calibration instruments and the corresponding hotwire velocity calculated with the calibration curve. The uncertainty can thus be evaluated for each velocity within the calibration data set. For a conservative estimate, the maximum relative uncertainty found across all tested calibration data sets is used on all subsequent velocity measurements.

For the hotwire calibration data, a Pitot-static tube connected to an MKS gauge pressure transducer to measure the dynamic pressure P_{dyn} and a T-type thermocouple are used to evaluate the flow velocity at the hotwire location. This calibration velocity is therefore written as:

$$U_1 = \sqrt{\frac{2P_{\mathrm{dyn}}}{\rho}} \tag{4.8}$$

with P_{dyn} the difference between total pressure and static pressure and ρ the air density. The associated uncertainty ΔU_1 can therefore be expressed as:

$$\Delta U_1 = \sqrt{\left(\frac{\partial U_1}{\partial P_{\mathrm{dyn}}}\Delta P_{\mathrm{dyn}}\right)^2 + \left(\frac{\partial U_1}{\partial \rho}\Delta \rho\right)^2} = \alpha U_1 \tag{4.9}$$

with

$$\alpha = \frac{1}{2}\sqrt{\left(\frac{\Delta \rho}{\rho}\right)^2 + \left(\frac{\Delta P_{\mathrm{dyn}}}{P_{\mathrm{dyn}}}\right)^2} \tag{4.10}$$

and

$$\Delta \rho = \sqrt{\left(\frac{\partial \rho}{\partial P_{\mathrm{atm}}}\Delta P_{\mathrm{atm}}\right)^2 + \left(\frac{\partial \rho}{\partial T}\Delta T\right)^2} \quad \text{since} \quad \rho = \frac{P_{\mathrm{atm}}}{RT}. \tag{4.11}$$

This first step allows to evaluate the uncertainty in the calibration velocity used to generate the hotwire calibration. Next, the velocity U_2, defined as the velocity calculated using the calibration curve fit, is expected to be slightly different from U_1 due to errors in the curve fit. The uncertainty ΔU_2 is therefore:

$$\Delta U_2 = \beta U_1 \tag{4.12}$$

with

$$\beta = \sqrt{\frac{\sum_{i=1}^{n} \left(\frac{\Delta U_{\text{fit}}}{U_1}\right)_i^2}{n}} \tag{4.13}$$

and

$$\Delta U_{\text{fit}} = U_2 - U_1. \tag{4.14}$$

The systematic uncertainty ΔU related to the hotwire calibration can finally be expressed as:

$$\Delta U = \sqrt{(\Delta U_1)^2 + (\Delta U_2)^2} \tag{4.15}$$

and is calculated for each point in the calibration curve. The maximum ΔU is then reported in the third column of Table 4.2.

The second method is based on statistical calibration. For a given calibration data set, a Markov-Chain Monte-Carlo method is used to generate probability density functions (PDF) of the hotwire calibration parameters (i.e., in this instance, m and b from King's law) based on the initial spread in the measurements for calibration velocity. The first step consists in determining a calibration curve and the statistical spread in parameters m and b (shown in Figure 4.18) due to the spread in the calibration velocity. The systematic uncertainty is thus quantified. A multivariate normal distribution based on these two strongly correlated (as shown in the scatter plot on Figure 4.18) parameters m and b is then generated and randomly sampled to determine the uncertainty from the calibration curve. Typical results are shown in Figure 4.19.

Next, hotwire raw data is converted from voltage to velocity using the previously established calibration curve. In this step, the contribution to uncertainty due to the spread in the input voltage data (i.e., the random uncertainty) is taken into account, in addition to the systematic uncertainty from the calibration. With this method, the total uncertainty is calculated for each data point using the RSS.

The second method used to evaluate the uncertainty in velocity measurements consists in using a method. A set of PDF of the hotwire calibration parameters from King's equation, m and b, is generated based on the statistical spread of the calibration velocity U, and is shown in Figure 4.18. A multivariate normal distribution based on these two strongly correlated parameters is then generated and randomly sampled to determine the uncertainty from the calibration curve. Typical results are shown in Figure 4.19.

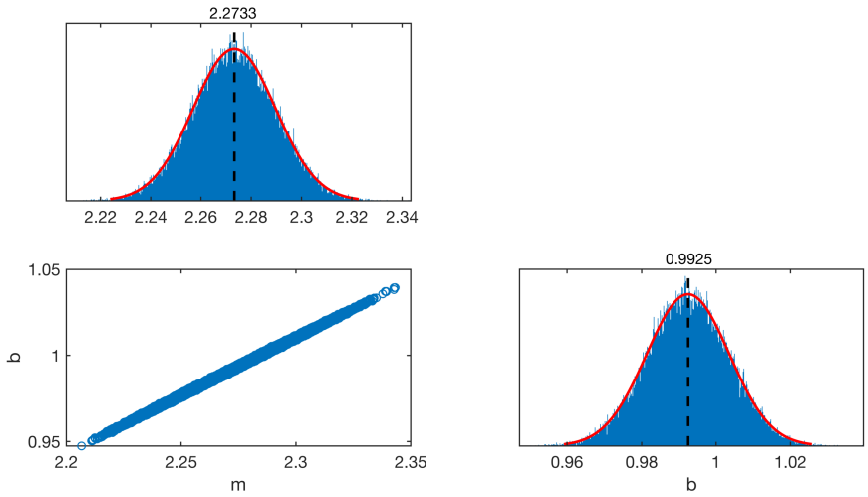

Figure 4.18. Probability Density Functions and scatter output from statistical calibration for Test 5.

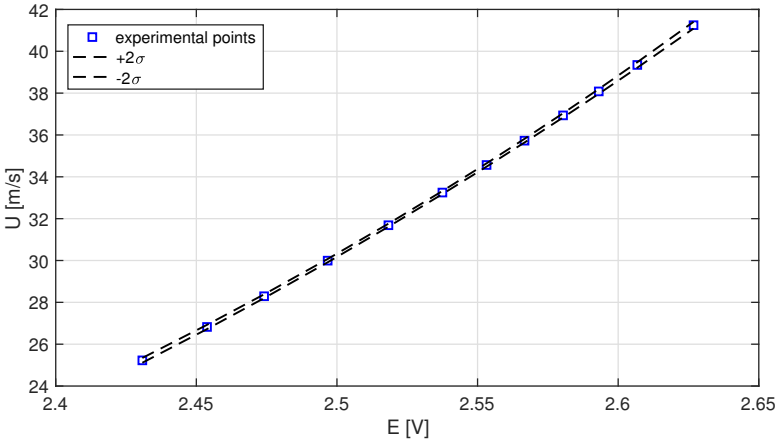

Figure 4.19. Calibration curve uncertainties ($\pm 2\sigma$) compared to experimental points for Test 5.

These calibration uncertainties are then propagated (using their multivariate normal distribution) when converting any voltage signal from a hotwire to a velocity. In addition to the systematic uncertainty from the calibration, the random uncertainty contribution related to the spread in the voltage measurements are also included such that King's law (Eq. 4.1) can be written as:

$$U = \left(\frac{E^2 - E_{o,c}^2}{b} \right)^m \quad \text{with} \quad E \sim \mathcal{N}(\bar{E}, e_{\text{rms}}) \quad \text{and}$$
$$[m, b] \sim \mathcal{N}([\bar{m}, \bar{b}], \text{covariance}[m, b])$$

In the present document, velocity measurements are mainly used for mean velocity boundary layer profiles and are normalized by the boundary layer edge velocity, U_e. To simplify notation in the following calculations, the variable U_{norm} is defined for any velocity U, such that:

$$\frac{U}{U_e} = U_{\text{norm}} \tag{4.16}$$

and so the uncertainty ΔU_{norm} of the normalized velocity is expressed as:

$$\Delta U_{\text{norm}} = \sqrt{\left(\frac{\partial U_{\text{norm}}}{\partial U} \Delta U \right)^2 + \left(\frac{\partial U_{\text{norm}}}{\partial U_e} \Delta U_e \right)^2}. \tag{4.17}$$

Wall-normal (y-) coordinate

Estimating the y-coordinate correctly in boundary layer profiles is critical because of its significant influence on boundary layer integral values. As mentioned previously, a correction y_c (i.e., a shift in all the y-coordinates) is applied to all boundary layer profiles to ensure that slope continuity is preserved between the (0,0) point, where the no-slip condition applies, and the first three measurements. The normalized y-coordinate y/δ_{99} (or y^* in this chapter, to simplify notation) is therefore evaluated using the following definition:

$$\frac{y}{\delta_{99}} (= y^*) = \frac{y + y_c}{\delta_{99} + y_c} \tag{4.18}$$

Based on this equation, the uncertainty Δy^* is:

$$\Delta y^* = \sqrt{\left(\frac{\partial y^*}{\partial y} \Delta y \right)^2 + \left(\frac{\partial y^*}{\partial \delta_{99}} \Delta \delta_{99} \right)^2 + \left(\frac{\partial y^*}{\partial y_c} \Delta y_c \right)^2} \tag{4.19}$$

In Equation 4.19, Δy and $\Delta\delta_{99}$ correspond to the systematic y-coordinate uncertainty provided by the instrument (Heidenhain), while the Δy_c is the random uncertainty. In the following case study, its values is determined using Equation 4.5 and using the correction values in the seven data sets presented.

Case study

Uncertainty calculations were performed on a boundary layer profile acquired at the same Reynolds number ($Re_x = 1.58{\cdot}10^6$) across seven independent data sets. This example therefore shows both uncertainty within a single test as well as across a range of different tests. Table 4.1 gives a summary of all the instrument's systematic uncertainties, as provided by the manufacturers.

Table 4.1. Instrument uncertainties as provided by manufacturer.

Instrument	**Systematic Uncertainty**	**Symbol**
Absolute Pressure (Digiquartz)	± 69 Pa (0.01% FS)	ΔP_{atm}
Relative Pressure (MKS)	± 0.3 Pa (0.01% FS)	ΔP_{dyn}
Gauge Pressure (SVMtec)	± 25 Pa (0.1% FS)	$\Delta P_{s,g}$
Temperature (T-type thermocouple)	± 2.5 K	ΔT
y-coordinate (Heidenhain)	± 5 µm	Δy

Table 4.2 is a summary of the different types of results obtained from each method. Using the classic method based on Yavuzkurt 1984, the output is the maximum relative uncertainty ΔU_{max} found for each calibration data set. As mentioned above, the largest ΔU_{max} across all seven tests is then used to provide a conservative uncertainty quantification. In the present case, the value is 1.09%, shown in bold in the table, and is used as an example on the mean velocity profile at $Re_x = 1.58{\cdot}10^6$ from Test 5 in Figure 4.20a. The uncertainty being expressed as a percentage of velocity, the points with the largest velocity have the largest uncertainty. Note that on the boundary layer profile figures, the uncertainty in the y-coordinate is also included. The methodology used to evaluate this type of uncertainty will be presented subsequently.

The output from the statistical calibration method are the mean parameters from King's law, $\bar{m}$ and $\bar{b}$ along with their respective standard deviations, σ_m and σ_b, reported in Table 4.2. Based on these parameters, and since m and b are strongly correlated, a multivariate normal distribution is generated and then randomly sampled. The total uncertainty using this second method is shown in Figure 4.20b for the same boundary layer profile as the one presented in Figure 4.20a. Comparing both methods, the statistical calibration provides smaller uncertainties than the classic method. However, regardless of the method, symbol size in the remainder of the graphs shown in this dissertation will always be chosen so as to contain uncertainties.

Next the uncertainty in the normalized y-coordinate is calculated using Equation 4.19 and the value for the y-coordinate ±5 µm (as listed in Table 4.1) for Δy and $\Delta\delta_{99}$. Across the seven test cases, the average y-correction is 40 µm ± 8 µm: the uncertainty Δy_{cor} is therefore set to 8 µm. The uncertainty for the normalized y-coordinates are reported in Figures 4.20. Once again, although the wall-normal coordinate uncertainty is visible, it can generally be approximated to be within symbol size.

Next, the uncertainty across all the different tests is examined by comparing the seven boundary layer profiles at $Re_x = 1.58{\cdot}10^6$ to each other and to a Blasius profile, as shown on Figure 4.21. Experimental profiles collapse relatively well between themselves, and are generally close to the theoretical profile. Good repeatability across various test cases is also established. For all subsequently shown boundary layer profiles, the uncertainties will be assumed to be

Table 4.2. Hotwire calibration data sets and related uncertainty parameters.

		Classic method	Statistical calibration method			
Test	Test Date	$(\Delta U)_{max}$	$\bar{m}$	σ_m	$\bar{b}$	σ_b
1	2018.01.25	0.40%	2.217222	0.078506	0.919559	0.050932
2	2018.02.21	0.64%	2.143080	0.065380	0.811557	0.040095
3	2018.03.06	0.71%	2.216240	0.067444	0.841672	0.039926
4	2018.03.09	0.38%	2.239154	0.075695	0.841771	0.043827
5	2018.09.12	0.38%	2.268272	0.081877	0.989772	0.053694
6	2019.02.13	**1.09%**	2.265482	0.084545	0.935810	0.052875
7	2019.02.21	0.43%	2.359809	0.067525	0.976035	0.041206

within symbol size.

4.3.2 Transition position

As mentioned previously, the onset of transition is determined once the non-dimensionalized velocity fluctuations start to increase at a rate equal or superior to $2{\cdot}10^{-4}$ mm^{-1}. Since streamwise traverses of the hotwire are performed at constant geometric altitude (as opposed to a constant altitude inside the boundary layer) the validity of this threshold value had to be established. Additionally, testing this criterion could allow to evaluate the error in transition position that could result from probing at a constant height, despite the growing boundary layer. To do so, multiple traverses at different constant geometric altitudes (200 µm, 300 µm, 400 µm, 500 µm and 800 µm) were performed. These heights are represented by the dashed black lines on Figure 4.22 to show their relative position with respect to the maximum TS amplitude.

Figure 4.23 then shows that traversing the hotwire at a constant height, and therefore not accounting for the growing boundary layer and varying TS profiles, does not induce a significant source of error in estimating the transition position. Additionally, using the slope criterion $2 \cdot 10^{-4}$ mm^{-1} on the traverses at all heights, the uncertainty in the the transition location can thus be estimated to be $\pm$ 15 mm or, in terms of Reynolds number, $\pm\, 3.9{\cdot}10^4$ (and approximately 5% depending on the transition location). Note that in this figure, the transition position is different from the one presented previously for the reference case. A different suction panel was used for this test and further information will be provided in the next chapter.

4.3.3 Pressure coefficient

The pressure coefficient, C_p, is another parameter that is recurrently checked to ensure repeatable conditions. Its definition at the streamwise location x_i is:

$$C_{p,i} = \frac{P_{s,i} - P_{s,o}}{P_{t,o} - P_{s,o}} = \frac{P_{s,g}}{P_{\text{dyn}}} \tag{4.20}$$

As such, the uncertainty ΔC_p can be expressed:

$$\Delta C_p = \sqrt{\left(\frac{\partial C_p}{\partial P_{s,g}} \Delta P_{s,g}\right)^2 + \left(\frac{\partial C_p}{\partial P_{\text{dyn}}} \Delta P_{\text{dyn}}\right)^2} \tag{4.21}$$

Based on these equations and the systematic uncertainties listed in Table 4.1, the uncertainties for the pressure coefficient are shown in Figure 4.24.

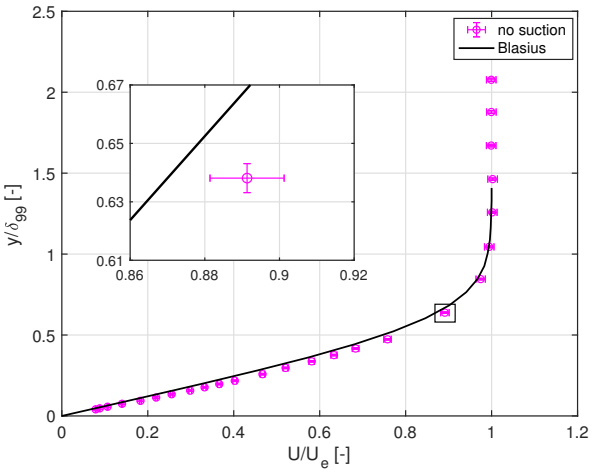

(a) With systematic 1.09% uncertainty.

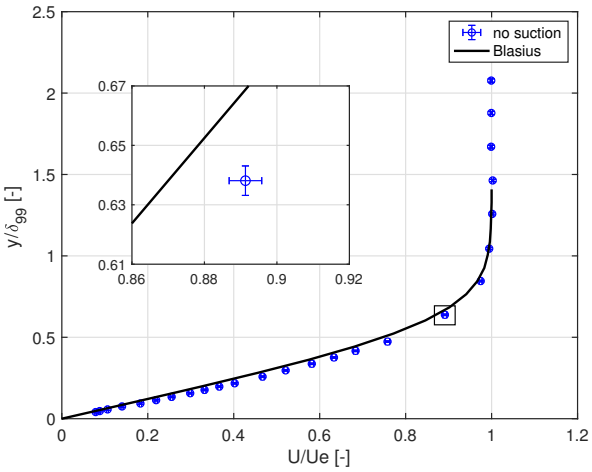

(b) With total uncertainty from statistical calibration.

Figure 4.20. Normalized mean velocity profile ($Re_x = 1.58{\cdot}10^6$) from Test 5 with uncertainties.

Summary

This chapter discussed the experimental facility and protocol that were developed and implemented to ensure that a proper basis for an experimental study of the laminar-turbulent transition was established. The freestream turbulence levels were shown to be low enough such that the "natural" path to transition, driven by TS instabilities, occurs. Flow characterization also demonstrated that the boundary layer developing over the flat plate was as close as possible to a two-dimensional Blasius boundary layer. Measurement uncertainty was also performed to provide a notion of what constitutes a more or less significant difference between different types of measurements. The next part will focus on the experiments that were then carried out, using the experimental protocol presented in this chapter.

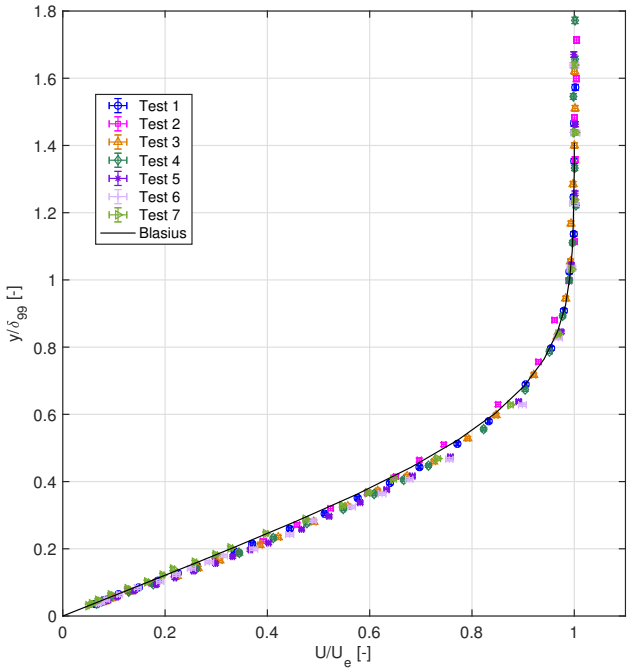

Figure 4.21. Normalized mean velocity profile ($Re_x = 1.58{\cdot}10^6$) for all tests with statistical calibration uncertainties.

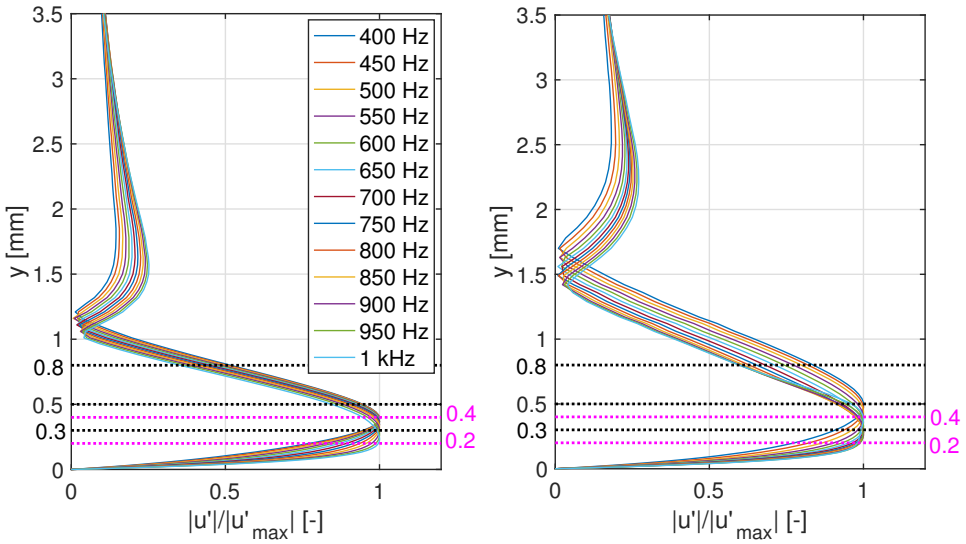

(a) TS profiles over range of frequency of interest at $Re_x = 5.4{\cdot}10^5$ m^{-1} *(x∼208 mm).*

(b) TS profiles over range of frequency of interest at $Re_x = 1.3{\cdot}10^6$ m^{-1} *(x∼508 mm).*

Figure 4.22. Numerical TS profiles evolution in the streamwise direction over a range of frequencies of interest with hotwire probe altitudes.

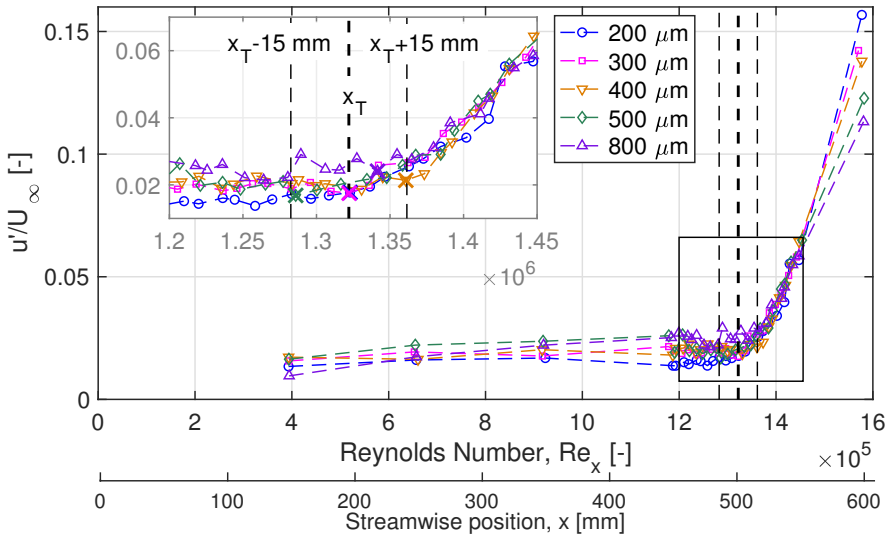

Figure 4.23. Streamwise velocity fluctuations for various constant height hotwire traverses (suction panel with porosity p = 1.34%).

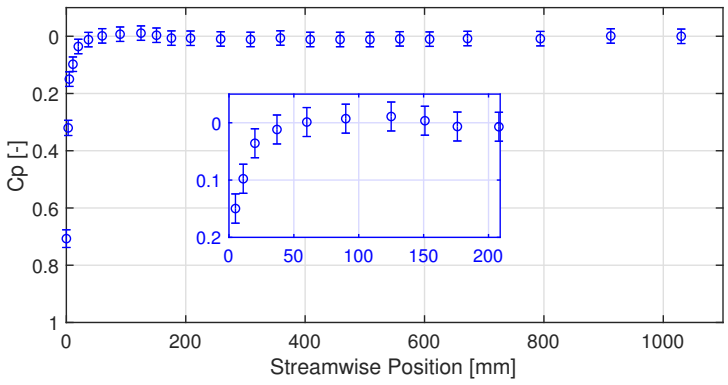

Figure 4.24. Nominal pressure coefficient distribution at Re = 2.6·10^6 m^{-1} with uncertainties.

Part III

Experimental Investigations on Transition with a Wall Suction System

Chapter 5

Wall Impedance and Suction Effects on Laminar-Turbulent Transition

Contents

5.1 Wall suction parameters and suction configurations 67
5.1.1 Suction panel geometric parameters 67
5.1.2 Summary of the reference 1995 study 68
5.2 Effects of a porous wall without suction 70
5.2.1 Experimental characterization 70
5.2.2 Numerical analysis 75
5.3 Effect of wall suction and suction distribution 79

In this chapter, all the effects associated with the implementation of wall suction technology are introduced. In the first section, an overview of all the wall suction parameters and chosen suction configurations is given, along with a summary of the findings from the previous experiment on which the present investigation is based (Section 5.1). The generally destabilizing effect on transition of a porous wall *without suction*, which is scarcely documented in the literature, is then characterized in the subsequent section (Section 5.2). Finally, the well-known stabilizing effects of wall suction on transition are discussed (Section 5.3). These wall suction results are presented to establish a reference for the smooth case (*i.e.*, without any surface defects) to enable a later comparison with the different types of surface defects, presented in the following chapter.

5.1 Wall suction parameters and suction configurations

5.1.1 Suction panel geometric parameters

As mentioned in Section 4.1.2 of the previous chapter, the suction region of the present flat plate spans an area of 0.450 m (x) by 0.350 m (z). The panels through which suction is applied consist of 0.9 mm-thick micro-perforated titanium sheets, flush-mounted with the rest of the flat plate's upper side. In addition to a solid wall panel, the two perforated panels that were tested for this study have porosities p of 0.26%, and 1.34%, with porosity defined as the ratio of the open area to the sheet's total surface area.

The panel with 0.26% porosity has, on average, 92 µm-diameter holes evenly spaced in a square pattern of dimensions 1.6 mm x 1.6 mm. Similarly, the panel with 1.34% porosity has, on average, 188 µm-diameter holes evenly spaced in a square pattern of dimensions 1.44 mm

Table 5.1. Panel parameters.

Panel	p [%]	Hole diameter, d [μm]	Hole spacing, s [mm]
P1	0	0	0
P2	0.26	92	1.6
P3	1.34	188	1.44

x 1.44 mm. All the panel characteristics are summarized in Table 5.1. In this table and for the remainder of the present document, panels are referred to as P1, P2 and P3. Since each panel has a different combination of porosity and hole diameter size, the individual effect of each parameter will not be determined using the experimental data available in the present study. The neutral nomenclature $P\#$ is therefore an attempt to reduce bias towards incriminating one parameter over the other.

For all test configurations with suction, total mass flow rate of the suction flow was kept constant at 0.4 g.s^{-1}, and only suction distribution varied. The mass flow rate was chosen to be identical to that of the previous experiment by Juillen et al. 1995 on which this experiment is based. The principal purpose of the current study was to investigate the combined effect of wall suction and surface defects on boundary layer transition: using identical suction parameters as in the 1995 study enabled to rapidly select the suction distributions of interest and to validate, albeit superficially, initial results.

5.1.2 Summary of the reference 1995 study

Note that, despite significant efforts, differences in the experimental conditions between the 1995 and present studies exist, either due to changes in the model or the wind tunnel facility. The results from the 1995 study are presented in this section to provide readers with the same background information used to determine the parameters of interest for the present study. Differences between both studies, either in terms of transition position or transition N factors, are therefore expected and inconsequential.

In this previous study, eleven different suction configurations (including a case without suction) were investigated in a flow with freestream unit Reynolds numbers $3.3{\cdot}10^6$ m^{-1} (approximately 48 m.s^{-1}). The flat plate and flap angles on attack were set to minimize the suction peak; however, the flow over the flat plate was still slightly accelerated. A 0.28 mm-thick micro-perforated nickel panel with a porosity of 0.36% and holes with an average diameter of 40 µm was mounted over the suction region. The results on the influence of suction distribution on transition are reported in Table 5.2.

Numerical analysis was concurrently performed using both LST and Non-Linear Parabolized Stability Equations (also referred to simply as "PSE" in the remainder of the chapter). The advantage of using PSE over LST is that the former allows to consider “weak" non-parallel effects (small streamwise variations, such as a growing boundary layer), thereby removing the “local" assumption imposed by LST, and accounting for the history of the disturbance. Additionally, with PSE, the disturbance amplitude (rather than amplitude growth) is calculated. Finally, the "non-linear" aspect of PSE allow the study of both primary and secondary instabilities, and therefore the early non-linear stages of transition. More details about PSE can be found in Herbert 1997.

The results from LST are shown in Table 5.2 in the N_T *Factor* column. Using Mack's relation (Equation 1.39), authors found that the theoretical N_T based on turbulence levels inside the test section should be close to 6. Only case 1 (no suction) is in agreement with this prediction: all the cases with suction have a transition N factor less than 6.

Table 5.2. Experimental transition positions for the different suction configurations tested in Juillen et al. 1995 and corresponding N_T.
(corresponds to cases where transition occurs downstream of the maximum N factor).*

Case	Chambers with suction	x_T [mm]	N_T Factor
1	0	740	5.8
2	1 through 9	1000	3.9
3	1	980	5.2
6	2,3,6,7	940	3.8
7	2,3,5,6,8,9	950	3.8
8	2,4,6,8	945	3.8
9	5	940	3.9
10	3	975	4.6
11	3,5	1005	4.2
4	9	920	4.4*
5	7	845	4.2*

Overall, suction distribution seems to have a relatively minor effect on the transition position, except for cases 4 and 5. These two cases, where suction is applied over the seventh and ninth chambers respectively, are also noteworthy by the fact that the experimental transition position occurs downstream of the maximum computed N factor. The use of LST and the e^N method with suction therefore seem to raise two points: the first is that different suction distributions have varying transition N_T values; and the second is that, in some cases, the transition occurs downstream of the maximum computed N factor.

To further investigate these issues, Casalis et al. 1996 performed some weakly non-linear PSE calculations for various theoretical suction configurations over a flat plate. In this set-up, a suction with normal velocity V_p of -0.01 m.s^{-1} was applied over various regions with streamwise lengths of 0.10 m. The streamwise amplitude evolution evaluated for the primary and secondary instabilities ($A_{2,0}$ and $A_{1,1}$ respectively) in the case without suction and for different suction regions is shown in Figure 5.1.

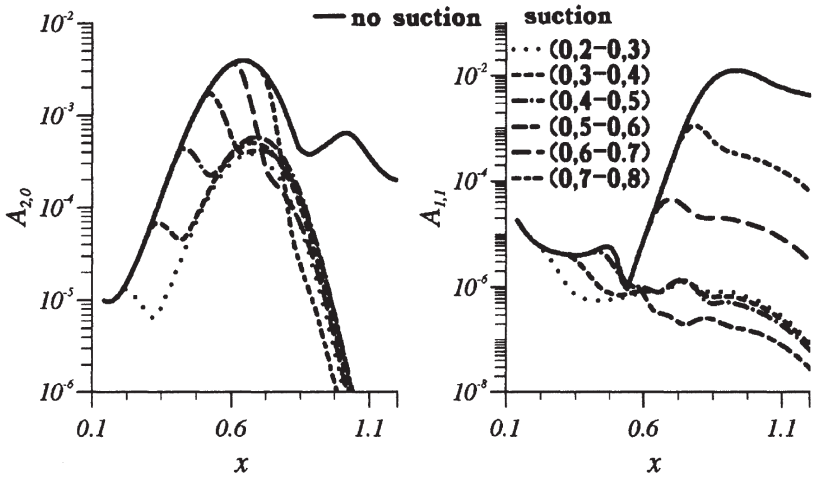

Figure 5.1. Amplitude evolution of the primary ($A_{2,0}$) and secondary ($A_{1,1}$) instabilities for cases with and without suction (from Casalis et al. 1996).

The left-hand graph shows the limited effect of suction location on the amplitude evolution

of the primary instabilities. Regardless of where suction is applied, the initially low-amplitude primary instability is effectively attenuated. Note that some non-linear effects are visible in the case without suction close to the 0.9 m x-position.

However, on the right-hand graph, there seems to be a streamwise position downstream of which suction can be less effective in attenuating secondary instabilities. For example, if suction is applied over regions [0.6 m - 0.7 m] or [0.7 m - 0.8 m], the secondary instabilities have already started amplifying and suction can only reduce the maximum amplitude. Additionally, comparing these two cases shows that as suction is applied further downstream, the maximum amplitude is also less effectively reduced.

These results have significant implications in terms of transition onset: past a threshold amplitude for the secondary instabilities, nonlinear instabilities from other modes start to amplify, thereby leading to transition. Suction cases over regions [0.6 m - 0.7 m] or [0.7 m - 0.8 m] therefore run the risk of being less effective in transition delay because secondary instabilities amplified enough such that breakdown to turbulence still occurs.

Based on these numerical results, suction should be applied before secondary instabilities, and subsequent non-linear instabilities, start to amplify to be most effective. Cases 4 and 5 from the 1995 experimental study cannot be properly modeled by LST, which only accounts for primary instabilities, because suction is probably applied after the significant amplification of secondary instability. Although non-linear PSE were able to provide some explanation for the cases where transition occurred downstream of the maximum N factor, the varying N_T values depending on the suction configuration were not explained. Authors hypothesized that different suction distributions could affect receptivity either by modifying the initial amplitude of different frequencies or by deteriorating the test section flow quality. As will be seen subsequently, the issue of the varying transition N factors with suction distribution will also be encountered in the present study.

5.2 Effects of a porous wall without suction

5.2.1 Experimental characterization

Even in the absence of wall-suction, a porous wall was found to have a generally destabilizing effect on boundary layer transition. An experimental characterization followed by a numerical analysis of this phenomenon were performed to further understand the underlying mechanisms in place.

Mean velocity profiles were acquired at four streamwise positions, ranging over the entire streamwise length of the suction panels as well as over one downstream position. For the first two streamwise positions, as shown on Figures 5.2a and 5.2b, regardless of the suction panel, the boundary layer profiles overlap well with each other and are close to the theoretical Blasius profile. At the next downstream position in Figure 5.2c, the profiles for cases P1 and P2 (with no or low porosity and hole diameter) are still laminar and overlapping, while for case P3, the boundary layer has undergone transition. At the last station, downstream of the panels, the configuration with panel P3 is now fully turbulent and the P2 profile is departing from the P1. As opposed to the no porosity case P1, case P2 is now undergoing transition. The streamwise evolution of the mean velocity profiles indicates that the onset of boundary layer transition begins at a lower Reynolds number for the perforated panels P2 and P3 than for the solid wall panel P1.

To determine the transition position for these three cases, the streamwise evolution of the voltage fluctuations e' is examined. First, the transition position for all panels is tested for two-dimensionality, as shown on Figure 5.3. The spanwise region over which the two-dimensionality

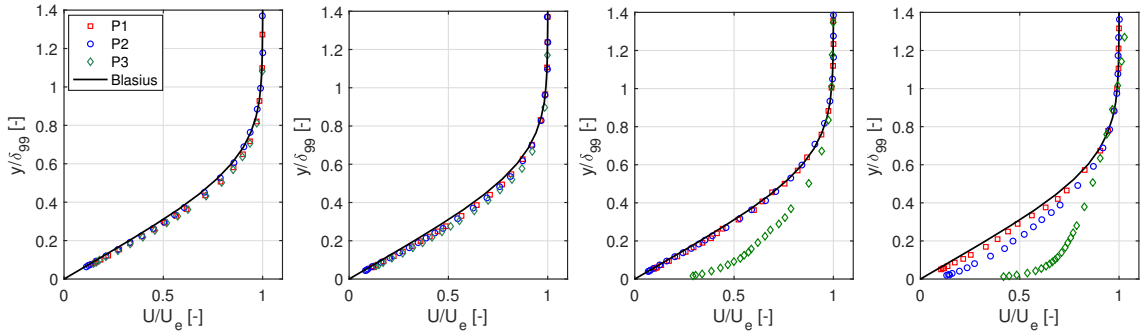

(a) $Re_x=5.3 \cdot 10^5$ (x ∼208 mm) *(center of chamber C1).*

(b) $Re_x=1.1 \cdot 10^6$ (x ∼408 mm) *(center of chamber C5).*

(c) $Re_x=1.6 \cdot 10^6$ (x ∼608 mm) *(center of chamber C9).*

(d) $Re_x=2.0 \cdot 10^6$ (x ∼750 mm) *(downstream chambers).*

Figure 5.2. Streamwise evolution of mean velocity profiles for all panels at Re = $2.6 \cdot 10^6$ m^{-1} without suction.

of panel P3 transition was checked had to be slightly reduced compared to the other panels: this difference is suspected to be the result of the more intense phenomena, related to the panel's greater porosity and hole diameter, occurring for this panel.

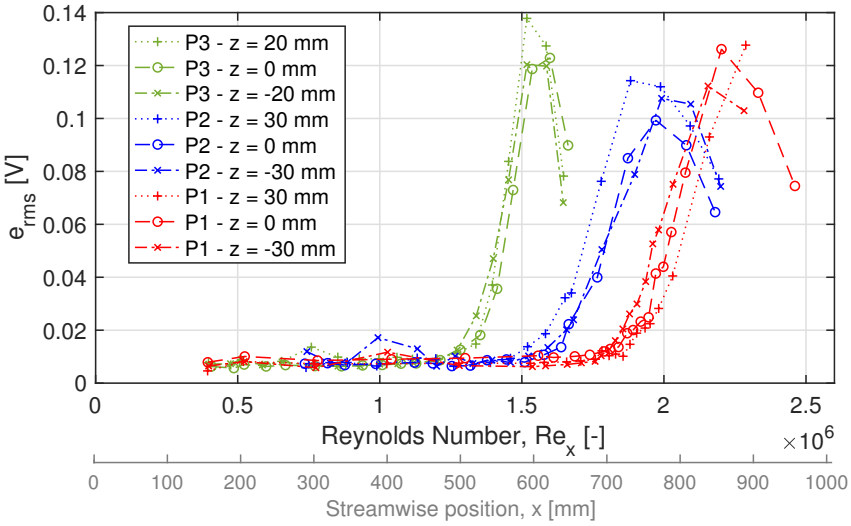

Figure 5.3. Two-dimensional transition position for all panels.

The transition positions for the different panels can then be compared at the centerline position, as shown in Figure 5.4. As suggested by the mean velocity profile evolution, the configuration with the largest porosity and hole diameter size, P3, has the transition position closest to the leading edge, whereas P1 (corresponding to the solid flat plate) has the transition position furthest from the leading edge. The case with intermediate porosity and hole diameter has an intermediate transition location. For the configurations under investigation, a porous wall through which no suction is being applied therefore seems to destabilize the boundary layer.

The first verification performed was to check that the destabilizing effect observed in the presence of porous walls was not related to an equivalent distributed roughness effect due to the perforations. The perforations were therefore obstructed with tape on the lower side (*i.e.*, the side not in contact with the main outer flow) of the suction panels P2 and P3. In this configura-

tion, no communication with the suction chamber underneath is possible while contact between the perforations and the boundary layer is maintained. As shown on Figure 5.4, once communication with the suction chambers is removed, the transition location for the perforated panels matches relatively well that of the solid wall panel. The surface roughness of the perforations therefore does not seem responsible for destabilizing the boundary layer.

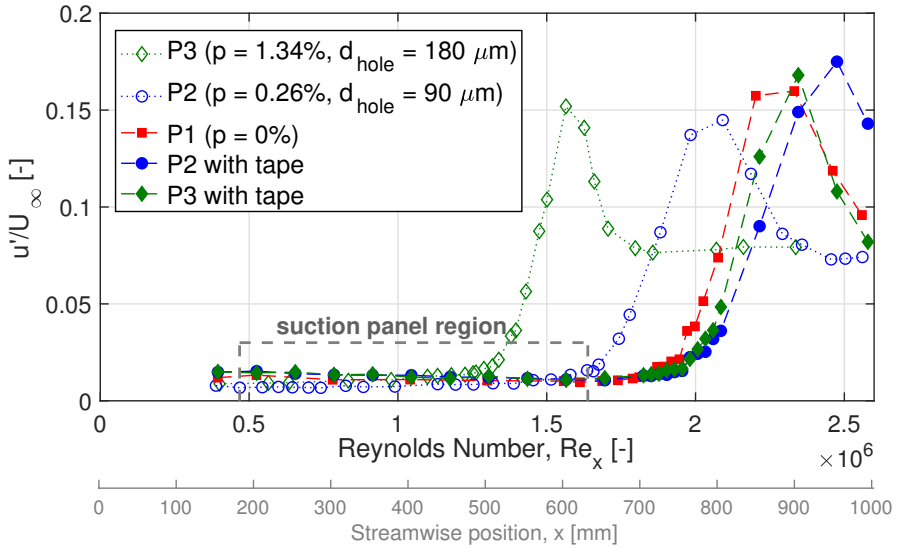

Figure 5.4. Streamwise velocity fluctuations for all panel configurations for the *no suction* configuration.

The combination of a micro-perforated panel mounted over suction chambers therefore seems to be responsible for phenomena affecting boundary layer stability. This configuration could crudely be modeled by a family of acoustic liners, characterized as Single Degree of Freedom (SDOF) liners. These types of liners are commonly mounted at the inlet of aeroengines to reduce noise emission by using the working principle of a Hemholtz resonator. They can consist of a thin micro-perforated plate mounted over a series of cavities (generally in the form of a honeycomb structure). Although the suction chambers have much larger plenum volume than any typical honeycomb structure, the similarities between the liners and the present configurations are compelling enough to allow the use of a liner model to perform the following numerical investigation. The interaction that can occur between the hydrodynamic perturbations found in the boundary layer and this liner-type surface are mainly governed by the surface's opposition to the flow. If the surface is porous, some absorption can occur: the interaction can therefore be modeled by a wall impedance boundary condition. When the porous panels were obstructed with tape, the wall impedance was therefore significantly reduced, and its effect on boundary layer stability became negligible to the point where the no porosity transition position was recovered. These first experimental results are in agreement with the findings from numerical studies, such as by Choudhari 1994, Carpenter and Porter 2001, and Tilton and Cortelezzi 2015.

Since wall impedance seems to have an effect on boundary layer stability, the next step is to determine its influence on the instabilities responsible for the laminar-turbulent transition, originally the TS instabilities in the solid wall P1 case. Since hotwire measurements are highly time-resolved, the analysis of the velocity fluctuations inside the boundary layer allows the identification of the most amplified frequencies, as shown in Figure 5.5. In this figure, the spectral analysis of the streamwise velocity fluctuations 300 µm from the wall is shown for each porous panel at a different streamwise positions, upstream of the respective transition location where the instabilities responsible for transition are sufficiently amplified to be identified in terms

of frequency. The streamwise positions are indicated in the figure's legend. Further information on the amplitude of these instabilities will be provided subsequently.

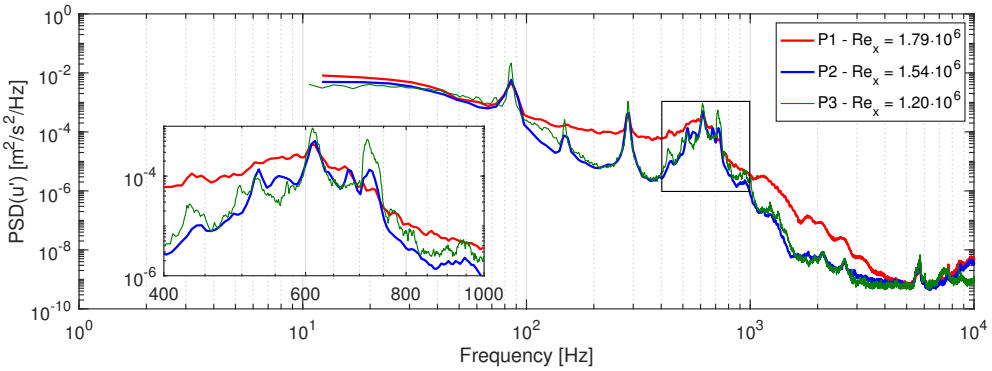

Figure 5.5. PSD(u') (y = 300 μm from wall) at a position upstream of the transition location where TS waves are visibly amplified.

The boxed region in Figure 5.5 zooms over the most amplified TS wave frequencies (400 Hz to 1 kHz), which are centered around approximately 600 Hz, regardless of the porosity. The three PSD have very similar overall shapes despite their different absolute streamwise positions, possibly indicating that the transition mechanism is not modified but simply *accelerated*.

This hypothesis is also supported by Figure 5.6, where the PSD for all three panels are compared at the same altitude inside the boundary layer and at the same streamwise position. In this comparison, the boundary layer over panel P3 is already undergoing transition whereas, over the two other panels, the flow is still laminar. Over the range of frequencies previously determined to be the instabilities responsible for transition, the P3 case, which transitions the earliest, has significantly greater amplitude than in the case of either P1 or P2. The fact that the amplified frequency range seems unchanged and that panel P3 has the largest instability amplitudes seem to strongly suggest that wall impedance does not change the fundamental transition mechanism but rather affect the instabilities' amplitude. However, these experimental data cannot be used to determine with certainty whether this effect occurs by either modifying the receptivity phase or the linear amplification of the instabilities because measuring initial amplitude levels (A_0) or amplification rates (α_i) with accuracy is not possible with the given set-up.

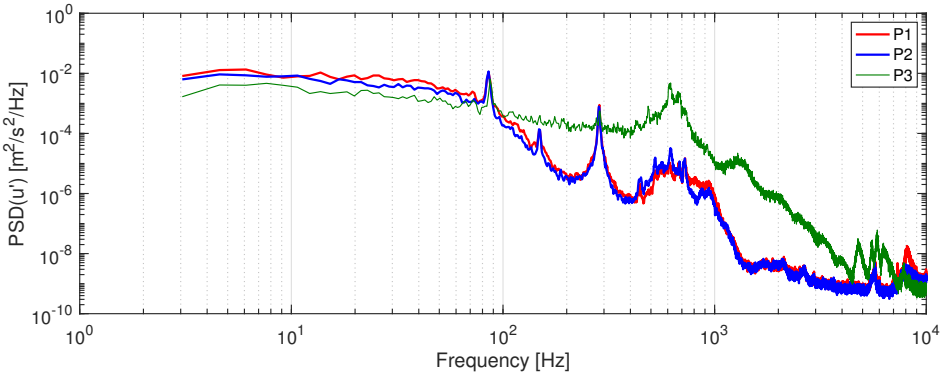

Figure 5.6. PSD(u') (y = 300 μm from wall) at $\mathrm{Re_x} = 1.32{\cdot}10^6$ (x ~508 mm) for all panels.

The evolution of the most amplified frequency can also be examined using profiles of the streamwise velocity fluctuations, which in terms of LST, would correspond to eigenfunctions.

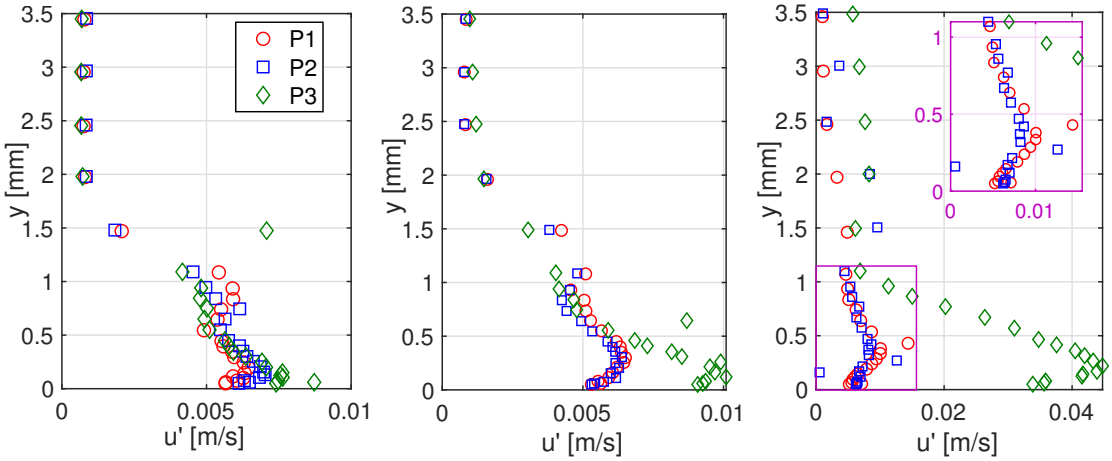

(a) $\mathrm{Re_x}$=5.41 · 10^5 (*center of chamber C1*).
(b) $\mathrm{Re_x}$=8.00 · 10^5 (*center of chamber C3*).
(c) $\mathrm{Re_x}$=1.06 · 10^6 (*center of chamber C5*).

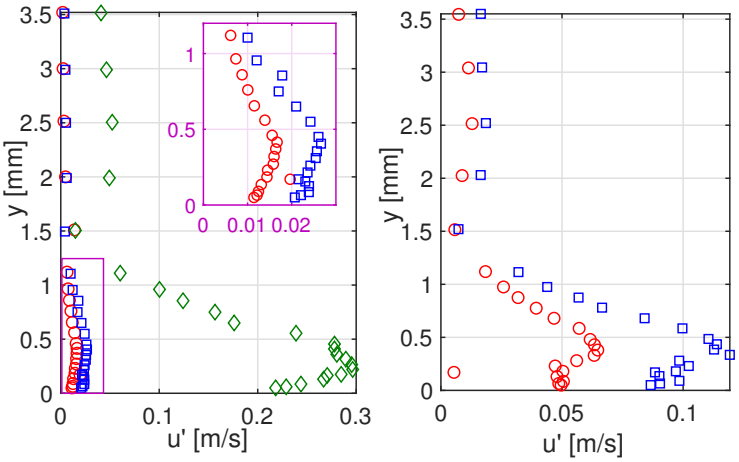

(d) $\mathrm{Re_x}$=1.32 · 10^6 (*center of chamber C7*).
(e) $\mathrm{Re_x}$=1.58 · 10^6 (*center of chamber C9*).

Figure 5.7. Streamwise evolution of velocity fluctuation profiles evaluated over frequency range [592-632] Hz for all panels without suction.

For each point of a boundary layer profile, the PSD of u' is calculated, and then integrated over a frequency band ranging 40 Hz, centered on the frequency of interest. Finally, to revert to units of velocity, the square root of these computed values is taken. In this study, the frequency range of integration was set to 592-632 Hz for all panels. Using this method, the u' profiles at different streamwise locations are extracted, as shown in Figure 5.7. For all three panels these profiles are generally found to correspond well to TS instabilities profiles, and therefore the same transition mechanism.

The first streamwise position, shown in Figure 5.7a is centered over the first chamber of the suction region. At this location, all u' profiles have similar shapes and comparable magnitudes, despite the abrupt change in wall impedance for cases P2 and P3. The next streamwise positions, shown in Figures 5.7b and 5.7c, are located upstream of the P3 transition position. The u' profiles for the P3 panel first starts to have slightly greater amplitude than the other two profiles (Figure 5.7b). At the next position, on Figure 5.7c, the profile then exhibits the pronounced features of a fully developed TS instabilities profile, and has significantly greater magnitude than that of the other two profiles.

At the next position (Figure 5.7d), located immediately upstream of the P3 transition location, the *u'* profile for P3 has undergone even greater amplification while the P1 and P2 profiles still have significantly lower magnitudes. However, the *u'* profile for panel P2 now has slightly greater amplitude than the P1 solid wall case as shown in the inset graph. This last trend is further amplified in Figure 5.7e, where the maximum amplitude of the *u'* profile for panel P2 is now approximately twice that of panel P1. As mentioned previously, although determining conclusively whether a porous wall acts on the receptivity or amplification phase, the profiles' evolution seem to indicate to an strong effect on the TS instabilities amplification phase.

The streamwise evolution of the maxima $\underset{y}{max}(u')$ of the *u'* profile (evaluated over the frequency range [592 Hz - 632 Hz]) is given for each suction panel in Figure 5.8. Over the first three suction chambers, the amplitudes are comparable, regardless of the panel. Beginning at the fourth streamwise position, the P3 maximum amplitudes depart from the two other panels, and start to amplify significantly until transition is detected close to Re_x equal to $1.3{\cdot}10^6$ ($\sim$510 mm). The difference between panels P1 and P2 becomes noticeable over the sixth suction chamber, after which each data seems to amplify at the different rate. Once again, this graph provides further evidence in favor of the hypothesis that the porous panel mainly affects the amplification of instabilities.

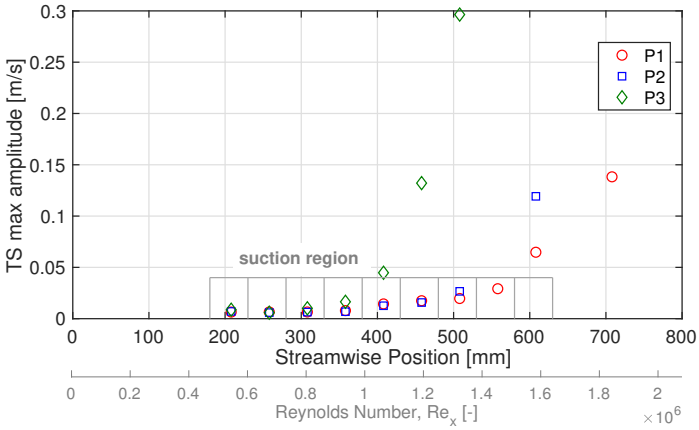

Figure 5.8. Streamwise evolution of the *u'* profile (evaluated over [532 Hz - 632 Hz]) maximum amplitude for all panels without suction.

5.2.2 Numerical analysis

The results presented in this section were performed in collaboration with A. Rouviere during his internship at ONERA. The purpose of the internship was to implement an impedance (*i.e.*, what is previously referred to as wall impedance) boundary condition and evaluate the resulting effects on the linear stability of a boundary layer. The general approach consisted in approximating the perforated panel and suction chamber assembly as a SDOF liner, and assuming that the liner was locally reacting and linear time invariant. Based on this approximation, the perforated panel and suction chamber assembly can be modeled as an impedance (or wall admittance) boundary condition, using existing acoustic liner models. The reduced specific impedance is defined, at a point location on the surface of interest, as:

$$Z(\omega) = \frac{\hat{p}(\omega)}{\rho_0 c_0 \hat{\boldsymbol{u}} \cdot \boldsymbol{n}} = R + i\chi \tag{5.1}$$

with $\hat{p}$ the fluctuating pressure, $\hat{\boldsymbol{u}}$ the fluctuating streamwise velocity, $\boldsymbol{n}$ the outward-pointing normal vector to the surface and ρ_0 and c_0 the density and acoustic velocity of the fluid. The

impedance Z is a complex variable, with the real component, R, corresponding to the resistance, and the imaginary component, χ, the reactance. The admittance is defined as the inverse of impedance, $1/Z$.

In practice, a base flow was initially calculated using ONERA's in-house boundary layer code using the pressure coefficient shown in Figure 4.13 and without suction. Next, the stability of the boundary layer was evaluated with an LST code that imposed the impedance boundary condition at the wall. To determine the value of the boundary condition, the "liner" total impedance was defined as the sum of the perforation impedance (based on the model by Crandall 1927) and cavity impedance (based on the definition by Bruneau 2006). Crandall's model is based on the incompressibility hypothesis because the minimum wavelength in the acoustic field under consideration is considered large compared to the perforation diameter.

Once the impedance boundary condition was implemented, a parametric study on the effect of real-only (Figure 5.9) and imaginary-only (Figure 5.10) impedances on Blasius boundary layer stability was performed. In general, as the real-only (*i.e.*, simply referred to as real subsequently) impedance decreases, the critical Reynolds number decreases and the range of amplified angular frequencies is increased with respect to the Blasius flow curve. In particular, for the two lowest tested value of impedance (Z equal to 5 and 10), the second branch of their neutral stability curves do not seem to tend to zero for increase $Re_{\delta 1}$ values, similar to inflection point instabilities. Additionally, as the real-only impedance decreases, the most amplified angular frequency shifts to a higher Re_{δ_1} and undergoes a higher rate of amplification. Note that the solid wall panel corresponds to the Z value of infinity.

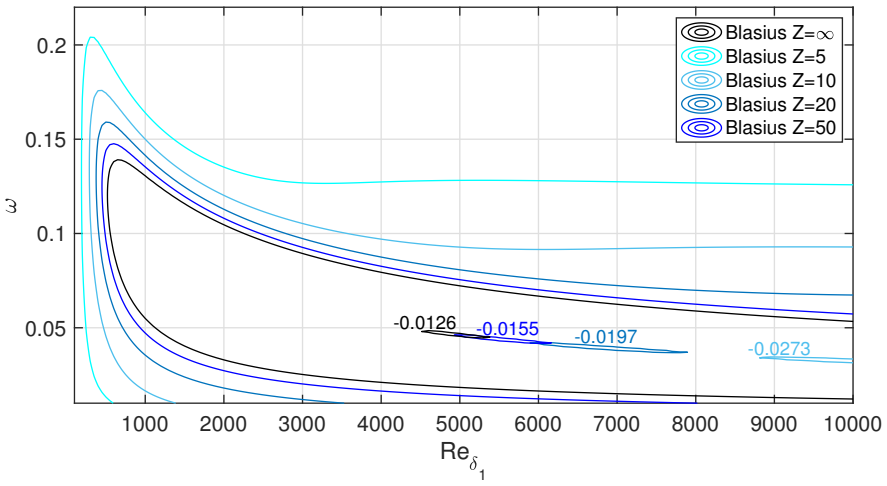

Figure 5.9. Neutral stability curve and maximum amplification rate comparison of real-only impedance on boundary layer stability with Blasius flow (without suction).

In the case of the imaginary-only (*i.e.*, simply referred to as imaginary subsequently) impedance, both positive and negative values were tested and found to affect the neutral stability curve compared to a Blasius flow. In general low absolute values of the imaginary impedance (Z equal to $5i$ and -$5i$) induce a greater shift in neutral stability curve than larger absolute values (Z equal to $20i$ and -$20i$).

More specifically however, as a positive imaginary impedance decreases, the critical Reynolds number decreases. Additionally the region covered by the lower branch of the neutral stability curve tends to increase while that of the upper branch tends to decrease, compared to the Blasius flow curve (*e.g.*, dotted lines). Although the maximum amplification rate does not change significantly, it is shifted towards lower $Re_{\delta 1}$ values for decreasing positive impedance values. On the other hand, an decreasing negative impedance seems to have a overall stabilizing

effect (*e.g.*, dashed lines): the critical Reynolds number increases and the region covered by the lower branch of the neutral stability curve is decreased while that of the upper branch is slightly increased with respect to the Blasius flow curve. Once again, the maximum amplification rate does not change significantly in its absolute value but shifts towards higher $Re_{\delta 1}$ for increasing negative impedance values.

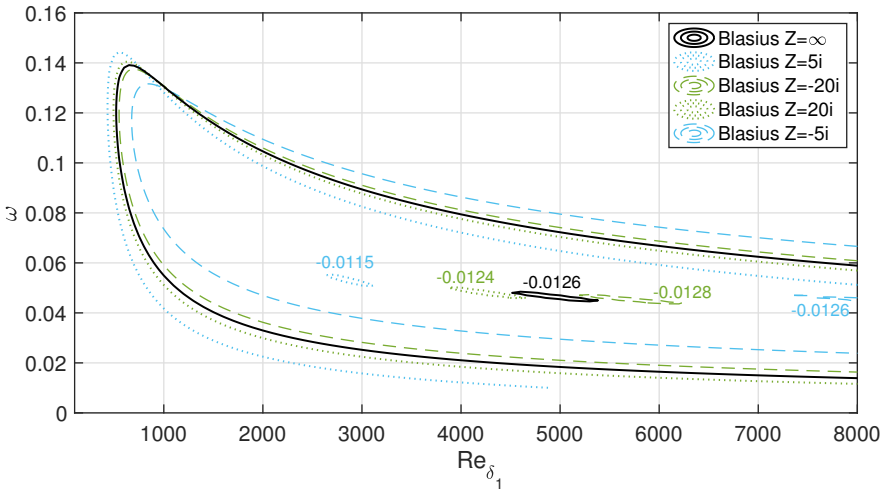

Figure 5.10. Neutral stability curve and maximum amplification rate comparison of imaginary-only impedance on boundary layer stability with Blasius flow (without suction).

From this initial parametric study, the individual effects of real and imaginary impedance could be observed. In general, wall impedance is shown to modify the stability properties (calculated using LST) of a Blasius boundary layer, as seen by the shift in neutral stability curves when impedance boundary conditions were applied.

Up to this point, a theoretical impedance boundary condition was imposed to understand its effect on boundary layer stability. The next step therefore involved using the acoustic liner models (for cavity and perforations) to evaluated an impedance boundary conditions based on the chamber dimensions and panel parameters summarized in Table 5.1. The corresponding impedance Z calculated for each panel is given in the last column of Table 5.3. By implementing these impedance values, the objective was now to observe their effect on boundary layer stability and compare with the experimental results, mostly in terms of transition position. If numerical and experimental results did not match, no inverse method was implemented to find the impedance values that would agree with the experiments.

The resulting neutral stability curves are shown in Figure 5.11. Qualitatively, the numerical analysis follows the same trend as the experimental results: panel P3 has the most visible and negative effect on the boundary layer stability by slightly reducing the critical Reynolds number and increasing the range of amplified frequencies. However, the effect from panel P2 is less pronounced than in experimental observations.

The differences between the numerical and experimental results for panel P2 are more noticeable when reported in terms of transition positions, as shown in Figure 5.12 and summarized in Table 5.3. Figure 5.12 is a comparison of the maximum N envelope curves calculated for each panel without suction. For the impedance values calculated for P2 and P3, the slope of the envelope curves is increased. Assuming that the value of N_T is equal to 6.2 (defined based on the transition for panel P1) and constant for all cases, the transition position for P2 and P3 occurs earlier than for P1.

The predicted transition position is within measurement uncertainty for the P3 case. However, the numerical analysis predicts a different frequency responsible for transition between

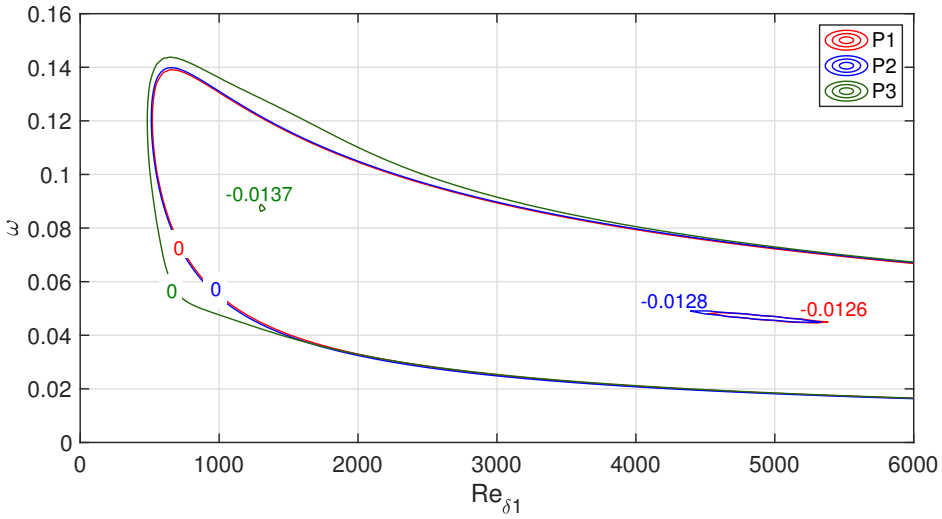

Figure 5.11. Neutral stability curves and maximum amplification rate based on experimental impedance values (without suction).

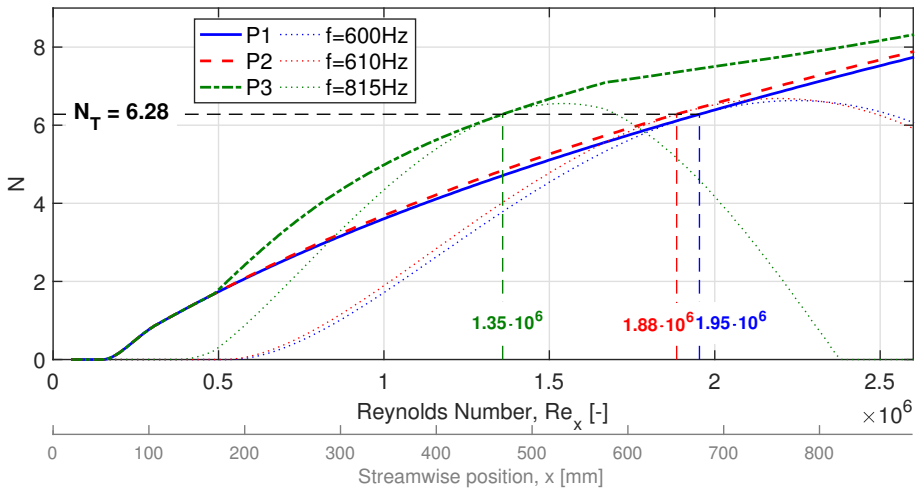

Figure 5.12. N factor envelope curves from numerical analysis with impedance and compared to experimental transition positions (without suction).

cases P1 (610 Hz) and P3 (815 Hz), whereas experiments do not reflect this frequency shift. Although the P3 frequency is still within the [400 Hz - 1 kHz] range of amplified frequencies that are experimentally observed, this difference seems to indicate some limitations that would need to be further investigated.

For the intermediate P2 case, the numerical and experimental transition locations do not match. The numerical analysis underpredicts the destabilizing effects of the porous wall. One reason for this difference could be related to limitations in the impedance model, which is general more suited to SDOF liners with much larger porosities and hole diameters. In support of this hypothesis is the fact that transition prediction was successful for the P3 case.

In conclusion, the experimental results seemed to indicate that the porous panels presented in this section tended to accelerate the transition mechanism. Numerically, an impedance boundary condition was implemented at the boundary layer wall in an attempt to reproduce this effect. The numerical analysis was able to capture the destabilizing effects of the porous panels and showed that the impedance could significantly affect TS amplification. These results therefore seem to

Table 5.3. Numerical and experimental transition position for all panels without suction.

Panel	$x_{\mathrm{T,exp}}$ [mm]	$x_{\mathrm{T,num}}$ [mm]	f_{RexT}	$Z(f_{\mathrm{RexT}})$
P1	740	740	600	∞
P2	640	713	610	518-0.34i
P3	510	515	815	24-20i

indicate that impedance mainly influences instability amplification, as opposed to receptivity. However, any effects on receptivity could not be established and are not dismissed.

5.3 Effect of wall suction and suction distribution

Laminar Flow Control using suction stabilizes the boundary layer by increasing the curvature of the mean velocity profile, thereby making it "fuller" ($\partial^2 U/\partial y^2$ more negative). According to linear stability theory, a fuller profile is more stable and has lower disturbance growth (Reed et al. 1996). To illustrate this point, Figure 5.13 compares the neutral stability curves and the isocontours of the amplification rate α_i for a Blasius profile and a slightly fuller profile, such as would result from suction. For the fuller profile, the amplification rates are in fact approximately an order of magnitude lower, and the critical Reynolds is much greater being equal to 11850, as opposed to 520 for the Blasius profile.

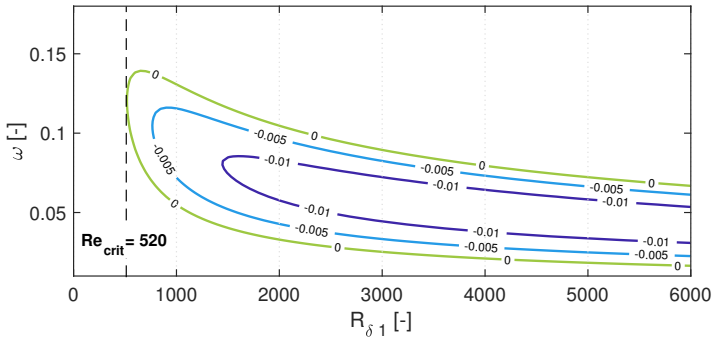

(a) Infinite plate without suction.

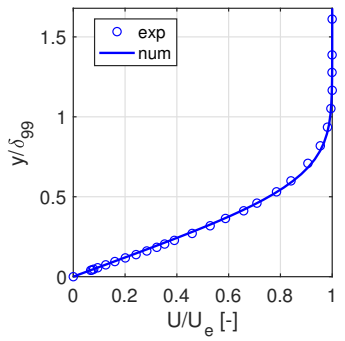

(b) *no suction* profile for (a).

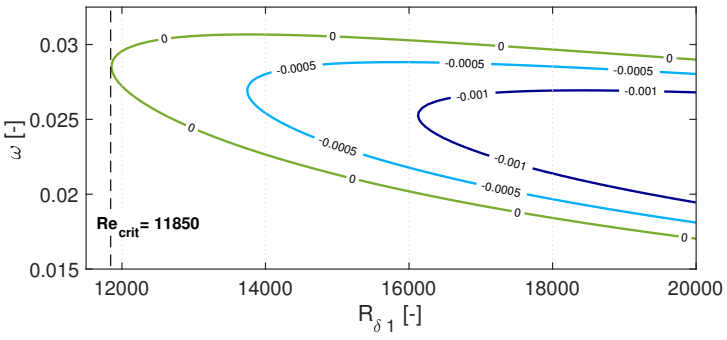

(c) Infinite plate with suction.

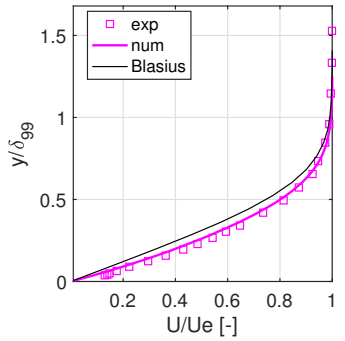

(d) Fitted profile for (c).

Figure 5.13. Isocontours of α_i from linear stability theory with and without suction.

Since the stabilizing effect of wall suction is an established fact, the purpose of this section is only to: first, verify the experimental set-up and protocol by reproducing and comparing re-

sults from the 1995 study by Juillen et al. 1995, and second establish reference smooth cases for different suction configurations. In the present case, four suction configurations were retained: *no suction*, C1/0.400, C3,5/0.200, and *full suction*. The configuration C1/0.400 is intended to illustrate the effects of applying suction as early as possible. On the other hand, C3,5/0.200 was chosen as a configuration that is as effective in delaying transition as the *full suction* configuration while only applying suction over two discontinuous chambers. Finally, the *full suction* configuration makes use of the entire suction region. All configurations have the same total mass flow rate of 0.4 g.s^{-1}, chosen to enable comparisons with the 1995 study. For all suction configurations of panel P2, boundary layer profiles were acquired at three streamwise positions of interest: over the first suction chamber C1 (x = 208 mm), over the last suction chamber C9 (x = 608 mm) and close to the flat plate trailing edge (x = 950 mm). The results are shown in Figure 5.14.

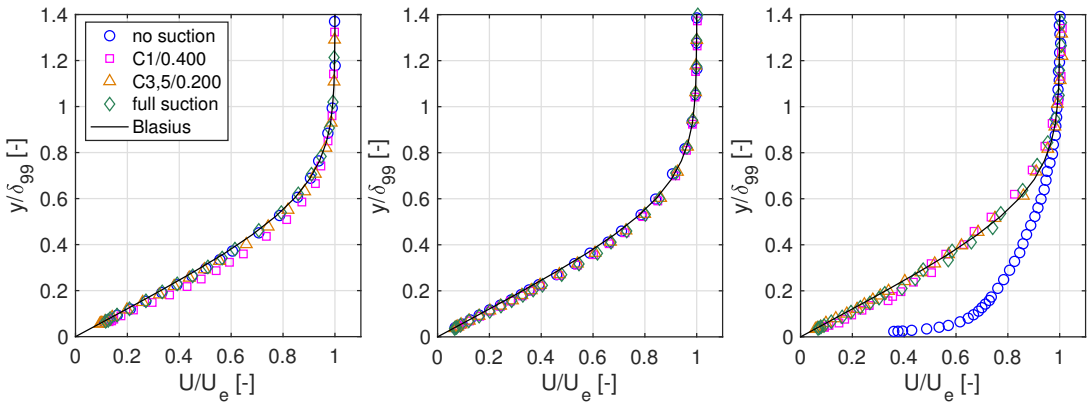

(a) Re_x=5.3 · 10^5, x ∼208 mm *(center of chamber C1).* **(b)** Re_x=1.6 · 10^6, x ∼608 mm *(center of chamber C9).* **(c)** Re_x=2.5 · 10^6, x ∼950 mm *(downstream suction region).*

Figure 5.14. Boundary layer profiles along different streamwise positions for all suction configurations (suction panel P2).

At both streamwise locations over suction chambers C1 and C9, boundary layer profiles for all suction configurations reveal that flow is laminar. In particular, over chamber C1, shown in Figure 5.14a, the profiles for cases *no suction* and C3,5/0.200 correspond, as expected, to a Blasius profile since no suction is locally being applied over this chamber. On the other hand, the boundary layer for case C1/0.400 has a slightly fuller profile due to the local effect of wall suction. In the *full suction* case, despite the presence of wall suction, the profile is close to a Blasius profile because suction velocity is so weak.

Experimentally, the effect of suction on the mean velocity profiles is only detectable for the strongest local suction velocity. Figure 5.15 compares the experimental and numerical profiles (calculated using ONERA's in-house boundary layer code) for each suction configuration at the position where the effect should be most noticeable. As expected, the numerical profiles are visibly all fuller than the Blasius profile and good agreement is found for the C1/0.400 and C3,5/0.200 experimental profiles. Agreement between the numerical and experimental profiles for the *full suction* configuration is also acceptable. However, the local effect of suction is so weak for this configuration that the difference between the Blasius and numerical profile cannot be captured by the experimental profile.

Continuing the boundary layer profile evolution to Figure 5.14b, profiles C1/0.400 and C3,5/0.200 over chamber C9 have both recovered the same shape as the *no suction* profile. The effect of suction on the mean velocity profile is therefore local. Once again, because of the weak suction velocities, the *full suction* profile is still close to the Blasius solution. Close to the

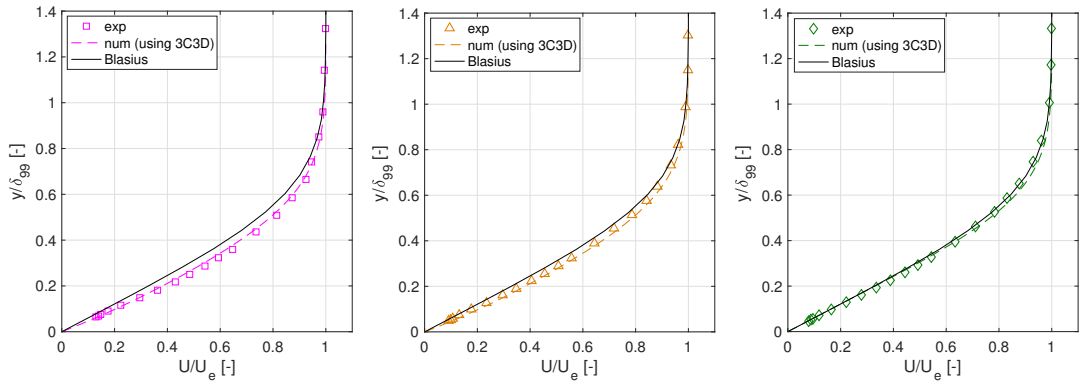

(a) C1/0.400 at Re_x=5.3 · 10^5, x ∼208 mm *(center of chamber C1)*.

(b) C3,5/0.200 at Re_x=8.01 · 10^5, x ∼308 mm *(center of chamber C3)*.

(c) *full suction* at Re_x=5.3 · 10^5, x ∼208 mm *(center of chamber C1)*.

Figure 5.15. Comparison of experimental and numerical boundary layer profiles with suction.

trailing edge (x = 950 mm, Figure 5.14c), the *no suction* configuration is fully turbulent. On the other hand, although boundary layers for C1/0.400, C3,5/0.200 and *full suction* are undergoing transition at this location (transition positions are given in Table 5.4), the mean velocity profiles do not yet reflect that event. An overview of the transition process, in terms of the streamwise evolution of the velocity fluctuations, for all suction configurations on panel P2 is given in Figure 5.16.

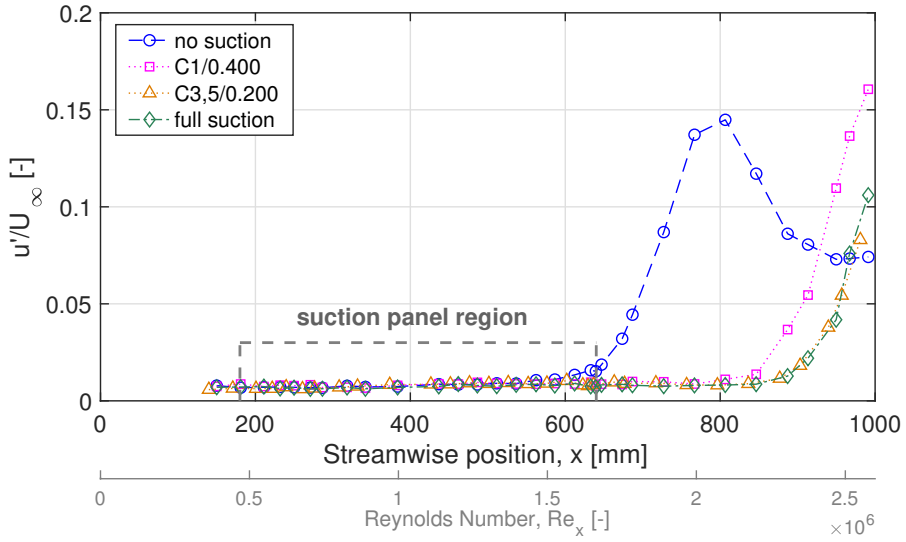

Figure 5.16. Streamwise velocity fluctuations for all suction configurations (suction panel P2).

The evolution of the boundary layer integral values, especially in terms of the shape factor, can also attest to the increase in curvature of a profile under the influence of suction. Figure 5.17 summarizes the streamwise evolution of the shape factor, as calculated based on experimental boundary layer profiles over panel P2 and for all suction configurations.

In particular, the shape factor over suction chamber C1 experiences a noticeable decrease for the C1/0.400 configuration, dropping to a value of 2.45, due to the profile with suction being "fuller". Over the other suction chambers, the displacement thickness for the *no suction* case seems to grow slightly thicker than the cases with suction. The effect of suction can therefore

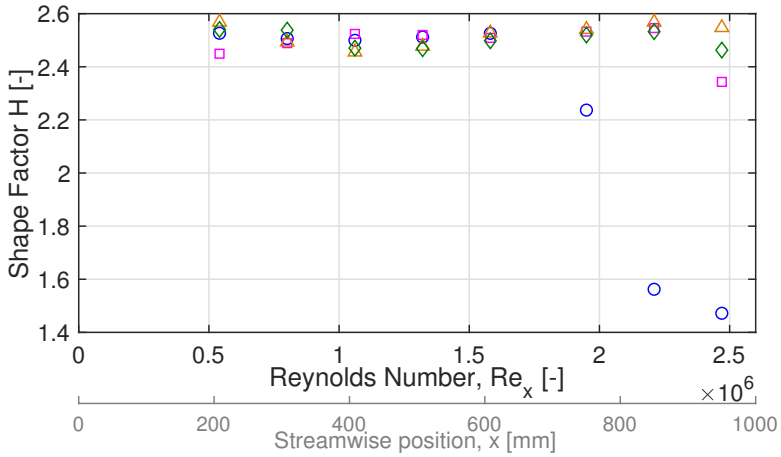

Figure 5.17. Streamwise evolution of experimentally-evaluated shape factor H.

also be observed on the boundary layer integral values.

Table 5.4. Transition positions for all suction cases and all suction panels.

	P2	P3	P1
suction case	Re_{xT} [-]	Re_{xT} [-]	Re_{xT} [-]
no suction	$1.66{\cdot}10^6$	$1.33{\cdot}10^6$	$1.92{\cdot}10^6$
C1/0.400	$2.20{\cdot}10^6$	$1.56{\cdot}10^6$	N/A
C3,5/0.200	$2.30{\cdot}10^6$	$1.66{\cdot}10^6$	N/A
full suction	$2.30{\cdot}10^6$	$1.59{\cdot}10^6$	N/A

For both panels, transition location for all configurations with suction was moved further downstream than in the case without suction, as recorded in Table 5.4. The suction distribution proved to be a parameter of influence: for the same mass flow rate, suction distributed over chambers C3 and C5 simultaneously or over all chambers delayed transition slightly more effectively than suction over chamber C1 only. Although having lower local suction velocities than C1/0.400, the C3,5/0.200 and *full suction* configurations delay transition more effectively. This difference must be due, as discussed in the 1995 reference study, to the fact that C3,5/0.200 and *full suction* apply suction between branch I of the stability curve and the start of secondary instabilities. On the other hand, suction in the C1/0.400 configuration seem to be applied "too early" with respect to the dangerous instabilities' amplification. This effect will be further investigated using LST at the end of the section.

However, the differences in transition position between panels P2 and P3 have significant consequences in term of suction system design. As mentioned above, regardless of the panel, and consequently on panel 3 in particular, the configurations *full suction* and C3,5/0.200 delayed transition the furthest downstream. However, even in this best suction configuration, the transition on panel P3 still occurred before the natural transition on panel P1, as shown on Figure 5.18. The destabilizing effect due to the porous wall, as discussed in the previous section, is so strong in the P3 case, that none of the tested suction configurations could provide a transition position as far downstream as in the solid wall case, for the chosen suction mass flow rate. (Changing the suction mass flow rate could prevent this issue, but this option might not always be available depending on limitations due to the suction pump performance.) The choice of the panel porosity and hole diameter (and suction mass flow rate) is therefore significant and, if done improperly, can result in the implementation of a system that is more detrimental to

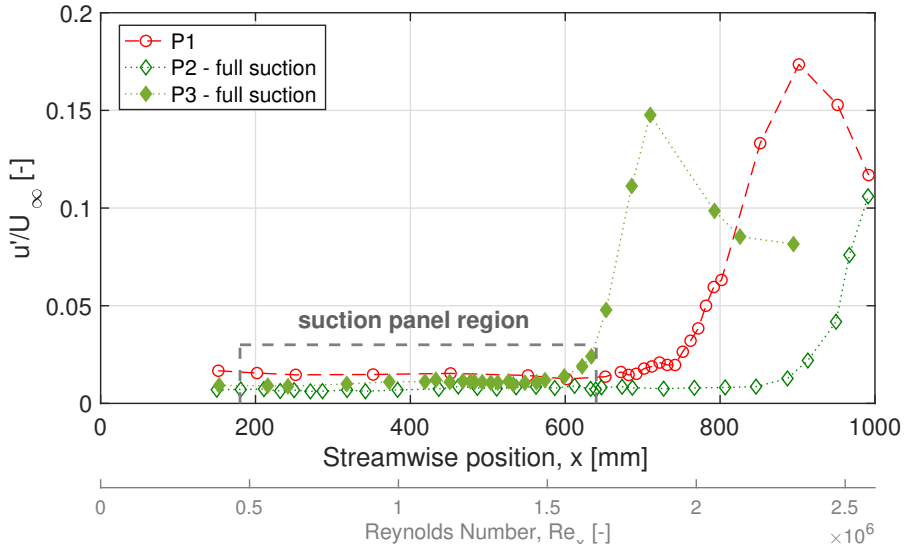

Figure 5.18. Streamwise velocity fluctuations for all suction panels and *full suction* for panels P2 and P3.

transition than a baseline solid wall.

The effect of wall suction on the boundary layer instabilities themselves can also be examined through the velocity fluctuation *u'* profiles. The *u'* profile is determined over the frequency range of [592 Hz - 632 Hz], which corresponds to the most amplified frequencies regardless of suction configuration or panel, based on the PSD(u'). In this experiment on a flat plate, the boundary layer evolves spatially in the streamwise direction: depending on the chamber, suction is applied to a boundary layer with instabilities at different stages of amplification. Figures 5.19 and 5.20 illustrate how, regardless of the panel, TS instabilities with wall suction are much more attenuated than in the *no suction* configuration.

More particularly, in Figure 5.19, the streamwise positions over which the *u'* profiles were acquired are located over the last few suction chambers and downstream of the suction region. Over the first two streamwise positions, located over the center of chambers C7 and C9, the *no suction* TS instabilities profile is well amplified and developed into its characteristic shape. On the other hand, the *u'* profiles on which suction is applied are visibly attenuated with respect to the *no suction* case. Between the different suction configurations, the C3,5/0.200 profile is slightly less amplified over chambers C7 and C9 than the C1/0.400 and *full suction* profiles. However, at these low amplitude levels, the difference can be considered negligible.

Downstream of the suction region, as shown on Figures 5.19c and 5.19d, the TS instabilities for the configurations with suction have undergone further amplification. (The *no suction* case is no longer shown because laminar-turbulent transition has already occurred.) At these positions, the C1/0.400 configuration has greater amplitude than the C3,5/0.200 or *full suction* configurations. This result is consistent with the fact that transition occurs earlier for C1/0.400 compared to C3,5/0.200 and *full suction*.

Similarly, the *u'* profiles at two streamwise positions over chambers C3 and C5 of panel P3 are shown in Figures 5.20a and 5.20b. Over chamber C5, the *no suction* case is visibly more amplified than the configurations with suction. In fact this profile reaches amplitudes that are already larger than those found for the *no suction* case on chamber C7 of panel P2. Even profiles with suction over chamber C3 of panel P3, shown on Figure 5.20a, have amplitudes similar to those found on chamber C9 of panel P2. These figures quantitatively emphasize the previous remark about choosing the appropriate suction panel. In the case of panel P3, the destabilizing

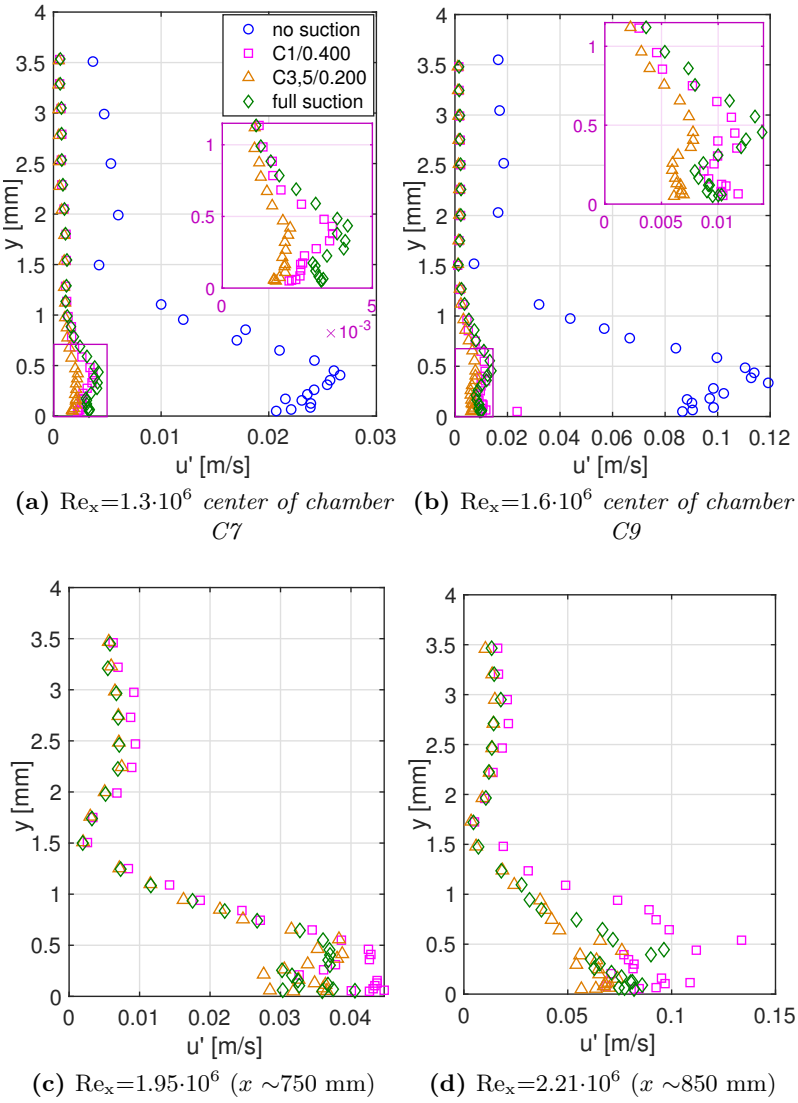

(a) $\mathrm{Re_x}$=1.3·10^6 *center of chamber C7* **(b)** $\mathrm{Re_x}$=1.6·10^6 *center of chamber C9*

(c) $\mathrm{Re_x}$=1.95·10^6 (x ∼750 mm) **(d)** $\mathrm{Re_x}$=2.21·10^6 (x ∼850 mm)

Figure 5.19. Effect of suction on u' profile evolution (evaluated over frequency range [592-632] Hz) for panel P2.

effect of the porous wall clearly accelerates the transition mechanism to such a point that wall suction cannot delay transition as effectively as in the case of panel P2.

A more general overview of the differences in the maximum u' amplitude of the TS instabilities is given in Figure 5.21. Although the data for panel P3 are limited, this graph shows the extent to which TS instabilities on panel P3, especially in the *no suction* case, reach higher amplitudes than on panel P2.

Linear stability calculations were then performed to replicate the four suction configurations that were experimentally tested. First, the effect of wall suction at any given suction chambers is modeled by a wall-normal velocity component in the boundary layer code at the corresponding streamwise positions. The imposed wall-normal velocity V_p is estimated by:

$$V_p = -\frac{\dot{m}}{\rho_\infty A_{suction}} \quad (V_p < 0 \quad \text{for suction}) \tag{5.2}$$

with $\dot{m}$ the suction mass flow rate, ρ_∞ the freestream density, and $A_{suction}$ the total area over which suction is applied. For example, the C1/0.400 configuration has a V_p of -0.02 m.s^{-1}.

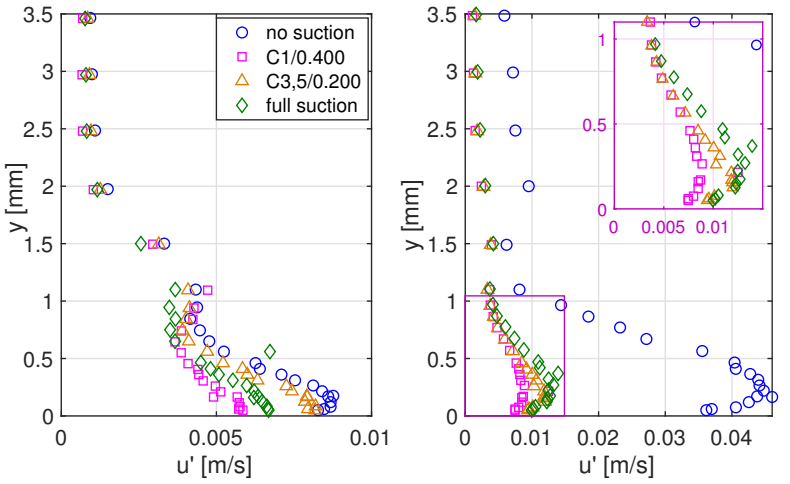

(a) $\mathrm{Re_x}$=8.0·10^5 *center of chamber C3* **(b)** $\mathrm{Re_x}$=1.1·10^6 *center of chamber C5*

Figure 5.20. Effect of suction on *u'* profile evolution (evaluated over frequency range [592-632] Hz) for panel P3.

Next, the linear stability calculations (without any impedance boundary conditions) were then performed using CASTET to evaluate the N factor evolution. Figure 5.22 shows the envelope curve of the overall maximum N factors of different frequencies ranging from 200 Hz to 1.6 kHz for all suction configurations.

At all positions where suction is applied, the N factor envelope curve decreases in amplitude, indicating the attenuation of the instabilities' amplification. In particular, this attenuation seems to subside slightly beyond the chamber over which suction is applied. For example, in the case of C1/0.400, although suction only covers the first chamber, the N factor envelope curve only resumes its growth over the second half of the second chamber. This lag corresponds to the streamwise distance that needs to be covered by the boundary layer before resuming its original profile shape, unperturbed by suction. Consequently, the lag is greater for larger local suction flow rates.

More generally, the varying effects of suction distribution (which experimentally results in different transition positions) can also be seen on Figure 5.22. Reporting the experimental transition positions for each suction configuration onto this graph results in a set of varying transition N factors N_T, as summarized in Table 5.5. Possible explanations for these suction-configuration dependent N_T could either be the unaccounted effect of wall impedance in the present numerical analysis or some receptivity effects due to suction. Compared to the results presented in Section 5.1.2, the spread in N_T is less striking for cases C3,5/0.200 and *full suction* with respect to the *no suction* case.

Table 5.5. Transition positions and N factors for all suction configurations (panel P2).

suction case	$\mathrm{Re_{xT}}$ [-]	N_T [-]
no suction	1.66·10^6	5.53
C1/0.400	2.20·10^6	6.26
C3,5/0.200	2.30·10^6	4.94
full suction	2.30·10^6	5.00

The present numerical results can also be used to explain why certain suction distributions

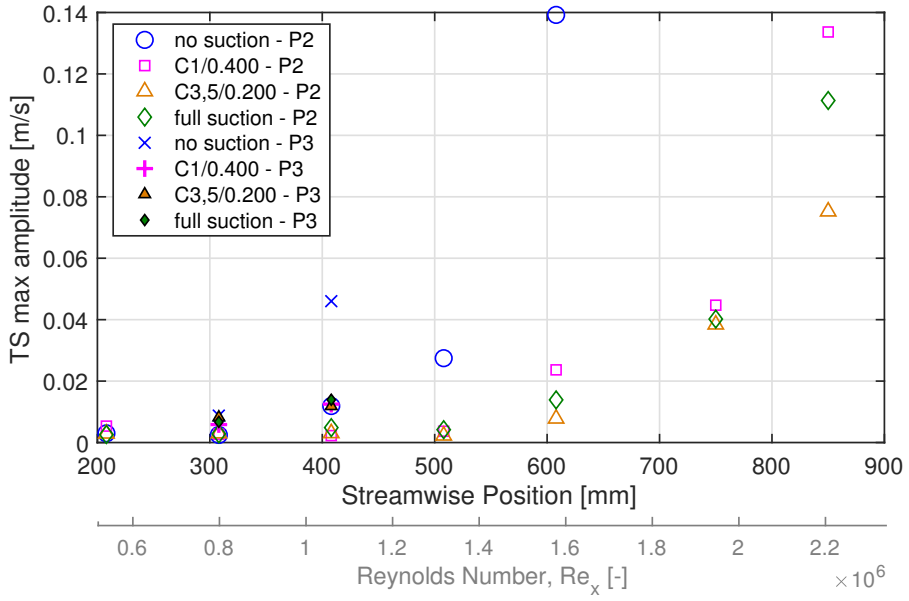

Figure 5.21. Streamwise evolution of the TS-profile maximum amplitude for all suction configurations of panels P2 and P3.

can be more effective than others. Figure 5.23 shows the N-factor evolution of three particular frequencies for all suction configurations. In a two-dimensional Blasius flow, different frequencies start to amplify at different streamwise positions. Suction can therefore be applied more or less effectively depending on its location with respect to the critical abscissa of the frequencies responsible for triggering transition.

For example, the instability at a frequency of 300 Hz, shown in Figure 5.23a, "naturally" starts to amplify over suction chamber C7. The configurations that apply suction exclusively over the upstream chambers delay the critical abscissa of the 300 Hz instability but the *full suction* case is most effective because suction is being applied directly to the region where the instability starts to be amplified.

This effect is even more visible on Figure 5.23b, which corresponds to the TS wave frequency which is responsible for the onset of transition. In particular, of all the suction configurations, C3,5/0.200 applies the strongest suction velocity over positions where the 600 Hz instability is amplified. This suction distribution is therefore the most effective in reducing the instability amplification.

Finally, Figure 5.23c illustrates the fact that the first suction chamber is most effective in attenuating high frequency instabilities, such as in this 1300 Hz case. However, this effectiveness is of limited use for the present application since, regardless of whether or not suction is applied, this instability disappears by the sixth suction chamber.

Since TS instabilities in a Blasius flow evolve in the streamwise direction, the effect of applying suction at various streamwise positions can greatly influence the amplification of given instabilities. In practical terms, the challenge resides in choosing a suction distribution that attenuates the relevant instabilities, *i.e.*, those responsible for transition, over the widest operating range possible.

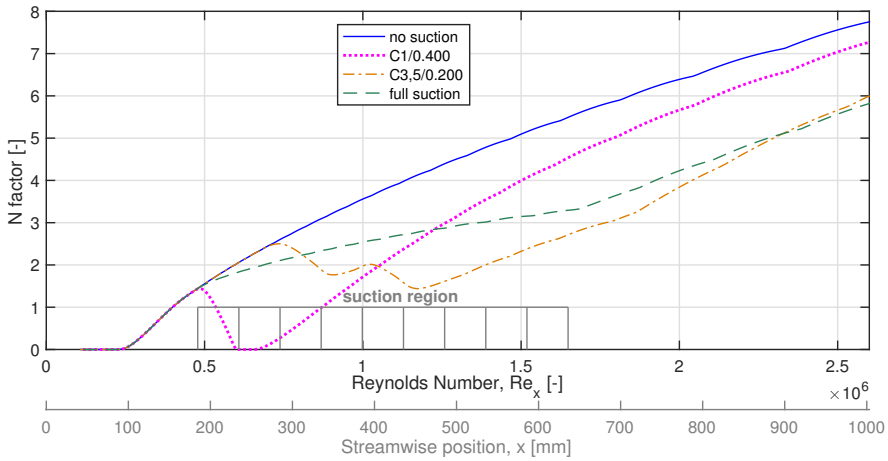

Figure 5.22. Maximum N factor envelope curve for all suction configurations.

Summary

The effect of wall impedance on boundary layer stability was initially observed experimentally. In particular, the suction panel with the largest porosity and perforation diameter was found to destabilize the boundary layer the most compared to the panel with lower porosity and perforation diameter. A numerical investigation, using models based on acoustic liners to define the impedance boundary condition, was then performed. Relatively good agreement was found between calculations and experiments for the different suction panels without suction. However, additional work is necessary to reproduce the effects of wall impedance combined with suction.

To establish a smooth case reference, four different suction configurations were chosen: *no suction*, C1/0.400, C3,5/0.200 and *full suction*. As expected, configurations with suction always delayed transition with respect to the *no suction* configuration (and regardless of the suction panel). Additionally, and in accordance with previous studies, the effect of suction distribution was observed: suction in the C1/0.400 configuration occurs slightly upstream of the critical abscissa of the TS instabilities and is therefore less effective than in the C3,5/0.200 and *full suction* configurations. Since the smooth case reference was established, the next three chapters will each introduce a different type of surface defect to the flat plate: wires, FFS, and gaps.

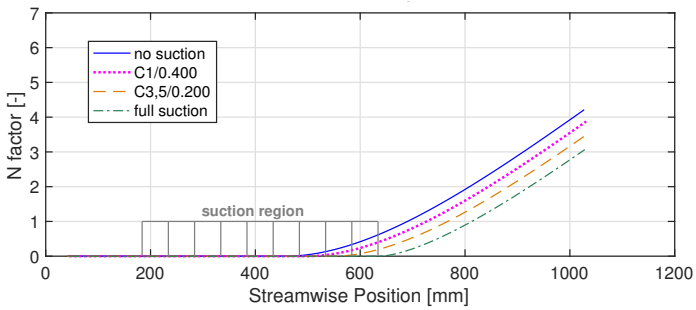

(a) N factor evolution for 300 Hz.

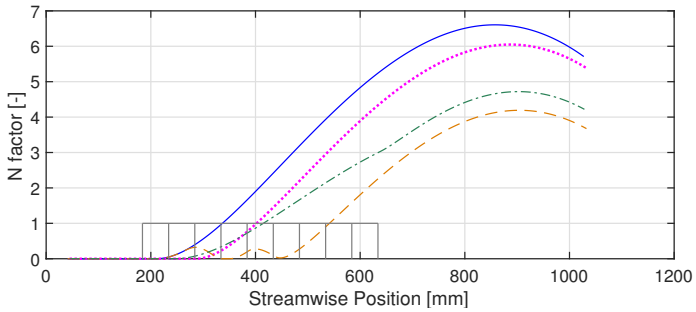

(b) N factor evolution for 600 Hz.

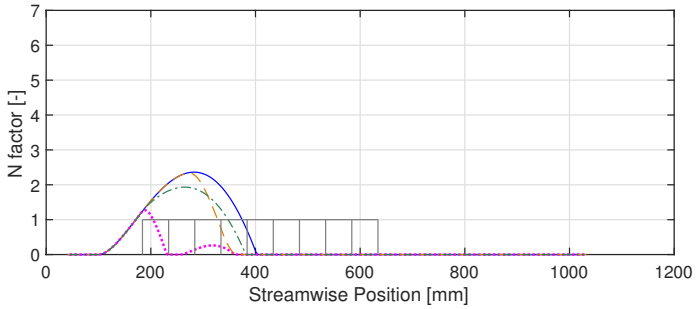

(c) N factor evolution for 1300 Hz.

Figure 5.23. Wall suction distribution effect on the instability at a particular frequency.

Chapter 6

Combined Effects of Wires and Wall Suction

Contents

6.1 Geometric characteristics of the wires 89
6.2 Transition location and mean flow 90
6.3 Spectral and numerical stability analyses 95

This chapter covers the experimental characterization and analysis of the combined effect of wires with wall suction on boundary layer stability. Wire geometry and positions are initially presented (Section 6.1) and their general effect of transition location and mean flow are discussed (Section 6.2). Spectral and numerical analyses are performed to provide additional information on the transition mechanisms involved in the presence of either a subcritical or critical wire (Section 6.3).

6.1 Geometric characteristics of the wires

Wires were the first type of surface defects that were tested because of their single degree of freedom (diameter, h) and their ease of installation. This type of surface imperfection could model a welding joint but is generally not characteristic of defects found on aerodynamic surfaces; however, this initial data set represents a proof-of-concept of the experimental set-up's capacity to study the combined effects of wall suction and surface imperfections on boundary layer transition. Additionally, these results extend previous studies (Klebanoff and Tidstrom 1972, Tani 1961) on the same type of surface defects.

The choice in wire diameters was based on relative height with respect to the local boundary layer displacement thickness δ_1 calculated without suction using the ONERA boundary layer code and shown in Figure 4.14. Diameter-to-displacement thickness ratios h/δ_1 averaging around 0.2, 0.4, 0.5 and 0.6 were tested. Wires were always mounted at the junction between two chambers so that the effect of each suction configuration could be more easily compared. Wire position was therefore chosen as the location where the combination of displacement thickness δ_1 and wire diameter h was closest to the desired h/δ_1 values. Ratio values h/δ_1 are given as averaged approximations because surface defect positions were not changed with suction configuration, thereby not accounting for the small change in local displacement thickness due to suction. However, the precise values of h/δ_1 for each wire dimension were computed using the ONERA boundary layer code 3C3D and used whenever reported on graphs.

Table 6.1. Summary of the wire (WIR) geometry and position

label	wire diameter, h [µm]	x_{WIR} [mm] ($\mathrm{Re}_{x,\mathrm{WIR}}$ $\cdot 10^{-6}$)	Note on x_{WIR}
WIR-100µm-330	100	330 (*0.87*)	located at junction of C3 and C4
WIR-300µm-640	300	640 (*1.65*)	located immediately downstream of C9
WIR-300µm-430	300	430 (*1.13*)	located at junction of C5 and C6
WIR-300µm-230	300	230 (0.61)	located at junction of C1 and C2

A summary of surface defect geometry and positions is given in Table 6.1 and illustrated in Figure 6.1 by the dashed lines and corresponding case numbers. Additionally, the local boundary layer thickness at the corresponding surface defect locations are presented in Table 6.2, along with the rounded average h/δ_1 that will also be used to reference the different cases. Finally, in terms of mounting, wires were adhered to the flat plate using spray glue applied directly to the defect so as to minimize additional thickness due to mounting and local blockage on the perforated sheet.

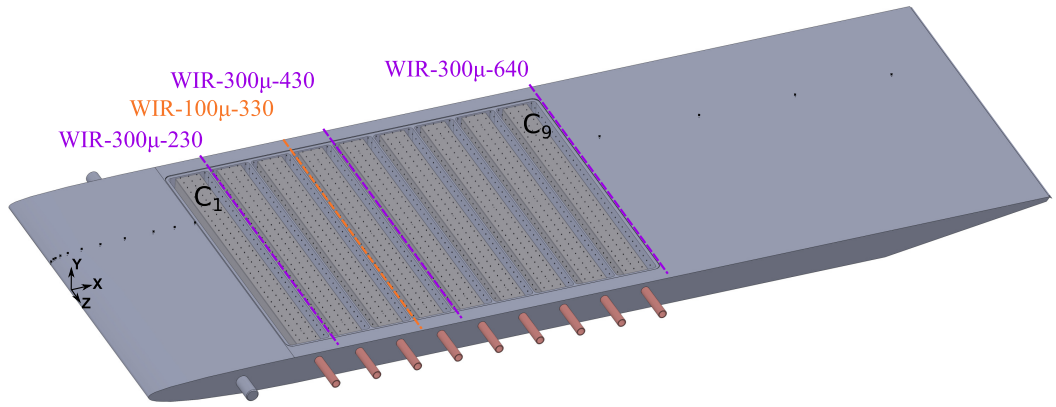

Figure 6.1. Overview of the flat plate with the different wire locations and dimensions tested.

6.2 Transition location and mean flow

In this section, the transition positions are determined and mean flow properties are compared between the different wire cases. Since wires were tested on all three panels (P1, P2, and P3), the panel used is always specified. As mentioned previously, the streamwise evolution of the *u'* velocity fluctuations are used to evaluate transition positions, as shown in Figure 6.2 for suction panel P2. For the subcritical case WIR-300µm-640 (Figure 6.2a), transition does not occur immediately downstream of the wire, and suction is still effective. Additionally, the various spatial distributions still result in different transition locations. In particular, C3,5/0.200 and *full suction* transition at the same location furthest downstream, while C1/0.400 is still less effective and transitions earlier. Furthermore, although the *no suction* configuration transitions at the wire location, this case is not critical either since this transition position also corresponds

Table 6.2. Local boundary layer thickness (numerical value) at surface defect location. (Asterisks correspond to critical wires.)

	δ_1 [µm] at x_{WIR} *(from 3C3D)*				
label	*no suction*	C1/ 0.400	C3,5/ 0.200	*full suction*	∼rounded (h/δ_1) (for reference)
WIR-100µm-330	605	569	547	585	∼0.2
WIR-300µm-640	839	819	804	793	∼0.4
WIR-300µm-430*	692	665	611	663	∼0.5
WIR-300µm-230*	506	421	506	496	∼0.6

to the smooth case. Once the wire reaches critical relative heights however, transition occurs at the wire location, regardless of the suction configuration, as shown in Figure 6.2b. (Note that the C3,5/0.200 configuration was also found to be critical but that the traverse data could not be presented.) Suction therefore does not seem effective in delaying transition once in the presence of critical wires.

Mean velocity profiles were then acquired one millimeter downstream of each surface defect for the different relative height ratios h/δ_1 and are shown in Figure 6.3. Some suction configurations do not appear because the profiles were not acquired for these configurations. Additionally, a Blasius boundary layer profile is included to allow for an easier comparison with the upstream laminar profiles, and to highlight the altitude shift of the inflection point. In all cases but one (WIR-300µm-230, C1/0.400), boundary layers for a given defect are overlapping, regardless of the suction configuration. Immediately downstream of the surface defect, the effect of the wire is therefore stronger than the effect of wall suction.
In cases WIR-100µm-330 and WIR-300µm-640, i.e., for h/δ_1 values ∼0.2 and ∼0.4, only a slight profile inflection is induced by the surface defect. In general, for these cases, all configurations with suction still transitioned further downstream than when no suction was applied, as discussed above and summarized in Table 6.4. Therefore, despite the similar mean velocity profiles immediately downstream of the surface defect, stabilization due to suction still proved effective.

This trend is confirmed through cases WIR-300µm-430 and WIR-300µm-230, where h/δ_1 increases to ∼0.5 and ∼0.6. Regardless of suction configuration, transition now occurs at the same position: the location of the surface defect. The corresponding mean velocity profiles for all suction configurations display well-defined inflection points, shown in Figures 6.3c and 6.3d. Although the first measurement points close to the wall might not capture small-velocity reversed flow because of the anemometry used in this study, the key feature in these graphs is the location of the inflection point. As the h/δ_1 ratio is raised between cases WIR-300µm-430 and WIR-300µm-230, the proportion of the boundary layer disrupted by the surface defect is consequently larger, which explains the increase in the height of the inflection point. Therefore, as the inflection point is further from the wall, the profile becomes more unstable (which is also similar to the findings related to the effects of an adverse pressure gradient on boundary layer stability in Mack 1977), and wall suction becomes less effective. In these cases, the instability caused by the wire could not be cancelled or lowered by any of the suction configurations, and transition therefore occurs at the location of the surface defect.
As mentioned at the beginning of this section, Figure 6.3d, for case WIR-300µm-230, exhibits one anomaly: the C1/0.400 profile, which has an inflection point at a greater height than the profiles from the other suction configurations. In this case, the surface defect is mounted immediately downstream of suction chamber C1, on which maximum suction flow rate is being applied. Through the action of wall suction, the C1/0.400 boundary layer at the surface defect location

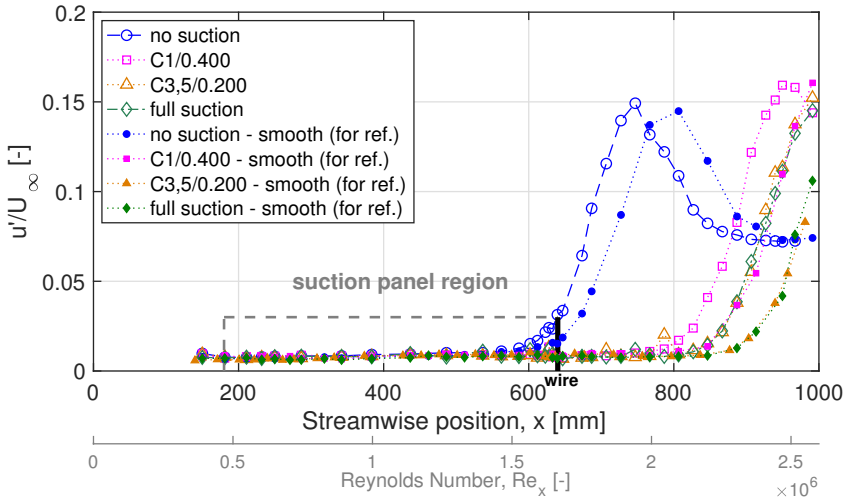

(a) WIR-300µm-640 (h/δ_1 ~0.4).

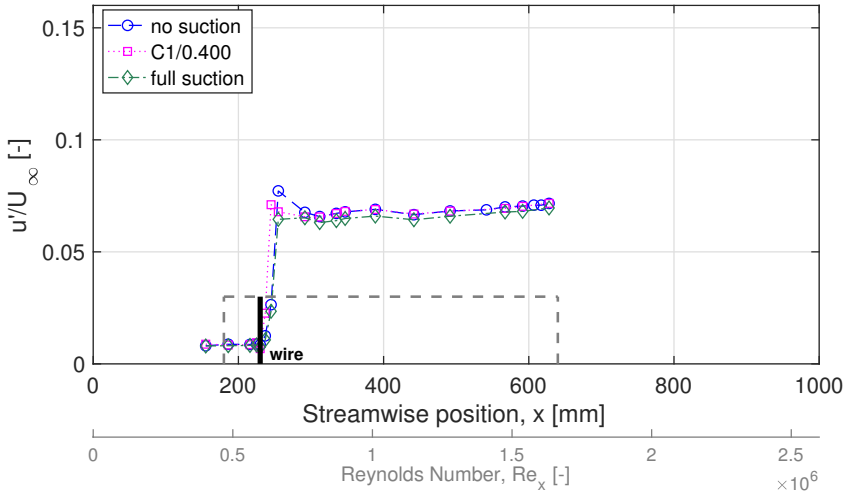

(b) WIR-300µm-230 (h/δ_1 ~0.6) (crit.).

Figure 6.2. Streamwise velocity fluctuations (at y = 300 µm) for different wire relative heights and suction configurations for suction panel P2.

is therefore noticeably thinner than in configurations *no suction* or *full suction* (respectively, Δ δ_1 = -85 µm and Δ δ_1 = -75 µm using the 3C3D boundary layer code, see Table 6.2). With this lower displacement thickness, h/δ_1 for C1/0.400 is actually closer to 0.7 than 0.6. In the previous paragraph, when the size of the surface defect with respect to displacement thickness increased, the height of the inflection point inside the boundary layer was increased. The anomaly of the C1/0.400 profile discussed here is therefore a direct consequence of the reduced boundary layer thickness due to wall suction. Although this anomaly could have been avoided by placing the profile in its own distinct category, this situation was a more vivid illustration of the competing effects between wall suction and surface defects. Translated to a more practical LFC situation for instance, a surface defect remaining at the same position would affect boundary layer stability differently depending on the local suction distribution.

For each suction configuration, the transition Reynolds number with and without a surface defect and over each of the three panels is summarized in Tables 6.3, 6.4 and 6.5 and graphed in Figure 6.4a. Reference data (from Tani 1961 and Feindt 1956) where the effects of circular wires on transition were investigated is also included. Since the reference case with *no suction* and

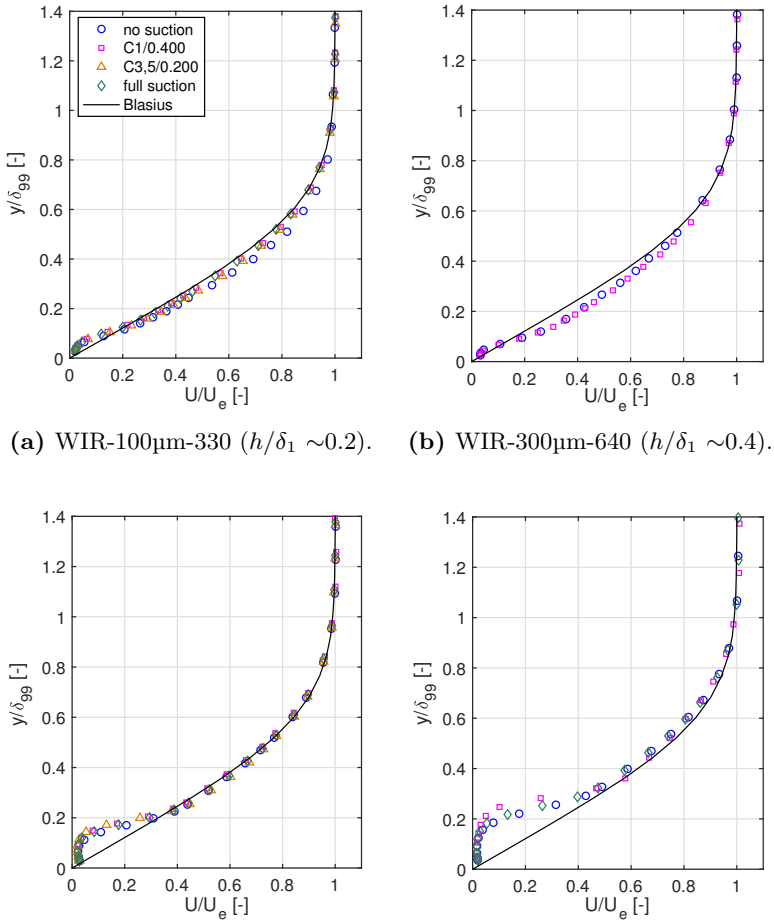

(a) WIR-100µm-330 (h/δ_1 ∼0.2). **(b)** WIR-300µm-640 (h/δ_1 ∼0.4).

(c) WIR-300µm-430 (h/δ_1 ∼0.5). **(d)** WIR-300µm-230 (h/δ_1 ∼0.6).

Figure 6.3. Boundary layer profiles 1 mm downstream of the wire position for different suction configurations over suction panel P2.

no surface defect for the present data has an absolute transition position Re_{xT} close to Tani's equivalent case, no attempt to normalize the data in Figure 6.4a was performed to account for potential differences between wind tunnels or experimental set-ups.
In general, the data in the present study show relatively good agreement with Tani's data, especially for the *no suction* case over suction panel P2. The trend for the panel P2 configurations with suction, although similar to the one without suction, is exacerbated. For the given two-dimensional positive surface defects in this study, wall suction is therefore only effective up to critical relative heights similar to those of a configuration without suction. Graphically, the effect of wall suction or wall porosity can be paralleled to the effect of freestream turbulence *Tu*, as shown by the data from Feindt 1956. Whether transition location is moved further downstream through the effect of lower freestream turbulence (i.e., lower initial amplitude of the instabilities) or boundary layer suction (i.e., lower amplification of the TS instabilities), transition Reynolds number is nearly independent of the surface defect's relative height up to values of h/δ_1 between 0.3 and 0.4. However, above their respective critical h/δ_1 ratio, all data sets seem to collapse to Tani's original curve, since neither freestream turbulence nor wall suction can counteract the boundary layer destabilization induced by the surface defect.

To enable comparisons between the different suction configurations and porosities to surface

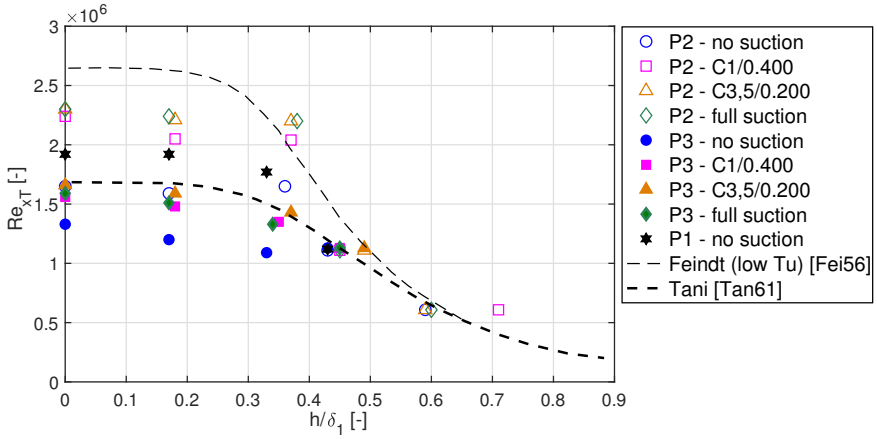

(a) Re_{xT} as a function of h/δ_1.

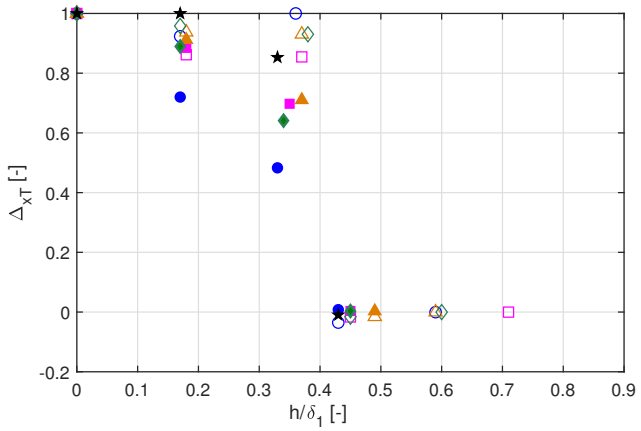

(b) Δ_{xT} as a function of h/δ_1.

Figure 6.4. Transition parameters variation with respect to relative wire height for all suction configurations.

defects with similar values of h/δ_1, a non-dimensional parameter Δ_{xT} was then introduced in Figure 6.4b and is defined as:

$$\Delta_{xT} = \frac{\mathrm{Re}_{xT,SD} - \mathrm{Re}_{x,SD}}{\mathrm{Re}_{xT,noSD} - \mathrm{Re}_{x,SD}} = \frac{x_{T,SD} - x_{SD}}{x_{T,noSD} - x_{SD}}. \tag{6.1}$$

This parameter will be used for all three types of surface defects investigated in the present study, hence the use of subscript "SD" for "Surface Defect". For any given suction configuration (and panel whenever indicated), variables $Re_{xT,SD}$ and $Re_{xT,noSD}$ correspond to the transition Reynolds number with and without a surface defect respectively, and $Re_{x,SD}$ corresponds to the location of the surface defect. The parameter Δ_{xT} can be used as an indicator of the relative change in transition position due to the presence of a surface defect, using the roughness element position as the reference. When Δ_{xT} is equal to 1, the surface defect has no effect on transition whereas when Δ_{xT} is equal to zero, transition occurs at the location of the surface defect.

Figure 6.4b thus shows that regardless of the porosity or suction configuration, the critical h/δ_1 seems to be the same, at an approximate value of 0.4. In the case of P2 (porosity equal to 0.26%), the *no suction* configuration seems less sensitive to the presence of a surface defect than configurations with suction: the latter depart from 1 more significantly before the critical h/δ_1. On the other hand, in the case of P3 (porosity equal to 1.34%), the *no suction* case is

Table 6.3. Re_{xT} for panel P1 ($p = 0\%$).

config \ h/δ_1	**0 *(ref.)***	∼0.2	∼0.4
no suction	$\mathbf{1.92{\cdot}10^6}$	$1.92{\cdot}10^6$	$1.77{\cdot}10^6$

Table 6.4. Re_{xT} for suction panel P2 ($p = 0.26\%$).

config \ h/δ_1	**no defect**	∼0.2	∼0.4
no suction	$\mathbf{1.66{\cdot}10^6}$	$1.59{\cdot}10^6$	$1.66{\cdot}10^6$
C1/0.400	$\mathbf{2.24{\cdot}10^6}$	$2.05{\cdot}10^6$	$2.04{\cdot}10^6$
C3,5/0.200	$\mathbf{2.30{\cdot}10^6}$	$2.21{\cdot}10^6$	$2.20{\cdot}10^6$
full suction	$\mathbf{2.30{\cdot}10^6}$	$2.24{\cdot}10^6$	$2.20{\cdot}10^6$

Table 6.5. Re_{xT} for suction panel P3 ($p = 1.34\%$).

config \ h/δ_1	**0 *(ref.)***	∼0.2	∼0.4
no suction	$\mathbf{1.33{\cdot}10^6}$	$1.20{\cdot}10^6$	$1.09{\cdot}10^6$
C1/0.400	$\mathbf{1.56{\cdot}10^6}$	$1.48{\cdot}10^6$	$1.35{\cdot}10^6$
C3,5/0.200	$\mathbf{1.66{\cdot}10^6}$	$1.59{\cdot}10^6$	$1.43{\cdot}10^6$
full suction	$\mathbf{1.59{\cdot}10^6}$	$1.51{\cdot}10^6$	$1.33{\cdot}10^6$

more sensitive to surface defects than the cases with suction, and decreases more rapidly to zero before the critical h/δ_1. Overall, between the two porous cases, the panel with higher porosity seems more sensitive to surface defects that with lower porosity. This difference could, in part, be explained by the additional contribution from the porous panel in destabilizing effect.

6.3 Spectral and numerical stability analyses

The effect of surface defects on transition can also be evaluated through spectral analysis using unsteady data from streamwise traverses at 300 μm from the wall, such as was initially presented in Figure 4.8b. First, the effect of suction for subcritical case WIR-300µm-640 (h/δ_1 ∼0.4) is shown for reference with the PSD of the velocity fluctuations u' for each suction configuration upstream of the wire, as shown in Figure 6.5. For all suction configurations and most particularly for *no suction*, a bulge ranging from 400 Hz to 800 Hz can be noticed. This bulge corresponds to the TS waves responsible for the onset of transition, as discussed in Chapter 2 on the experimental facility. As expected, the configuration without suction reaches much larger magnitudes over this amplified frequency range compared to the cases with suction.

Figure 6.6 then shows the PSD of *u'* for each suction configuration at a position closest to (approximately 20 mm upstream of) the corresponding transition Reynolds number, i.e., where instabilities responsible for transition can be observed by their noticeably larger magnitudes.

In subcritical cases WIR-100µm-330 and WIR-300µm-640, shown in Figures 6.6a and 6.6b, where a surface defect is present and transition is simply shifted upstream, the general shape of the curves and the values of the PSD amplitudes reached by the TS instabilities are similar to the ones found for the *no suction* case. This seems to indicate that the mechanisms leading to transition are unchanged but that, in this case, the presence of the surface defect slightly increased the amplification process of the TS waves.

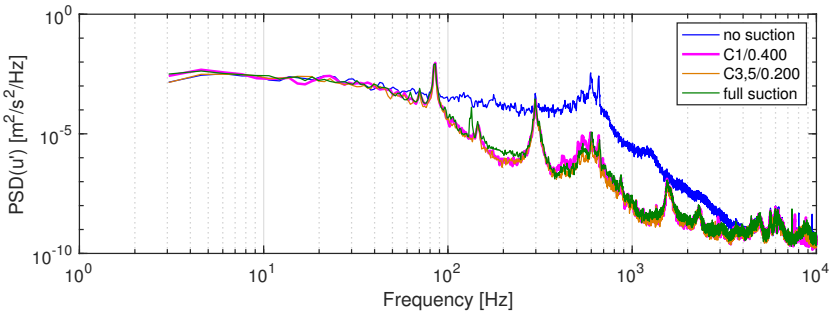

Figure 6.5. PSD of streamwise velocity fluctuations *u'* (probed at $y = 300\mu m$ from wall) upstream (x = 610 mm) of WIR-300µm-640 for all suction configurations (suction panel P2).

However, in cases WIR-300µm-430 and WIR-300µm-230, where transition occurs immediately downstream of the surface defect position, in Figures 6.6c and 6.6d respectively, the general shape of the curves changes. A new bulge, covering a wide range of high frequencies from 1.5 kHz to 5 kHz for WIR-300µm-430 and 3 kHz to 10 kHz for case WIR-300µm-230, has now clearly appeared. This phenomena is similar to the one described by Mack 1977 and experimentally observed by Watanabe and Kobayashi 1991 who also studied the effect of wires on transition.

These ranges of high frequencies seem to be responsible for transition since they did not appear in any of the previous cases where transition due to TS instabilities occurred. In this case, the mechanism by which transition is triggered seems to have been modified by the presence of the surface defect. This modification can be explained by the presence of the noticeable inflection point in the mean velocity profiles immediately downstream of the wire, as seen in Figures 6.3c and 6.3d. The transition mechanism seems to shift from being viscosity-driven to being the result of an inflection-type instability (Rayleigh 1880), which is generally known to be a higher frequency instability (Mack 1977).

Note that some PSD in Figures 6.6b and 6.6d are shifted in amplitude with respect to the *no suction* case. This difference can be attributed to differences in the height of the hotwire during traverses. In particular, in Figure 6.6d for C1/0.400, the boundary layer thickness is significantly different from the other suction configurations, as explained above. In all these cases, the hotwire is therefore exploring slightly different relative heights y/δ_1 or y/δ_{99} inside the boundary layer, where velocity fluctuation levels are different.

The results from linear stability theory, shown for the *no suction* case without a surface defect as well as with a critical surface defect of h/δ_1 equal to 0.43 (corresponding to the ∼0.5 category) in Figure 6.7, also confirm this change in transition mechanism. In both graphs, the neutral stability curve and the isocontours of the amplification α_i are plotted as a function of the angular frequency ω and the displacement thickness Reynolds number, $Re_{\delta 1}$. Negative values of α_i indicate that instability waves are being amplified, since the perturbations are formulated as:

$$q = \hat{q}(y) \cdot e^{-\alpha_i x} \cdot e^{i(\alpha_r x - \omega t)} \tag{6.2}$$

where q is any perturbation quantity. In Figure 6.7d, where there is a critical surface defect and transition is due to the inflection point in the boundary layer, the range of unstable frequencies is much larger than for the case without surface defect case. Note that, although the Figure 6.7d is labeled *no suction*, the mean velocity profiles downstream of a critical defect are similar, regardless of the suction configuration. The following observations, related to the effect of an inflection point on stability, are therefore applicable to all suction configurations.

With the critical WIR-300µm-430, the neutral stability curve spans over a much wider range of unstable angular frequencies, and these unstable frequencies are much higher than in the no surface defect case. This observation agrees with the PSD results where a range of high

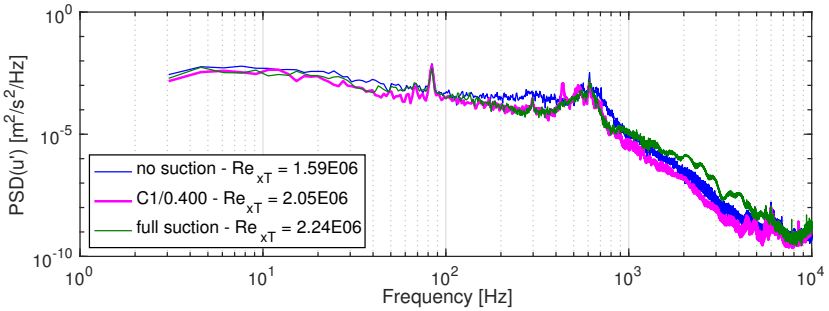

(a) WIR-100µm-330 (h/δ_1 ∼0.2).

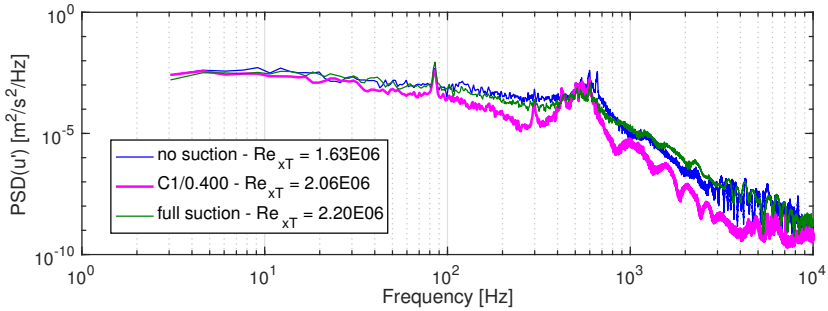

(b) WIR-300µm-640 (h/δ_1 ∼0.4).

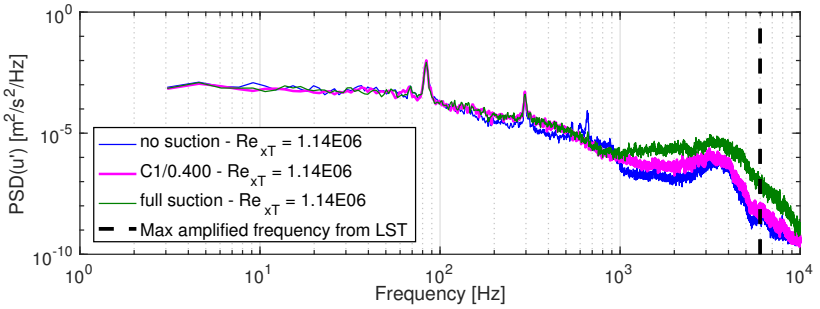

(c) WIR-300µm-430 (h/δ_1 ∼0.5).

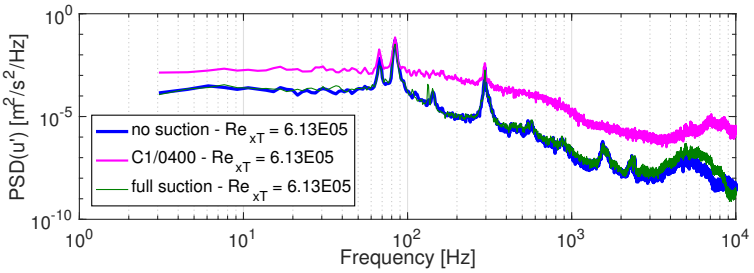

(d) WIR-300µm-230 (h/δ_1 ∼0.6).

Figure 6.6. PSD(u') (y = 300µm) just upstream of corresponding transition location $\mathrm{Re_{xT}}$ for each suction configuration for different wire relative height ratios (suction panel P2).

frequencies (above 2 kHz) were found to be amplified in the critical cases where transition occurred very close to the surface defect. Additionally, the absolute values of the amplification α_i are also found to be one to two orders of magnitude greater in the case of inflection-type instabilities compared to the viscosity-driven instabilities as shown in Figures 6.7b and 6.7e.

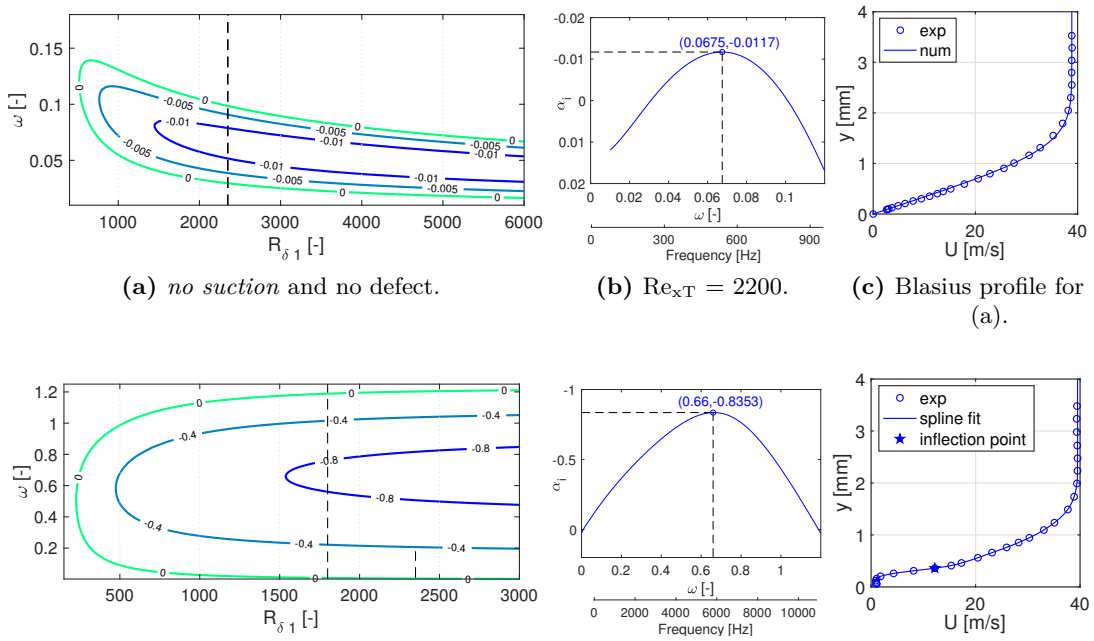

(a) *no suction* and no defect. **(b)** $\mathrm{Re_{xT}} = 2200$. **(c)** Blasius profile for (a).

(d) *no suction* and critical case WIR-300µm-430 (h/δ_1 ~0.5). **(e)** $\mathrm{Re_{xT}} = 1800$. **(f)** Fitted profile for (d).

Figure 6.7. Neutral stability curves and isocontours of the amplification α_i (the imaginary component of the wave number) from linear stability theory.

Summary

Wall suction is therefore still effective in delaying transition in the presence of subcritical wires. However, once wire with critical relative heights h/δ_1 are introduced, the boundary layer transition mechanism rapidly changes from being the result of TS instability amplification (i.e., viscosity-driven) to that of an inflection-type instability. Because of this change in transition mechanism, wall suction is now ineffective and the critical wire dimension is the same (h/δ_1 ~0.4) regardless of whether suction is applied or not. The next type of surface defect that will be investigated is another positive surface defect: forward-facing steps.

Chapter 7

Combined Effects of Forward-Facing Steps and Wall Suction

Contents

7.1 Geometric characteristics of the FFS 99
7.2 Transition location and mean flow 100
7.3 Unsteady data analysis 106
7.4 Numerical analysis and comparison with existing ΔN models 112

Similar to the previous chapter, this chapter now covers the effects forward-facing steps combined with wall suction on boundary layer stability. The FFS geometry and positions are initially presented (Section 7.1) and their general effect of transition location and mean flow are discussed (Section 7.2). Unsteady data analysis is performed to provide additional information on the transition mechanisms involved in the presence of either a subcritical or critical FFS (Section 7.3). Finally, ΔN values based on the present experimental data are established through numerical analysis and compared with existing ΔN data sets or models (Section 7.4).

7.1 Geometric characteristics of the FFS

In general, steps, as opposed to wires, are more representative of surface discontinuities found on aerodynamic surfaces. This type of surface defect can typically be found in HLFC configurations at the junction between suction and solid wall panels.

Forward-facing steps were formed by adhering plastic shims of varying thickness and with square edges to achieve desired height-to-displacement thickness (h/δ_1) values, similar to the wire installation. The FFS were mounted at two different streamwise positions, to allow for a wide range of h/δ_1 values, and over two panels, P1 (solid wall) and P2 (porosity p equal to 0.26%). The two streamwise positions, x_{FFS}, tested are located at 430 mm and 640 mm from the leading edge. An overview of a plastic shim mounted at x_{FFS} equal to 640 mm to form a step is shown in Figure 7.1. The first position corresponds to the junction between chambers C5 and C6, and the second between the end of the suction region and the flat plate. Only FFS were tested because thickness could be added to the flat plate; BFS, on the other hand, were not tested because their implementation required major modifications to the flat plate, which were not practical. All the different FFS tested over both panels and streamwise positions are summarized in Tables 7.1, 7.2, and 7.3 along with the local boundary layer displacement thickness δ_1, calculated using the boundary layer code 3C3D, and the resulting h/δ_1 values.

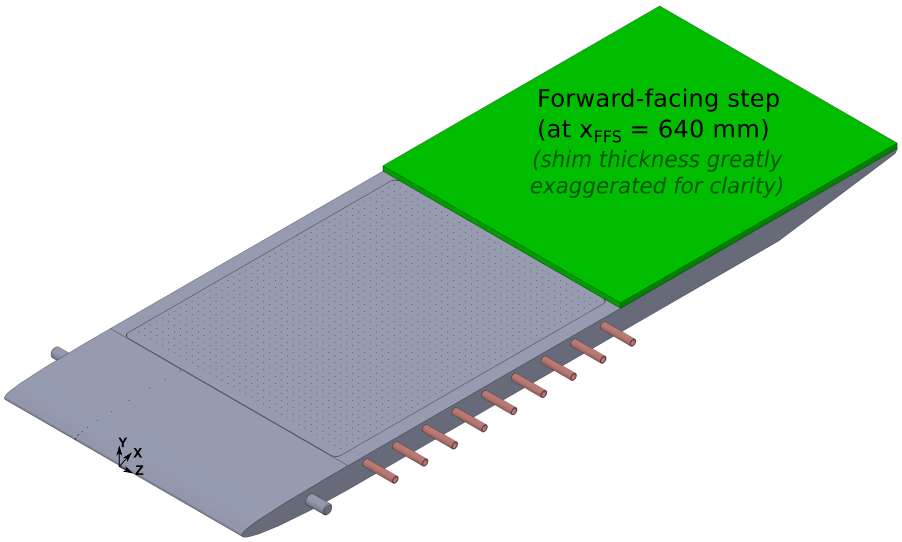

Figure 7.1. Overview of the flat plate with an FFS (x_{FFS} = 640 mm).

Table 7.1. Relative heights for FFS at streamwise position x_{FFS} = 430 mm ($Re_x = 1.12{\cdot}10^6$, junction between chambers C5 and C6) for panel P2. (Asterisks correspond to critical FFS.)

		x_{FFS} = 430 mm				
		no suction	C1/0.400	C3,5/0.200	*full suction*	
	δ_1 (3C3D) [µm]	700	670	610	660	
label	FFS h [µm]	h/δ_1				∼rounded h/δ_1
FFS-150µm-430	150	0.21	0.22	0.25	0.23	∼0.2
FFS-550µm-430	550	0.79	0.82	0.90	0.83	∼0.8
FFS-800µm-430	800	1.14	1.19	1.31	1.21	∼1.2
FFS-900µm-430	900	1.29	1.34	1.48	1.36	∼1.4
FFS-1050µm-430 *	1050	1.5	1.57	1.72	1.59	∼1.6

Table 7.2. Relative heights for FFS at streamwise position x_{FFS} = 640 mm ($Re_x = 1.66{\cdot}10^6$, junction between the end of the suction region and flat plate) for panel P2. (Asterisks correspond to critical FFS.)

		x_{FFS} = 640 mm				
		no suction	C1/0.400	C3,5/0.200	*full suction*	
	δ_1 (3C3D) [µm]	840	820	800	800	
label	FFS h [µm]	h/δ_1				∼rounded h/δ_1
FFS-500µm-640	500	0.60	0.61	0.63	0.63	∼0.6
FFS-650µm-640	650	0.77	0.79	0.81	0.81	∼0.8
FFS-750µm-640	750	0.89	0.91	0.94	0.94	∼0.9
FFS-850µm-640	850	1.01	1.04	1.06	1.06	∼1.0
FFS-950µm-640	950	1.13	1.16	1.19	1.19	∼1.2
FFS-1050µm-640*	1050	1.25	1.28	1.31	1.31	∼1.3
FFS-1150µm-640*	1150	1.37	1.40	1.44	1.44	∼1.4

7.2 Transition location and mean flow

Although a wide array of FFS were tested, three representative step heights (h/δ_1) approximately equal to 0.60, 1.0 and 1.4 located at x_{FFS} equal to 640 mm (i.e., at the end of the suction region)

Table 7.3. Relative heights for FFS and panel P1.

	x_{FFS} = 430 mm	x_{FFS} = 640 mm
δ_1 (3C3D) [µm]	700	840
h [µm]	h/δ_1	
550	0.79	*N/A*
800	*N/A*	0.95

are mainly shown in the following section. Regardless of the suction configuration, the relative heights approximately equal to 0.6 and 1.0 correspond to subcritical cases, whereas h/δ_1 ∼1.4 is critical, i.e., transition occurs immediately downstream of the step. To simplify notation, FFS relative heights will be referred to on figures by the rounded relative height, $\sim h/\delta_1$. However, the precise value of h/δ_1, computed with 3C3D, is used whenever the parameter is graphed (e.g., on Figure 7.6) to account for the local variations in boundary layer displacement thickness due to the suction configuration.

Figure 7.2 shows, for the three steps mentioned above, the streamwise evolution of velocity fluctuations for all suction configurations used to determine the onset of transition. Cases h/δ_1 ∼0.6 and h/δ_1 ∼1.0 with suction are visibly subcritical: velocity fluctuations only start to increase over an extended streamwise region further downstream from the FFS, located at the end of the suction region. Note that, in these two cases, the initial abrupt increase in velocity fluctuations at the step location is a result of the constant-height hotwire traverse. Since the boundary layer changes thickness when crossing the step, the hotwire ends up probing a slightly different altitude inside the boundary layer. As mentioned in the previous chapter on the experimental facility, the transition criterion is still valid despite this altitude change. Therefore, when velocity signals for configurations with a surface defect contain two regions of fluctuation increase, the transition position is determined based on the second region, downstream of the defect position. Finally, Figure 7.2c shows the streamwise evolution of velocity fluctuations for the critical h/δ_1 ∼1.4 case: regardless of the suction configuration, fluctuations increase in one region, immediately downstream of the FFS.

Figures 7.3 and 7.4 show the streamwise evolution of the mean velocity boundary layer profiles in the region close to the FFS located at x_{FFS} equal to 640 mm. Both Figures 7.3a and 7.4a are located 4 mm upstream of the FFS and exhibit an inflection point that is more pronounced for the larger FFS relative height, $h/\delta_1 \sim 1.4$. The height of the inflection point is influenced by the recirculation zone located at the FFS face: a greater step height results in a larger recirculation zone and therefore a higher inflection point altitude.

Immediately downstream (1 mm) of the step, the boundary layer profile seems accelerated, as shown by the difference between the experimental profiles shown in Figures 7.3b and 7.4b and the Blasius profile. Because of the blockage induced by the step, the flow is locally accelerated, regardless of the FFS height. A disruption in the near wall region is also visible for the critical step height $h/\delta_1 \sim 1.4$, indicating a slight recirculation region. However, still further downstream (10 mm) of the step, and regardless of the step height, the experimental profiles from Figures 7.3c and 7.4c have recovered a shape closer to that of a Blasius profile. Note however, that the streamwise position in Figure 7.4c corresponds to the position where the onset of transition occurs for all suction configurations. Since the velocity fluctuations are still relatively small compared to the mean velocity, the profiles do not yet reflect the advent of transition.

Figures 7.3 and 7.4 also show that, in the region near the step, the effect of wall suction is not visible in terms of mean velocity profiles. Regardless of whether or not suction is applied, the boundary layer profiles overlap relatively well. For FFS located at the junction between the suction and solid regions, the difference in displacement thickness due to suction is not

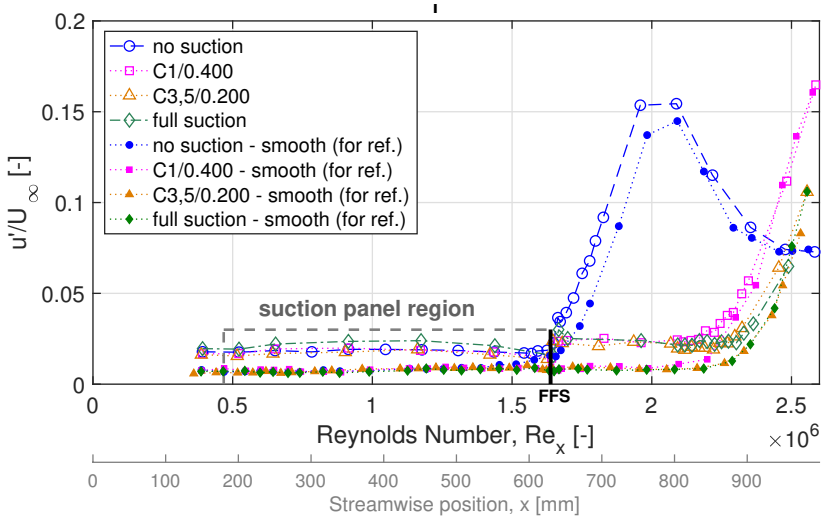

(a) h/δ_1 ∼0.6.

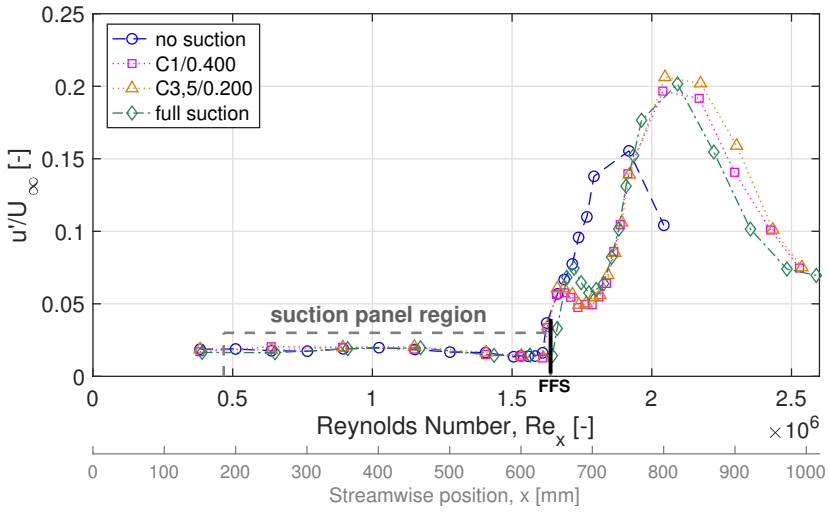

(b) h/δ_1 ∼1.0.

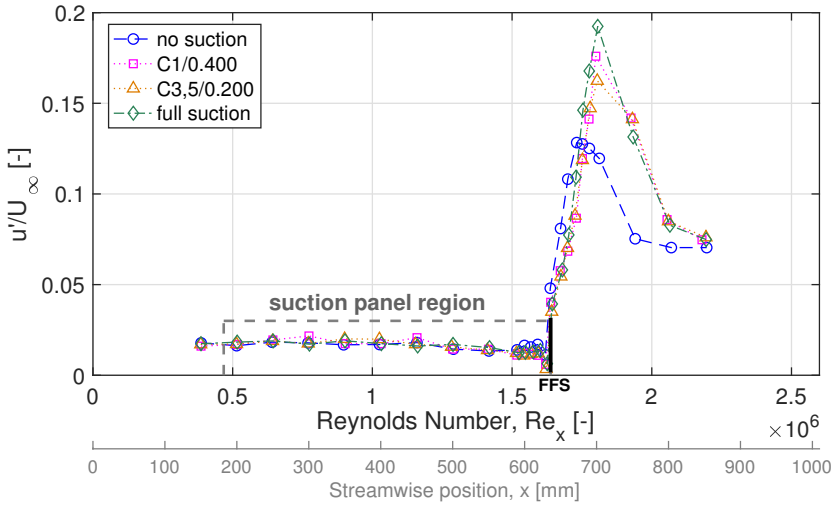

(c) h/δ_1 ∼1.4 (crit.).

Figure 7.2. Streamwise velocity fluctuations (y = 300 µm) for different FFS relative heights and all suction configurations (x_{FFS} = 640 mm) for suction panel P2.

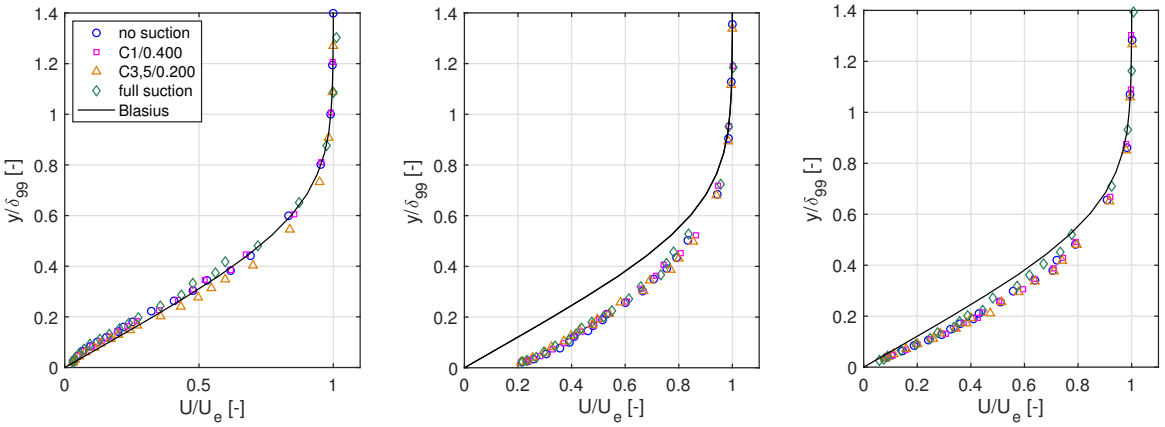

(a) $x = x_{FFS}$ - 4 mm. **(b)** $x = x_{FFS}$ + 1 mm. **(c)** $x = x_{FFS}$ + 10 mm.

Figure 7.3. Mean velocity profiles in the FFS region for h/δ_1 ∼0.6 and $x_{\mathrm{FFS}} = 640$ mm (suction panel P2).

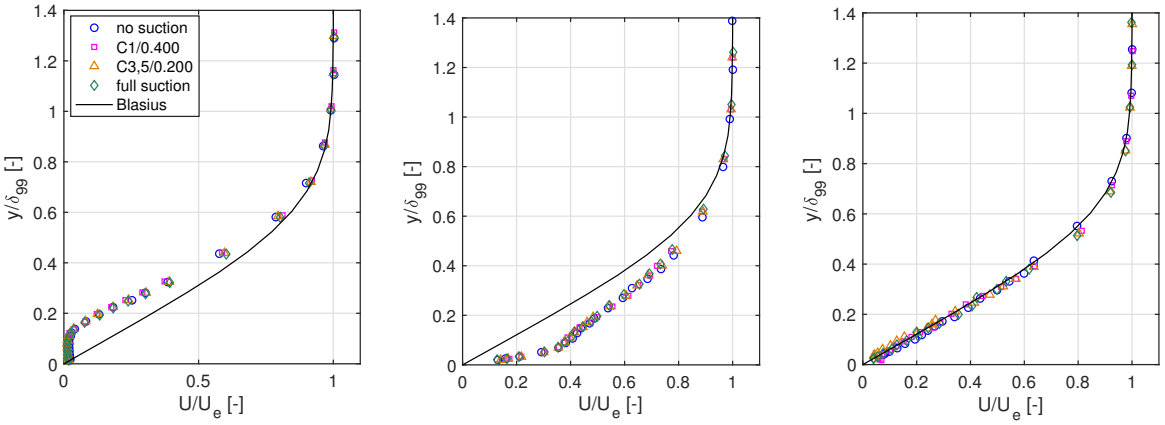

(a) $x = x_{FFS}$ - 4 mm. **(b)** $x = x_{FFS}$ + 1 mm. **(c)** $x = x_{FFS}$ + 10 mm.

Figure 7.4. Mean velocity profiles in the FFS region for h/δ_1 ∼1.4 (crit.) and $x_{\mathrm{FFS}} = 640$ mm (suction panel P2).

significant enough to have a visible effect on the inflection point height.

Because of the similarity between different suction configurations, the *full suction* case is chosen to compare the streamwise evolution of mean velocity profiles for three different step heights h/δ_1: 0.6, 1.0, and 14. Figure 7.5a shows how the increase in step height induces a higher inflection point. At the next position, in Figure 7.5b, all profiles are disrupted due to the local acceleration induced by the step blockage. However, the profiles corresponding to the two cases with the largest $h/delta_1$ values also have an additional bulge in the near wall region, which seems to indicate the presence of a recirculation zone. However, at the final position, in Figure 7.5c, the profiles do not show significant differences: the effect of the step on the mean velocity distribution is therefore localized to the region of the step and is not significant further downstream.

A summary of all the transition positions, expressed in terms of transition Reynolds number Re_{xT}, with respect to the FFS relative heights is given in Figure 7.6a. Note that the case *no suction* for a step at location x_{FFS} equal to 640 mm is not included because the natural transition position on the smooth plate with panel P2 is already located at the position of the

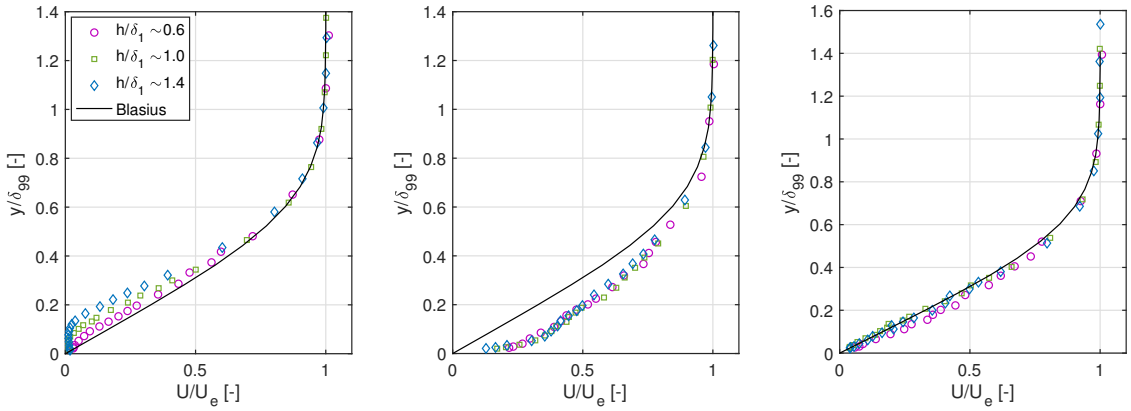

(a) $x = x_{FFS}$ - 4 mm. **(b)** $x = x_{FFS}$ + 1 mm. **(c)** $x = x_{FFS}$ + 10 mm.

Figure 7.5. Mean velocity profile in the FFS region for different FFS height for *full suction* and $x_{\mathrm{FFS}} = 640$ mm (suction panel P2).

surface defect. Data from the current study are also compared to data presented by Wang and Gaster 2005, where FFS were also tested on a flat plate in a different wind tunnel facility.

For a given data set (FFS at $x_{\mathrm{FFS}} = 640$ mm, FFS at $x_{\mathrm{FFS}} = 430$ mm and Wang and Gaster 2005), the transition Reynolds number seems to be bounded by two limits. The upper limit, corresponding to the smooth case, is set by either the freestream turbulence level or the panel and suction configuration. The lower limit, corresponding to the critical case, is set by the position of the surface defect, shown as th dashed and dotted lines on Figure 7.6a.

In order to remove the effect of these two test facility-dependent parameters (freestream turbulence and FFS location), the Δ_{xT} parameter is once again used and shown on Figure 7.6b as a function of the FFS relative height. Similar to the post-processing performed for the wire, the Δ_{xT} parameter is equal to 1 in the absence of any surface defect effect, and 0 when the surface defect is critical. The few cases where $\Delta_{xT,FFS}$ is greater than one correspond to cases where the transition position with a surface defect was slightly further downstream than the smooth case, but still within measurement uncertainty. Data from the present study seem to gather around a trendline, although the critical relative heights seem to be scattered between 1.3 and 1.7. On the other hand, the Δ_{xT} parameter does not enable the overlapping of the present data with data from Wang and Gaster, where the critical relative height is closer to 2.5. This difference seems to indicate that the relative height h/δ_1 does not encompass all the necessary information to determine a universal critical value.

One of the most distinct differences between the present data and the data from Wang and Gaster is that the experiments were conducted in two different wind tunnel facilities. In their publication, Wang and Gaster mention that in the smooth case, the transition N factor is equal to 7.4. Using Mack's relation, the turbulence level for their wind tunnel is therefore assumed to be approximately 0.14%, regardless of their freestream velocity. (In their study, Wang and Gaster modified h/δ_1 by varying step height and freestream velocity.) As a reminder, the turbulence intensity in the present wind tunnel is approximately 0.18%. To attempt to include freestream turbulence information into a potential "universal" parameter, the quantity $h/\delta_1 * Tu^2$ is proposed. Physically, $h/\delta_1 * Tu^2$ is a non-dimensional parameter that represents an FFS' relative height weighed by the squared freestream turbulence level, which is dimensionally equivalent to an energy. The implications of this parameter are that for lower turbulence level flows, the critical relative height will be greater.

The Δ_{xT} parameter is graphed in function of $h/\delta_1 * Tu^2$ on Figure 7.6c. In this figure, all

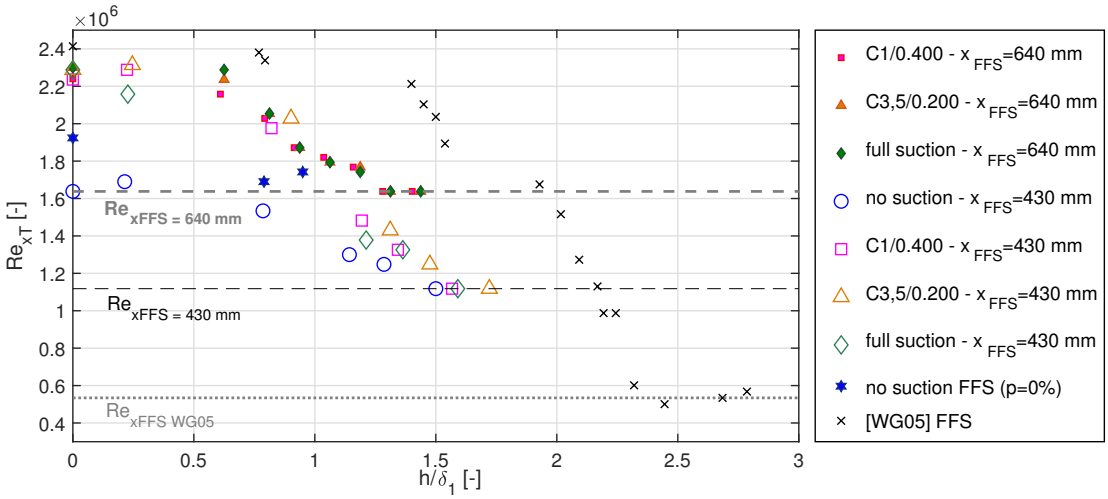

(a) Transition Reynolds Number Re_{xT} as a function of relative height h/δ_1.

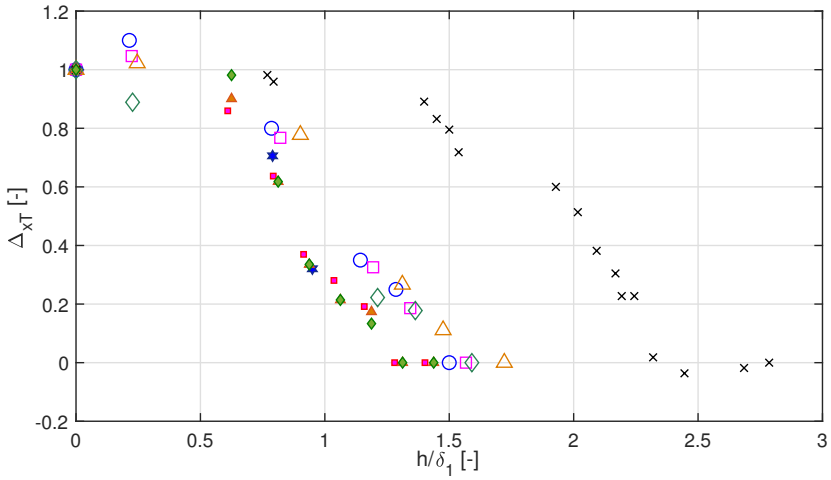

(b) Transition parameter $\Delta_{xT,FFS}$ as a function of relative height h/δ_1.

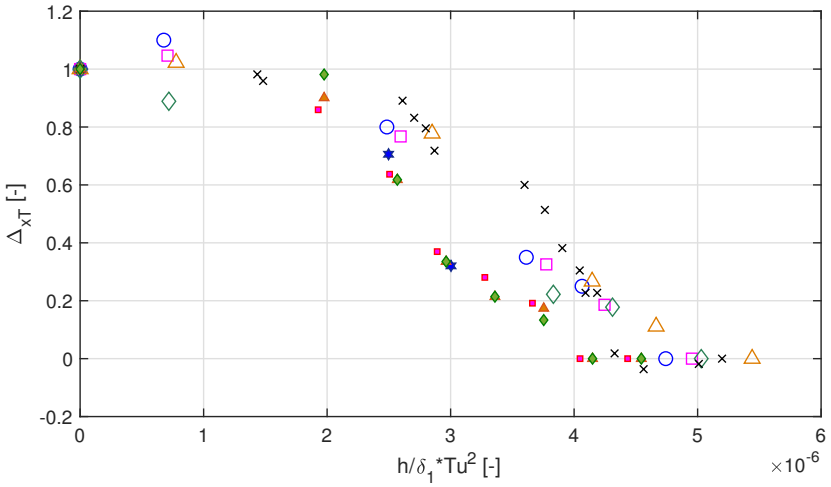

(c) Transition parameter $\Delta_{xT,FFS}$ as a function of relative height h/δ_1 corrected by the test section freestream turbulence Tu^2.

Figure 7.6. Transition position summary for all tested FFS and compared to data from Wang and Gaster 2005.

three data sets now seem to gather around a single trendline (although the spread in the critical FFS height is still present). The validity of the $h/\delta_1 * Tu^2$ parameter is not definitely proven but its definition seems to suggest the influence of freestream turbulence in determining critical FFS data. The reason why such a parameter would be necessary for surface defects like FFS, as opposed to wires, will be further discussed in the following section, which determines the effect of FFS on the transition mechanism.

7.3 Unsteady data analysis

Unsteady data analysis is used to further understand how an FFS modifies the transition position by determining the effect on TS instabilities. For a general overview of the frequency evolution for the subcritical FFS relative height equal to ∼1.0 (and located at $x_{\mathrm{FFS}} = 640$ mm), power spectral densities of the streamwise velocity fluctuations upstream and downstream of the surface defect are shown in Figure 7.7. To improve clarity, the C3,5/0.200 case is not included but can be assumed to be similar to that of the *full suction* case. Upstream of the step, the *no suction* configuration exhibits a significantly amplified frequency band between 400 Hz and 800 Hz (corresponding to the TS frequencies), compared to configurations C1/0.400 and *full suction*. Downstream of the surface defect, the *no suction* configuration, which is now undergoing transition, has a much more broadband signal, tending towards a turbulent spectrum, with greater amplitude. The two configurations with suction also experienced an overall increase in magnitude, especially over the TS frequency range. In these subcritical cases, although the step was responsible for significant amplification of TS frequencies, suction was effective enough to prevent TS frequencies from reaching an amplitude resulting in the onset of transition. Eventually, transition of the subcritical cases with suction is still the result of TS amplification, as shown by the PSD at the respective transition positions in Figure 7.8.

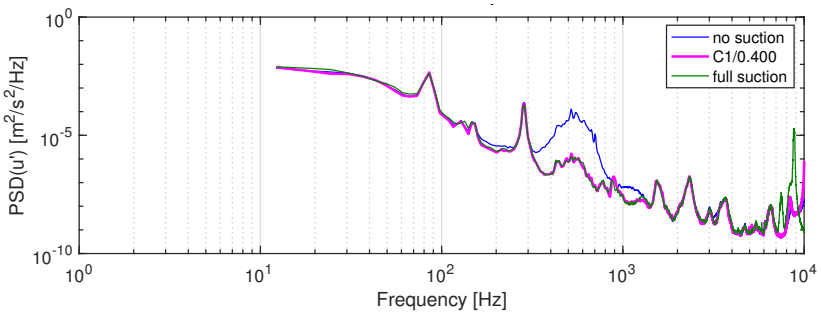

(a) $x = 600$ mm ($\mathrm{Re}_x = 1.56{\cdot}10^6$).

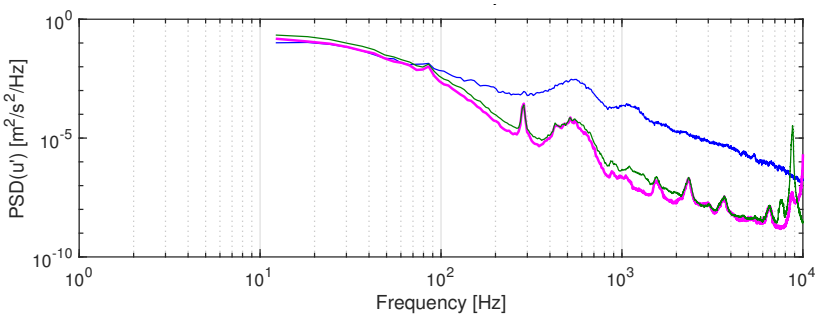

(b) $x = 650$ mm ($\mathrm{Re}_x = 1.69{\cdot}10^6$).

Figure 7.7. PSD(u') ($y = 300$ µm) upstream (a) and downstream (b) of the subcritical FFS ($x_{\mathrm{FFS}} = 640$ mm) for h/δ_1 ∼1.0 (suction panel P2).

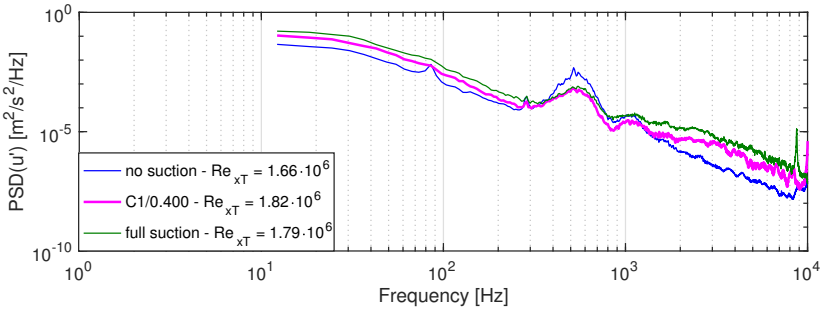

Figure 7.8. PSD(u') ($y = 300$ µm) at the transition Reynolds number for the subcritical FFS ($x_{\mathrm{FFS}} =$ 640 mm) for h/δ_1 ∼1.0 (suction panel P2).

Next, a comparison of the PSD from three FFS located at x_{FFS} equal to 640 mm and with relative heights ∼0.6, ∼1.0 and ∼1.4 is shown in Figure 7.9. All three relative heights for the suction configuration C1/0.400 are compared 10 mm upstream of the surface defect on Figure 7.9a, and 10 mm downstream of the surface defect on Figure 7.9b. Upstream of the surface defect (and of the recirculation zone in front of the step), the PSD for all three steps are comparable, both in terms of magnitude and in terms of the amplified TS frequencies, which span a range between 400 Hz and 800 Hz. This result is normal given that, up to this streamwise position, the boundary layer for all three steps experiences the same flow conditions. However, differences appear downstream of the surface defect. The smallest step height induces the smallest overall amplitude increase, whereas the largest (and critical) step height results in a broadband PSD, very close to that of a turbulent flow. The intermediate FFS with h/δ_1 equal to 1.0 is still subcritical, and results in a stronger amplification of the TS instabilities than the h/δ_1 equal to 0.6.

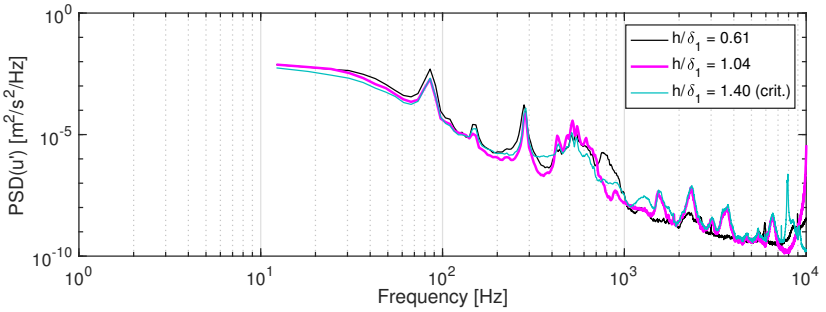

(a) $x = 630$ mm ($\mathrm{Re}_x = 1.64{\cdot}10^6$).

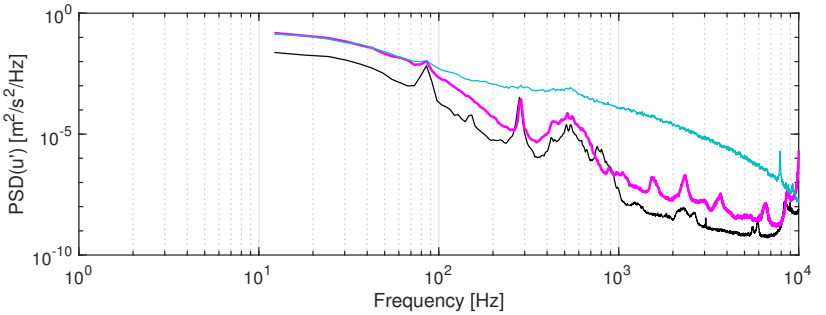

(b) $x = 650$ mm ($\mathrm{Re}_x = 1.69{\cdot}10^6$).

Figure 7.9. PSD(u') ($y = 300$ µm) upstream (a) and downstream (b) of the FFS ($x_{\mathrm{FFS}} = 640$ mm) for C1/0.400 (suction panel P2).

Transition still seems to be the result of TS amplification regardless of the step height, as shown by the PSD on Figure 7.10 taken at the respective transition positions. The high frequency band could be the result of the inflection point induced in the boundary layer profile upstream of the step. However, recall that in the case of the critical wire that modified the transition mechanism, only the amplified high frequency band was visible and no trace of TS frequencies could clearly be discerned. In the present case of a critical FFS, the amplified TS frequency band is still visible and has greater magnitude than the amplified high frequencies, therefore suggesting that transition is still the result of TS amplification.

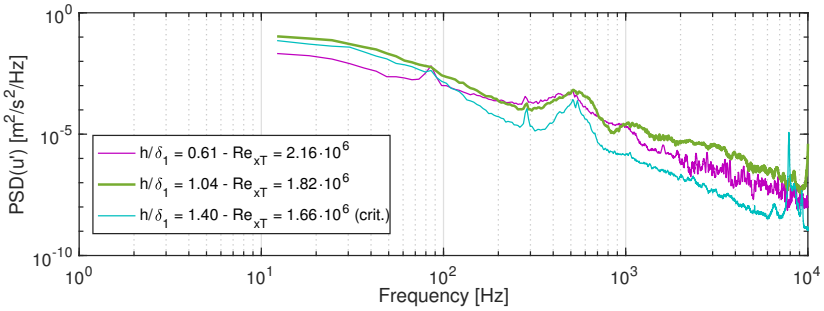

Figure 7.10. PSD(u') (y = 300 µm) at the transition Reynolds number for C1/0.400 (suction panel P2).

Since TS instabilities seem responsible for the onset of transition, the unsteady data from boundary layer profile acquisitions are used to define streamwise velocity fluctuations profiles at the TS frequencies. Figure 7.11 shows the streamwise evolution of these *u'* profiles, evaluated between frequencies from 492 Hz to 532 Hz, upstream (Figures 7.11a and 7.11b) and downstream (Figures 7.11c and 7.11d) of the FFS located at x_{FFS} equal to 640 mm in the *no suction* configuration.

At the initial position in Figure 7.11a, all profiles, regardless of the step height, have a typical TS profile shape and their maximum amplitudes are all relatively close, ranging between 0.10 m.s^{-1} and 0.14 m.s^{-1}. However, at the next position, located immediately upstream of the step, a spread in the profile maxima already appears. In this region, the significant recirculation zone, which forms in the presence of large relative step heights, can already affect the boundary layer. In one category, profiles in Figure 7.11b for the subcritical cases (less than or equal to 1.0) overlap relatively well, near a maximum *u'* value of 0.3 m.s^{-1} (approximately equivalent to 0.7% of U_e). On the other hand, the cases with critical relative heights (∼1.3 and ∼1.4) form another category where profile maxima are much greater: in particular, the case with h/δ_1 ∼1.4 has its maximum close 0.7 m.s^{-1} (approximately equivalent to 1.8% of U_e). Additionally, although case ∼1.2 is not critical, it belongs to the latter category, where the effect of the recirculation zone on its velocity fluctuations' maximum is also noticeable. Finally, all the profile maxima in Figure 7.11b experience a general shift upwards in altitude with respect to the previous streamwise position. This shift is more pronounced for cases with h/δ_1 greater than or equal to ∼1.2, which seems to indicate an effect from the recirculation zone.

Immediately downstream of the FFS, all the profiles have undergone some amplification but the two categories mentioned above can still be defined, as seen in Figure 7.11c. The profiles in subcritical cases with h/δ_1 less than or equal to 1.0 maintain amplitudes that are relatively close to each other, although some spread is starting to appear. On the other hand, for h/δ_1 values greater than or equal to 1.13, an increase in relative step height results in a larger profile maximum value. The double local maxima located below y/δ_{99} less than 1 are also an indication of the presence of the recirculation zone that was observed in the mean velocity profiles in Figure 7.5b. At the last station, shown in Figure 7.11d, the differences between all

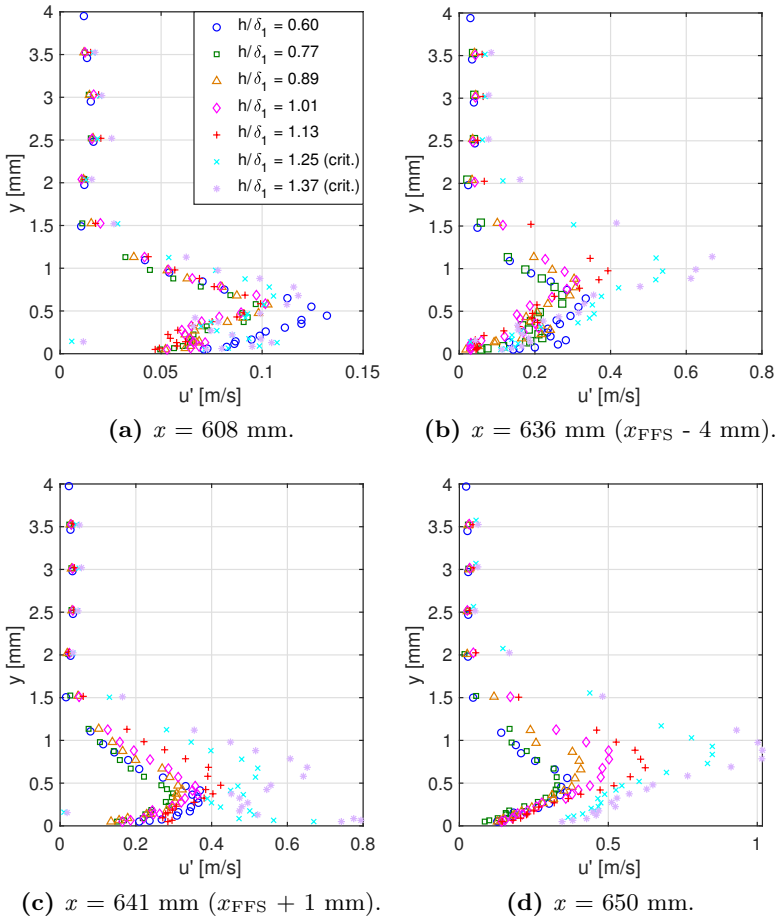

(a) x = 608 mm. **(b)** x = 636 mm (x_{FFS} - 4 mm).

(c) x = 641 mm (x_{FFS} + 1 mm). **(d)** x = 650 mm.

Figure 7.11. Velocity fluctuation profiles evaluated over [492-532] Hz upstream and downstream of the FFS position (x_{FFS} = 640 mm) for the *no suction* configuration (suction panel P2).

the profiles are more distinguishable and the effect of increasing FFS relative heights clearly results in greater amplification of the velocity fluctuations.

Similar profiles over the same frequencies of interest ([492-532] Hz) were generated for configurations C1/0.400 (Figure 7.12) and *full suction* (Figure 7.13). Since suction is applied, the profiles at the initial location in Figures 7.12a and 7.13a have not yet developed into a TS profile shape, and their velocity fluctuations have amplitudes approximately an order of magnitude lower than those of the *no suction* configuration at the same location. At the next streamwise position (immediately upstream of the FFS) all profiles in Figures 7.12b and 7.13b start to have a shape closer to that of a TS profile, and already exhibit increasing profile maxima for increasing FFS height. This spread was not visible at this location for the *no suction* configuration. The initially lower amplitude *u'* profiles due to suction therefore seem to be more sensitive to the size of the recirculation zone upstream of the step.

As the boundary layer crosses the step, the spread between the profiles is further increased at x equal to 641 mm (Figures 7.12c and 7.13c) and 650 mm (Figures 7.12d and 7.13d). For all step heights at the last station, the *u'* profiles have the general shape of a TS profile, scaled according to a larger maximum value for larger FFS step heights. Regardless of whether or not the step height is critical, the FFS therefore do not seem to change the transition mechanism (like wires) but rather further amplify the already-existing TS instabilities. In the case of critical steps, the additional amplification induced by the step is strong enough to trigger the onset of transition

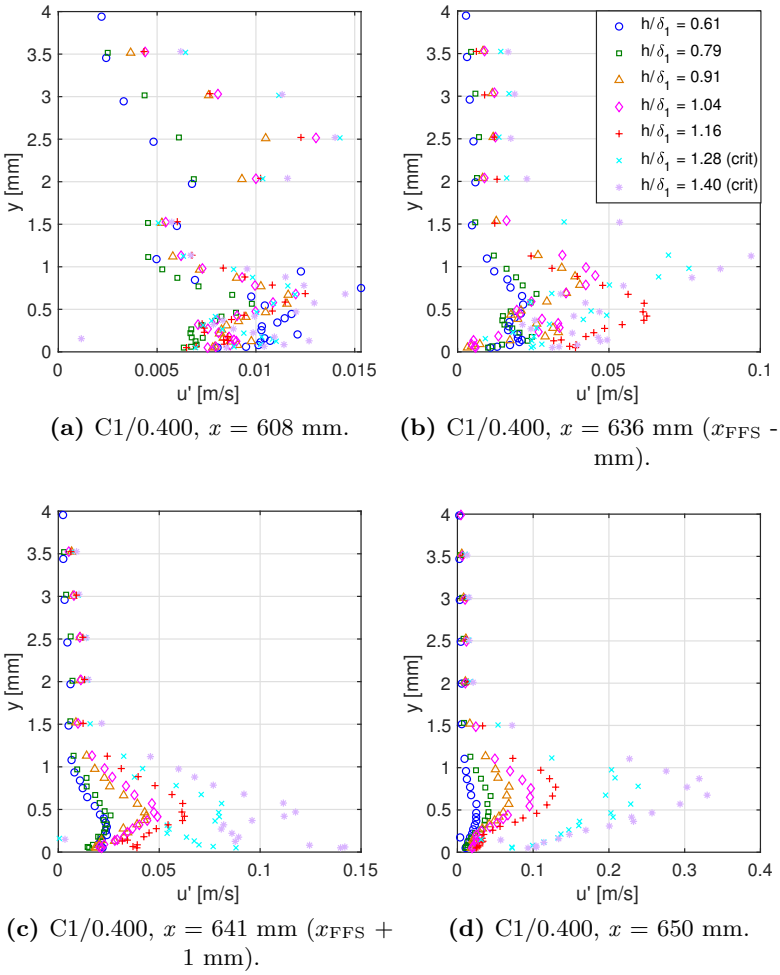

(a) C1/0.400, x = 608 mm.

(b) C1/0.400, x = 636 mm (x_{FFS} - 4 mm).

(c) C1/0.400, x = 641 mm (x_{FFS} + 1 mm).

(d) C1/0.400, x = 650 mm.

Figure 7.12. Velocity fluctuation profiles evaluated over [492-532] Hz around the FFS position (x_{FFS} = 640 mm) for the C1/0.400 configuration.

at the step location. Note however, that once again as step heights increase, the altitude of the profile maximum also increases, probably due to an effect from the recirculation zone upstream of the step.

Figure 7.14 compares the effect of suction and step height at upstream (x = 608 mm) and downstream (x = 650 mm) locations from the step, which were already used in Figures 7.11, 7.12 and 7.13. This representation overlays the different orders of magnitude involved depending on the suction configuration and the FFS relative height.

In Figure 7.14a, the amplification due to the subcritical FFS with h/δ_1 equal to 0.6 seems to be relatively the same: across the step, amplitudes are approximately multiplied by 3, which could also be expressed as an amplification of approximately e^1. The effectiveness of wall suction in attenuating instabilities is also clearly visible since even downstream of the step, the profiles with suction are still an order of magnitude lower than the *no suction* profile upstream of the step. Finally, all profiles have a shape close to that of a TS profile.

For a larger but still subcritical step height, shown in Figure 7.14b, the resulting amplification is different depending on the suction configuration. As mentioned above, *u'* profiles with low initial amplitudes seem to be more amplified (approximately ten-fold) by large ($\geq$ 1.0) step heights than TS profiles that are already well developed, as in the *no suction* configuration, where fluctuations are increased by five-fold. For this h/δ_1 value, the profiles with suction

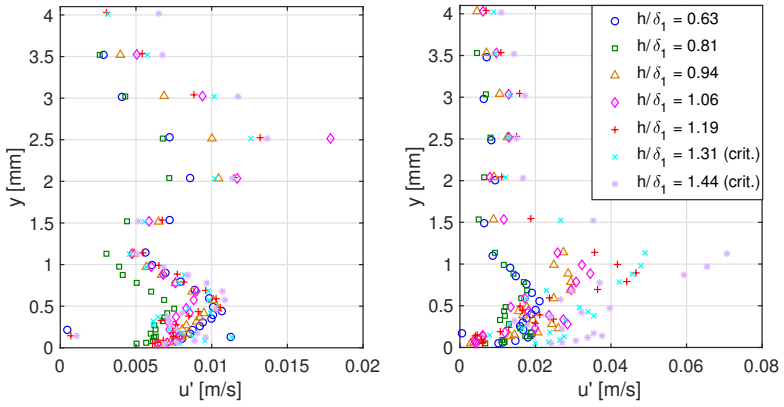

(a) *full suction*, $x = 608$ mm. **(b)** *full suction*, $x = 636$ mm (x_{FFS} - 4 mm).

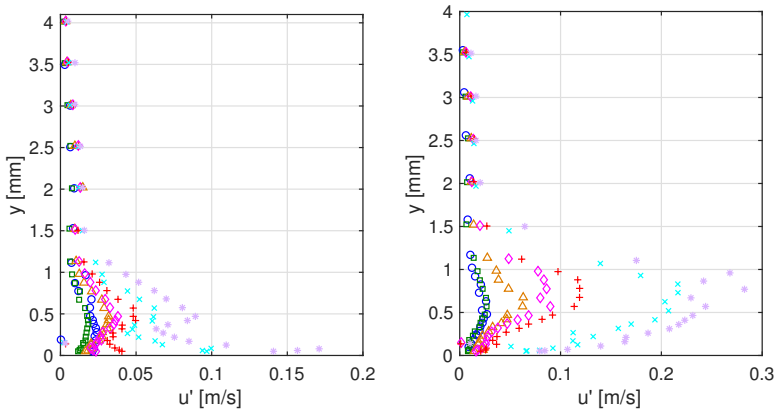

(c) *full suction*, $x = 641$ mm (x_{FFS} + 1 mm). **(d)** *full suction*, $x = 650$ mm.

Figure 7.13. Velocity fluctuation profiles evaluated over [492-532] Hz upstream and downstream of the FFS position ($x_{\mathrm{FFS}} = 640$ mm) for the *full suction* configuration.

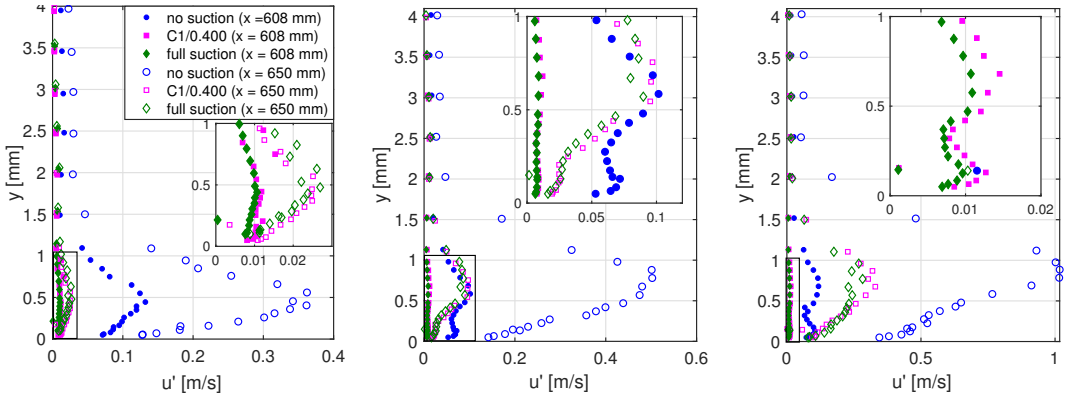

(a) h/δ_1 ∼0.6. **(b)** h/δ_1 ∼1.0. **(c)** h/δ_1 ∼1.4 (crit.).

Figure 7.14. Evolution of TS profiles between streamwise positions $x = 608$ mm and $x = 650$ mm for different FFS heights and suction configurations.

downstream of the step reach amplitudes similar to those of the *no suction* upstream of the defect. Additionally, the step also starts to influence upstream *u'* profiles, most noticeably in

the *no suction* case. Although well upstream of the recirculation region, the *no suction* profile at x equal to 608 mm is disrupted by the presence of the step, as shown by the additional local maximum in the near wall region. This second maximum has a lower amplitude than the principal maximum located at a higher altitude inside the profile.

Finally, in the critical case from Figure 7.14c, all of the effects mentioned for the previous step height are even further exacerbated. Across the step, the profiles with suction undergo an amplification close to twenty-fold whereas that of the *no suction* configuration is closer to ten-fold. The upstream influence of the step on the profiles is also more pronounced for this larger h/δ_1 value: for example, in the *no suction* configuration, the two maxima are almost equal. The presence of these two maxima from the step's upstream influence can also be seen for the cases with suction by the modulation of the two profiles in the inset graph. Downstream of the FFS, the *u'* profiles with suction recover a shape close to a TS profile, while the *no suction* profile has a modified TS profile shape, especially in the near-wall region.

For a more general overview, Figure 7.15 shows the amplification of the maxima of *u'* profiles (evaluated over frequency range [492-532] Hz) across extended streamwise regions for step location x_{FFS} equal to 640 mm. For the *no suction* configuration, Figure 7.15a clearly shows the increasing influence of growing steps both upstream and downstream of the step location. Since the smooth case transition for the *no suction* configuration already occurs at x_{FFS}, these amplitude differences do not have any consequences on the transition position, but rather the size of the transition region.

On the other hand, the two suction configurations with wall suction, shown on Figures 7.15b and 7.15c do experience a progressive upstream shift in transition position as the FFS relative height is increased. Although the initial difference between the amplitudes immediately downstream of the FFS location are small, the increased influence of steps of growing h/δ_1 on the instabilities' amplification is clear when considering the different slopes associated to each step.

All of the previous figures therefore seem to confirm the fact that the critical FFS that were presently tested tend to further amplify existing instabilities, as opposed to critical wires that seem to immediately change the transition mechanism to an inflection-type instability. Each type of surface defect also had very different critical h/δ_1 values: the value for the critical wire was closer to 0.4, while that of the critical FFS was approximately 1.3.

The fact that both subcritical and critical FFS simply amplify existing instabilities could offer an explanation as to the use of such a parameter as $h/\delta_1 * Tu^2$ to define "universal" critical FFS heights. Including the freestream turbulence offers a way to include information about the already existing instabilities. This factor, to account for differences in freestream turbulence, did not seem necessary when defining critical wire heights: regardless of the data set, all Re_{xT} *vs.* h/δ_1 curves seemed to converge towards a single curve past the critical h/δ_1. One possible reason could be that critical wires change the transition mechanism to an inflection-type (and inviscid) instability. In this case, the state of the existing instabilities is thus not as important as the altitude of the inflection point and the change in curvature at this point. These last two parameters can both be encompassed by the h/δ_1 parameter.

7.4 Numerical analysis and comparison with existing ΔN models

One objective of the present investigation is to assess whether existing ΔN models for FFS, such as the ones presented in Section 3.3.2, can still be of use in the presence of a boundary layer undergoing wall suction. Based on the results from the previous section, which show that all FFS, regardless of suction configuration, only amplify existing instabilities, the ΔN approach seems more justified than in the case of wires, for example.

The first step required determining the ΔN values for all experimental test cases. Using LST, the maximum N factor envelope curve is calculated for the smooth case and for each suction configuration. The N_T is then determined based on the experimental transition position, as was listed in Table 5.5 from the previous chapter and is assumed to be constant for a given suction configuration. Next the N factor at the transition position with a surface defect, $N_{xT,FFS}$ is determined using the same maximum N factor envelope curve. The ΔN is then defined as:

$$\Delta N = N_{T,smooth} - N_{xT,FFS}. \tag{7.1}$$

Figure 7.16 visually shows the results from this process for the solid panel, where only two FFS were tested, each at different x_{FFS}.

The ΔN was evaluated for all suction configurations and FFS; however, a first check was performed by comparing results from the solid panel and the *no suction* configuration only with existing ΔN data, shown on Figure 7.17. The model labeled "[CKN06]" was developed by Crouch et al. 2006 and the data set "[WG05]" was taken from Wang and Gaster 2005. For the range of h/δ_1 values that were evaluated, the present ΔN seem to fall within the range of previous solid panel studies and the FFS model. As expected, the model by Crouch is the most conservative due to the fact that both adverse and favorable pressure gradient data were used for its definition. In turn, the present data results in larger ΔN values than those recorded by Wang and Gaster for similar h/δ_1 values.

Finally, the ΔN values evaluated for all suction configuration and FFS location are reported on Figure 7.18 and compared to the [CKN06] model and the [WG05] data set. Open symbols correspond to x_{FFS} equal to 640 mm, and full symbols to x_{FFS} equal to 430 mm. Data from the suction configurations with x_{FFS} at 640 mm seem to match the [CKN06] model relatively well. On the other hand, for the upstream FFS position, the suction configurations have ΔN values that significantly diverge from both [WG05] and [CKN06].

Summary

In this chapter, the FFS that were tested were found to simply enhance the amplification of the existing instabilities. Wall suction still delayed transition in the presence of subcritical FFS (similar to subcritical wires), although less effectively than in the smooth case. However, wall suction was, once again, unable to prevent or delay critical transition compared to the *no suction* configuration. Because no abrupt change in transition mechanism occurred once the critical FFS dimension was reached, the range of subcritical FFS was wider. Consequently, the critical h/δ_1 was equal to $\sim$1.3 (as opposed to $\sim$0.4 for wires). The constant transition mechanism as well as the wide range of subcritical FFS warranted the use of the ΔN method. Comparison with previous studies found relatively good agreement in terms of the general trends, but configurations with suction seemed to induce larger ΔN than similar-size FFS on a solid wall or in the *no suction* configuration. The final type of surface defect, gaps, will presented in the following chapter.

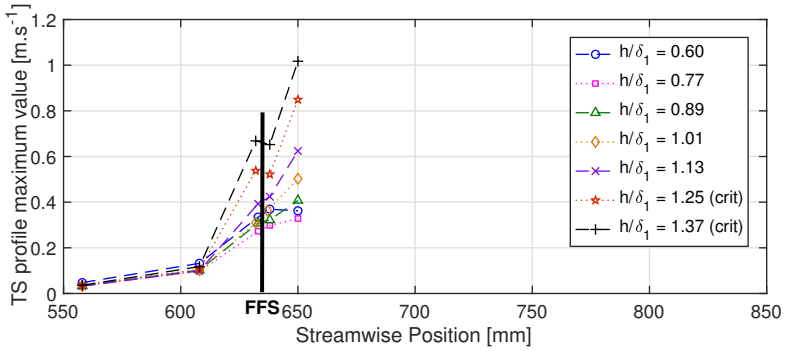

(a) *no suction.*

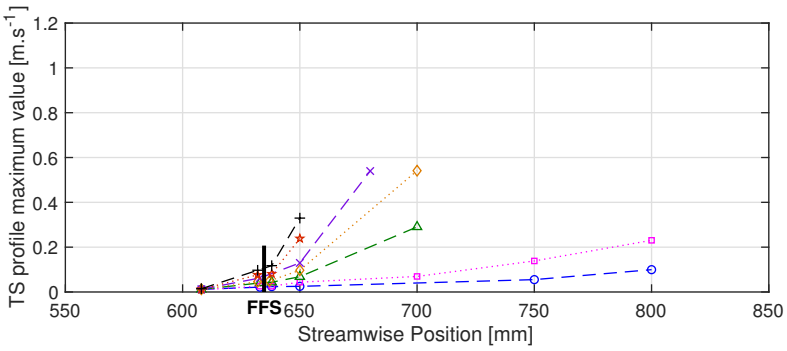

(b) C1/0.400.

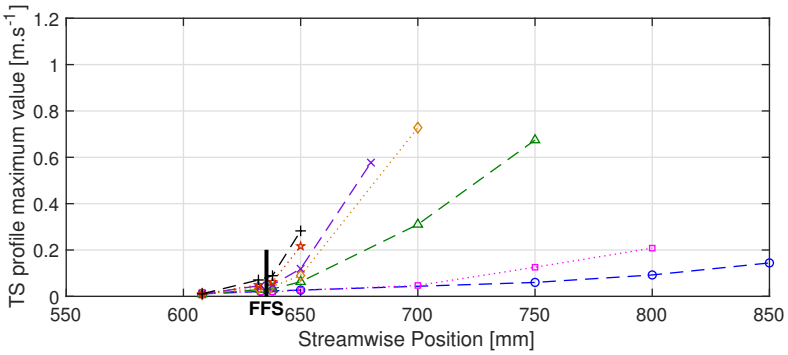

(c) *full suction.*

Figure 7.15. Evolution of the TS profiles maximum value for different suction configurations.

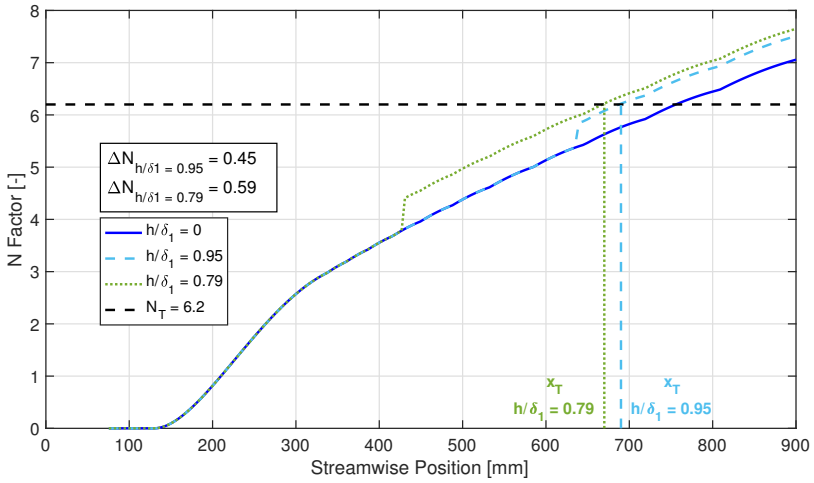

Figure 7.16. ΔN evaluation for the solid panel with FFS.

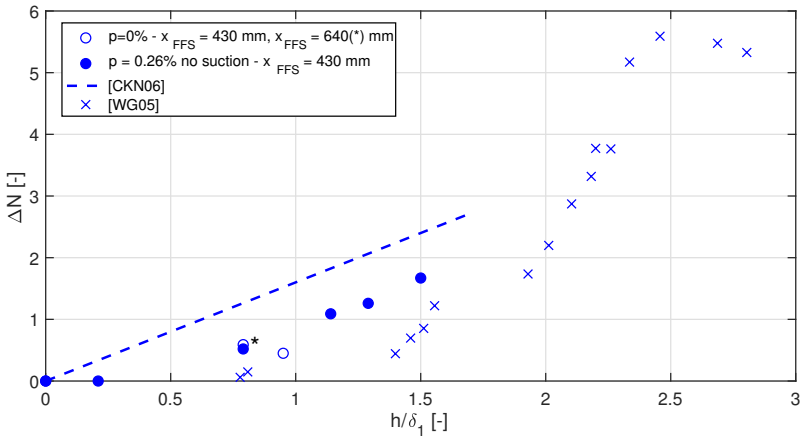

Figure 7.17. ΔN as a function of h/δ_1.

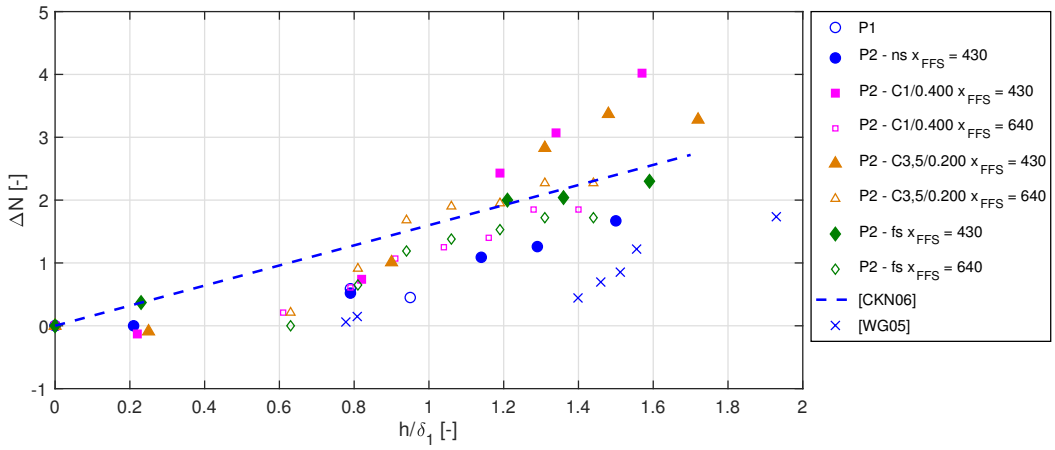

Figure 7.18. All suction configurations with FFS compared with ΔN model for FFS from Crouch et al. 2006 and with measurements from Wang and Gaster 2005.

Chapter 8

Combined Effects of Gaps and Wall Suction

Contents

8.1 Geometric characteristics of the gaps 117
8.2 Transition location and mean flow 118
8.3 Unsteady data analysis 123
8.4 Numerical analysis and comparison with an existing model 131

In keeping with the two previous chapters, this chapter now covers the effects gaps combined with wall suction on boundary layer stability. The gap geometry and positions are initially presented (Section 8.1) and their general effect of transition location and mean flow are discussed (Section 8.2). Unsteady data analysis is performed to provide additional information on the transition mechanisms involved in the presence of either a subcritical or critical gap (Section 8.3). Finally, ΔN values based on the present experimental data are established through numerical analysis and compared with existing ΔN data sets or models (Section 8.4).

8.1 Geometric characteristics of the gaps

The flat plate model was then modified to include gap inserts either at the junction between the suction and solid regions or inside the suction region (more specifically in chamber C4), as shown on Figure 8.1. Experiments were only performed on suction panel P2 for this type of defect. Gaps were only inserted at one location at a time so that only the effect of a single gap on transition was being investigated. The leading edge coordinate of the gap is used to refer to each gap location since regardless of the gap dimension this position remained fixed. Gaps inside the suction region have a leading edge position at x_{GAP} equal to 360 mm and those at the junction between the suction and solid region at 640 mm.

To achieve a wide test matrix, inserts with gaps of varying dimensions were designed for easy mounting and installation, and were 3D-printed to allow for rapid manufacturing. The different gap dimensions are summarized in Tables 8.1 and 8.2, along with their corresponding label, which follow the convention: GAP-hµm-$b$mm, where h corresponds to the depth and b to the width of the gap.

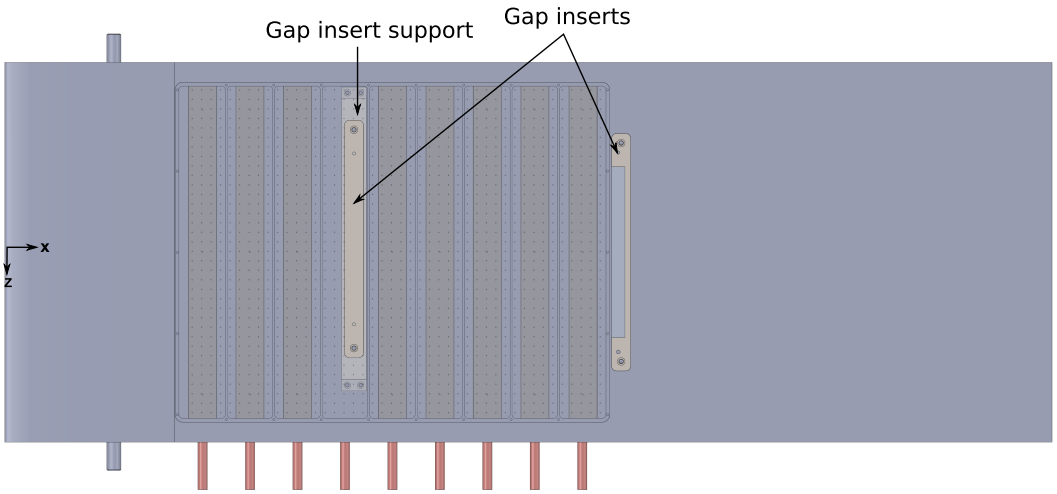

Figure 8.1. Overview of the flat plate with the two gap inserts.

Table 8.1. All tested gap dimensions for $x_{\mathrm{GAP}} = 640$ mm. (Asterisks correspond to critical gaps.)

				no suction		C1/0.400		C3,5/0.200 *full suction*	
		δ_1 (3C3D) [µm]		840		820		800	
Label	h [mm]	b [mm]	b/h	h/δ_1	b/δ_1	h/δ_1	b/δ_1	h/δ_1	b/δ_1
GAP-400µm-14mm	0.4	14	35	0.5	16.7	0.5	17.1	0.5	17.5
GAP-800µm-8mm	0.8	8	10	1	9.5	1	9.8	1	10
GAP-800µm-12mm	0.8	12	15	1	14.3	1	14.6	1	15
GAP-800µm-14mm	0.8	14	17.5	1	16.7	1	17.1	1	17.5
GAP-1200µm-2.4mm	1.2	2.4	2	1.4	2.9	1.5	2.9	1.5	3
GAP-1200µm-6mm	1.2	6	5	1.4	7.1	1.5	7.3	1.5	7.5
GAP-1200µm-8mm	1.2	8	6.7	1.4	9.5	1.5	9.8	1.5	10
GAP-1200µm-12mm	1.2	12	10	1.4	14.3	1.5	14.6	1.5	15
GAP-1200µm-14mm	1.2	14	11.7	1.4	16.7	1.5	17.1	1.5	17.5
GAP-1200µm-16mm	1.2	16	13.3	1.4	19	1.5	19.5	1.5	20
GAP-1200µm-18mm	1.2	18	15	1.4	21.4	1.5	22	1.5	22.5
GAP-1200µm-20mm*	1.2	20	16.7	1.4	23.8	1.5	24.4	1.5	25
GAP-1600µm-8mm	1.6	8	5	1.9	9.5	2	9.8	2	10
GAP-2400µm-12mm	2.4	12	5	2.9	14.3	2.9	14.6	3	15
GAP-4000µm-8mm	4	8	2	4.8	9.5	4.9	9.8	5	10
GAP-4000µm-12mm	4	12	3	4.8	14.3	4.9	14.6	5	15
GAP-5000µm-4mm	5	4	0.8	6	4.8	6.1	4.9	6.25	5
GAP-8000µm-8mm	8	8	1	9.5	9.5	9.8	9.8	10	10
GAP-8000µm-12mm	8	12	1.5	9.5	14.3	9.8	14.6	10	15
GAP-15000µm-8mm	15	8	0.5	17.9	9.5	18.3	9.8	18.75	10
GAP-15000µm-12mm*	15	12	0.8	17.9	14.3	18.3	14.6	18.75	15

8.2 Transition location and mean flow

Similar to the previous chapter, only a selected number of representative gap dimensions will be in shown in this section. To investigate the effect of width b, subcritical and critical defect for

Table 8.2. All tested gap dimensions for x_{GAP} = 360 mm. (Asterisks correspond to critical gaps.)

		no suction		C1/0.400		C3,5/0.200		*full suction*	
h/δ_1 (3C3D) [µm]		631		600		590		610	
Label	b/h	h/δ_1	b/δ_1	h/δ_1	b/δ_1	h/δ_1	b/δ_1	h/δ_1	b/δ_1
GAP-1200µm-2.4mm	2	1.9	3.8	2.0	4.0	2.0	4.1	2.0	3.9
GAP-1200µm-8mm	6.7	1.9	12.7	2.0	13.3	2.0	13.6	2.0	13.1
GAP-1200µm-14mm	11.7	1.9	22.2	2.0	23.3	2.0	23.7	2.0	23.0
GAP-1200µm-18mm*	15	1.9	28.6	2.0	30.0	2.0	30.5	2.0	29.5
GAP-15000µm-8 mm	0.5	23.8	12.7	25.0	13.3	25.4	13.6	24.6	13.1

each gap location will be shown such that: for x_{GAP} equal to 640 mm, subcritical GAP-1200µm-8mm and critical GAP-1200µm-20mm are discussed; and for x_{GAP} equal to 360 mm, subcritical GAP-1200µm-2.4mm and critical GAP-1200µm-18mm are discussed. In addition to these four cases, critical GAP-15000µm-12mm will also be presented in this subsection to compare the extent of the transition region in the presence of a critical gap mainly driven by its depth h or width b.

Figure 8.2 shows the streamwise evolution of velocity fluctuations for all three gaps located at x_{GAP} equal to 640 mm and for all suction configurations. For the subcritical case GAP-1200µm-8mm in Figure 8.2a, all configurations with suction have a transition position significantly further downstream from the gap location. Note that the *no suction* configuration is not critical, despite its transition position being at the gap location: even in the smooth case, the "natural" transition occurs at this coordinate. Figures 8.2b and 8.2c show two critical gaps. In the first case, GAP-1200µm-20mm, the transition is mainly driven by the gap width b since the width was being varied for a constant depth value. Since this critical gap located at x_{GAP} equal 640 mm is shallow and its leading and trailing edges are therefore relatively far apart, the transition positions for the suction configurations are actually located immediately downstream of the gap. On the other hand, for the deep critical gap GAP-15000µm-12mm, all transition positions are located at the leading edge of the gap. In both cases though, once the boundary layer encounters a gap with critical dimensions, wall suction become ineffective.

Similarly, Figure 8.3 shows the velocity fluctuation's streamwise evolution for gaps with x_{GAP} equal to 360 mm. For this gap location however, the effect of deep and shallow gaps are different. In Figure 8.3a, the gap GAP-1200µm-2.4mm is subcritical, as expected. Configurations with suction are moved upstream from their smooth case reference, but each configuration case can still effectively delay transition compared to the *no suction* configuration. The C1/0.400 configuration, however, seems to be more significantly moved upstream than the C3,5/0.200 and *full suction* configurations.

More surprisingly, GAP-15000µm-8mm (Figure 8.3b) actually seems to have a lesser destabilizing effect than GAP-1200µm-2.4mm. Additionally, this trend is opposite to that of the geometrically-similar but critical case, GAP-15000µm-12mm, at x_{GAP} equal to 640 mm. One possible explanation could be related to the fact that, as seen in previous studies (Charwat et al. 1961, Sarohia 1977, Sinha et al. 1982, Zahn and Rist 2015), deep gaps can contain complex flow patterns, as well as act as resonators (which could couple with the boundary layer instabilities). Since hotwire probing inside these deep gaps was not possible in the scope of the present study, the results related to these gaps are restricted to streamwise hotwire traverses at a constant altitude.

Finally, the critical gap GAP-1200µm-18 mm shown in Figure 8.3c exhibits a more conventional behavior, where, regardless of the suction configuration the onset of transition occurs at the same position. Note however, that, although this gap is shallow and its leading and trailing

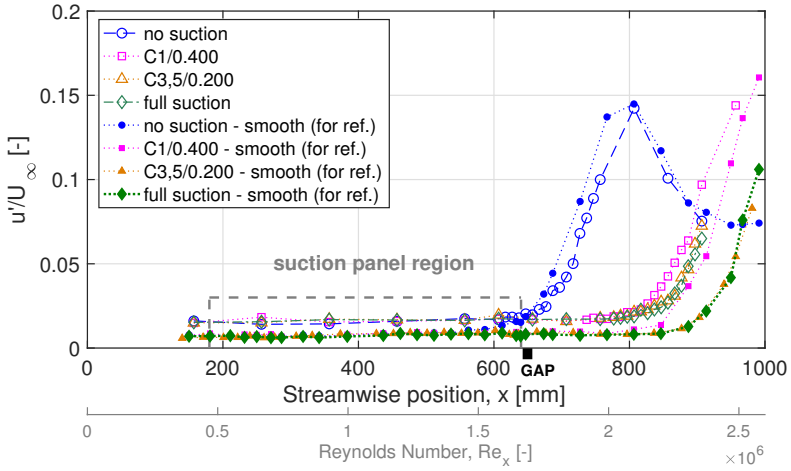

(a) GAP-1200µm-8mm ($b/h = 6.7$).

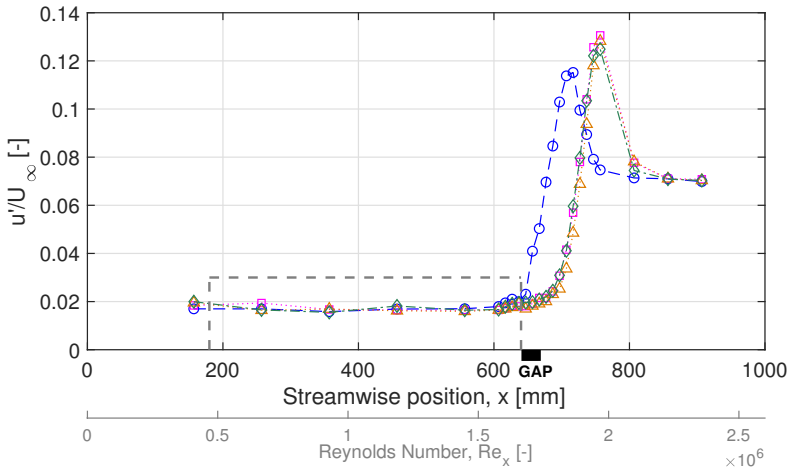

(b) GAP-1200µm-20mm ($b/h = 16.7$) (crit.).

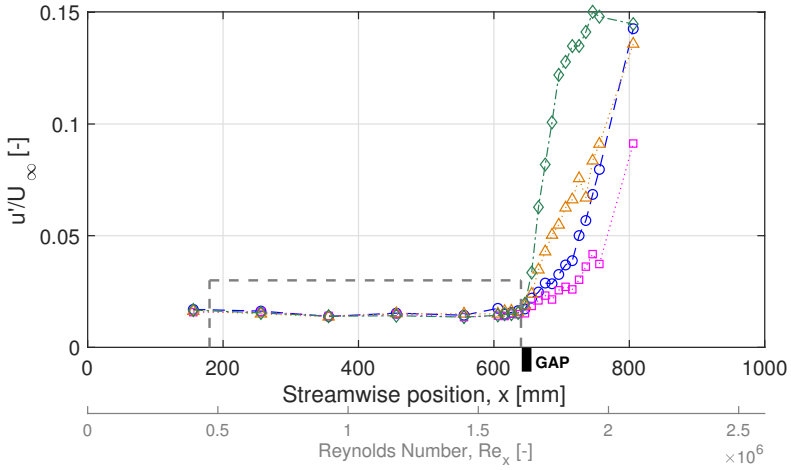

(c) GAP-15000µm-12mm ($b/h = 0.8$) (crit.).

Figure 8.2. Streamwise velocity fluctuations for different gaps ($x_{\mathrm{GAP}} = 640$ mm).

edges are relatively far apart, transition is triggered closer to the gap's leading edge, suggesting an immediate effect of the gap on the boundary layer stability.

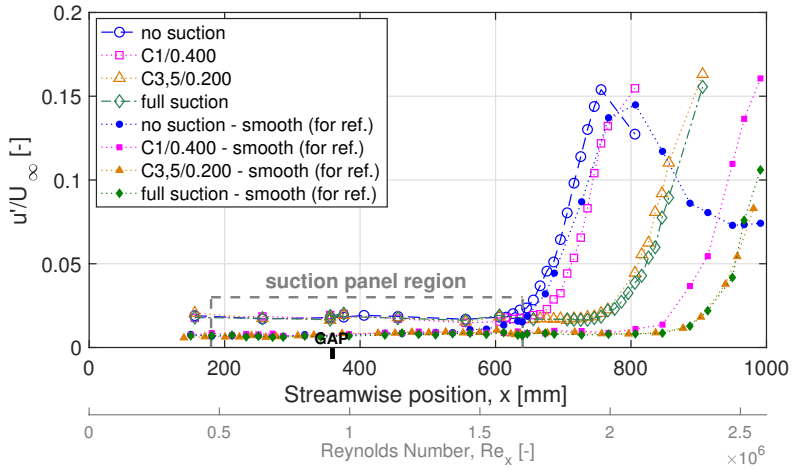

(a) GAP-1200µm-2.4mm ($b/h = 2$).

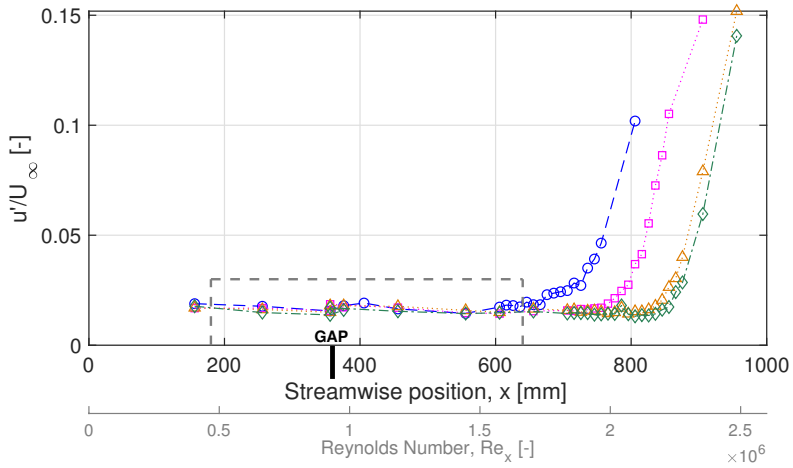

(b) GAP-15000µm-8mm ($b/h = 0.5$).

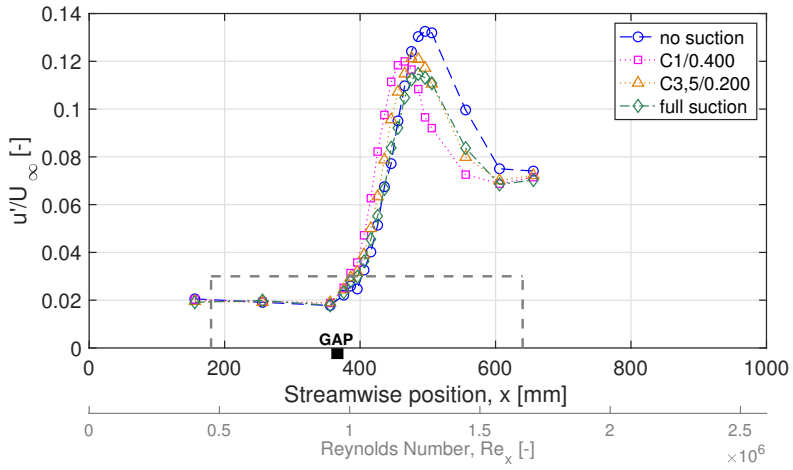

(c) GAP-1200µm-18mm ($b/h = 15$) (crit.).

Figure 8.3. Streamwise velocity fluctuations ($y = 300$ mm) for different gap dimensions for all suction configurations ($x_{\mathrm{GAP}} = 360$ mm).

Next the streamwise evolution of the mean velocity profiles for the critical case GAP-1200µm-20mm are shown in Figure 8.4. These profiles, one of which could be obtained inside the gap

due to its shallowness, can be taken to be representative of the flow in all shallow gaps region. Upstream of the gap, profiles for the *no suction* and C1/0.400 case overlap quite closely with each other and the Blasius profiles, while the *full suction* profile is still undergoing wall suction, and therefore is slightly fuller than the others.

Halfway inside the gap, all profiles are overlapped, regardless of the suction configuration, and a well-defined inflection point is present. The depth of the gap cross-section on the schematic and the size of the boundary layer profile graph were set to correspond in terms of the relative height. The inflection point is therefore approximately located at the altitude of the leading and trailing edges of the gap. This observation is consistent with those of previous surface defects where, as wire or FFS size was increased, so did the altitude of the inflection point in profiles affect by the local recirculation zones. Since the profile is equidistant from either the leading or trailing edges, the influence of the main edge is difficult to determine.

Finally, downstream of the gap, all suction configurations still have overlapping profiles that are starting to slightly deviate from the Blasius profile. This profile deformation is natural since the boundary layer is now at the beginning of the transition region.

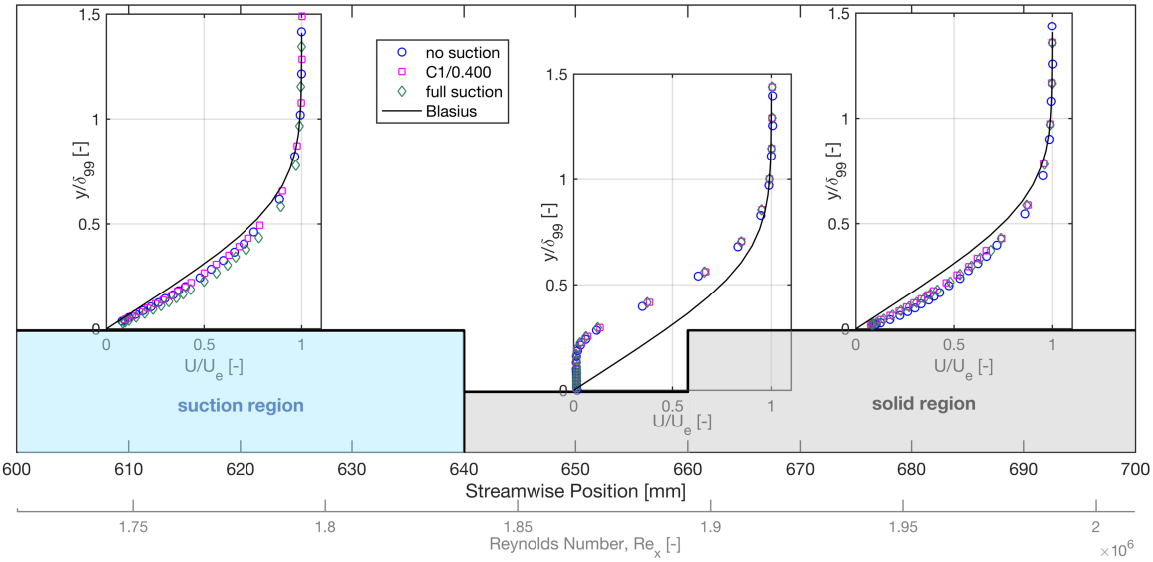

Figure 8.4. Evolution of the mean velocity profiles over critical gap GAP-1200 µm-20 mm ($x_{\mathrm{GAP}} = 640$ mm).

All transition positions for both gap locations are summarized in Figures 8.5 and 8.6, which is the same Δ_{xT} parameter mentioned in previous chapters but for the present gaps. As before, the Δ_{xT} parameter enables the comparison of all suction configurations and all gap positions. In Figure 8.6a, the Δ_{xT} parameter is graphed as a function of the b/h ratio (aspect ratio). Cases where Δ_{xT} is greater than one correspond to transition positions that are slightly downstream of the smooth case, but still within transition position measurement uncertainty. Although, once again, increasing the b/h generally moves the transition further upstream, this trend is not as obvious for deep (here, $b/h < 1$) or shallow gaps (here, $b/h > 12$). Some explanations for this lack of a definite trend at either extremes could include the fact that, as mentioned above, deep gaps can act as resonators and have complex flow patterns, while wide gaps could start behaving like a combination of a backward- and forward-facing step.

Furthermore, configurations with suction show much greater sensitivity to the gap's destabilizing effect compared to the *no suction* configuration for x_{GAP} at 360 mm. Suction distribution also has a significant influence, as shown by the spread in data points for a given b/h. For aspect ratios b/h values less than 10, the C1/0.400 configuration generally experiences the largest

reductions in laminar flow, especially when the gap is at x_{GAP} equal to 360 mm for the reasons mentioned above. Across both gap locations, C3,5/0.200 and *full suction* stay generally close together, further indicating that applying the same suction mass flow rate over all chambers or over C3 and C5 only is equivalent in most cases. Using Figure 8.6b, the width seems to be once again the main parameter driving all the above-mentioned observations, compared to the depth (Figure 8.6c).

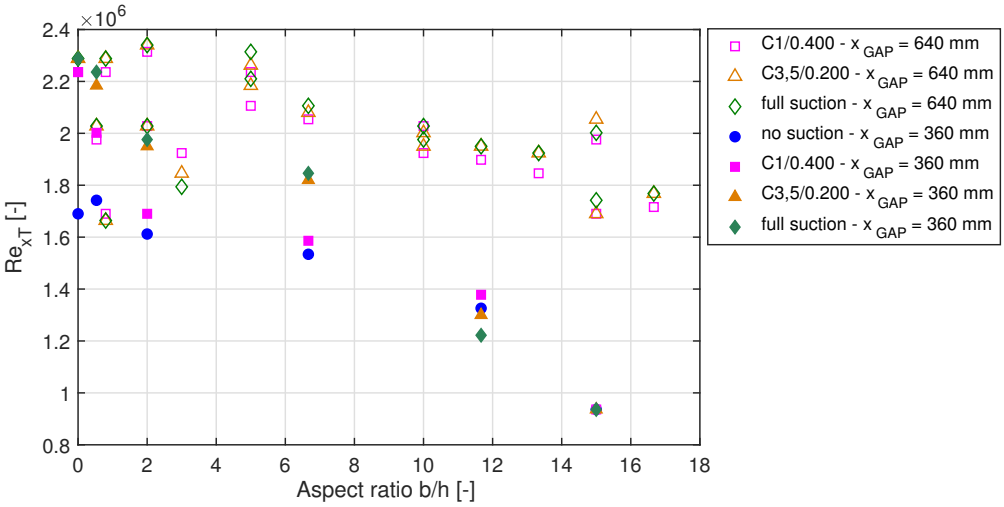

Figure 8.5. Re_{xT} as a function of b/h.

The few critical gap dimensions are reported on Figure 8.7 to be compared to data obtained in previous ONERA investigations (Olive and Blanchard 1982, Séraudie 2010, and Gentili 2012) based on which critical relative width ($b/\delta_1 \geq 18$) and height ($h/\delta_1 \geq 2$) dimensions were determined. The present critical gap data are consistent but fall just outside of the critical limits established in previous studies. A couple of explanations for these differences include: first, some of the investigations were performed on ONERA-D airfoils (i.e., with pressure gradients); and second, in all of these experiments, the gaps were introduced much further upstream from the smooth case transition position than in the present study.

8.3 Unsteady data analysis

The evolution of the transition mechanisms due to the introduction of a gap can further be investigated through spectral analysis of unsteady data to examine frequency amplification.

First, the effect of wall suction on a subcritical gap case, GAP-1200mu-8mm at x_{GAP} equal to 640 mm is verified, as shown by the PSD of the streamwise velocity fluctuations in Figure 8.8. Upstream of the gap (Figure 8.8a), the bulge ranging from 400 Hz to 800 Hz especially visible for the *no suction* configuration corresponds to the TS waves that amplified up to this point. Note that these instabilities are about to undergo transition, given that in the smooth *no suction* case, the transition position is approximately the same as the x_{GAP} position studied in this figure. The two configurations with suction have almost identical PSD and the frequencies in the range of the TS instabilities are strongly attenuated with respect to *no suction*.

Downstream of the gap, Figure 8.8b shows that TS instabilities experience significant amplification regardless of the suction configuration. However, since at this position, *no suction* already “naturally" transitioned, the suction configurations reveal more explicitly the fact that gaps tend to further amplify existing instabilities.

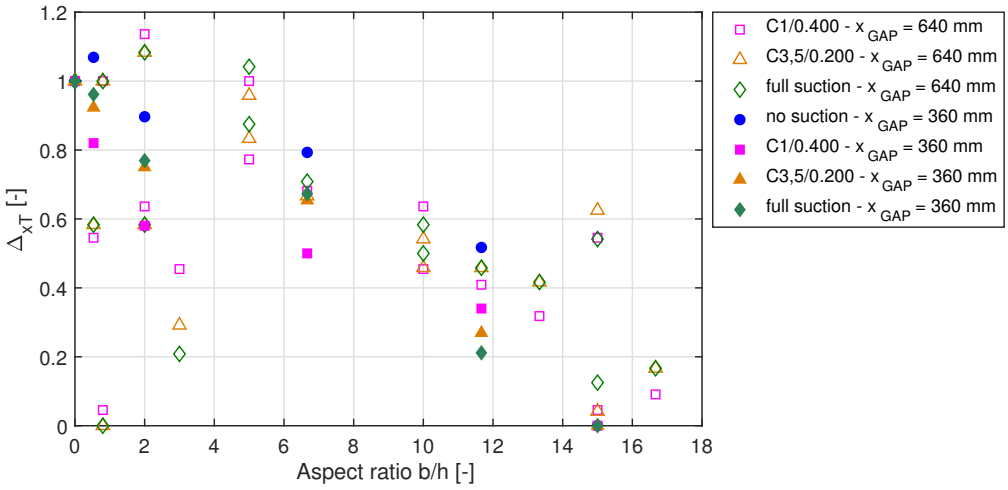

(a) Δ_{xT} as a function of b/h.

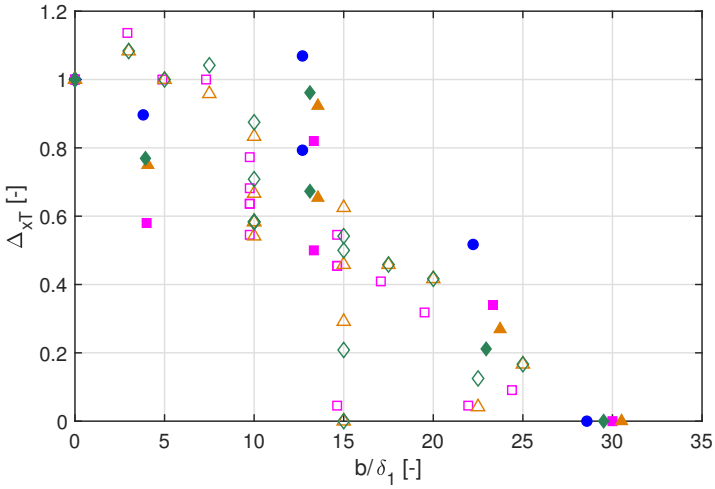

(b) Δ_{xT} as a function of b/δ_1.

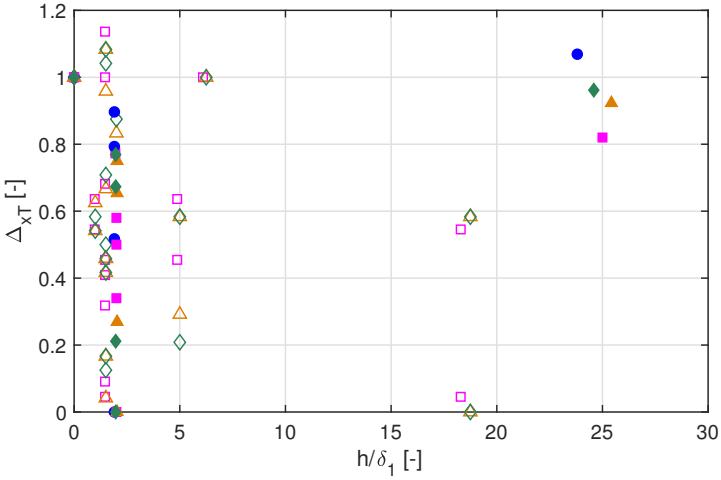

(c) Δ_{xT} as a function of h/δ_1.

Figure 8.6. Δ_{xT} vs different gap parameters.

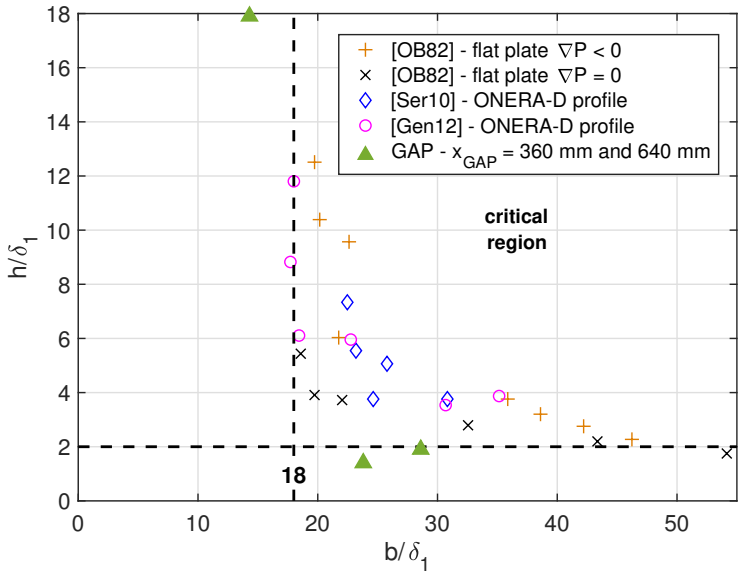

Figure 8.7. Comparison with experimental data from previous ONERA studies with existing critical limits.

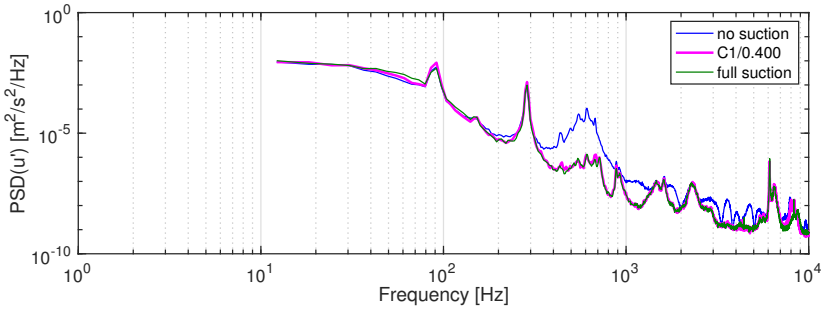

(a) $x = 610$ mm (Re_x ~$1.59{\cdot}10^6$).

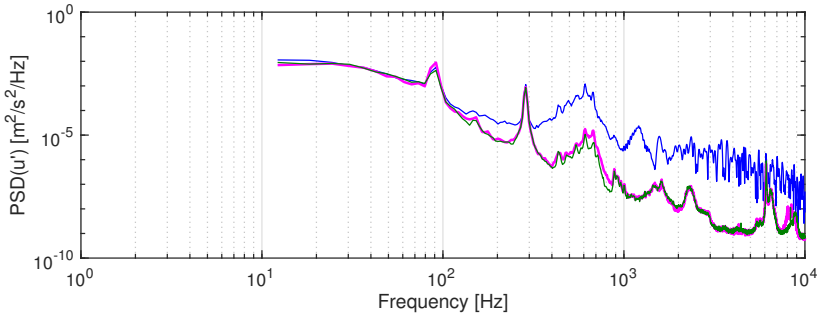

(b) $x = 660$ mm (Re_x ~$1.72{\cdot}10^6$).

Figure 8.8. PSD (probed at $y = 300$ µm from wall) of the streamwise velocity fluctuation upstream (a) and downstream (b) of the subcritical GAP-1200µm-8mm ($x_{\mathrm{GAP}} = 640$ mm) for all suction configurations.

A subcritical gap therefore does not change the transition mechanism but rather increases TS amplification below the threshold amplitude necessary to trigger immediate transition, as shown in Figure 8.9. On this graph, the PSD of u' at the respective transition positions of each suction configuration all exhibit a bulge at the TS instabilities, which cover the range of 400 Hz

to 800 Hz. Since suction is still effective in delaying transition, the transition Reynolds numbers for the suction configurations are greater than in the *no suction* case, and the TS instabilities covered enough streamwise distance to experience a slight shift towards lower frequencies. For the subcritical gap at x_{GAP} equal to 640 mm, the transition mechanism is therefore unchanged such that transition can still be delayed by wall suction.

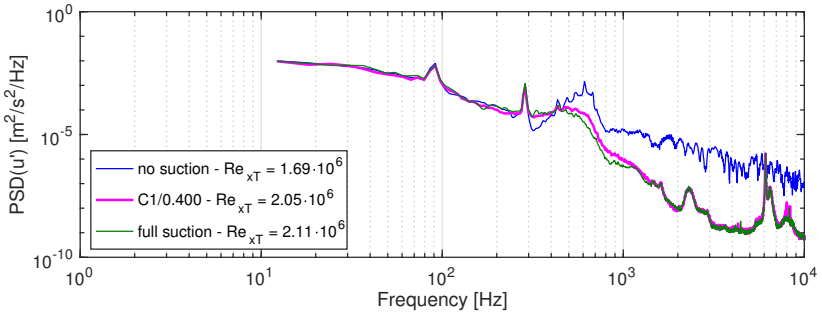

Figure 8.9. PSD(u') (y = 300 µm) at the transition position for subcritical GAP-1200µm-8mm (x_{GAP} = 640 mm) for all suction configurations.

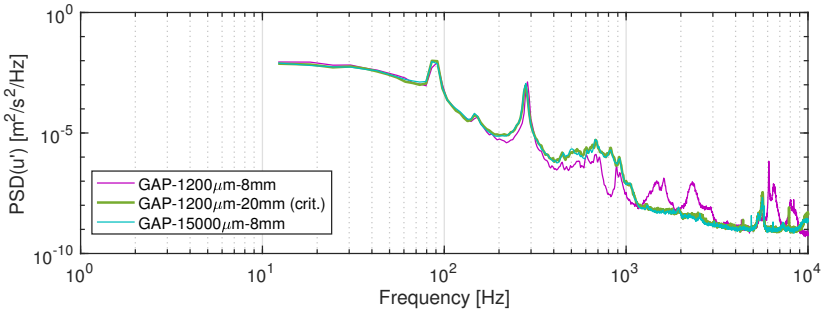

(a) x = 610 mm (Re_x ~1.59·10^6).

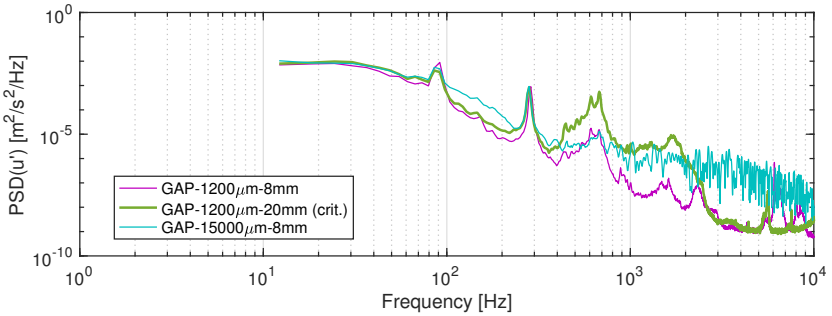

(b) x = 660 mm (Re_x ~1.72·10^6).

Figure 8.10. PSD(u') (at y = 300 µm) upstream (a) and downstream (b) of gaps at x_{GAP} = 640 mm for C1/0.400.

Next the PSD evolution upstream and downstream of gaps with various dimensions for the C1/0.400 configuration is shown in Figure 8.10. Two subcritical gaps, GAP-1200µm-8mm and GAP-15000µm-8mm, and one critical gap GAP-1200µm-20mm are presented. Upstream of the gaps (Figure 8.10a), the TS instabilities are visible by the bulge between frequencies ranging 400 Hz and 800 Hz. Most noticeable is the fact that subcritical GAP-15000µm-8mm and critical GAP-1200µm-20mm cases both seem to have an upstream influence on the boundary layer instabilities, since their frequencies are slightly more amplified than in the subcritical GAP-

1200µm-8mm case.

In Figure 8.10b downstream of the gaps, both subcritical gaps display relatively similar amplitudes over the frequency range of the TS instabilities. On the other hand, the critical gap GAP-1200µm-20mm exhibits two bulges of amplified frequencies. The main one still corresponds to the TS instabilities (ranging 400 Hz to 800 Hz), while the second is closer to the [1.5 kHz-2 kHz] range. This second frequency band is reminiscent of the high frequency bulge found in the PSD of critical wires due to the introduction of an inflection point in the mean velocity profile. Additionally, this high frequency bulge also seems to corresponds relatively well to the frequency that would be predicted based on the Strouhal number (approximately 0.8) found for critical gap instabilities studied by Forte et al. 2015.

As shown previously on Figure 8.4, the boundary layer profiles inside this critical GAP-1200µm-20mm case exhibit well-defined inflection points, which introduce the high frequency bulge, in addition to the existing TS instabilities. Downstream of the gap, transition still seems to be governed by TS waves because of their dominating amplitude; however, because of its initial strength inside the gap, the inflection-type instability is still present.

Finally, the PSD at the transition position are compared in Figure 8.11 for the three gaps at x_{GAP} equal to 640 mm. As expected, the TS instabilities bulge is present in all cases, while the critical case displays the additional high frequency bulge due to the inflection-type instability introduced inside the gap.

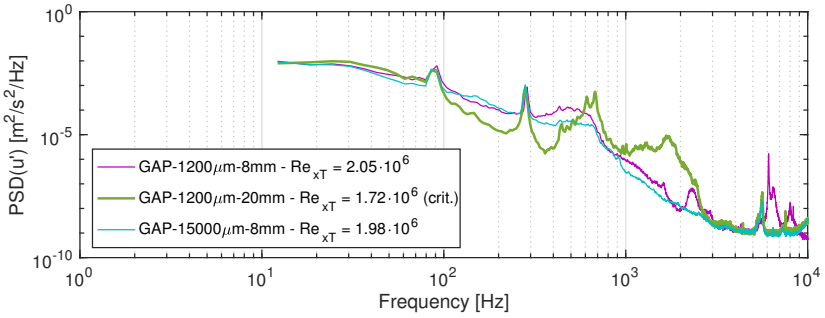

Figure 8.11. PSD(u') (y = 300 µm) at the transition position of different gaps at x_{GAP} = 640 mm for C1/0.400.

For the critical GAP-1200µm-18mm case located further upstream (x_{GAP} = 360 mm), the streamwise evolution of the PSD across the gap for all suction configurations is shown in Figure 8.12. At the gap's leading edge (Figure 8.12a), no visible difference between any of the suction configurations is noticeable: even in the *no suction* case, the TS instabilities have not yet started to amplify significantly. However, immediately downstream of the gap (Figure 8.12b), the second high frequency bulge is now clearly visible and completely overshadows the TS instabilities. In this scenario, since TS instabilities are not significantly amplified yet, transition could be the result of an inflection-point instability introduced inside the gap. Finally, 10 mm further downstream, Figure 8.12c shows how the broadband spectra is becoming similar to that of a turbulent flow.

Regardless of the suction configuration, and whether the gap is critical or not, transition is generally the result of the amplification of TS instabilities (when these instabilities are already significantly amplified). The streamwise evolution of u' profiles' evaluated over the frequencies ranging from 500 Hz to 540 Hz can therefore provide quantitative information about the instabilities' amplification. For both gap locations, profiles in a subcritical and critical case will be presented.

To further investigate the evolution of the TS instabilities, the u' profiles can be examined. Data were acquired for the subcritical GAP-1200µm-8mm at x_{GAP} equal to 640 mm and are

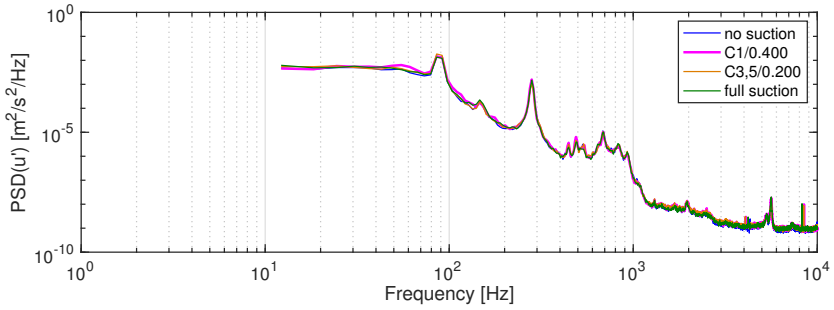

(a) x_T = 360 mm (Re_{xT} ~$9.36{\cdot}10^5$).

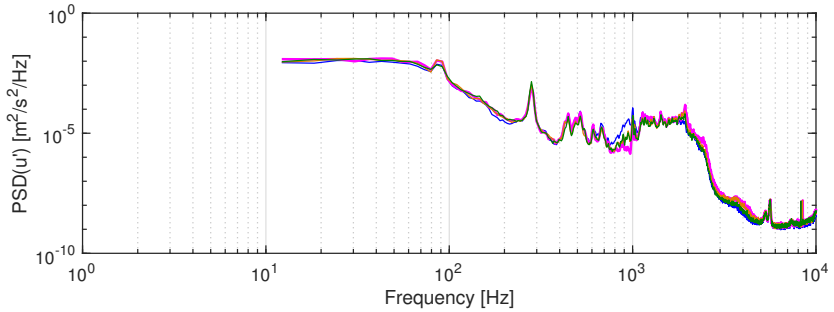

(b) x = 380 mm (Re_x ~$9.88{\cdot}10^5$).

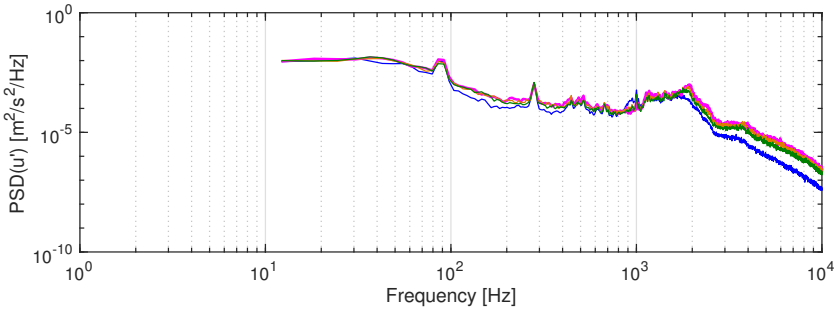

(c) x = 390 mm (Re_x ~$1.01{\cdot}10^6$).

Figure 8.12. PSD(u') (at y = 300 µm) downstream of critical GAP-1200µm-18mm (x_{GAP} = 360 mm) for all suction configurations.

shown in Figure 8.13. Upstream (Figure 8.13a) and downstream (Figure 8.13c) of the gap, all configurations with suction overlap relative closely, and have significantly lower amplitudes than the *no suction* configuration. In particular, *no suction* experiences greater amplification (approximately five-fold), as opposed to the cases with suction that have their amplitudes approximately tripled. Further downstream (Figure 8.13c), as expected, the C1/0.400 case starts to amplify more than either C3,5/0.200 or *full suction*. Note that at x equal to 750 mm, the suction configurations have amplitudes that are of the same order of magnitude as the *no suction* profile over x equal to 608 mm.

Similar profile evolution can be observed for the subcritical GAP-1200µm-2.4mm case, shown in Figure 8.14. Upstream (Figure 8.14a) and downstream (Figure 8.14b) of the gap, the profiles for all configurations with and without suction experience approximately the same increased amplification due to the gap.

Surprisingly, downstream of the gap, C3,5/0.200 and *full suction* are actually slightly more amplified than C1/0.400 and *no suction*. At these early positions, the stabilizing effect of suction is not immediately visible: C3,5/0.200 and *full suction* on Figure 8.14b could almost

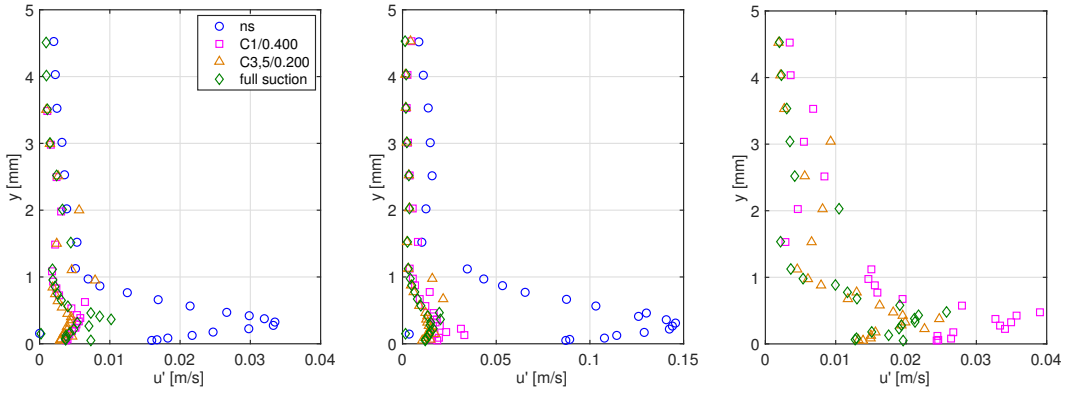

(a) $x = 608$ mm. **(b)** $x = 650$ mm. **(c)** $x = 750$ mm.

Figure 8.13. Evolution of *u'* profiles (evaluated over [500-540] Hz) between $x = 608$ mm and $x = 750$ mm for GAP-1200µm-8mm and all suction configurations ($x_{GAP} = 640$ mm).

be considered less effective at this stage. The explanation for this last effect is that the gap is located within chamber C4, and so the boundary layers that crossed the gap for cases C3,5/0.200 and *full suction* were slightly thinner due to the action of suction.

For all subsequent downstream positions, the overall benefits of suction and the familiar behaviors are then recovered: *no suction* starts amplifying faster than all other suction configurations; C1/0.400 is the first case with suction that starts to amplify; and finally, the C3,5/0.200 and *full suction* are always in the same order of magnitude, although the C3,5/0.200 case is slightly more amplified.

For both the critical cases of x_{GAP} at 640 (Figure 8.15) and 360 mm (Figure 8.16), although the upstream and downstream positions are not situated at exactly the same relative positions with respect to the gaps, the magnitude of all profiles changes increases tenfold, at the minimum. More particularly, for x_{GAP} equal to 640 mm, wall suction was able to effectively attenuate TS instabilities upstream of the gap, as shown on Figure 8.15a. Subsequently, downstream of the defect (Figure 8.15b), although transition has occurred for all configurations, the *no suction* case maintains its significantly greater maximum amplitude with respect to the cases with suction. This difference seems to confirm that gaps simply boost existing instabilities since despite their increased amplitudes, configurations with suction still have lower amplitudes than those without suction.

On the other hand, for the x_{GAP} equal to 360 mm, no significant differences between the profiles of any suction configuration are visible in Figure 8.16a, similar to Figure 8.14a. Surprisingly, downstream of the gap (Figure 8.16b), although all profiles have undergone critical amplifications, the C1/0.400 case has the larger maximum amplitude, whereas *no suction* has the lowest. Cases with suction therefore seem to be more destabilized by the critical gap. Similar to the subcritical case, boundary layers that have undergone suction have slightly reduced thicknesses and are therefore going over a slightly greater relative-sized gap.

All of these results are synthesized by the streamwise evolution of the *u'* profile maxima. Figure 8.17 compares the the maximum amplitudes for the subcritical and critical gaps located at x_{GAP} equal to 640 mm. Larger amplifications are visibly shown for the *no suction* configurations compared to the cases with suction, regardless of the gap dimension. For the gap located 360 mm from the leading edge (Figure 8.18), the “thinner boundary layer effect" is also clearly displayed, with the *no suction* case having the lowest amplitudes at the next one or two positions downstream of the gap. Further downstream for the subcritical case, suction recovers its effectively in delaying transition.

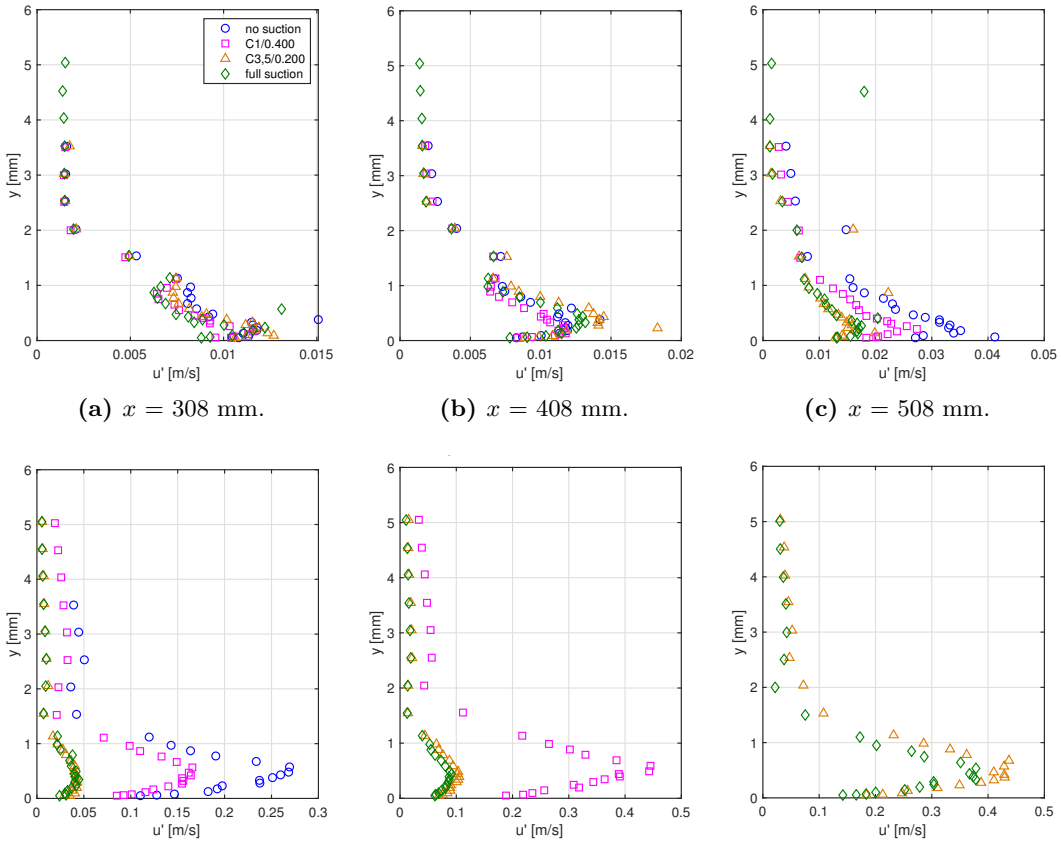

(a) $x = 308$ mm. **(b)** $x = 408$ mm. **(c)** $x = 508$ mm.

(d) $x = 650$ mm. **(e)** $x = 700$ mm. **(f)** $x = 800$ mm.

Figure 8.14. Evolution of u' profiles (evaluated over [500-540] Hz) between $x = 308$ mm and $x = 408$ mm for GAP-1200µm-2.4mm and all suction configurations ($x_{\mathrm{GAP}} = 360$ mm).

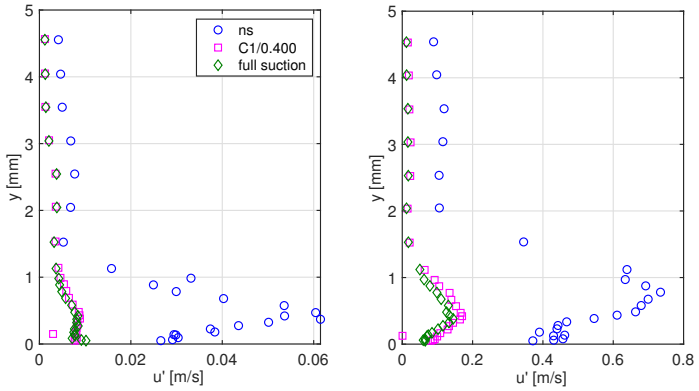

(a) $x = 608$ mm. **(b)** $x = 675$ mm.

Figure 8.15. Evolution of u' profiles (evaluated over [500-540] Hz) between $x = 608$ mm and $x = 675$ mm for critical GAP-1200µm-20mm and all suction configurations ($x_{\mathrm{GAP}} = 640$ mm).

Finally, a comparison of the u' profile maxima for all four gap dimensions discussed above is presented for the C1/0.400 configuration in Figure 8.19. Interestingly, the subcritical case for x_{GAP} equal to 360 mm has a comparable evolution with the critical case with x_{GAP} equal to

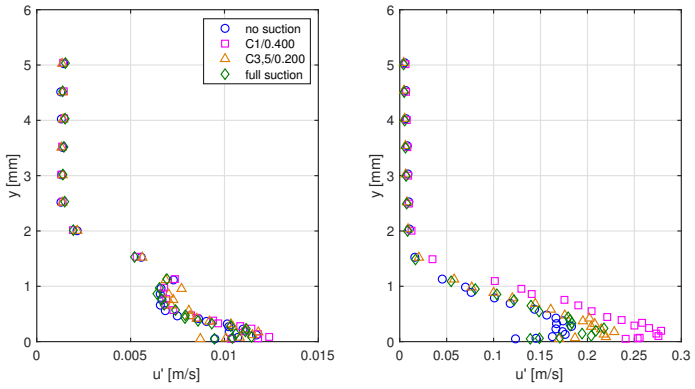

(a) $x = 308$ mm. **(b)** $x = 408$ mm.

Figure 8.16. Evolution of u' profiles (evaluated over [500-540] Hz) between $x = 308$ mm and $x = 408$ mm for critical GAP-1200µm-18mm and all suction configurations ($x_{GAP} = 360$ mm).

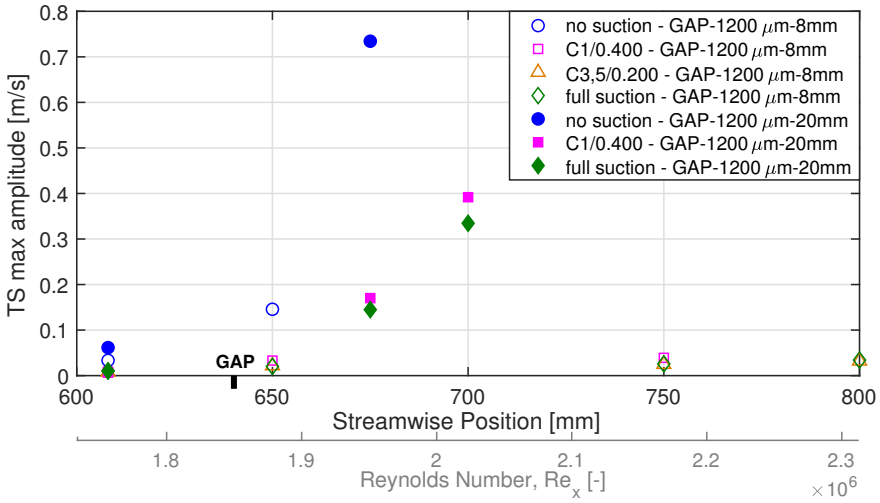

Figure 8.17. Evolution of the TS profiles (evaluated over [592-632] Hz) maximum for a subcritical (open symbols) and critical (full symbols) gap and all suction configurations ($x_{GAP} = 640$ mm).

640, although the latter case is much steeper slope than the former.

8.4 Numerical analysis and comparison with an existing model

Using the same procedure as for FFS, the ΔN value for all gap dimensions were evaluated using LST calculations and are reported on Figure 8.20. Similar to FFS, configurations with suction seem to be more sensitive (i.e., have larger ΔN values) than the *no suction* configuration. Since in most cases, gaps tended to further amplify the existing TS instabilities, the stabilizing suction is therefore in direct competition with the destabilizing defects.

In addition to the experimental data from the present study, ΔN models developed by Perraud et al. 2014 are reported for both gaps locations and are labeled as [PAK14] on Figure

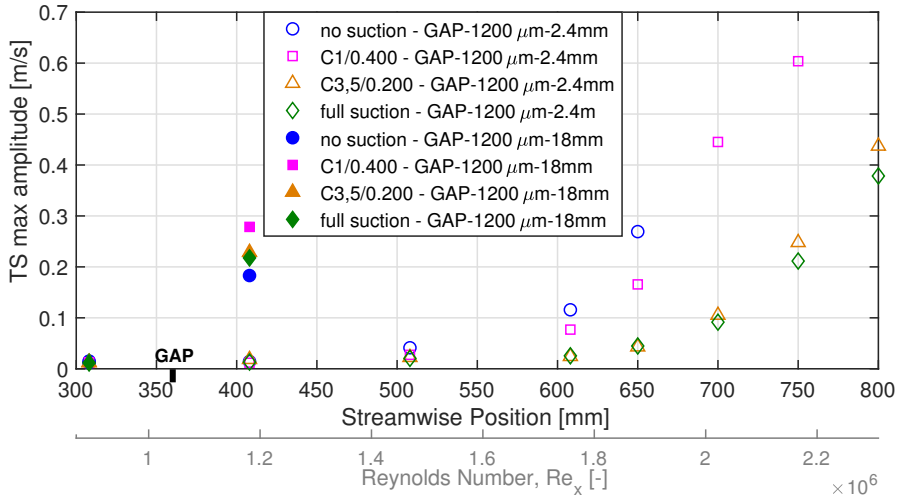

Figure 8.18. Evolution of the TS profiles (evaluated over [500-540] Hz) maximum for a subcritical (open symbols) and critical (full symbols) gap and all suction configurations (x_{GAP} = 360 mm).

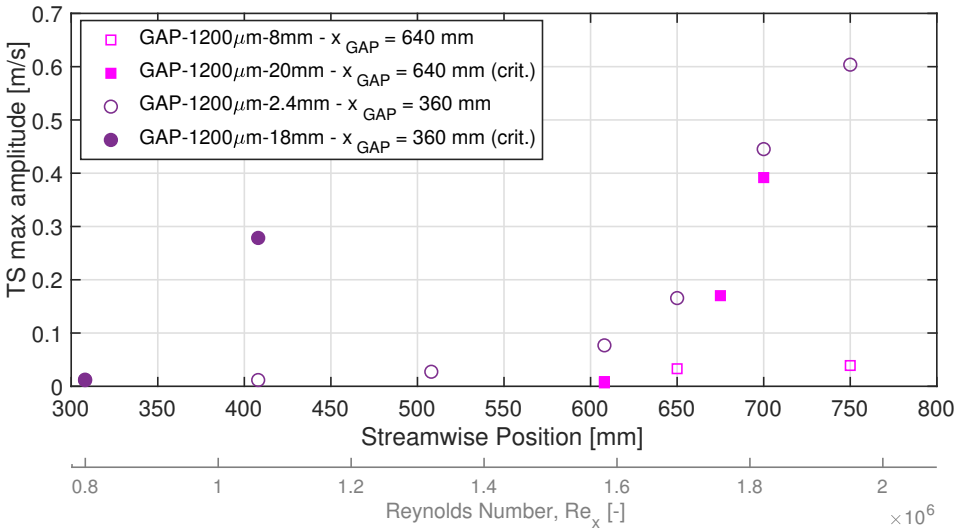

Figure 8.19. Comparison of the *u'* profile (evaluated over [500-540] Hz) maxima for subcritical (open symbols) and critical (full symbols) gap at both gap locations for C1/0.400.

8.21. As a reminder the model used is:

$$\Delta N = 8.6 \cdot 10^{-3} \frac{Re_b}{Re_{\theta,GAP}} + 3.5 \cdot 10^{-5} Re_b - 2.4 \cdot 10^{-3} Re_{\theta,GAP} + 2.244. \tag{8.1}$$

Based on this equation, the ΔN values depend on the absolute gap width, the local boundary layer thickness ($Re_{\theta,GAP}$), and the relative gap width ($Re_b/Re_{\theta,GAP}$). Figure 8.21, showing the ΔN evolution as a function of the relative width b/δ_1, indicates strong disagreement between the model and the experimental data. One particular issue with the model is that its validity is questionable for low values of b/δ_1, since even in the absence of a defect, the resulting ΔN is sometimes non-zero. The model and the experimental data also disagree in the general slope of each data set. One explanation could be related to the fact that, especially in the x_{GAP} equal to 640 mm, the instabilities could be reaching amplification levels that are close to or at the level where non-linear instabilities start to appear. Since the model was based on Laminar

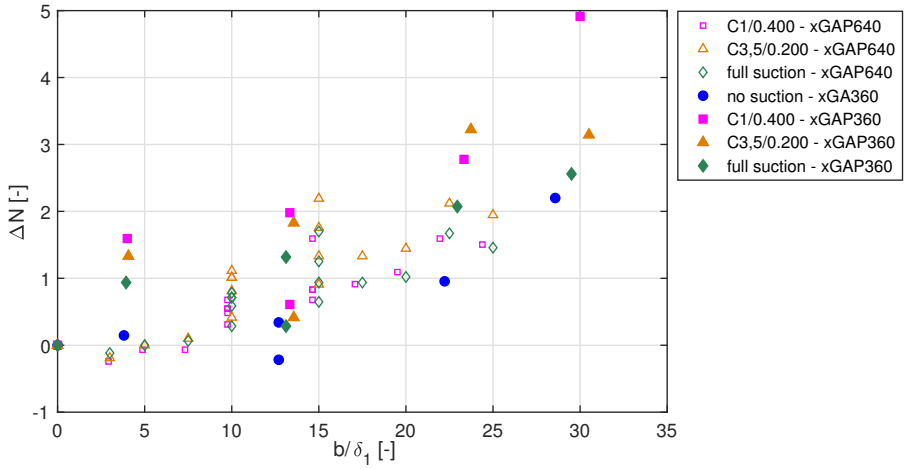

Figure 8.20. ΔN values evaluated for all suction configurations and gap dimensions.

Navier-Stokes calculations, the assumptions in the calculations might not be valid for the gaps tested in this configuration.

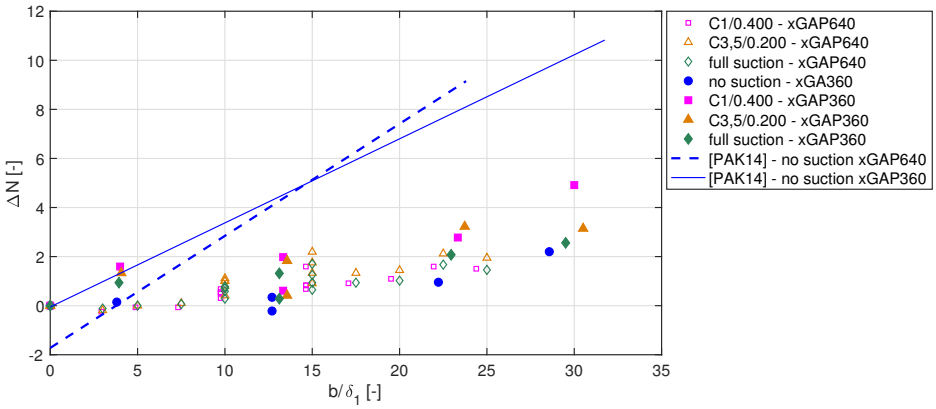

Figure 8.21. All suction configurations with gaps compared with ΔN model for gaps from Perraud et al. 2014.

Summary

Similar to the case of both wires and FFS, wall suction was able to reduce the destabilizing effect of a subcritical gap and delay transition with respect to the configuration without suction. However, once again, wall suction was unable to prevent or delay the effect of a critical gap once its dimensions of relative depth and relative width were greater than h/δ_1 ~1.4 and h/δ_1 ~14 respectively (compared to h/δ_1 ~0.4 for wires and h/δ_1 ~1.3 for FFS). The transition mechanisms induced by a gap include both further amplification of existing TS instabilities, as well as a inflection-point instability introduced inside the gap itself, which compete depending on the level of amplification of the TS instabilities at the gap location.

All three types of surface defects that were tested were individually presented. The following chapter will summarize and compare the findings of all defects with respect to each other.

Chapter 9

Comparison of the effects of all surface defects combined with suction

Contents

9.1 Transition criteria 135
9.2 Transition mechanisms 136

Since, in the three previous chapter, surface defects were discussed individually, the purpose of the present chapter is to provide a summary compilation to compare the effects of all surface defects on the transition of a boundary layer with suction. The difference between the critical dimensions of the different defects is first discussed (Section 9.1). Attempts to provide explanations for these differences in terms of the defect's influence on the transition mechanisms are then presented (Section 9.2).

9.1 Transition criteria

First, the evolution of the Δ_{xT} parameter for wires and FFS is compared, since the relevant dimension, h/δ_1, is the same for both defects. Figure 9.1 shows the all data for wires and FFS, with no details on the panel or suction configurations to allow only the effect from the surface defect type to emerge. The first main different is that the critical wire h/δ_1 has much lower dimension ($\sim$0.4) than that of the critical FFS ($\sim$1.3). Wires with a given relative height can therefore have a much more destabilizing effect on the boundary layer than an equivalent-height FFS. This observation made for porous panels in particular was also verified through various previous studies on solid walls.

The reduced range of subcritical wires makes the development of a ΔN model less advantageous as opposed to defining a "universal" criterion above which transition occurs at the wire location. On the other hand, FFS have a much wider range of subcritical h/δ_1 that gradually move the transition position further upstream, up to the defect position. In this case, a ΔN model is justified, as confirmed by the various existing models.

Next, Figure 9.2 provides more details on the data sets, showing that no significant difference can be established either based on the suction configuration or panel. This lack of difference is consistent with the findings from the previous chapters: for subcritical wires and FFS, the transition mechanisms are unchanged. Since in these cases, TS instabilities are still responsible for the onset of transition, wall suction can still be effective, despite the local reduction in boundary layer thickness induced (and thus the local increase in the relative h/δ_1).

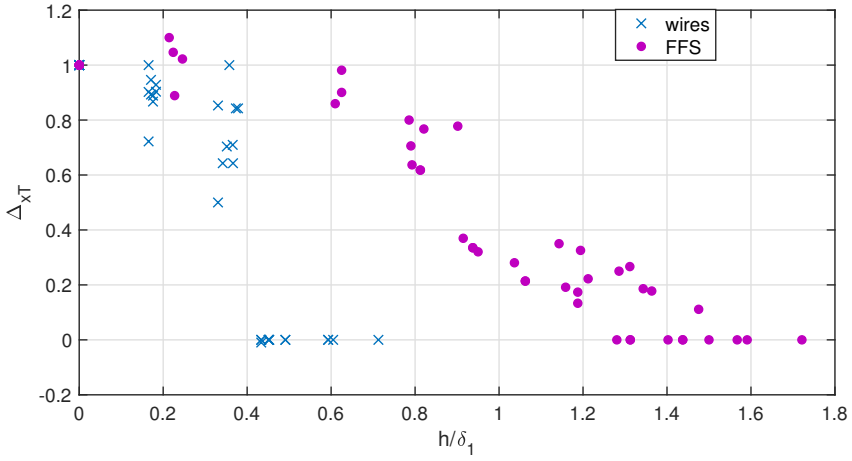

Figure 9.1. Comparison of the Δ_{xT} parameter for all wires and FFS tests (including all panels and suction configurations without detail).

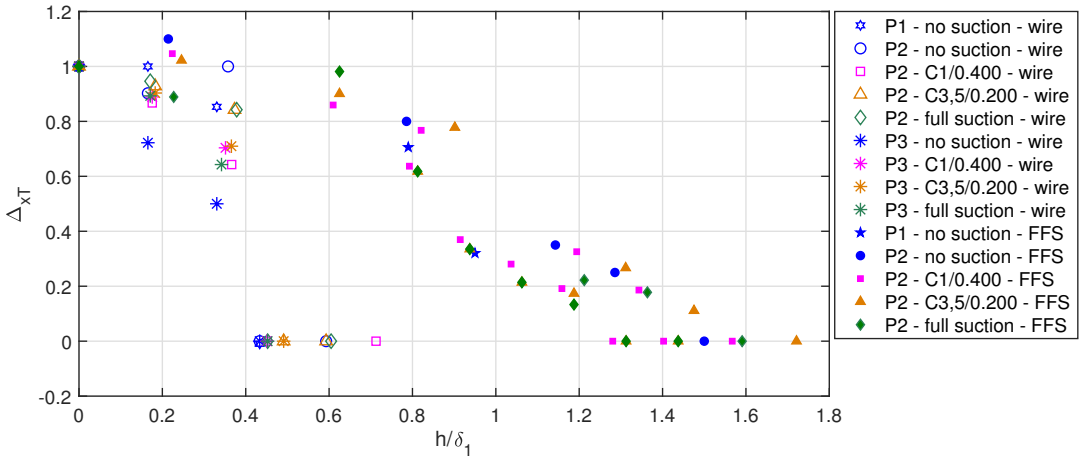

Figure 9.2. Comparison of the Δ_{xT} parameter for all wires and FFS tests (including all panels and suction configurations with detail).

Since gaps have two geometric dimensions (width b, and depth h), and therefore three relevant parameters (b/δ_1, h/δ_1, and b/h), their corresponding data could not be included properly in the previous graphs. However, as a reminder, the gap criteria developed by Olive and Blanchard 1982 were equal to $(h/\delta_1)_{crit} \geq 2$ and $(b/\delta_1)_{crit} \geq 18$ and were of the same order for data from the present study ($(h/\delta_1)_{crit} \geq 1.4$ and $(b/\delta_1)_{crit} \geq 14$). Compared to wires and FFS, gaps have the largest critical dimensions with respect to the boundary layer displacement thickness.

However, when comparing the y-coordinate dimensions (i.e., the relative height for wires and FFS, and the relative depth for gaps), gaps and FFS from the present study have critical dimensions that are closer to each other than to those of wires. The determining factor to explain this difference could be related to the effect of each defect on the transition mechanism.

9.2 Transition mechanisms

For any subcritical surface defect, transition is the result of the amplification of TS instabilities, as shown for example for the *full suction* configuration on Figure 9.3. On this graph, the PSD of *u'* (taken slightly upstream of the transition position) for the subcritical cases WIR-300µm-

640, FFS-850µm-640 and GAP-1200µ-8mm all display the familiar bulge between frequencies 400 Hz and 800 Hz that is characteristic of the TS instabilities in this study. The slight shift between the bulges for the wire and FFS and that of the gap is most probably related to the fact that the flat plate model had to be removed from the test section to machine the gap inserts. Although great care was taken to ensure that the model was remounted as closely as possible to its initial position, some slight difference could remain and result in the shift in the TS instabilities' frequencies. This shift, however, does not modify the conclusion that, regardless of the subcritical defect, the transition mechanism is unchanged and subcritical defects enhance the amplification of existing TS instabilities inside the boundary layer.

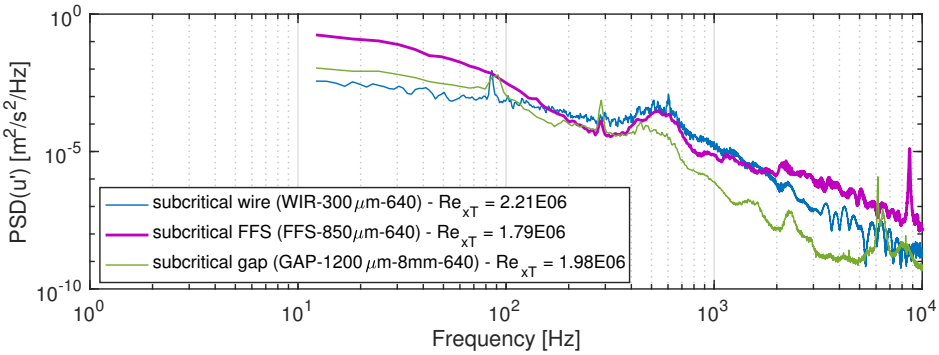

Figure 9.3. PSD of streamwise velocity fluctuations *u'* (probed at $y = 300\mu m$ from wall) at the transition Reynolds number for selected subcritical defects for *full suction*.

Once the respective critical thresholds are reached (namely, h/δ_1 >0.4 for wires, h/δ_1 >1.3 for FFS and h/δ_1 >1.4 and b/δ_1 >14 for gaps), the PSD of *u'* for each surface defect exhibit their particularities, as shown in Figure 9.4, once again on the *full suction* configuration. The critical wire shifts the transition mechanism from being driven by TS instabilities to being the result of the introduction of an inflection point in the mean velocity profile. On the other hand, the critical FFS simply increases the TS amplification past the threshold to trigger transition at the step location. And finally, the critical gap GAP-1200µm-20mm seems to have a hybrid effect by increasing the TS amplification as well as amplifying some high frequencies because of an inflection point introduced in the boundary layer profile inside the gap. For gaps located sufficient downstream to have TS instabilities that are significantly amplified compared to the high frequency inflection-point instability, the transition mechanism is still driven by the TS waves. However, for gaps located closer to the leading edge, the low amplitude TS instabilities and the inflection-point instabilities start to compete: in this case, no transition mechanism can systematically be selected.

The reason that FFS and gaps have similar critical dimensions in the y-coordinate could therefore be related to the fact that both types of defects act on the boundary layer transition by increasing the amplification of the already-existing TS instabilities, rather than changing the transition mechanism like wires. Since their effect is similar, the critical dimensions are also in the same order of magnitude. Additionally, because in these cases the transition mechanism remains unchanged, when subcritical FFS or gaps are introduced, wall suction can still delay transition up to the critical point, although with somewhat reduced effectiveness. This gradual decrease in effectiveness can be capture through ΔN models.

The wire, on the other hand, is the most dangerous defect (i.e., has the lowest critical dimension) out of the three that were tested. This difference is justified by that fact that a critical wire introduces a significant inflection point in the boundary layer profile located immediately downstream of the defect. As opposed to the gap, where the profile with an inflection point is contained within the gap itself, the distorted profile downstream of a critical wire is free to

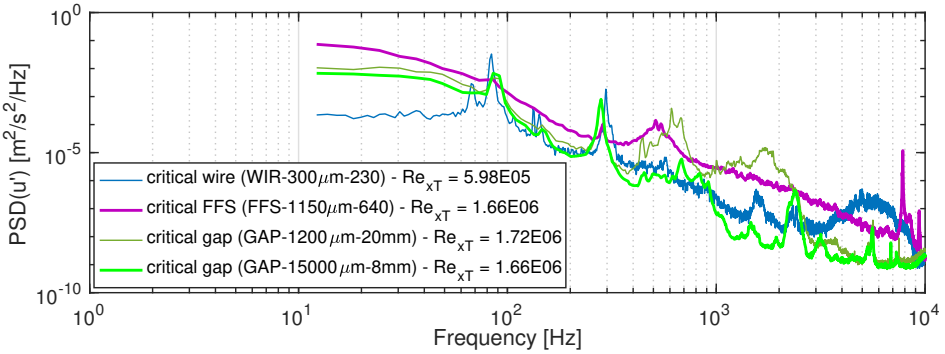

Figure 9.4. PSD(u') ($y = 300\mu m$) at the transition Reynolds number for selected critical defects for *full suction*.

continue its development. With the introduction of an inflection point so high in the boundary layer that the transition mechanism changes to an inviscid inflection-type instability, transition then rapidly occurs downstream of the wire. In the presence of subcritical wires, wall suction can still delay transition; however, the extent of subcritical dimensions where the transition position moves gradually upstream is so restricted that developing a ΔN model is less advantageous than developing a single criterion above which transition occurs are the wire position.

Despite the differences between wires on one side, and FFS and gaps on the other, suction can still delay transition in the presence of subcritical defects of any type, albeit less effectively than in the smooth case. Wall suction therefore offers some robustness when competing against the destabilizing effects of a subcritical defect but cannot delay or prevent the critical defect threshold determined for cases without suction. For subcritical defects, the benefits from slightly increasing the profile curvature and attenuating TS amplification thus mainly outweigh the locally-reduced boundary layer thickness (and consequently increased relative defect dimensions) as a result of suction.

Conclusion

Summary

An experimental investigation was designed and performed to study the effects of surface defects on the laminar-turbulent transition of a boundary layer undergoing wall suction. The first objective was to further understand the competing effects of the stabilizing wall suction coupled to destabilizing surface defects that are likely to occur, for example at the junction between suction and solid panels. The second objective was to provide critical surface defect dimensions that could be used as tolerances for surfaces intended to include laminar flow technology.

First, an experimental protocol was developed and implemented to ensure that the aerodynamic conditions in the facility were adequate to perform a laminar-turbulent transition investigation. The wind tunnel facility used presently was originally designed for transition studies, and, in particular, was already equipped with a noise-reduction chamber located between the test section and the downstream driving fan to minimize any upstream-travelling perturbations from the latter. The flat plate, which was also designed for a previous study, was designed with a numerically-optimized leading edge to minimize the extent and maximum value of the suction peak. These two elements provided a valuable basis for any subsequent transition experiment.

Next, the aerodynamic quality of the flow in the test section was characterized by measuring the freestream pressure fluctuations and turbulence levels. Spectra of the pressure fluctuations across all tested velocities did not display peaks greater than 90 dB. Additionally, the maximum turbulence level, evaluated at the maximum (and nominal) freestream velocity over the range [3 Hz - 10 kHz], remained below 0.18%, both with and without the flat plate mounted in the test section. These two verifications ensured that perturbations inside the test section were low enough to ensure an extended region of a laminar boundary layer over the flat plate and thus perform a study on a TS wave transition scenario study properly.

A two-dimensional incompressible flow was chosen for the basis of this study to reproduce as closely as possible a Blasius boundary layer. The flat plate and flap angles of attack were therefore set to establish, within the limits of experimentation, a zero pressure gradient flow over the flat region of the plate. Both the pressure coefficient and the experimentally-evaluated boundary layer shape factor were used to validate this first condition. The two-dimensionality of the flow was then validated by checking that the transition position remained constant at various spanwise positions. Finally, verification that transition was indeed the result of the amplification of TS instabilities was performed by comparing the experimental profiles of the streamwise velocity fluctuations u' to the eigenfunction calculated using Linear Stability Theory (LST) at the corresponding frequency. Measurement uncertainty was also evaluated for the main parameters of interest (boundary layer profiles, pressure coefficient, and transition position).

The following step involved establishing reference conditions for the smooth case with suction. In the course of these experiments, the effect of a porous wall without suction on boundary layer transition was determined and further investigated, both experimentally and numerically. After verifying that this effect was not due to the distributed roughness from the perforations, the panel with the largest porosity and hole diameters (panel P3) was found to destabilize the boundary layer more compared to the panel with lower porosity and hole diameters (panel P2). (The dominant effect between porosity and hole diameter could not be determined because of only two porous panels were available.) Using a numerical model originally developed for acoustic liners, this destabilizing effect was reproduced relatively well by implementing impedance boundary conditions at the wall when performing LST calculations. The first main contribution from this dissertation is therefore the experimental validation that a porous wall can affect boundary layer stability, through a wall impedance effect.

The two porous panels were then tested with suction. For the chosen suction flow rate and distribution, the transition on panel P2 was effectively delayed with respect to that of solid panel P1; however, panel P3 with suction actually transitioned at an earlier position than the solid wall panel P1. These results demonstrated that for a given suction distribution and flow rate (which could be limited by the suction system performance), the suction panel should be carefully designed to prevent its potentially destabilizing effects from cancelling any benefits from wall suction. Numerically, the combination of the wall impedance effect and suction could not be properly reproduced so further work will be necessary.

For the reference smooth case, the suction mass flow rate was kept constant at 0.4 $g.s^{-1}$ and three suction distributions were chosen: C1/0.400 (over chamber C1 only), C3,5/0.200 (divided between chambers C3 and C5) and *full suction* (distributed over the entire suction region). In addition to these distributions, the case without suction, labelled *no suction*, was also always acquired to provide a baseline case.

Wall suction was therefore found to always delay transition with respect to the *no suction* configuration. By locally changing the mean velocity profile curvature, suction increased the boundary layer stability and TS instabilities were less amplified. Suction distribution was also a parameter of influence: although configurations C3,5/0.200 and *full suction* transitioned at the same position, C1/0.400 transitioned earlier. This difference could, in part, be explained by the fact that C1/0.400 could not properly stabilize the TS instabilities that tended to develop further downstream from chamber C1. Instead, C1/0.400 mainly stabilized high frequency instabilities, which were eventually naturally attenuated, even in the *no suction* configuration. Suction concentrated over chamber C1 is therefore only applied upstream of branch I of the "dangerous" TS frequencies responsible for transition. On the other hand, C3,5/0.200 and *full suction* acted at the proper positions in the boundary layer development to effectively attenuate the most relevant TS instabilities. In this case, both suction configurations actually delayed transition down to the same downstream location.

Subsequently, three types of surface defects were introduced on the flat plate to investigate their effect, coupled with wall suction, on boundary layer transition. For all three types of defects, wall suction was unable to modify the critical defect dimensions: regardless of the suction distribution (including the *no suction* configuration), the critical thresholds were the same. The local change in boundary layer thickness, induced by suction, was therefore not significant enough to influence the transition criteria. However, in the presence of subcritical defects, suction still delayed transition, although less effectively than in the smooth case. Wall suction therefore exhibited some robustness in the presence of subcritical defects, demonstrating that the benefits of slightly increasing the profile curvature to attenuate TS instabilities can overcome

the increased amplification due to the presence of a defect. Despite all these similarities, several particularities were still observed between the different defects.

For wires, the critical relative height h/δ_1 was determined to be approximately 0.4. For subcritical wires, transition is still driven by TS instabilities, but because of the restricted subcritical range, a ΔN model is not as justified as defining a simple transition criteria. The particularity of wires resides in the fact that, once the critical wire height was reached, a significant inflection point was introduced relatively high in the downstream mean velocity profile. Since the boundary layer can freely develop past this point, the transition mechanism switched to being an inflection point instability, and transition occurred immediately downstream of the defect.

Overall, forward-facing steps and gaps had a similar effect on transition. The critical h/δ_1 for FFS was approximately 1.3 while the conjunct criteria for gaps was approximately 1.4 for the relative depth h/δ_1 and 14 for the relative width b/δ_1. For critical FFS, the transition mechanism was entirely governed by TS instabilities: the critical step increased the amplification of the existing TS waves past the critical threshold, after which transition was triggered. On the other hand, when inspecting the PSD of the streamwise velocity fluctuations *u'*, critical gaps seemed to combine both TS instabilities (with a bulge over the typical frequencies ranging from 400 Hz to 1 kHz) and inflection point instabilities (with frequencies closer to 2 kHz). Despite these indications, the TS waves had larger amplitudes than the inflection point instabilities: transition for a critical gap was thus determined to still be governed by the amplification of TS instabilities, similar to critical FFS.

Although unable to prevent or delay the critical dimensions of any defect, wall suction still proved to be an effective laminar flow control technology in the presence of subcritical defects. As manufacturing and assembly of aerodynamics surface improve, the resulting reduced tolerances on surface defects could become a significant argument in favor of implementing wall suction on commercial aircraft.

Recommendations for future work

The present investigation provided an analysis, along with an experimental database, on the competing effects of wall suction combined with three types of surface defects on the laminar-turbulent transition of a boundary layer in two-dimensional incompressible flow. Several recommendations for future work can therefore be suggested to widen the scope of this study, either experimentally or numerically.

“More experiments" is the obvious and tempting suggestion for future work. Being keenly aware of the infinite possibilities given an interesting topic and good funds as well as of the limited time in an experimentalist's day, my intention is to suggest only a few experiments that I consider most valuable, as well as offer some recommendations for future transition experiments.

In the direct continuation of the present study, widening the test matrix for critical gaps is necessary to enable further comparison with the transition criteria that were previously established without suction. Testing backward-facing steps would also provide a missing piece in the puzzle. Similarity between gaps and FFS were established (in particular the larger transition criteria), in part because both types of defect contain their effects on the boundary layer in a relatively restricted region around the defect itself. Determining a potential similarity between BFS and wires could enable categorizing defects in a more relevant manner. Additionally, BFS are a common type of defect that can be found on aerodynamic surfaces: consequently, determining their critical heights, along with the freestream turbulence level of the flow in which the test was performed, could provide relevant information to define a proper transition criteria.

Next, additional work should be performed on the effect of impedance on transition, both with and without suction. Experimentally, suction panels with identical porosities but varying hole diameters and *vice versa* could be tested to determine which, between porosity or hole diameter, has the dominant effect. Improving the numerical model to reproduce the effect of impedance on a boundary layer with wall suction is also necessary. The lack of numerical models that can reliably predict the effects of wall suction is a significant obstacle to the more widespread implementation of this technology. Having a model that includes the effect of impedance could therefore improve prediction accuracy and promote the use of wall suction as a viable drag reduction technology.

Another suggestion pertaining to expanding the scope of the present study would be to reproduce a similar experiment as presented here but on an airfoil or wing section, where three-dimensional instabilities, such as crossflow instabilities that are extremely sensitive to surface finish, would participate in the transition process. Testing higher Reynolds number and Mach number would also enable to determine the influence of compressibility. In this more complex environment, verifying that wall suction can still effectively delay transition in the presence of any subcritical surface defect would provide surface tolerancing information and further arguments in favor of its implementation on commercial aircraft.

Finally, the last, and more general, suggestion for additional work is to pursue feasibility studies on the integration and maintenance of an aerodynamic surface with wall suction. The effectiveness of suction in delaying transition was proven for many decades, and experiments and numerical models have greatly improved during this time frame, providing strong arguments in favor of wall suction. However, the fundamental issues of determining how and where to install a suction system and how to maintain porous panels unclogged are still major issues that need to be addressed before aircraft manufacturers will be likely to implement this technology at a full industrial scale.

The final two recommendations presented below could also be interpreted as a retrospective wishlist.

First, the clear difference in the critical FFS relative height between data from the present study and from Wang and Gaster 2005 seem to indicate that the h/δ_1 parameter is not sufficient to define a universal transition criteria. An attempt to include information about the flow's transition criteria was made with the proposed $h/\delta_1 * Tu^2$ parameter, but its validity is questionable considering its limited physical meaning and its basis on two data sets. The first recommendation is therefore to explicitly include the Tu, along with the frequency range used for its evaluation, in all future reports of transition studies on surface defects. This additional information could contribute in determining whether or not a unique universal step transition criteria is conceivable.

The second recommendation would be to try to design experiments that include a two-dimensional (at minimum) measurement technique or flow visualization. “A picture is worth a thousand words" could here be translated as “A 2D measurement is not necessarily equivalent (in terms of information) to a thousand single data points but it sure gives a better idea of what is going on." For example, in the particular case of the present study, the flow's two-dimensionality was considered a *sine qua non* condition to allow any further experiments. If flow visualization, such as that provided by infra-red thermography, could have been implemented, a much more immediate sense of the disturbances preventing two-dimensionality could have been established and troubleshooting could have been facilitated.

Part IV

Appendices

Appendix A

Flat plate leading edge geometry

In this appendix, the coordinates of the flat plate's leadgin edge geometry are provided. The leading edge shape that was numerically optimized to minimize any suction peak on the working (upper) side, where measurements are acquired. Potential flow calculations over the flat plate were performed and the leading edge geometry was modified, so that the cost function, defined as the velocity at the suction peak, was minimum. The lower side is semi-elliptical, while the upper side is defined by a third-order Béziers polynomial, which has been used in other leading edge optimization studies, such as the one by J. H. Fransson 2004 for example.

Table A.1. Leading edge coordinates on the lower side.

x [mm]	0	0.02	0.074	0.167	0.3	0.7
y [mm]	0	-0.33	-0.67	-0.98	-1.31	-1.96
x [mm]	1.18	1.85	2.66	3.12	4.15	4.7
y [mm]	-2.62	-3.27	-3.89	-4.24	-4.88	-5.2
x [mm]	5.33	6.65	7.36	8.9	10.6	13.34
y [mm]	-5.52	-6.15	-6.47	-7.09	-7.71	-8.63
x [mm]	15.36	17.52	21	23.49	28.84	34.7
y [mm]	-9.23	-9.83	-10.71	-11.28	-12.4	-13.48
x [mm]	39.4	46.1	55.04	62.67	72.75	83.38
y [mm]	-14.25	-15.25	-16.43	-17.31	-18.33	-19.25
x [mm]	99.07	118	140.2	165.7	168.2	178.5
y [mm]	-20.37	-21.4	-22.25	-22.69	-22.73	-22.75

Table A.2. Leading edge coordinates on the upper side.

x [mm]	0	0.09	0.24	0.48	0.83	1.5
y [mm]	0	0.88	1.33	1.78	2.24	2.85
x [mm]	2.2	3.05	4.1	4.94	5.9	6.9
y [mm]	3.31	3.77	4.23	4.54	4.84	5.15
x [mm]	8.05	9.32	10.71	12.24	14.78	17.65
y [mm]	5.45	5.75	6.04	6.34	6.77	7.19
x [mm]	20.87	23.22	25.73	28.42	31.29	35.95
y [mm]	7.61	7.88	8.15	8.41	8.67	9.04
x [mm]	39.29	42.84	48.55	52.62	56.91	61.43
y [mm]	9.28	9.51	9.85	10.06	10.27	10.47
x [mm]	66.18	68.64	71.17	73.75	76.4	84.72
y [mm]	10.66	10.75	10.84	10.92	11	11.25
x [mm]	99.9	109.8	116.75	147.5	178.5	
y [mm]	11.59	11.77	11.87	12.17	12.25	

Appendix B

Wall suction uniformity across chambers

Contents

B.1 Suction uniformity tests for each suction chamber 147
B.2 Suction uniformity tests for the suction configurations used in present study 151

In this appendix, the verifications performed to validate suction uniformity within each and across all suction chambers are presented.

B.1 Suction uniformity tests for each suction chamber

The first test consisted in verifying that suction could be applied to a selected suction chamber with minimal inter-chamber leak. To perform this verification, suction with varying mass flow rates was applied over each chamber, using panel P2. The pressure drop across the panel, measured as the difference between the atmospheric pressure and the average pressure across all three ports inside a chamber, is recorded in the tables below for all chambers. Since the uncertainty for the pressure measurements using the SVMtec is ±25 Pa, the chambers are considered to be relatively independent of one another to within the limit of the pressure scanner uncertainty.

In addition to this airtight test, the pressure uniformity inside chambers C1 and C3 is also shown for selected suction configurations in the Figures B.1 and B.2.

Table B.1. Suction chamber pressure drop measurements for airtight test over chamber C1.

	C1	C2	C3	C4	C5	C6	C7	C8	C9
C1/0.100	**-57**	-7	0	-1	-1	-1	2	-4	-2
C1/0.200	**-120**	-12	0	-1	-1	-1	2	-5	-2
C1/0.300	**-190**	-16	-1	-1	-1	-1	2	-4	-2
C1/0.400	**-265**	-19	-1	-1	-1	-1	2	-4	-2
C1/0.500	**-346**	-23	-1	-1	-1	-1	2	-4	-2
C1/0.600	**-433**	-25	-1	-1	-1	-1	2	-5	-2
C1/0.900	**-701**	-29	-1	0	0	-2	2	-4	-1

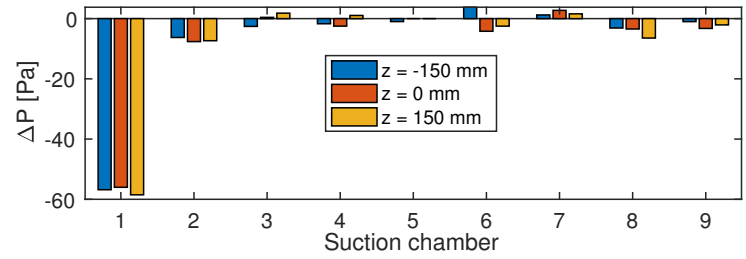

(a) C1/0.100

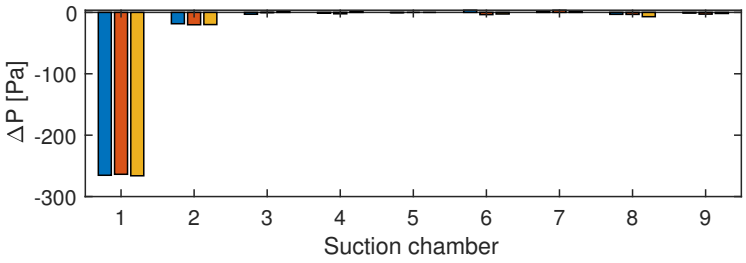

(b) C1/0.400

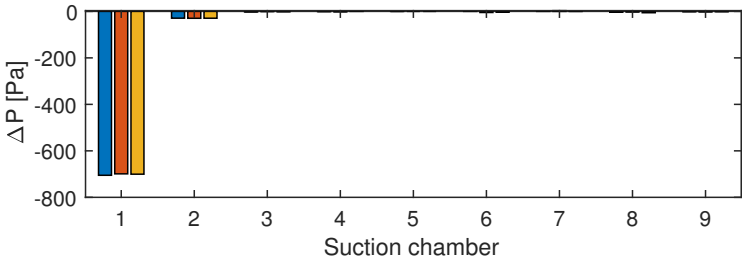

(c) C1/0.900

Figure B.1. Suction uniformity inside chamber C1 for three different suction configurations.

Table B.2. Suction chamber pressure drop measurements for airtight test over chamber C2.

	C1	C2	C3	C4	C5	C6	C7	C8	C9
C2/0.100	-6	**-49**	-2	-1	-1	1	2	-3	-2
C2/0.200	-12	**-105**	-3	-1	-1	1	2	-3	-2
C2/0.300	-16	**-167**	-5	-1	-1	1	1	-3	-2
C2/0.400	-20	**-231**	-6	-2	-1	1	2	-3	-2
C2/0.500	-24	**-300**	-8	-2	-1	1	1	-3	-2
C2/0.600	-28	**-375**	-9	-2	-1	1	1	-3	-2
C2/0.900	-64	**-560**	-12	-1	0	-2	2	-3	-1

Table B.3. Suction chamber pressure drop measurements for airtight test over chamber C3.

	C1	C2	C3	C4	C5	C6	C7	C8	C9
C3/0.100	0	-2	**-46**	-2	-2	1	2	-3	-2
C3/0.200	0	-3	**-112**	-6	-3	1	2	-3	-2
C3/0.300	-1	-5	**-175**	-8	-3	1	2	-3	-2
C3/0.400	-1	-7	**-242**	-10	-4	1	1	-3	-2
C3/0.500	-1	-8	**-313**	-12	-4	1	2	-3	-2
C3/0.600	-1	-9	**-390**	-14	-5	1	2	-3	-2
C3/0.900	-20	-31	**-566**	-18	-3	-2	2	-3	-2

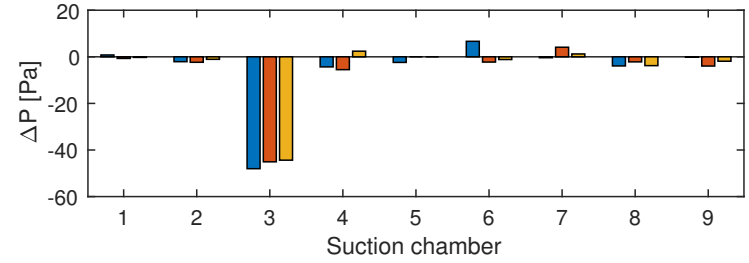

(a) C3/0.100

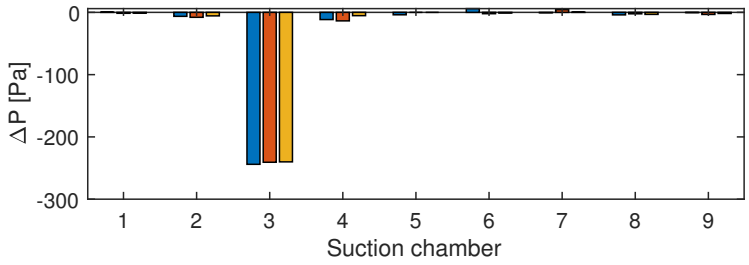

(b) C3/0.400

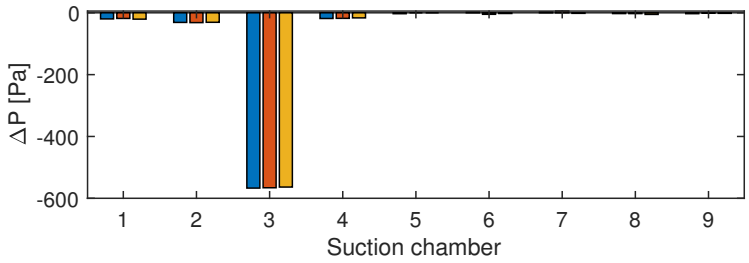

(c) C3/0.900

Figure B.2. Suction uniformity inside chamber C3 for three different suction configurations.

Table B.4. Suction chamber pressure drop measurements for airtight test over chamber C4.

	C1	C2	C3	C4	C5	C6	C7	C8	C9
C4/0.100	0	0	-3	**-47**	-9	0	2	-3	-2
C4/0.200	0	0	-5	**-100**	-16	0	1	-4	-2
C4/0.300	0	-1	-8	**-156**	-21	-1	1	-3	-2
C4/0.400	0	0	-10	**-217**	-26	-2	2	-3	-2
C4/0.500	0	-1	-12	**-283**	-31	-2	2	-3	-2
C4/0.600	0	-1	-14	**-352**	-36	-2	1	-3	-2
C4/0.900	-2	-3	-21	**-562**	-42	-5	2	-4	-2

Table B.5. Suction chamber pressure drop measurements for airtight test over chamber C6.

	C1	C2	C3	C4	C5	C6	C7	C8	C9
C6/0.100	0	0	0	-1	-6	**-50**	1	-4	-2
C6/0.200	0	0	0	-2	-11	**-105**	-1	-4	-2
C6/0.300	0	0	0	-3	-15	**-167**	-2	-4	-2
C6/0.400	0	0	0	-4	-18	**-231**	-3	-4	-2
C6/0.500	0	0	0	-4	-21	**-300**	-4	-4	-2
C6/0.600	0	0	-1	-5	-24	**-375**	-5	-5	-2
C6/0.900	0	-1	-1	-7	-29	**-604**	-9	-5	-2

Table B.6. Suction chamber pressure drop measurements for airtight test over chamber C7.

	C1	C2	C3	C4	C5	C6	C7	C8	C9
C7/0.100	0	0	0	0	-2	0	**-47**	-11	-2
C7/0.200	0	0	0	0	-2	-1	**-101**	-17	-2
C7/0.300	0	0	0	0	-2	-2	**-160**	-23	-2
C7/0.400	0	0	0	0	-3	-3	**-222**	-28	-2
C7/0.500	0	0	0	0	-3	-4	**-291**	-33	-2
C7/0.600	0	0	0	0	-3	-5	**-364**	-37	-2
C7/0.900	0	0	0	-1	-2	-10	**-589**	-47	-3

Table B.7. Suction chamber pressure drop measurements for airtight test over chamber C8.

	C1	C2	C3	C4	C5	C6	C7	C8	C9
C8/0.100	0	0	0	0	-2	1	-8	**-52**	-3
C8/0.200	0	0	0	0	-2	1	-15	**-108**	-3
C8/0.300	0	0	0	0	-2	1	-20	**-170**	-3
C8/0.400	1	0	0	0	-2	1	-26	**-236**	-3
C8/0.500	0	0	0	0	-2	1	-30	**-306**	-3
C8/0.600	0	0	0	0	-2	0	-35	**-382**	-4
C8/0.900	0	0	0	-1	-1	-2	-58	**-569**	-4

Table B.8. Suction chamber pressure drop measurements for airtight test over chamber C9.

	C1	C2	C3	C4	C5	C6	C7	C8	C9
C9/0.100	0	0	0	0	-2	2	0	-3	**-72**
C9/0.200	0	0	0	0	-2	2	-1	-3	**-154**
C9/0.300	0	0	0	0	-2	1	-1	-4	**-243**
C9/0.400	0	0	0	0	-2	2	-1	-4	**-340**
C9/0.500	0	0	0	0	-2	1	-1	-4	**-446**
C9/0.600	0	0	0	0	-2	1	-1	-5	**-562**
C9/0.900	0	0	0	0	-1	-1	-3	-5	**-974**

B.2 Suction uniformity tests for the suction configurations used in present study

Figure B.3 shows the suction uniformity across all chambers for the three suction configurations that were used in the present stude, namely C1/0.400, C3,5/0.200 and *full suction*. Note that only the centerline pressure port was used in chamber C5.

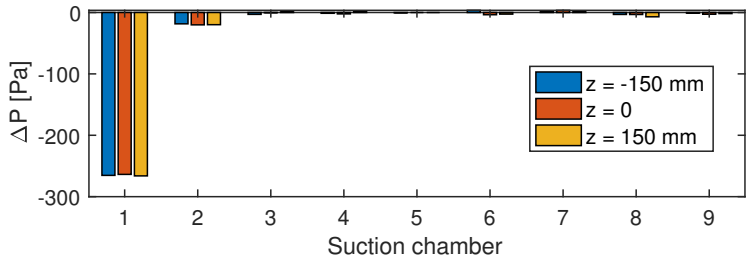

(a) C1/0.400

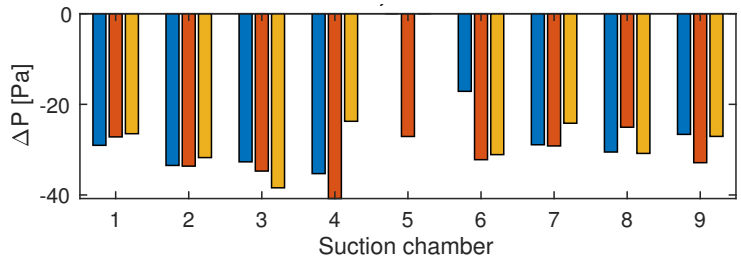

(b) C3,5/0.200

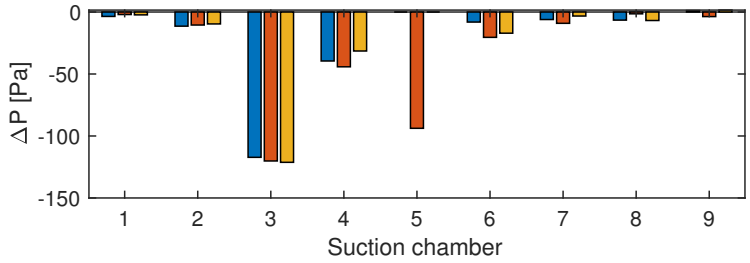

(c) *full suction*

Figure B.3. Suction uniformity all chambers for all suction configurations used in the present study.

Part V

French summary / Résumé

Étude expérimentale de l'influence de défauts de surface sur la transition laminaire-turbulent d'une couche limite aspirée

par

Jeanne Methel

Résumé

L'accroissement prévu du trafic aérien s'accompagne de forts enjeux économiques et environnementaux, nécessitant en particulier de réduire la consommation en carburant des aéronefs modernes. Pour cela, l'aspiration pariétale est une méthode qui permet de retarder la transition laminaire-turbulent des couches limites qui se développent à la surface des aéronefs, entrainant une réduction significative de la force de traînée et donc de la consommation en carburant. En effet, le coefficient de frottement d'une couche limite en régime laminaire est beaucoup plus faible qu'en régime turbulent. Toutefois, l'installation d'un système d'aspiration induit inévitablement des discontinuités géométriques (ou défauts de surface), en particulier à la jonction entre la zone aspirée et la zone pleine (sans aspiration). Or, ces défauts sont susceptibles de déclencher une transition prématurée, pouvant ainsi complètement annuler l'effet positif de l'aspiration.

L'objectif de cette thèse est d'étudier expérimentalement l'effet de défauts de surface sur la transition d'une couche limite aspirée dans un écoulement incompressible et bidimensionnel. Dans un premier temps, un protocole expérimental a été mis en place pour vérifier la qualité de l'écoulement de la soufflerie et préciser un cas de référence pour la configuration lisse, sans défaut. En particulier, l'influence de la distribution longitudinale de l'aspiration sur la position de la transition a été étudiée, confirmant ainsi que tous les cas avec aspiration, qu'elle qu'en soit la distribution, permettaient de repousser la transition vers l'aval. En parallèle, il a été observé qu'une couche limite se développant au-dessus d'une paroi poreuse sans aspiration pouvait être déstabilisée. Dans un second temps, l'influence de trois types de défauts de surface (fils, marches montantes et rainures) a été étudiée. Les mesures ont montré le même comportement sur paroi pleine et sur paroi aspirée. En particulier, les dimensions critiques des défauts (hauteur et/ou largeur) à partir desquelles la transition a lieu au niveau du défaut restent inchangées. Toutefois, dans le cas de défauts sous-critiques, pour lesquels la transition n'est pas déclenchée immédiatement, l'aspiration permet toujours de retarder la transition.

Mots-clés : transition laminaire-turbulent, ondes de Tollmien-Schlichting, aspiration pariétale, contrôle actif d'écoulement, défauts de surface.

La partie suivante est une synthèse des travaux présentés dans le manuscrit de thèse rédigé en anglais et intitulé "Experimental Investigation of the Effects of Surface Defects on the Laminar-Turbulent Transition of a Boundary Layer with Wall Suction". Pour plus de détails sur l'ensemble des résultats, il est recommandé de consulter ce manuscrit.

Chapitre F1

Introduction et objectifs

L'accroissement prévu du trafic aérien couplé à l'épuisement des ressources fossiles impliquent des enjeux économiques et environnementaux qui nécessitent la réduction de la consommation en carburant des aéronefs modernes. Sur un avion commercial classique, la traînée de frottement représente plus de 40% de la traînée totale et constitue ainsi une composante dont la réduction aurait un impact direct sur la consommation en carburant de l'avion. Une solution envisageable à cette problématique serait de retarder le déclenchement de la transition laminaire-turbulent grâce à l'aspiration pariétale de la couche limite. De nombreuses études en soufflerie et en vol ont démontré les avantages notables de ce système de contrôle actif d'écoulement Braslow 1999.

Par ailleurs, des défauts de surface dus à la fabrication et à l'assemblage des ailes et des gouvernes sont inévitables et sont susceptibles de déclencher une transition prématurée. Plusieurs critères de déclenchement ont donc été définis dans le cas de défauts de surface bidimensionnels (du type marches et rainures) sur des parois pleines, mais de tels critères n'existent pas pour des surfaces poreuses avec aspiration. L'extension de tels critères à des cas aspirés est de première importance car la jonction entre zone aspirée et zone pleine ne peut être envisagée sans une discontinuité de type rainure qui serait susceptible de déclencher la transition, ou du moins avoir un effet négatif sur la stabilité de la couche limite. Un état de l'art sur la transition laminaire-turbulent et des effets de l'aspiration puis des défauts de surface sur celle-ci est donné dans les **Chapitres 1, 2 et 3** respectivement.

L'objectif de cette thèse est donc de concevoir, de réaliser et d'exploiter un dispositif expérimental permettant d'étudier l'influence de défauts de surface au sein d'une couche limite aspirée. Cette étude permettra d'étendre les critères de déclenchement existant pour des couches limites se développant sur parois poreuses et sur parois hybrides (paroi poreuse avec aspiration/paroi pleine sans aspiration).

Chapitre F2

Protocole expérimental pour une étude sur la transition laminaire-turbulent

Contents

F2.1 Présentation du montage 159
F2.2 Validation du protocole expérimental 160

Ce chapitre a pour objectif de présenter le protocole et les moyens expérimentaux utilisés lors de la réalisation de cette thèse qui sont présentés en détails dans le **Chapitre 4** du manuscrit.

F2.1 Présentation du montage

Cette étude a été réalisée dans la soufflerie subsonique TRIN2 (figure F2.1) dont la vitesse en veine peut varier entre 20 $m.s^{-1}$ et 50 $m.s^{-1}$ (soit en terme de nombre de Reynolds unitaire Re = $1{\cdot}10^6$ m^{-1} et $3{\cdot}10^6$ m^{-1}).

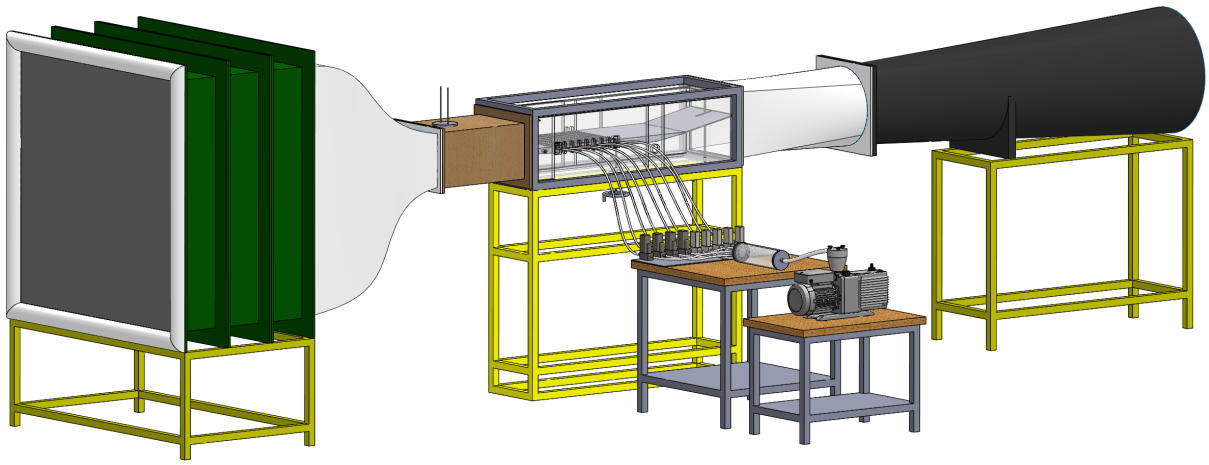

Figure F2.1. CAO de la soufflerie subsonique TRIN 2.

L'écoulement dans la soufflerie est généré par un ventilateur axial situé en aval et séparé

du diffuseur pas une chambre anéchoïque qui permet d'éviter la remontée de perturbation, notamment acoustiques, dans la veine d'essai. La soufflerie a un taux de turbulence en veine toujours inférieur à 0.18% (évalué sur la gamme de fréquence entre 3 Hz et 10 kHz) ce qui la rend adaptée aux études de laminarité. À sa section d'entrée, la veine mesure 0.3 m de haut sur 0.4 m de large.

Une plaque plane en aluminium a été installée horizontalement dans la veine d'essai (figure F2.2). Elle est composée d'un bord d'attaque, du corps de la plaque plane avec les caissons d'aspiration et d'un volet de braquage. Les incidences de la plaque plane et du volet ont chacune été réglées pour obtenir un écoulement avec un gradient de pression aussi proche que possible de zéro. De plus, la forme du bord d'attaque a été optimisée pour minimiser le pic de survitesse au raccord avec la plaque. La zone d'aspiration a pour dimensions 0.450 m dans la direction longitudinale x, 0.350 m en envergure z et 0.019 m de profondeur y et se situe à 0.18 m du bord d'attaque. Elle est composée de neuf caissons d'aspiration, ayant chacun un débitmètre dédié, qui sont ensuite tous reliés à une nourrice branchée sur une pompe à vide.

Les principales mesures effectuées lors de cette étude sont de trois types: la pression, la vitesse longitudinale de l'écoulement et le débit. Des prises de pressions ont été percées tout le long de la plaque plane, à une position décalée de 0.08 m en envergure du centre veine, ainsi qu'à l'intérieur des caissons pour vérifier l'uniformité, en evergure, de l'aspiration. Les mesures d'anémométrie ont été réalisées avec une sonde à fil chaud (mesure monodimensionnelle), étalonnée *in situ* au début et à la fin de chaque essai. Finalement, des débitmètres-régulateurs à électro-vanne sont utilisés pour évaluer et contrôler le débit massique d'apiration pour chaque caisson. Plus de détails sur le montage peuvent être trouvés dans la Section 4.1.

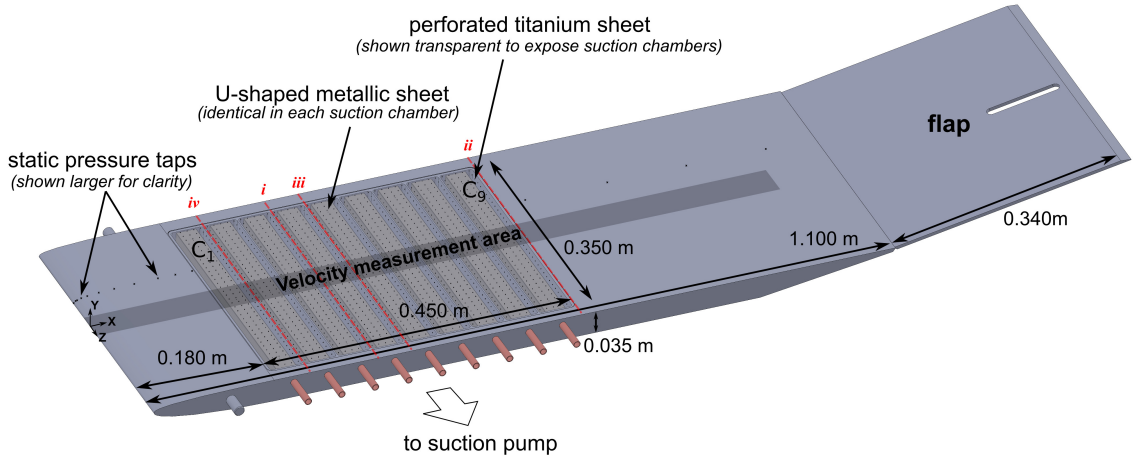

Figure F2.2. Vue isométrique de la plaque plane

F2.2 Validation du protocole expérimental

Dans un premier temps, une caractérisation de l'écoulement de la veine d'essai a montré que le taux de turbulence, évalué sur la gamme de fréquence [3 Hz - 10 kHz], avec et sans la plaque plane en veine était toujours inférieur à 0.18% (figure F2.3).

Pour ces faibles valeurs de turbulence extérieure, c'est le mécanisme de transition dit modal ou naturel qui se produira. En particulier, dans notre cas bidimensionnel et à basse vitesse, c'est l'amplification des ondes de TS qui sera responsable du déclenchement de la transition. Dans un premier temps, la figure F2.4a montre que la couche limite qui évolue dans la région laminaire de la plaque plane est proche de la solution de Blasius. Pour chaque point du profil, des données

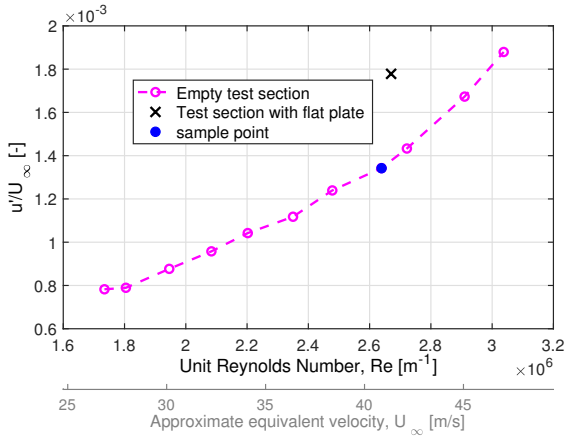

(a) Niveau de u'/U_∞ dans la veine avec et sans maquette

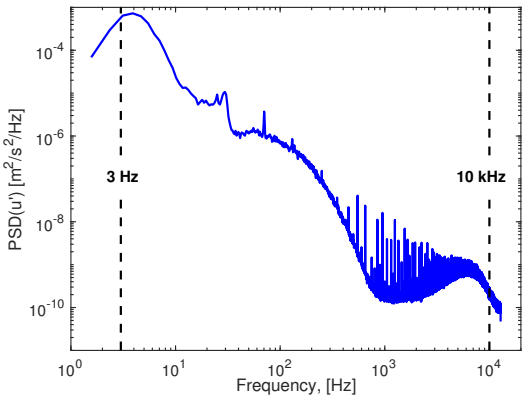

(b) DSP(u') au point "sample" dans (a) avec bande d'intégration

Figure F2.3. Caractérisation de l'écoulement dans la veine d'essai

instationnaires sont disponibles et un exemple de la densité spectrale de puissance (DSP) des fluctuations de vitesse longitudinale *u'*, évaluée à partir de ces données, est donné sur la figure F2.4c. À partir de ces DSP, le profil de fluctuations de vitesse *u'* a été défini en intégrant une gamme de fréquences allant de 592 Hz à 632 Hz (figure F2.4b). L'accord entre ce profil et celui calculé grâce à la théorie de la stabilité linéaire (TSL) pour une fréquence similaire (qui est aussi la fréquence responsable de la transition prévue par la TSL, *cf.* figure F2.5) semble indiquer que la transition est effectivement pilotée par les ondes de TS.

En effet des calculs de stabilité linéaire sur les équations d'Orr-Sommerfeld ont été réalisés sur le profil de Blasius au Reynolds unitaire nominal. Les facteurs N pour chaque fréquence sont reportés sur la figure F2.5. À partir de la position de transition expérimentale ($x = 740$ mm du bord d'attaque), le facteur N de transition N_T est évalué à 6.2 et la fréquence responsable de la transition est d'environ 600 Hz.

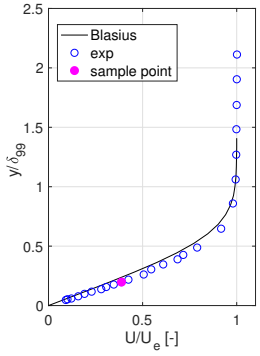

(a) Profil de couche limite adimensionné ($x = 558$ mm)

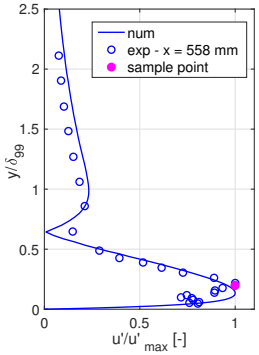

(b) Comparaison des profils de *u'*

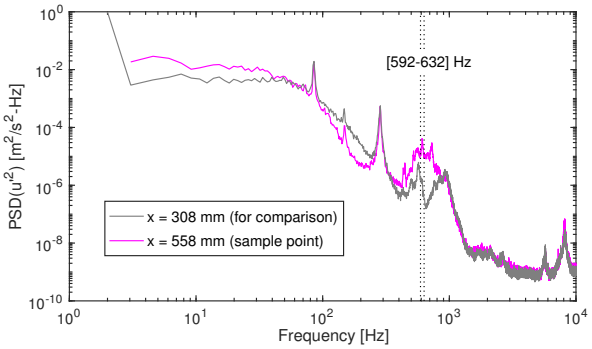

(c) DSP du point "sample" du profil (558 mm, 400μm)

Figure F2.4. Vérification du mécanisme de transition par ondes de Tollmien-Schlichting

Pour plus de détails sur la validation du protocole expérimentale ainsi que sur la quantification des incertitudes de mesures, *cf.* Sections 4.2 et 4.3 respectivement.

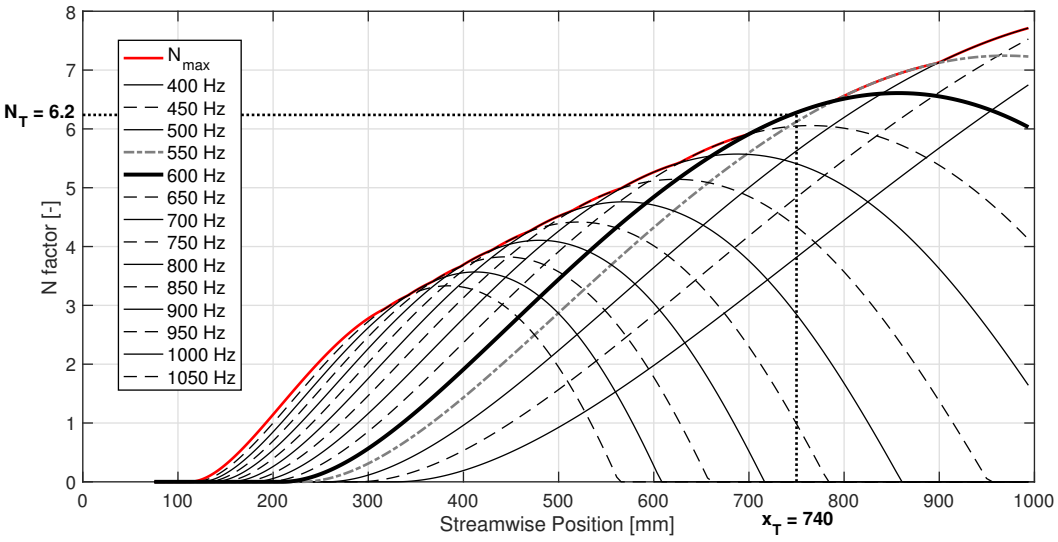

Figure F2.5. Évolution du facteur N pour l'écoulement sans gradient de pression à Re = $2.6{\cdot}10^6$ m^{-1}

Chapitre F3

Effets de l'impédance et de l'aspiration pariétale sur la transition laminaire-turbulent

Contents

F3.1 Effet de l'impédance de paroi 163
F3.2 Effet de l'aspiration pariétale 166

Ce chapitre a pour objectif de premièrement présenter l'effet de l'impédance de paroi sur la stabilité de la couche limite puis celui de l'aspiration pariétale sur la transition. Ces derniers résultats seront ensuite utilisés dans le chapitre suivant comme référence pour la configuration plaque plane lisse. Plus de détails sur cette partie peuvent être trouvés dans le **Chapitre 5** du manuscrit.

F3.1 Effet de l'impédance de paroi

Trois panneaux différents ont été successivement installés sur la zone d'aspiration lors de nos expérimentations: leur caractéristiques sont résumées dans le tableau F3.1.

Il a été observé qu'en l'absence d'aspiration, la simple présence d'une paroi poreuse pouvait influencer la stabilité de la couche limite. Ainsi, les deux panneaux perforés P2 et P3 provoque une transition prématurée par rapport au panneau solide P1. En effet, sur la figure F3.1 qui montre l'évolution longitudinale des fluctuations de vitesse *u'*, la position de transition est définie comme l'abscisse à partir de laquelle les fluctuations commencent à augmenter avec une pente de plus de $2{\cdot}10^{-4}$ mm^{-1} (plus de détails sur la justification de ce critère empirique défini dans le cadre de cette étude sont donnés dans la Section 4.1.3 du manuscrit). Cette figure met d'abord en évidence la présence d'un écoulement bidimensionnel par l'invariance de la position de la transition en envergure. Ensuite, l'effet déstabilisant des parois poreuses est aussi visible par

Table F3.1. Caractéristiques des panneaux

Panneau	p [%]	Diamètre trous, d [μm]	Pas, s [mm]
P1	0	0	0
P2	0.26	92	1.6
P3	1.34	188	1.44

leur position de transition plus proche du bord d'attaque que celle de la paroi pleine. Nous avons également montré que ce résultat n'était pas lié à un effet destabilisant éventuel d'une augmentation de la rugosité moyenne de surface (présence des trous).

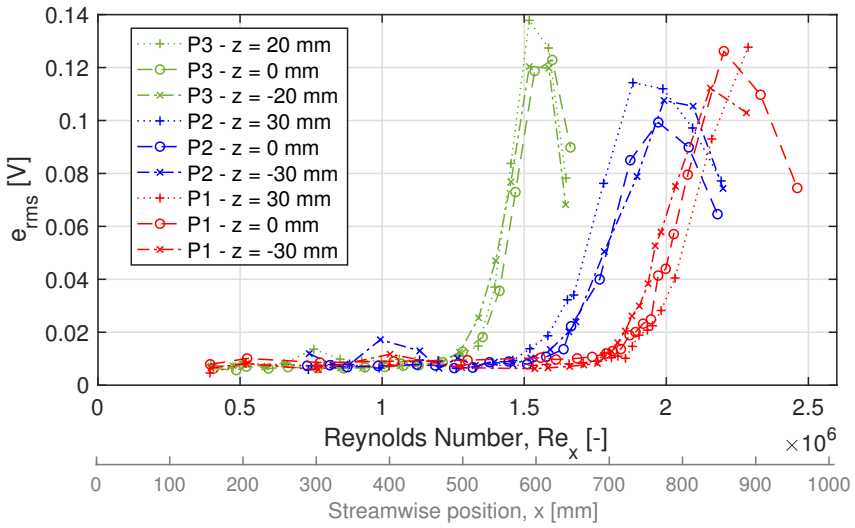

Figure F3.1. Positions de transition bidimensionnelles pour les trois panneaux sans aspiration.

Les DSP de u' situées légèrement en amont des positions de transition respectives pour chaque panneau révèlent que le mécanisme de transition est inchangé: ce sont les fréquences entre 400 Hz et 800 Hz qui sont toujours les plus amplifiées (figure F3.2). De plus, l'évolution longitudinale des profils de u' (figure F3.3) semble indiquer que les parois poreuses influencent surtout l'amplification des ondes de TS.

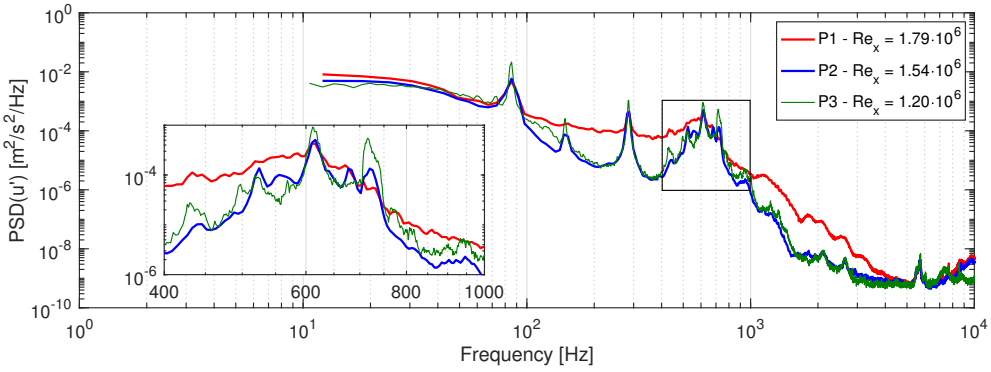

Figure F3.2. DSP (y = 300 μm de la paroi) juste en amont de la position de transition où les ondes de TS sont fortement amplifiées.

Une étude numérique, réalisée en collaboration avec A. Rouvière dans le cadre d'un stage de fin d'étude, a montré que cet effet déstabilisant des panneaux d'aspiration pouvait être modélisé en imposant une condition d'impédance Z à la paroi lors des calculs de stabilité. L'approche générale a d'abord consisté à réaliser des calculs de couche limite sans aspiration puis à résoudre les équations de stabilité linéaire d'Orr-Sommerfeld avec un condition d'impédance à la paroi. Pour évaluer la valeur de cette impédance, les parois poreuses ont été comparées à des "liners" acoustiques dont l'impérance peut être définie comme la somme de l'impédance de perforation (selon le modèle de Crandall Crandall 1927) et de cavité (d'après le modèle de Bruneau Bruneau 2006). Ces modèles d'impédance ont permis de retrouver numériquement la

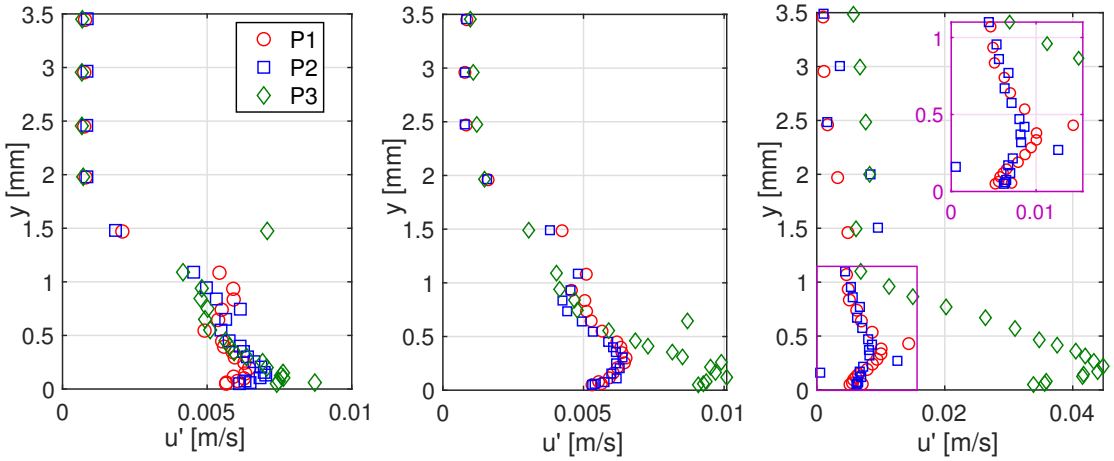

(a) $\mathrm{Re_x}$=5.41 · 10^5 (*centre du caisson C1*)

(b) $\mathrm{Re_x}$=8.00 · 10^5 (*centre du caisson C3*)

(c) $\mathrm{Re_x}$=1.06 · 10^6 (*centre du caisson C5*)

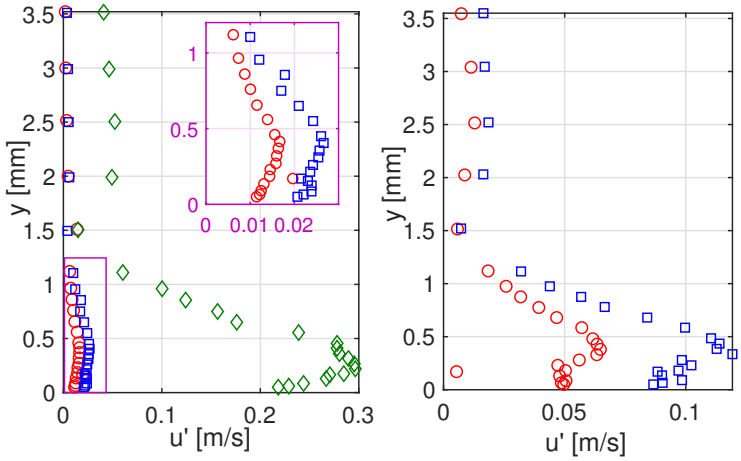

(d) $\mathrm{Re_x}$=1.32 · 10^6 (*centre du caisson C7*)

(e) $\mathrm{Re_x}$=1.58 · 10^6 (*centre du caisson C9*)

Figure F3.3. Profils des fluctuations de vitesses *u'* évalués sur la bande de fréquence [592-632] Hz pour tous les panneaux sans aspiration.

Table F3.2. Positions de transition expérimentale et numérique pour les panneaux sans aspiration.

Panneau	$x_{T,exp}$ [mm]	$x_{T,num}$ [mm]	f_{RexT} [Hz]	$Z(f_{RexT})$
P1	740	740	600	∞
P2	640	713	610	518-0.34i
P3	510	515	815	24-20i

position de transition expérimentale avec plus ou moins de succès. Une synthèse des principaux résultats expérimentaux et numériques est donnée dans le Tableau F3.2, avec f_{RexT} la fréquence responsable du déclenchement de la transition, évaluée numériquement. Plus de détails sont fournis dans la Section 5.2.

F3.2 Effet de l'aspiration pariétale

Quatre cas ont été retenus pour constituer les configurations de référence pour la plaque plane lisse (*i.e.*, sans défaut de surface). Les trois cas avec aspiration, ayant tous le même débit total de 0.4 g.s^{-1}, correspondent à une aspiration: concentrée sur le premier caisson uniquement (C1/0.400), divisée entre les caisson C3 et C5 (C3,5/0.200) et distribuée sur toute la zone d'aspiration (*full suction*). Dans ce dernier cas, le débit par caisson est de 0.044 g.s^{-1}. Aucune aspiration n'est appliquée pour le cas de référence *no suction*. Les positions de transition pour les trois panneaux et tous les cas correspondants d'aspiration sont résumées dans le Tableau F3.3. Tous les cas avec aspiration ont une position de transition plus reculée par rapport à celle du cas sans aspiration. De plus, comme cela avait été observé précédemment par Juillen et al. 1995, la distribution de l'aspiration à iso-débit peut modifier la position de transition. En particulier, le cas C1/0.400 semble moins efficace à repousser la transition que C3,5/0.200 et *full suction*.

Table F3.3. Positions de transition pour tous les cas d'aspiration et tous les panneaux

	P2	P3	P1
cas d'aspiration	Re_{xT} [-]	Re_{xT} [-]	Re_{xT} [-]
no suction	$1.66{\cdot}10^6$	$1.33{\cdot}10^6$	$1.92{\cdot}10^6$
C1/0.400	$2.20{\cdot}10^6$	$1.56{\cdot}10^6$	N/A
C3,5/0.200	$2.30{\cdot}10^6$	$1.66{\cdot}10^6$	N/A
full suction	$2.30{\cdot}10^6$	$1.59{\cdot}10^6$	N/A

Le principe de l'aspiration consiste à faiblement augmenter la courbure ($\partial^2 U/\partial y^2$) du profil de vitesse de couche limite afin de le stabiliser. Toutefois le mécanisme de transition est inchangé et reste gouverné par l'amplification des ondes de TS. La comparaison des profils de u' pour les quatre cas d'intérêt sur le panneau P2 (figure F3.4) souligne que l'aspiration atténue effectivement l'amplification des ondes de TS, ce qui recule la transition par rapport au cas sans aspiration.

Des calculs de stabilité linéaire ont ensuite été réalisés pour étudier numériquement les quatre cas expérimentaux. L'effet de l'aspiration est pris en compte dans les calculs de couche limite (effectués avec le code 3C3D) en imposant une vitesse normale à la paroi V_p aux positions longitudinales correspondantes. La vitesse V_p est calculée par:

$$V_p = -\frac{\dot{m}}{\rho_\infty A_{suction}} \quad (V_p < 0 \quad \text{for suction}) \tag{F3.1}$$

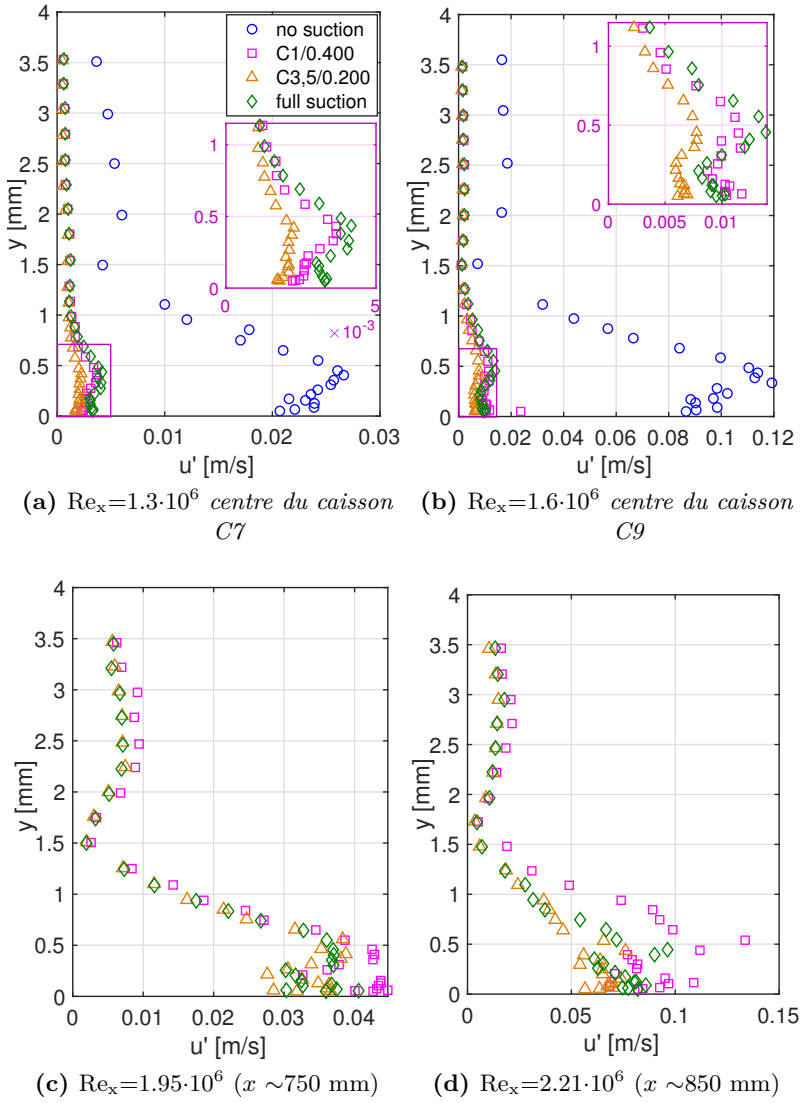

(a) $\mathrm{Re_x}$=1.3·10^6 *centre du caisson C7* **(b)** $\mathrm{Re_x}$=1.6·10^6 *centre du caisson C9*

(c) $\mathrm{Re_x}$=1.95·10^6 (x ∼750 mm) **(d)** $\mathrm{Re_x}$=2.21·10^6 (x ∼850 mm)

Figure F3.4. Effet de l'aspiration sur les profils de *u'* évalués sur la bande de fréquence [592-632] Hz) pour le panneau P2.

où $\dot{m}$ est le débit total d'aspiration, ρ_∞ la masse volumique de l'écoulement infini amont, et $A_{suction}$ la surface sur laquelle l'aspiration est appliquée. Ensuite des calculs de stabilité linéaire sont réalisés (sans condition d'impédance) avec le code CASTET pour déterminer l'évolution des facteurs N pour des fréquences comprises entre 200 Hz et 1.6 kHz. Les courbes enveloppes des facteurs N maximum pour tous les cas d'intérêt sont tracées sur la figure F3.5 et les facteurs N de transition sont résumés dans le Tableau F3.4. L'analyse de l'effet de la distribution de l'aspiration sur des fréquences différentes a montré que le cas C1/0.400 n'atténuait pas les fréquences "dangereuses" des TS aussi efficacement que possible car celles-ci n'étaient pas encore amplifiées au niveau du caisson C1. La distribution spatiale est donc un paramètre pouvant fortement influencer l'efficacité de l'aspiration pariétale. Quoi qu'il en soit, ces calculs seront utilisés comme référence dans les parties suivantes pour estimer l'effet déstabilisant des défauts pour chaque cas d'aspiration.

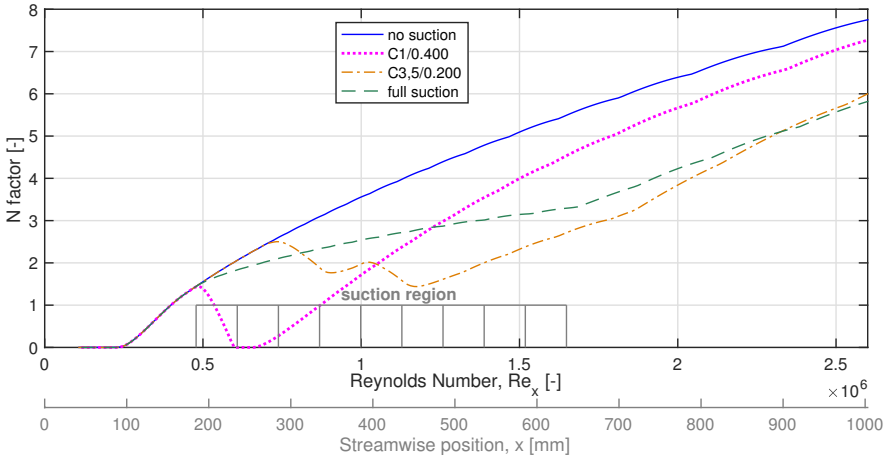

Figure F3.5. Courbe enveloppe des facteurs N maximum pour tous les cas d'aspiration (sans condition d'impédance).

Table F3.4. Positions de transition et facteurs N pour tous les cas d'aspirations (panneau P2).

suction case	Re_{xT} [-]	N_T [-]
no suction	$1.66{\cdot}10^6$	5.53
C1/0.400	$2.20{\cdot}10^6$	6.26
C3,5/0.200	$2.30{\cdot}10^6$	4.94
full suction	$2.30{\cdot}10^6$	5.00

Chapitre F4

Effets conjugués de différents type de défauts de surface et de l'aspiration pariétale sur la transition

Ce chapitre présente un résumé des résultats sur les effets conjugués des trois types de défauts de surface testés avec l'aspiration sur la transition. Pour tous les détails, chaque défaut (fils, marches montantes, rainures) est traité individuellement dans les **Chapitres 6, 7, 8** respectivement. Une synthèse des résultats relatifs aux trois défauts est aussi apportée dans le **Chapitre 9**.

F4.1 Critères de transition

Trois types de défauts de surface ont été testés: des fils cylindriques, des marches montantes et des rainures. Les dimensions d'intérêt pour les fils et les marches montantes sont leur hauteur relative par rapport à l'épaisseur local de la couche limite, h/δ_1 et pour les rainures la profondeur relative h/δ_1, et la largeur relative b/δ_1.

Quel que soit le type de défaut, les dimensions critiques (à partir desquelles la transition à lieu au niveau du défaut même) ne dépendent pas de la présence ou non de l'aspiration. Ceci peut être d'abord observé à l'aide du paramètre Δ_{xT} est défini tel que:

$$\Delta_{xT} = \frac{Re_{xT,SD} - Re_{x,SD}}{Re_{xT,noSD} - Re_{x,SD}} = \frac{x_{T,SD} - x_{SD}}{x_{T,noSD} - x_{SD}}. \tag{F4.1}$$

Dans cette relation, xT, SD correspond à la position de transition avec défaut de surface, x_{SD} à la position du défaut de surface, $x_{T,noSD}$ la position de transition dans la configuration lisse et toutes les variables Re correspondent aux nombres de Reynolds correspondants. Quand le paramètre Δ_{xT} est égal à 1, la position de transition est équivalente à celle du cas lisse, alors que lorsqu'il est égal à 0, la position de transition est au niveau du défaut de surface et le défaut est critique. La figure F4.1 montre l'évolution de ce paramètre pour les fils (wires) et les marches montantes (FFS) en fonction de leur hauteur relative pour tous les cas d'aspiration et tôles poreuses. Aucune tendance particulière n'émerge selon les cas d'aspiration mais chaque type de défaut de surface présente une hauteur critique propre. La valeur critique de h/δ_1 pour les fils et pour les marches montantes est de $\sim$0.4 et $\sim$1.3 respectivement.

De la même façon, les dimensions critiques pour les rainures sont aussi indépendantes des cas d'aspiration. Les valeurs critiques de profondeur et de largeur relatives sont reportées sur la figure F4.2 par les triangles verts, où elles sont comparées à des études antérieures. Il existe

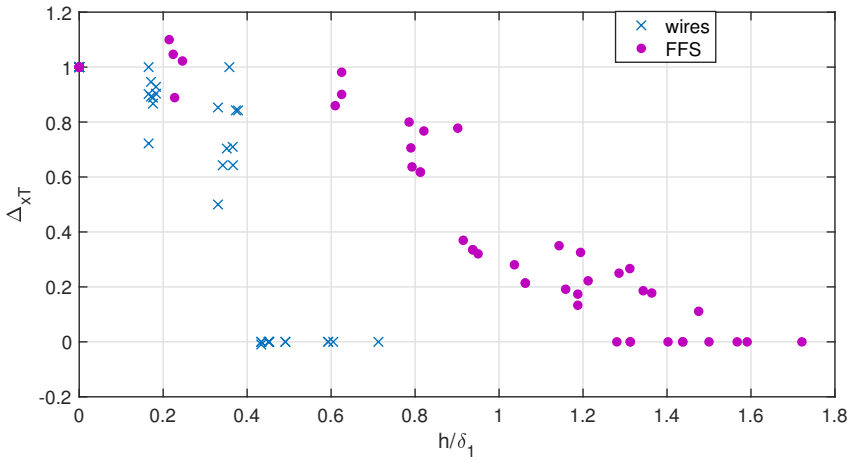

Figure F4.1. Comparaison du paramètre Δ_{xT} pour tous les fils et marches montantes.

globalement un bon accord entre les résultats passés et présents. Toutefois, les rainures testées dans cette étude ont des dimensions critiques un peu plus faibles (h/δ_1 ∼1.4 et b/δ_1 ∼14) que celles définies par Olive and Blanchard 1982 (h/δ_1 ∼2 et b/δ_1 ∼18). Cette différence pourrait être expliquée par la différence de position longitudinale par rapport à la transition des rainures entre les deux études.

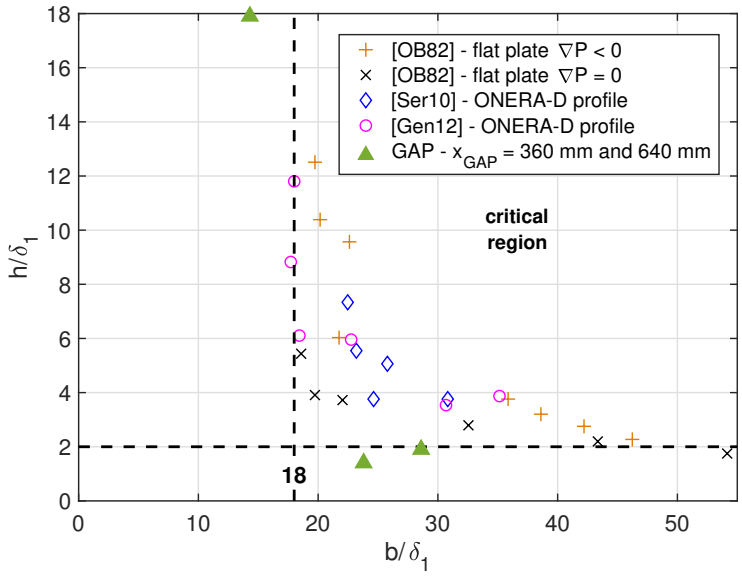

Figure F4.2. Comparaison avec des données expérimentales d'études ONERA antérieures sur des rainures avec des dimensions critiques.

F4.2 Mécanismes de transition

Les différences de valeur des dimensions critiques entre les types de défauts peuvent être, en partie, expliquées par l'effet des défauts sur les mécanismes de transition. Pour les défauts sous-critiques, où la transition a lieu en aval du défaut, la transition est toujours le résultat de l'amplification des ondes de TS. En effet, sur la figure F4.3, la gamme de fréquences entre 400 Hz

et 800 Hz (qui correspond aux ondes de TS) est fortement amplifiée à une position légèrement en amont de la transition, pour chaque type de défaut sous-critique.

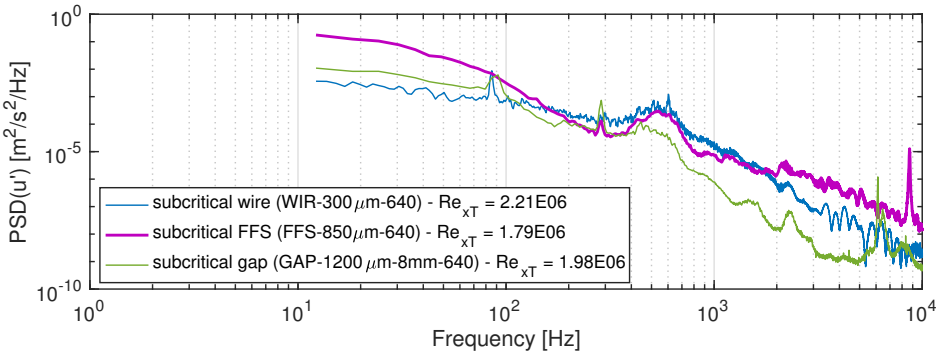

Figure F4.3. DSP(u') (à $y = 300\mu m$ de la paroi) au nombre de Reynolds de transition pour des défauts sous-critiques choisis pour le cas *full suction* (panneau P2).

Une fois que les dimensions critiques sont atteintes, les effets sur les mécanismes de transitions varient selon le type de défaut. La figure F4.4 montre les spectres de flucuations de vitesse pour quatre type défauts critiques: un fil, une marche montante, une rainure large et une rainure profonde.

La marche montante critique ne fait qu'amplifier les instabilités déjà existantes puisque seules les fréquences entre 400 Hz et 800 Hz sont toujours fortement amplifiées sur le spectre: la transition est donc toujours gouvernée par les ondes de TS.

Dans le cas du fil critique, il n'y a plus de traces des ondes de TS, mais ce sont plutôt de très hautes fréquences (autour de 6 kHz) qui sont amplifiées. Les profils de couche limite au niveau de la transition affichent des points d'inflexion marqués. Dans ce cas, le mécanisme de la transition est maintenant de type inflexionnel (et non de type visqueux, *i.e.*, lié aux ondes de TS).

Finalement, pour les rainures critiques, il semblerait que les deux mécanismes (inflexionnel et visqueux) se produisent. Les fréquences correspondant aux ondes de TS sont visibles pour les deux rainures critiques, ce qui sous-entend que les rainures contribuent à l'amplification accrue des instabilités déjà existantes. Toutefois, pour la rainure large (GAP-1200µm-20mm), des plus hautes fréquences de l'ordre de 2 kHz sont aussi visibles. Les profils de couche limite cantonnés à l'intérieur de cette rainure affichent aussi des points d'inflexion marqués, ce qui peut expliquer la présence de cette bande de hautes fréquences amplifiées.

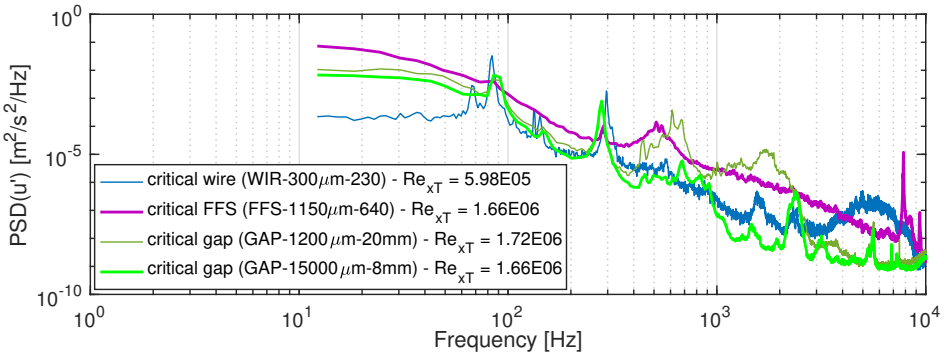

Figure F4.4. DSP(u') ($y = 300\mu m$) au nombre de Reynolds de transition pour des défauts critiques pour le cas *full suction* (panneau P2).

Les marches montantes et les rainures semblent donc contribuer à l'amplification des insta-

bilités existantes qui sont ici les ondes de TS. De plus, leurs dimensions critiques sont élevées, notamment par rapport aux fils. Ces deux facteurs permettent d'envisager l'utilisation de la méthode du ΔN, défini, pour chaque cas d'aspiration, par:

$$\Delta N = N_{T,smooth} - N_{xT,SD}. \tag{F4.2}$$

avec $N_{T,smooth}$ la valeur du N de transition pour la configuration lisse et $N_{xT,SD}$ celle pour la configuration avec une marche montante ou une rainure ("SD" pour "surface defect").

Les valeurs de ΔN pour les marches montantes sont reportées sur la figure F4.5 et comparées au modèle de Crouch et al. 2006 et aux données expérimentales de Wang and Gaster 2005, respectivement [CKN06] et [WG05] sur le graphique. Les valeurs de ΔN pour les configurations sans aspiration sont en bon accord avec les données des autres études, qui avaient été réalisées sur des plaques planes pleines (sans aspiration). Les configurations avec aspiration en présence des marches montantes les plus proches du bord d'attaque ont des valeurs de ΔN importantes et même plus élevées que celles prévues par le modèle [CKN06], déjà conservateur. Ceci semblerait indiquer qu'un modèle de ΔN pourrait être développé pour prendre en compte la plus grande sensibilité des configurations avec aspiration à la présence de marches montantes.

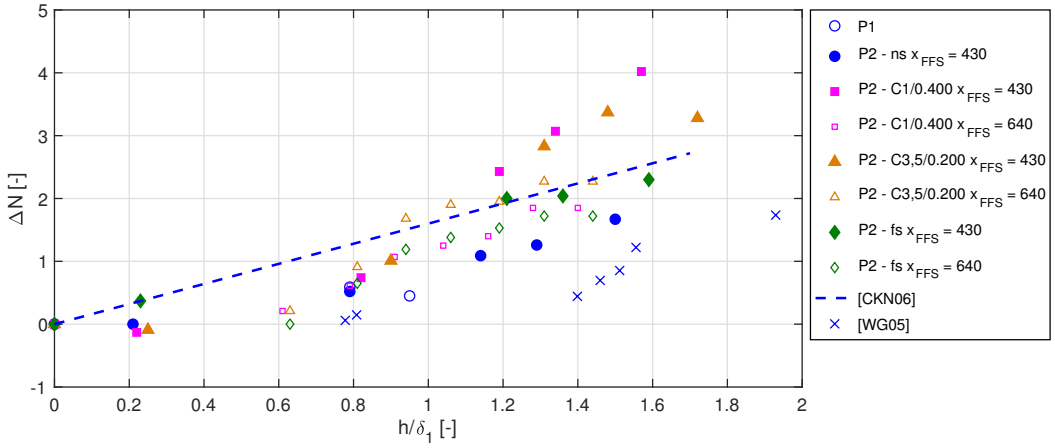

Figure F4.5. Comparaison de tous les cas d'aspiration des marches montantes avec le modèle de ΔN de Crouch et al. 2006 et les mesures de Wang and Gaster 2005.

Pour les rainures, la même procédure a été utilisée pour évaluer le ΔN et les valeurs sont reportées sur la figure F4.6. Ces données pourraient servir de base au développement d'un modèle du ΔN.

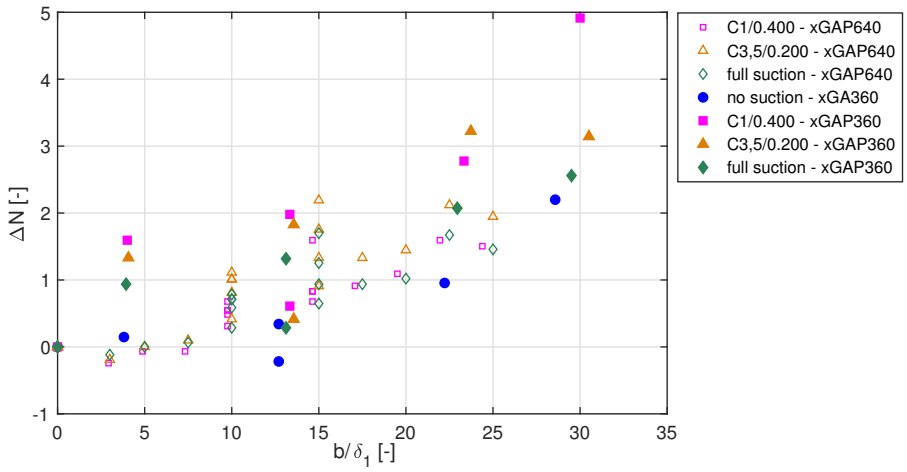

Figure F4.6. Valeurs de ΔN évaluées pour toutes les dimensions de rainures et cas d'aspiration.

Chapitre F5

Conclusions et perspectives

Une étude expérimentale sur l'influence de défauts de surface sur la transition laminaire-turbulent d'une couche limite aspirée a été effectuée. Le premier objectif est dédié à l'analyse et la compréhension de l'effet conjugué de défauts de surface et de l'aspiration sur la stabilité d'une couche limite. Le second objectif a consisté à proposer des dimensions critiques pour chaque type de défauts pour définir des tolérances d'usinage pour les surfaces laminaires.

F5.1 Conclusion

Dans un premier temps, un protocole expérimental a été mis en place pour vérifier que la qualité de l'écoulement dans la veine était convenable pour une étude de transition. Une caractérisation rigoureuse de l'écoulement dans la veine et sur la plaque plane a ensuite été réalisée.

Dans un deuxième temps, la configuration plaque plane lisse a été étudié. Il a d'abord été observé que la présence d'une paroi poreuse, sans aspiration, pouvait influencer la stabilité de la couche limite. Une analyse numérique complémentaire a ensuite démontré que cet effet pouvait être modélisé en modifiant la condition d'impédance à la paroi. Cette influence de la paroi poreuse sur la stabilité de la couche limite est donc un paramètre à prendre en compte lors de la conception d'un système d'aspiration. L'effet de la distribution spatiale de l'aspiration sur la transition a ensuite été caractérisé. Comme vu dans des études précédentes, les cas avec aspiration avaient une position de transition systématiquement retardée par rapport à celle du cas sans aspiration. De plus, la distribution spatiale était aussi un facteur à prendre en compte. En effet, pour le cas où l'aspiration était uniquement appliquée sur le premier caisson, la position de transition n'était pas aussi reculée que lorsque l'aspiration était divisée entre les caissons C3 et C5 ou sur toute la zone d'aspiration.

Dans un troisième temps, trois types de défauts de surface ont été introduits sur la plaque plane: des fils, des marches montantes et des rainures. Il a été observée que les dimensions critiques de ces trois types de défauts n'étaient pas influencées par l'aspiration. Toutefois, ces dimensions critiques dépendaient fortement du type de défaut. Pour les fils la hauteur critique était de $h/\delta_1 \sim 0.4$, pour les marches montantes de $h/\delta_1 \sim 1.3$ et pour les rainures la profondeur critique était de $h/\delta_1 \sim 1.4$ et la largeur critique de $b/\delta_1 \sim 14$. L'étude des données instationnaires a démontré que pour tous les défauts sous-critiques, où la transition avait lieu en aval du défaut, la transition était toujours gouvernée par les ondes de TS. Ceci est toujours vrai dans le cas des marches montantes. Pour les fils de hauteur relative critique, le mécanisme de transition bascule immédiatement du type visqueux au type inflexionnel, ce qui explique la hauteur critique relativement faible par rapport aux deux autres types de défauts. Finalement, dans le cas de la rainure critique, l'amplification des instabilités déjà existantes (ondes de TS) est augmentée et

une instabilité de type inflexionnelle est aussi introduite à l'intérieur de la rainure. Toutefois, comme les marches montantes et les rainures critiques ont toutes les deux tendances à augmenter l'amplification des ondes de TS, l'utilisation de la méthode du ΔN est justifiée pour modéliser leur effet sur la transition.

F5.2 Perspectives

Dans le cadre de cette étude, l'influence de trois types de défauts de surface a été étudié. La première recommandation pour de futurs travaux serait d'aumgenter le nombre de cas de rainures pour inclure plus de rainures critiques. Il serait aussi intéressant d'introduire des marches descendantes et de voir si leur comportement se rapproche plutôt des marches montantes/rainures ou des fils.

La deuxième proposition serait de réaliser une étude similaire à celle présentée ici mais sur un profil ou une section d'aile à des nombres de Reynolds et de Mach plus représentatifs de ceux rencontrés en vol. Ceci permettrait de vérifier que les conclusions issues de l'étude présente sont toujours valables et que l'aspiration retarde effectivement l'aspiration même en présence de défauts de surface sous-critiques. Ces conclusions fourniraient des arguments supplémentaires pour intégrer la technique d'aspiration sur les avions commerciaux.

Finalement, la dernière recommandation serait de continuer les travaux se concentrant sur la faisabilité de l'intégration et de la maintenance liée à l'intégration d'un système d'aspiration sur un avion commercial. L'efficacité de l'aspiration pariétale à retarder la transition est connue depuis plusieurs décennies et de nombreuses études jusqu'à maintenant l'ont démontrée. Toutefois, les problèmes pratiques liés à l'installation et la maintenance d'un tel système sont encore des obstacles non-négligeables qui doivent être résolus pour convaincre les avionneurs d'adopter cette technologie à une échelle industrielle.

Bibliography

Arnal, D., J. Perraud, and A. Séraudie (2008). "Attachment line and surface imperfection problems". In: *Advances in Laminar–Turbulent Transition Modeling, RTO-EN-AVT-151-09*, pp. 1–20 (cit. on p. 28).

Arnal, D., A. Séraudie, and J. Archambaud (2000). "Influence of surface roughness and of suction on the receptivity of a swept wing boundary layer". In: *Laminar-Turbulent Transition*. Springer, pp. 589–594. DOI: 10.1007/978-3-662-03997-7_91 (cit. on p. 21).

Béguet, S., J. Perraud, M. Forte, and J.-P. Brazier (2016). "Modeling of Transverse Gaps Effects on Boundary-Layer Transition". In: *Journal of Aircraft* 54.2, pp. 794–801. DOI: 10.2514/1.c033647 (cit. on pp. 30, 34–36).

Braslow, A. (1999). "A history of suction-type laminar flow control with emphasis on flight research". In: *Monographs in Aerospace History* 13 (cit. on pp. xxii, 19, 157).

Bruneau, M. (2006). *Fundamentals of acoustics*. London: ISTE Ltd. ISBN: 978-1-90-520925-5 (cit. on pp. 76, 164).

Burden, H. (1970). "The Effect of Wall Porosity on the Stability of Parallel Flows Over Compliant Boundaries". PhD thesis. University of Pennsylvania (cit. on p. 23).

Carmichael, B. (1959). *Surface waviness criteria for swept and unswept laminar suction wings*. Tech. rep. Northrop Aircraft Inc. NOR-59-438 (BLC-123) (cit. on p. 39).

Carmichael, B. and W. Pfenninger (1959). *Surface imperfection experiments on a swept laminar suction wing*. Tech. rep. Northrop Aircraft Inc. NOR-59-454 (BLC-124) (cit. on p. 39).

Carmichael, B., R. Whites, and W. Pfenninger (1957). *Low drag boundary layer suction experiments in flight on the wing glove of an F-94A airplane*. Tech. rep. Northrop Aircraft Inc. NAI-57-1163 (BLC-101) (cit. on p. 39).

Carpenter, P. (1990). "Status of transition delay using compliant walls". In: *Viscous drag reduction in boundary layers* 123, pp. 79–113. DOI: 10.2514/5.9781600865978.0079.0113 (cit. on p. 22).

Carpenter, P. and L. Porter (2001). "Effects of passive porous walls on boundary-layer instability". In: *AIAA Journal* 39.4, pp. 597–604. DOI: 10.2514/3.14775 (cit. on pp. 23, 24, 72).

Casalis, G., M.-L. Copie, C. Airiau, and D. Arnal (1996). "Nonlinear analysis with PSE approach". In: *IUTAM Symposium on Nonlinear Instability and Transition in Three-Dimensional Boundary Layers*, pp. 237–246. DOI: 10.1007/978-94-009-1700-2_23 (cit. on p. 69).

Charwat, A., J. Roos, and F. Dewey (1961). "An investigation of separated flows-Part I: the pressure field". In: *Journal of the Aerospace Sciences* 28.6, pp. 457–470. DOI: 10.2514/8.9037 (cit. on pp. 33, 119).

Choudhari, M. (1994). *Effect of nonzero surface admittance on receptivity and stability of compressible boundary layer*. Tech. rep. NASA 4621 (cit. on pp. 24, 72).

Costantini, M., S. Risius, and C. Klein (2015). "Experimental investigation of the effect of forward-facing steps on boundary layer transition". In: *Procedia IUTAM* 14, pp. 152–162. DOI: 10.1016/j.piutam.2015.03.036 (cit. on pp. 30, 35).

Cousteix, J. (1988). *Aérodynamique: couche limite laminaire*. Toulouse, France: Cepadues (cit. on p. 7).

Crandall, I. (1927). *Theory of Vibrating Systems and Sound*. New York, U.S.A.: van Nostrand Company (cit. on pp. 76, 164).

Crouch, J. (1994). "Theoretical studies on the receptivity of boundary layers". In: *Fluid Dynamics Conference*, p. 2224. DOI: 10.2514/6.1994-2224 (cit. on p. 24).

— (1997). "Transition prediction and control for airplane applications". In: *28th Fluid Dynamics Conference*, p. 1907. DOI: 10.2514/6.1997-1907 (cit. on p. 15).

Crouch, J., V. Kosorygin, and L. Ng (2006). "Modeling the effects of steps on boundary-layer transition". In: *IUTAM Symposium on Laminar-Turbulent Transition*. Springer, pp. 37–44. DOI: 10.1007/1-4020-4159-4_4 (cit. on pp. 36–38, 113, 115, 172).

Crowley, B. and C. Atkin (2016). "Investigation of the discrete effects of suction in large scale arrays for Laminar flow control". In: *34th AIAA Applied Aerodynamics Conference*, p. 3117. DOI: 10.2514/6.2016-3117 (cit. on p. 21).

Dovgal, A. and V. Kozlov (1990). "Hydrodynamic instability and receptivity of small scale separation regions". In: *Laminar-turbulent transition*. Springer, pp. 523–531. DOI: 10.1007/978-3-642-84103-3_47 (cit. on pp. 29, 31).

Dovgal, A., V. Kozlov, and A. Michalke (1994). "Laminar boundary layer separation: instability and associated phenomena". In: *Progress in Aerospace Sciences* 30.1, pp. 61–94. DOI: 10.1016/0376-0421(94)90003-5 (cit. on p. 28).

Dryden, H. (1953). "Review of published data on the effect of roughness on transition from laminar to turbulent flow". In: *Journal of the Aeronautical Sciences* 20.7, pp. 477–482. DOI: 10.2514/8.2693 (cit. on p. 29).

Fage, A. (1943). "The smallest size of a spanwise surface corrugation which affects boundary-layer transition on an aerofoil". In: *British Aerospace Research Council, Reports and Memoranda* 2120 (cit. on p. 29).

Feindt, E. (1956). "Investigation on the dependence of laminar-turbulent transition on surface roughness and pressure gradient". In: *Schiffbautechnischen Geselschaft Jahrbach* 50 (cit. on pp. 92, 93).

Forte, M., L. Gentili, S. Béguet, J. Perraud, and G. Casalis (2015). "Experimental and Numerical Study of the Effect of Gaps on the Laminar-Turbulent Transition for Two-Dimensional Incompressible Boundary-Layers". In: *50^{th} 3AF International Conference on Applied Aerodynamics*. DOI: 10.1016/j.piutam.2015.03.073 (cit. on pp. 30, 33, 36, 127).

Franco-Sumariva, J. and S. Hein (2018). "Adaptive Harmonic Linearized Navier-Stokes equations used for boundary-layer instability analysis in the presence of large streamwise gradients". In: *2018 Aerospace Sciences Meeting, AIAA Scitech Forum* AIAA2018-1548. DOI: 10.2514/6.2018-1548 (cit. on p. 39).

Fransson, J. H. (2004). "Leading edge design process using a commercial flow solver". In: *Experiments in fluids* 37.6, pp. 929–932. DOI: 10.1007/s00348-004-0858-3 (cit. on pp. 45, 145).

Fransson, J. and P. Alfredsson (2003). "On the disturbance growth in an asymptotic suction boundary layer". In: *Journal of Fluid Mechanics* 482. DOI: 10.1017/s0022112003003926 (cit. on p. 25).

Gaster, M. (1962). "A note on the relation between temporally-increasing and spatially-increasing disturbances in hydrodynamic stability". In: *Journal of Fluid Mechanics* 14.2, pp. 222–224. DOI: 10.1017/s0022112062001184 (cit. on p. 12).

Gentili, L. (2012). *Experimental study of the effect of gaps on the laminar/turbulent transition for incompressible boundary layers*. Tech. rep. ONERA (cit. on p. 123).

Goldstein, M. (1985). "Scattering of acoustic waves into Tollmien-Schlichting waves by small streamwise variations in surface geometry". In: *Journal of Fluid Mechanics* 154, pp. 509–529. DOI: 10.1017/s0022112085001641 (cit. on p. 29).

Gregory, N. (1962). *On critical suction conditions for laminar boundary-layer control by suction in perforation*. Tech. rep. Aeronautical Research Council Report No. 24 (cit. on p. 21).

Hahn, M. and W. Pfenninger (1973). "Prevention of transition over a backward step by suction". In: *Journal of Aircraft* 10.10, pp. 618–622. DOI: 10.2514/3.60269 (cit. on p. 39).

Head, M. (1955). "The boundary layer with distributed suction". In: *British A.R.C. Reports & Memoranda* 2783 (cit. on p. 19).

Heinrich, R., M. Choudhari, and E. Kerschen (1988). "A comparison of boundary layer receptivity mechanisms". In: *1st National Fluid Dynamics Conference*, p. 3758. DOI: 10.2514/6.1988-3758 (cit. on pp. 23, 24).

Herbert, T. (1988). "Secondary instability of boundary layers". In: *Annual Review of Fluid Mechanics* 20.1, pp. 487–526. DOI: 10.1146/annurev.fluid.20.1.487 (cit. on p. 11).

— (1997). "Parabolized Stability Equations". In: *Annual Review of Fluid Mechanics* 29.1, pp. 245–283. DOI: 10.1146/annurev.fluid.29.1.245 (cit. on p. 68).

Holmes, B., C. Obara, G. Martin, and C. Domack (1985). "Manufacturing tolerances for natural laminar flow airframe surfaces". In: *SAE Transactions*, pp. 522–531. DOI: 10.4271/850863 (cit. on pp. 17, 35).

Houdeville, R. (1992). "Three-dimensional boundary layer calculation by a characteristic method". In: *Fifth symposium on Numerical and Physicals Aspects of Aerodynamic Flows, Long Beach, CA* (cit. on p. 16).

Hunt, L., R. Downs, M. Kuester, E. White, and W. Saric (2010). "Flow quality measurements in the Klebanoff-Saric wind tunnel". In: *27th AIAA Aerodynamic Measurement Technology and Ground Testing Conference, AIAA2010-4538*. DOI: 10.2514/6.2010-4538 (cit. on p. 51).

Joslin, R. (1998). *Overview of laminar flow control*. Tech. rep. NASA/TP-1998-208705 (cit. on pp. 19, 21).

Juillen, J., G. Casalis, and D. Arnal (1995). *Aspiration discontinue : résultats expérimentaux et comparaisons aux résultats de calculs de stabilité*. Tech. rep. CERT DERAT 107/5018.93 (cit. on pp. 20, 68, 69, 80, 166).

Juillen, J., J. Reneaux, and D. Arnal (1999). *Etude expérimentale et théorique sur les problèmes liés à l'aspiration de la couche limite. Partie A : étude expérimentale*. Tech. rep. CERT RT 2/5118.34 (cit. on p. 20).

Klebanoff, P. and K. Tidstrom (1972). "Mechanism by Which a Two-Dimensional Roughness Element Induces Boundary-Layer Transition". In: *The Physics of Fluids* 15.7, pp. 1173–1188. DOI: 10.1063/1.1694065 (cit. on pp. 28, 29, 32, 89).

Krishnan, K., O. Bertram, and O. Seibel (2017). "Review of hybrid laminar flow control systems". In: *Progress in Aerospace Sciences* 93, pp. 24–52. DOI: 10.1016/j.paerosci.2017.05.005 (cit. on pp. 21, 22).

Lekoudis, S. (1978). "Stability of boundary layers over permeable surfaces". In: *16th Aerospace Sciences Meeting*, p. 203. DOI: 10.2514/6.1978-203 (cit. on p. 23).

Al-Maaitah, A., A. Nayfeh, and S. Ragab (1990). "Effect of suction on the stability of subsonic flows over smooth backward-facing steps". In: *AIAA Journal* 28.11, pp. 1916–1924. DOI: 10.2514/6.1989-983 (cit. on pp. 39, 40).

Mack, L. (1977). "Transition and laminar instability". In: *JPL Publication 77-15* (cit. on pp. xxii, 15, 91, 96).

MacManus, D. and J. Eaton (1996). "Predictions and observations of the flow field induced by laminar flow control microperforations". In: *Experimental thermal and fluid Science* 13.4, pp. 395–407. DOI: 10.1016/s0894-1777(96)00094-5 (cit. on p. 20).

Maddalon, D. (1991). "Hybrid Laminar Flow Control flight research". In: *Research and Technology, NASA, TM* 4331, p. 47 (cit. on p. 20).

Maddalon, D., F. Collier, L. Montoya, and R. Putnam (1990). "Transition flight experiments on a swept wing with suction". In: *Laminar-Turbulent Transition*. Springer, pp. 53–62. DOI: 10.1007/978-3-642-84103-3_4 (cit. on p. 20).

Marec, J.-P. (2001). "Drag reduction: a major task for research". In: *Aerodynamic Drag Reduction Technologies*. Springer, pp. 17–27. DOI: 10.1007/978-3-540-45359-8_3 (cit. on pp. xxi, 17).

Meyer, J., K. de Groot, C.-P. Kruckeberg, T. Weddig, M. Sitzmann, and K. Horstmann (2003). "System layout and instrumentation of a laminar flow system for the DLR Do 228 test vehicle". In: *CEAS Conference, London, U.K.* (Cit. on p. 22).

Michalke, A. and A. Al-Maaitah (1992). "On the receptivity of the unstable wall boundary layer along a surface hump excited by a 2-D Dirac source at the wall". In: *European Journal of Mechanics B Fluids* 11, pp. 521–542 (cit. on p. 29).

Morkovin, M., E. Reshotko, and T. Herbert (1994). "Transition in open flow systems-a reassessment". In: *Bull. Am. Phys. Soc.* 39, p. 1882 (cit. on pp. 11, 49, 51).

Nayfeh, A., S. Ragab, and A. Al-Maaitah (1987). "Effect of roughness on the stability of boundary layers". In: *4th Joint Fluid Mechanics, Plasma Dynamics and Lasers Conference*, p. 1044. DOI: 10.2514/6.1986-1044 (cit. on p. 32).

Nayfeh, A., S. Ragab, and J. Masad (1990). "Effect of a bulge on the subharmonic instability of boundary layers". In: *Physics of Fluids A: Fluid Dynamics* 2.6, pp. 937–948. DOI: 10.1063/1.857654 (cit. on p. 29).

Nenni, J. and G. Gluyas (1966). "Aerodynamic design and analysis of an LFC surface". In: *Astronautics & Aeronautics* 4.7, p. 52 (cit. on pp. 35, 45).

Olive, M. and A. Blanchard (1982). *Etude expérimentale du déclenchement de la transition par des cavités en écoulement incompressible*. Tech. rep. CERT DERAT OA18/5007 (cit. on pp. 33, 36, 123, 136, 170).

Perraud, J. (1997). *Étude de l'influence de rugosités bidimensionnelles - marches et rainures - sur la transition laminaire-turbulent. Approche locale.* Tech. rep. CERT DERAT 126/5118.35 (cit. on pp. 31, 37).

Perraud, J., D. Arnal, and W. Kuehn (2014). "Laminar-turbulent transition prediction in the presence of surface imperfections". In: *Int. J. Engineering Systems Modelling and Simulation* 6.3/4, pp. 162–170. DOI: 10.1504/ijesms.2014.063129 (cit. on pp. 33, 34, 38, 131, 133).

Perraud, J. and A. Séraudie (2000). "Effects of steps and gaps on 2D and 3D transition". In: *European Congress on Comp. Methods in Applied Science and Eng., ECCOMAS*, pp. 11–14 (cit. on pp. 31, 32).

Prandtl, L. (1904). "Motion of fluids with very little viscosity". In: *Heidelberg Mathematical Congress, English translation available as NASA-TM-452* (cit. on pp. xxi, 3).

Rayleigh, J. (1880). "On the stability, or instability, of certain fluid motions". In: *Proc. London Math. Soc.* 9, pp. 57–70. DOI: 10.1112/plms/s1-11.1.57 (cit. on pp. 28, 96).

Reed, H., W. Saric, and D. Arnal (1996). "Linear stability theory applied to boundary layers". In: *Annual Review of Fluid Mechanics* 28.1, pp. 389–428. DOI: 10.1146/annurev.fl.28.010196.002133 (cit. on p. 79).

Reneaux, J. and A. Blanchard (1992). "The design and testing of an airfoil with hybrid laminar flow control". In: *DGLR/AAAF/RAeS 1st European Forum on Laminar Flow* (cit. on p. 20).

Reynolds, G. and W. Saric (1986). "Experiments on the stability of the flat-plate boundary layer with suction". In: *AIAA Journal* 24.2, pp. 202–207. DOI: 10.2514/3.9246 (cit. on p. 19).

Rossiter, J. (1964). *Wind tunnel experiments on the flow over rectangular cavities at subsonic and transonic speeds*. Tech. rep. Ministry of Aviation, Royal Aircraft Establishment (cit. on p. 33).

Saric, W. (2008). "Experiments in 2-D Boundary Layers: stability and receptivity". In: *Advances in Laminar-Turbulent Transition Modelling, NATO Educational Notes*, pp. 8–1 (cit. on pp. 45, 51).

Saric, W., A. Carpenter, and H. Reed (2011). "Passive control of transition in three-dimensional boundary layers, with emphasis on discrete roughness elements". In: *Philosophical Transactions of the Royal Society A: Mathematical, Physical and Engineering Sciences* 369.1940, pp. 1352–1364. DOI: 10.1098/rsta.2010.0368 (cit. on p. 18).

Sarohia, V. (1977). "Experimental investigation of oscillations in flows over shallow cavities". In: *AIAA Journal* 15.7, pp. 984–991. DOI: 10.2514/6.1976-182 (cit. on pp. 33, 119).

Schlichting, H. (1930). "Über das ebene Windschattenproblem". In: *Ingenieur-Archiv* 1.5, pp. 533–571. DOI: 10.1007/bf02079870 (cit. on p. 11).

Schrauf, G. (2004). "Large-scale laminar flow tests evaluated with linear stability theory". In: *Journal of Aircraft* 41.2, pp. 224–230. DOI: 10.2514/1.9280 (cit. on p. 21).

Schubauer, G. and H. Skramstad (1948). "Laminar-boundary-layer oscillations and transition on a flat plate". In: *NACA Report 909*. DOI: 10.6028/jres.038.013 (cit. on p. 11).

Séraudie, A. (2010). *Influence of gaps and holes on boundary layer, in 2D and 3D flows*. Tech. rep. ONERA RT-4/14790 (cit. on p. 123).

Sinha, S., A. Gupta, and M. Oberai (1981). "Laminar separating flow over backsteps and cavities. I-Backsteps". In: *AIAA journal* 19.12, pp. 1527–1530. DOI: 10.2514/3.7885 (cit. on p. 31).

— (1982). "Laminar separating flow over backsteps and cavities. II-Cavities". In: *AIAA journal* 20.3, pp. 370–375. DOI: 10.2514/3.7918 (cit. on pp. 33, 34, 36, 119).

Smith, A. and N. Gamberoni (1956). *Transition, pressure gradient and stability theory*. Tech. rep. Douglas Aircraft Co. ES 26388 (cit. on p. 15).

Squire, H. B. (1933). "On the Stability for Three-Dimensional Disturbances of Viscous Fluid Flow between Parallel Walls". In: *Proceedings of the Royal Society A: Mathematical, Physical and Engineering Sciences* 142.847, pp. 621–628. DOI: 10.1098/rspa.1933.0193 (cit. on p. 12).

Stuper, J. (1949). "The influence of surface irregularities on transition with various pressure gradients". In: *Division of Aeronautics, Australia Report* A59 (cit. on p. 30).

Tani, I. (1961). "Effect of two-dimensional and isolated roughness on laminar flow". In: *Boundary layer and flow control*. Elsevier, pp. 637–656. DOI: 10.1016/b978-1-4832-1323-1.50004-x (cit. on pp. xxiii, 28, 30, 31, 89, 92).

Tani, I. and F. Hama (1953). "Some experiments on the effect of a single roughness element on boundary-layer transition". In: *Journal of the Aeronautical Sciences* 20.4, pp. 289–290. DOI: 10.2514/8.2613 (cit. on p. 30).

Tilton, N. and L. Cortelezzi (2015). "Stability of Boundary Layers over Porous Walls with Suction". In: *AIAA Journal* 53.10, pp. 2856–2868. DOI: 10.2514/1.j053716 (cit. on pp. 24, 25, 72).

Tollmien, W. (1929). "Über die entstehung der turbulenz. Nachr. Ges. Wiss. Göttingen 21–24". In: *English translation 1931, NACA TM609*. DOI: 10.1007/978-3-662-33791-2_4 (cit. on p. 11).

Van Ingen, J. (1956). "A suggested semi-empirical method for the calculation of the boundary layer transition region". In: *Technische Hogeschool Delft, Vliegtuigbouwkunde, Rapport VTH-74* (cit. on p. 15).

Wang, Y. and M. Gaster (2005). "Effect of surface steps on boundary layer transition". In: *Experiments in Fluids* 39.4, pp. 679–686. DOI: 10.1007/s00348-005-1011-7 (cit. on pp. 31, 36, 38, 104, 105, 113, 115, 142, 172).

Watanabe, T. and R. Kobayashi (1991). "Effect of a single roughness element on boundary layer transition over a wedge". In: *Experimental Thermal and Fluid Science* 4.5, pp. 558–566. DOI: 10.1016/0894-1777(91)90034-o (cit. on pp. 32, 96).

Wetmore, J., J. Zalovcik, and P. R.C. (1941). *A flight investigation of the boundary layer characteristics and profile drag of the NACA 35-215 laminar-flow airfoil at high Reynolds numbers*. Tech. rep. NACA WR L-532 (cit. on p. 19).

Wörner, A., U. Rist, and S. Wagner (2003). "Humps/Steps Influence on Stability Characteristics of Two-Dimensional Laminar Boundary Layer". In: *AIAA Journal* 41, pp. 192–197. DOI: 10.2514/2.1960 (cit. on pp. 32, 35, 39).

Yavuzkurt, S. (1984). "A guide to uncertainty analysis of hot-wire data". In: *ASME, Transactions, Journal of Fluids Engineering* 106.2, pp. 181–186. DOI: 10.1115/1.3243096 (cit. on pp. 56, 59).

Zahn, J. and U. Rist (2015). "Impact of Deep Gaps on Laminar–Turbulent Transition in Compressible Boundary-Layer Flow". In: *AIAA Journal* 54.1, pp. 66–76. DOI: 10.2514/1.j054112 (cit. on pp. 34, 119).

— (2018). "Study About Boundary-Layer Suction at a Juncture for Sustained Laminar Flow". In: *New Results in Numerical and Experimental Fluid Mechanics XI*. Springer, pp. 349–358. DOI: ttps://doi.org/10.1007/978-3-319-64519-3_32 (cit. on pp. 21, 40).

An Experimental Investigation of the Effects of Surface Defects on the Laminar-Turbulent Transition of a Boundary Layer with Wall Suction

Abstract The projected increase in air traffic volume has led to a renewed interest in drag reduction research to reduce aviation's environmental impact. One solution is wall suction, which can effectively postpone the laminar-turbulent transition of a boundary layer developing over an aircraft's wetted area. Since a boundary layer in the laminar regime has lower skin-friction coefficient than in the turbulent regime, a delayed transition results in lower drag and reduced fuel consumption. However, implementing a suction system is likely to introduce surface defects, especially at the junction between the suction and solid panels. Additionally, surface defects generally tend to promote transition, and could therefore cancel any drag reduction achieved by wall suction.

The aim for the present research is to study the combined effects of surface defects and wall suction on the transition of a Blasius boundary layer in two-dimensional incompressible flow. First, an experimental protocol was developed and implemented to verify the quality of the aerodynamic conditions in the test facility, and establish a reference for the smooth case with different suction distributions. As expected, wall suction always delayed transition, compared to the configuration without suction, and had varying effectiveness depending on the suction configuration. Concurrently, porous panels without suction were found to destabilize the boundary layer. Subsequently, three types of surface defects (wires, forward-facing steps and gaps) were tested with wall suction. No significant differences between configurations with and without suction were observed. In particular, the critical defect dimensions (height and/or width), for which transition occurs at the defect location, were identical regardless of the suction configuration. For subcritical defects (where transition is not triggered immediately) however, wall suction could still delay transition, albeit less effectively than in the smooth case.

Keywords: Boundary layer, Laminar-turbulent transition, Laminar Flow Control, Tollmien-Schlichting instabilities, Wall Suction, Surface defects.

Étude expérimentale de l'influence de défauts de surface sur la transition laminaire-turbulent d'une couche limite aspirée

Résumé L'accroissement prévu du trafic aérien s'accompagne de forts enjeux économiques et environnementaux, nécessitant en particulier de réduire la consommation en carburant des aéronefs modernes. Pour cela, l'aspiration pariétale est une méthode qui permet de retarder la transition laminaire-turbulent des couches limites qui se développent à la surface des aéronefs, entrainant une réduction significative de la force de traînée et donc de la consommation en carburant. En effet, le coefficient de frottement d'une couche limite en régime laminaire est beaucoup plus faible qu'en régime turbulent. Toutefois, l'installation d'un système d'aspiration induit inévitablement des discontinuités géométriques (ou défauts de surface), en particulier à la jonction entre la zone aspirée et la zone pleine (sans aspiration). Or, ces défauts sont susceptibles de déclencher une transition prématurée, pouvant ainsi complètement annuler l'effet positif de l'aspiration.

L'objectif de cette thèse est d'étudier expérimentalement l'effet de défauts de surface sur la transition d'une couche limite aspirée dans un écoulement incompressible et bidimensionnel. Dans un premier temps, un protocole expérimental a été mis en place pour vérifier la qualité de l'écoulement de la soufflerie et préciser un cas de référence pour la configuration lisse, sans défaut. En particulier, l'influence de la distribution longitudinale de l'aspiration sur la position de la transition a été étudiée, confirmant ainsi que tous les cas avec aspiration, qu'elle qu'en soit la distribution, permettaient de repousser la transition vers l'aval. En parallèle, il a été observé qu'une couche limite se développant au-dessus d'une paroi poreuse sans aspiration pouvait être déstabilisée. Dans un second temps, l'influence de trois types de défauts de surface (fils, marches montantes et rainures) a été étudiée. Les mesures ont montré le même comportement sur paroi pleine et sur paroi aspirée. En particulier, les dimensions critiques des défauts (hauteur et/ou largeur) à partir desquelles la transition a lieu au niveau du défaut restent inchangées. Toutefois, dans le cas de défauts sous-critiques, pour lesquels la transition n'est pas déclenchée immédiatement, l'aspiration permet toujours de retarder la transition.

Mots clés: couche limite, transition laminaire-turbulent, contrôle d'écoulement, instabilités de Tollmien-Schlichting, aspiration pariétale, défauts de surface